Growth of Narrow Band Gap Semiconductor Nanowires on Silicon and Graphitic substrates by Droplet Epitaxy

by

Anyebe, Ezekiel Anyebe

M.Sc (Hons)

June 2015

A thesis submitted in fulfilment for the degree of Doctor of Philosophy

Faculty of Science and Technology

Department of Physics

Lancaster University

Abstract

This thesis is focused on the growth of narrow band gap semiconductor nanowires (NWs) on silicon and graphite by droplet epitaxy. First, the growth conditions of In droplets suitable for the nucleation of NWs was identified. Vertically-aligned and non-tapered InAs NWs were then realized on bare Si. It is shown that the diameter and areal density of NWs are defined by the geometry of pre-deposited In droplets. The NWs exhibit a dominant PL peak associated with the band to band (BtB) emission in addition to a distinct BtB temperature dependent red-shift, strong emission efficiency (up to 250^0C) and record narrow spectral linewidth of ~20 meV (at 10K) which is relatively smaller than previously reported values. This demonstrates the high optical properties of the droplet epitaxy grown InAs NWs.

Vertically-aligned and non-tapered $InAs_{1-x}Sb_x$ NWs have been demonstrated on Si without the commonly used NWs stems. In addition, the effect of Sb addition to the morphology of self-catalyzed InAsSb NWs grown directly on Si is systematically investigated for the first time. It is shown that trace Sb flux significantly promotes lateral NWs growth while at the same time suppressing axial growth. Furthermore, Sb-induced crystal phase evolution is elucidated as a function of Sb content. Although, pure InAs NWs show a mixture of Wurtzite (WZ) and Zinc-Blende (ZB) phases, a crystal phase evolution from a highly polytypic InAs to a quasi-pure WZ InAsSb NWs (2-4% Sb content) and a quasi-pure ZB InAsSb NWs crystals (~10% Sb content) is demonstrated in addition to a significant reduction in the stacking fault density in as-grown NWs with increasing Sb content.

The recent discovery of flexible graphene has triggered a new wave of optoelectronic revolution. In order to fully exploit the enormous potential of functional monolithic NWs/graphene hybrid structures, the optimal growth conditions for realizing morphologically and structurally superior InAs NWs on graphitic substrates has been identified. Vertically well-

ii

aligned and thin InAs NWs were obtained in a narrow growth window of 420-450ºC while a high yield of NWs was realized within a restricted domain of growth rate and V/III flux ratio. Compared to the growths on Si, the graphitic substrate is shown to enhance adatom mobility and enable growth at high growth rate which is highly promising for cost-effective devices. In addition, the NWs on graphite show a significantly reduced density of defect in comparison to the growth on conventional Si substrates owing to van der Waals epitaxy growth technique resulting from the absence of dangling bonds.

Moreover, high aspect ratio NWs are essential for functional device applications however, the growth of thin $InAs_{1-x}Sb_x$ NWs is extremely challenging owing to Sb-induced lateral growth. The growth of ultra-high aspect ratio $InAs_{1-x}Sb_x$ NWs ($0 \leq x \leq 0.12$) on graphite is demonstrated for the first time at highly As-rich conditions with potential for applications in ultra-sensitive, eco-friendly, flexible and cost-effective infrared photodetectors. It is shown that the graphitic thin film promotes Sb incorporation and is more favourable for InAsSb NWs growth in comparison to Si substrates.

Finally, a morphological evolution from InN NCs to three dimensional (3D) InN islands is demonstrated with increasing growth temperature attributable to lowered surface free energy of the growing crystals with disproportionate growth velocities along different growth fronts.

Acknowledgements

List of Publications

1. **E. A. Anyebe**, Q. Zhuang, A. M. Sanchez, S. Lawson, A. J. Robson, L. Ponomarenko, A. Zhukov, O. Kolosov, *"Self-catalysed growth of InAs nanowires on bare Si substrates by droplet epitaxy"*, Phys. Status Solidi (RRL) **8**, 658 (2014).

2. Q. Zhuang, **E. A. Anyebe**, A. M. Sanchez, M. K. Rajpalke, T. D. Veal, A. Zhukov, B. J. Robinson, F. Anderson, O. Kolosov, V. Fal'ko, *"Graphitic platform for self-catalysed InAs nanowires growth by molecular beam epitaxy"* Nanoscale Res. Lett. **9**, 321 (2014).

3. **E.A. Anyebe**, Q. Zhuang, M. Kesaria, A. Krier, *"The structural evolution of InN nanorods to microstructures on Si (111) by molecular beam epitaxy"*, Semicond. Sci. Technol. **29**, 085010 (2014).

4. **E. A. Anyebe**, Q. Zhuang, *"Self-catalysed InAs$_{1-x}$Sb$_x$ nanowires grown directly on bare Si substrates"*, Mater. Res. Bull. **60**, 572 (2014).

5. **E. A. Anyebe**, M. K. Rajpalke, T. D. Veal, C. J. Jin, Z. M. Wang and Q. Zhuang, "Surfactant effect of antimony addition to the morphology of Self-catalyzed InAs$_{1-x}$Sbx nanowires" Nano Research, **8**, 1309 (2015)

6. Q. D. Zhuang**, E. A Anyebe**, R. Chen, H. Liu, A.M Sanchez, M. K Rajpalke, T. D. Veal, Z. M. Wang, Y. Z. Huang, H. D. Sun, *"Sb-induced phase control of InAs nanowires grown by molecular beam epitaxy"*, Nano. Lett. **15**, 1109 (2015).

7. **E. A. Anyebe**, Q. Zhuang, M. K. Rajpalke, T. D. Veal, A. M. Sanchez, B. J. Robinson, O. Kolosov, V. Fal'ko, *"Graphite platform for the realization of vertically-aligned InAsSb nanowires with ultra-high aspect ratio"*
(Under Review for Nano. Lett.)

Conference Presentations

1. **E.A. Anyebe**, Q. Zhuang, B. Robinson, O Kolosov, V. Fal'ko, A. Krier, *"Semiconductor nanowires for highly efficient optoelectronic device applications"*, Postgraduate Research Conference 2014, 22nd March, Lancaster, UK (Oral presentation).

2. **E.A. Anyebe**, Q. Zhuang, B. Robinson, O. Kolosov, V. Fal'ko, *"Van der waals heteroepitaxy of high quality InAs nanowires on graphite for high-performance flexible devices"*, Nanowires workshop 2013, 12-15th November, Rehovot, Israel (Oral presentation).

3. **E.A. Anyebe**, Q. Zhuang, B. Robinson, O Kolosov, V. Fal'ko, D. Hynes, F. Anderson, *"Heteroepitaxial growth of free-standing InAs nanowires on Graphite for flexible devices"*, 22nd European workshop on Heterostructure Technology (HETECH) 2013, 9-11th September, Glasgow, Scotland (Oral presentation).

4. Q. Zhuang, **E.A. Anyebe**, B. Robinson, O. Kolosov, V. Fal'ko, "InAsSb nanowires on graphite for flexible and cost-effective devices", 16th international conference on Narrow Gap systems 2013, 2-6th August, China (Oral presentation).

5. **E.A. Anyebe**, Q. Zhuang, B. Robinson, O Kolosov, V. Fal'ko, **"***Towards flexible and low-cost devices: Growth of Semiconductor nanowires on Graphite"*,** Postgraduate Research Conference 2013, 13th July, Lancaster, UK, (Oral presentation).

6. **E.A. Anyebe**, Q. Zhuang, O Kolosov, V. Fal'ko D. Hynes, F. Anderson and A. Krier, *"High-quality InAs nanowires grown on Si (111) by droplet epitaxy"*,UK Semiconductor Conference 2013, 3-4th July, Sheffield, UK (Oral presentation).

7. *E. A. Anyebe, Q. Zhuang, A. Krier, "Semiconductor Nanowires: Properties and potential applications"*, Postgraduate Research Conference 2014, 22nd March, Lancaster, UK, (Poster presentation).

8. **E.A. Anyebe**, Q. Zhuang, *"InAsSb nanowires for flexible and cost-effective devices"*, Internatonal conference on one-dimensional nanomaterials, (ICON) 2013, 23 – 26th September, Annecy, France, (Poster presentation).

9. **E.A. Anyebe**, Q. Zhuang, *"Temperature-induced evolution of InN Nanorods by Molecular Beam epitaxy"*, Internatonal conference on one-dimensional nanomaterials, (ICON) 2013, 23 – 26th September, Annecy, France, (Poster presentation).

10. **E.A. Anyebe**, Q. Zhuang, A. Krier, *"Growth and characterization of InN Nanostructures"*, Postgraduate Research Conference 2013, 13th July, Lancaster, UK (Poster presentation).

11. **E.A. Anyebe**, Q. Zhuang, A. Krier, "*Structural characterization of strain-free InN Islands grown on Si (111) by Plasma-assisted Molecular Beam Epitaxy",* UK Semiconductor Conference 2013, 3-4th July, Sheffield, UK (Poster presentation).

12. **E.A. Anyebe**, Q. Zhuang, A. Krier, "*MBE droplet epitaxy of highly uniform InAs nanowires on bare Si (111)"*, 7th Nanowire growth workshop 2013, 10-12th June, Lausanne, Switzerland (Poster presentation).

13. **E.A. Anyebe**, Q. Zhuang, A. Krier, "*Optimizing MBE growth conditions towards InN NanoRods"*, 7th Nanowire growth workshop 2013, 10-12th June, Lausanne, Switzerland (Poster presentation).

14. ***E. A. Anyebe**, Q. Zhuang, A. Krier, "Strain-free InN Micro-grains Grown by Plasma-assisted Molecular Beam Epitaxy",* UK Semiconductor Conference 2012, 4-5th July, Sheffield, UK (Poster presentation).

15. **E. A. Anyebe**, Q. Zhuang, A. Krier, "*MBE Growth of InGaN Nanowires on Si for Low Cost and Highly Efficient Hybrid Solar Cells",* Faculty of Science and Technology, Lancaster University Christmas Conference 2011, 20th December, Lancaster, UK (Poster presentation).

Contents

List of Figures

List of Tables

List of Abbreviations

AFM   -   Atomic Force Microscopy

CBE -   Chemical Beam Epitaxy

EDX -   Energy Dispersive X-ray

FWHM   -   Full Width at Half Maxima

LED -   Light-Emitting Diode

MBE -   Molecular Beam Epitaxy

MOCVD -   Metal Organic Chemical Vapour Deposition

MoS_2 - Molybdenum disulphide

MOVPE -   Metal-Organic Vapour Phase Epitaxy

NWs -   Nanowires

PL -   Photoluminescence

RHEED -   Reflection High-Energy Electron Diffraction

SEM -   Scanning Electron Microscopy

SFs -   Stacking Faults

Si -   Silicon

SiOx -   Silicon Oxide

TEM -   Transmission Electron Microscopy

TPL - Triple Phase Line

TPs - Twin Planes

UHV - Ultra high vacuum

VLS - Vapor Liquid Solid

VS - Vapor Solid

WZ - Wurtzite

XRD - X-ray Diffraction

ZB - Zinc Blende

Chapter 1

Introduction

Fuelled by the top-down miniaturization and increased packing density of silicon complementary metal–oxide–semiconductor (CMOS) transistors in a single microelectronic chip, the exponential rise in the power of electronics with significant improvements in speed and logic performance has triggered a microelectronic revolution[1, 2]. This extraordinary advancement in the electronic industry is founded on Moore's law[3] which proposes an exponential rise in the number of transistors cramped onto an integrated circuit (single silicon chip) without increasing the unit cost while leading to faster and more powerful devices. This is illustrated in Figure 1.1[4]. For instance, a single microprocessor can contain a 32-gigabyte memory with as many ~256 billion transistors[1]. However, the transistor dimensions have shrunk to such an extent that it significantly degrades the electrical characteristics of devices, threatening to end the current revolution. In particular, the downscaling is constrained by excessive power density dissipation with an accompanying risk of increased packaging and cooling costs which is impractical for most applications[2]. Aside from the dearth of suitable technique for carving out ever-smaller structures, the control of the quality and uniformity of bulk crystals are compromised on the nanoscale[5]. The "bottom-up" approach which involves the atom-by-atom assembly of nanoscale device components from their fundamental components, as opposed to the ''top-down'' approach where materials in bulk form are shaped down to nanoscale via etching strategies[6] is potentially considered a leading candidate for circumventing this challenge. In particular, semiconductor nanowires (NWs) are highly promising low-dimensional materials for driving the 21st century microelectronic revolution owing to their extraordinary optical, electronic and structural properties coupled with their

reproducible and precisely controlled synthesis and geometry[7-10] which are key requirements for functional device applications. The bottom-up approach has emerged as a 21st century's cutting edge technique which has enabled the fabrication of sophisticated NWs
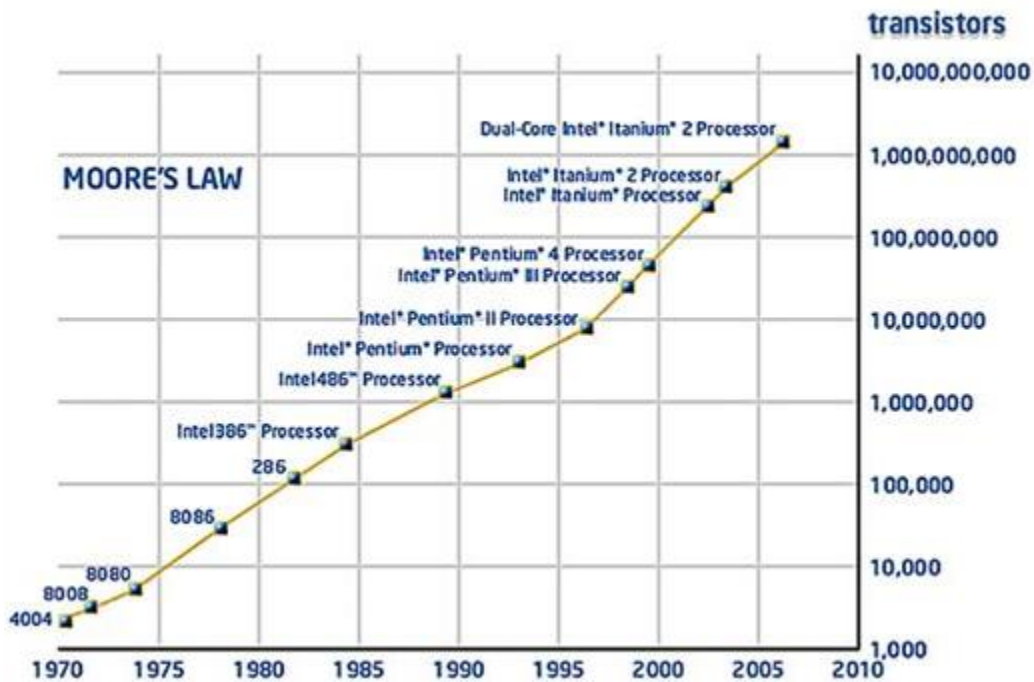
Figure 1.1 Moore's Law from 1970 - 2005 (Intel) (Extracted from Ref. 4).

devices otherwise not possible with conventional top-down approaches[11, 12]. The properties and functionality of NWs are dictated by an increased understanding of optimized growth technique as well as the ability to reliably and precisely predict and control their dimensions, structures, distribution and optical properties at an atomic level. It is on this premise that this thesis seeks to investigate the optimum conditions for the fabrication of high quality narrow band gap semiconductor NWs with improved structural and optical properties for applications in highly efficient infrared photodetectors and high speed devices. In addition, it explores controllable, cost-effective and time-efficient route to fabricating functional monolithic hybrid structures of narrow band gap semiconductor NWs on silicon and graphitic substrates.

The outline of the thesis is structured as follows:

Chapter 1 highlights the motivation for this research.

Chapter 2 unravels key theoretical concepts in relation to narrow band gap semiconductors, NWs growth mechanism and growth technique.

Chapter 3 presents a review of existing literature focused on InAs(Sb) and InN semiconductors NWs

In chapter 4, the various experimental techniques employed for the investigation of the properties of NWs are reported. In particular, the MBE growth apparatus and the basic set ups utilized for the morphological, structural and optical characterization of as-grown NWs are described.

Chapter 5 details the procedure for optimizing the growth conditions of In droplets suitable for NWs nucleation. In addition, the results of In-assisted InAs NWs growth on bare silicon are reported along with studies focused on the effect of growth parameters on NWs morphology and spatial distribution. Finally, the photoluminescence properties of as-grown NWs are presented.

Chapter 6 elucidates the growth and characterization of InAsSb NWs. The effect of Sb addition on the morphology and structural property of InAsSb NWs is also explicated.

Chapter 7 highlights the growth procedure of InAs(Sb) NWs on graphitic substrates as well as the growth parameter studies of as-grown NWs.

The growth and characterization of InN NWs on bare Si (111) substrates is presented in chapter 8. Additionally, it expounds on the effects of growth temperature on InN NWs growth.

Chapter 9 presents the conclusion, outlook and future directions.

Chapter 2

Theoretical Concepts

Basic theoretical concepts relevant to this study are presented in this chapter including semiconductor materials, nanowires, droplet epitaxy, van der Waals epitaxy and nanowires deposition techniques.

2.1   Semiconductors Material

Semiconductors have revolutionised every facet of the human life as drivers of modern electronic and optoelectronic devices including transistors, solar cells, light-emitting diodes (LEDs) and integrated circuits. They exhibit electrical conductivity in between metals and insulators. Most common semiconducting materials are crystalline solids and their properties largely depend on their crystalline structure[13]. Electrons in semiconductor crystals are arranged in energy levels or bands; the conduction band above and the valence band below, separated by a forbidden region also known as the band gap (E_g) defined as the energy difference between the lowest point of the conduction band (conduction band edge) and the highest point of the valence band (valence band edge) denoted as E_C and E_V respectively. Materials are categorized as insulators, semiconductors or conductors depending on the width of the band gap (in energy units) as illustrated in figure 2.1 with the chemical potential (μ) of electrons in a semiconductor material at 0K known as the Fermi level. The conductivity or otherwise of a pure material to an applied electric field is strongly dependent on the ease with which electrons are transferred from the valence to conduction band as a function of the band gap. Compared to insulators with filled or empty energy bands and very large band gaps, conductors have overlapping bands or partly filled band with small or no band gaps consequently they are very good conductors as opposed to insulators which exhibit poor

conductivity. Semiconductors possess slightly filled or slightly empty bands[13] with small band gaps in between that of insulators and metals such that electrons from the valence band can easily gain sufficient energy ($> E_g$) to migrate into the conduction band.
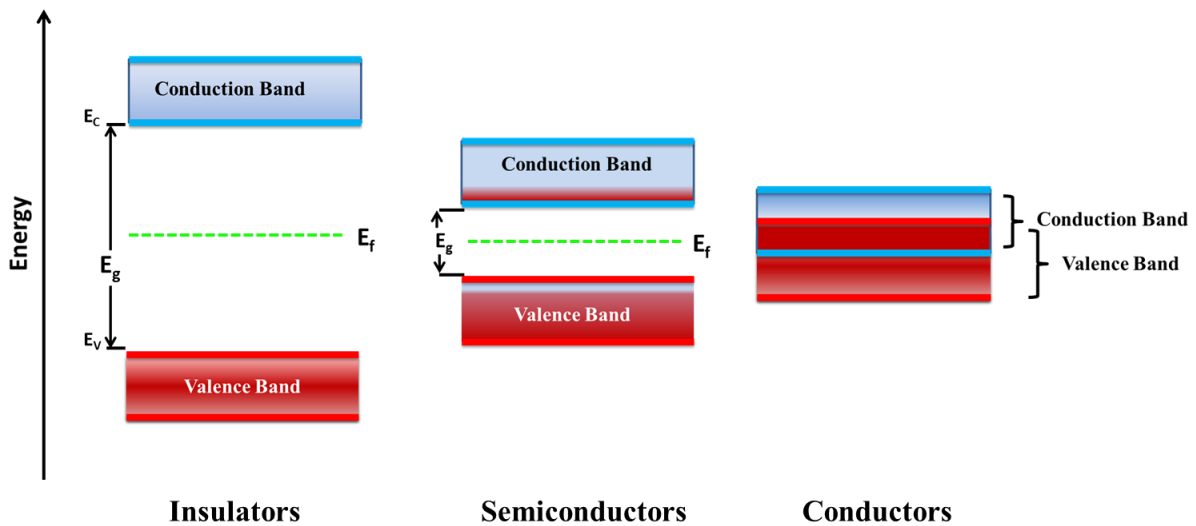
Figure 2.1 Schematic illustration of energy bands showing (a) completely filled valence band and an empty conduction band of an insulator; (b) Slightly empty valence band and slightly filled conduction band of a semiconductor (c) overlapping bands of a metal. The brown areas indicate the regions filled with electrons while light blue areas indicate empty bands

2.2 Narrow Band Gap Semiconductors

Among semiconductor materials, the III−V compound semiconductors such as GaAs, GaSb, GaP, GaN, AlAs, AlSb, AlP, AlN, InAs, InSb, InP, and InN composed of group III and V elements provide the material basis for a number of well-established commercial technologies, as well as new cutting-edge electronic and optoelectronic devices[14]. Among them, the Narrow Band-gap (NB) semiconductors are technologically important optoelectronic materials with narrow band-gaps. The possibility of exploiting their small band gaps for functional optoelectronic applications has attracted considerable research interest. This work focuses on NB semiconductors such as InAs, InAsSb and InN which have emerged as the materials of

choice for many applications in the Infrared region[15]. Most III-V materials as well as NB semiconductors including InAs and InAsSb adopt the Zinc blende (ZB) bulk crystal structure but InN crystallize in the Wurtzite (WZ) structure[16]. Figure 2.2 schematically depicts the band gap versus lattice constant of some NB and III-Nitride semiconductors. The low temperature band gap, lattice parameters and effective electron mass (m_e^*) of some NB semiconductors as reported by Vurgaftman et al[14, 17] are presented in table 2.1. The following section elaborates on some of the unique properties of selected NB semiconductors.
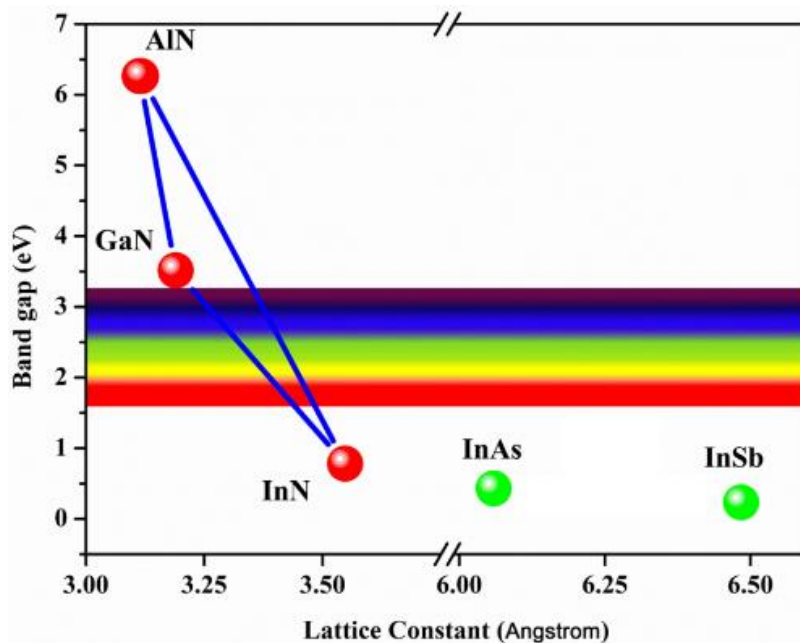
Figure 2.2 Schematic representation of the band gap versus lattice constant of some narrow band gap and III-Nitride Semiconductors.

Table 2.1 Basic Parameters of some Narrow Band-Gap Semiconductors

Material	Crystal Structure	Band Gap, E_g (0K) (eV)	Lattice Constant a (Å)	c (Å)	Effective Mass (m_e^*)
InAs	Zinc Blende	0.417	6.058	-	$0.026 m_0$
InSb	Zinc Blende	0.235	6.479	-	$0.0135\ m_0$
InN	Wurtzite	0.78	3.545	5.703	$0.07\ m_0$

m_0 is the electron rest mass

2.2.1 Indium Arsenide Antimonide alloys

Indium Arsenide (InAs) is considered one of the most promising semiconductor materials due to its outstanding properties including a narrow direct band gap (0.35eV)[18], small electron effective mass and extremely high electron mobility in the range of ~30 000 cm^2/Vs at 300K[19] which makes it highly suitable for mid infrared photo detection and high-speed electronics. Perhaps one of the most fascinating applications of InAs is in the investigation of important material-related properties such as spin-orbit coupling and quantum confinement effects which occur at larger dimensions than in materials of larger effective mass and wider gap. Owing to its small effective mass, it has a large Bohrs Bulk radius (a_B) of 34nm[20-22] which is significantly larger than most semiconductor materials such as Si where a_B ~ 3nm[23, 24], making it an ideal candidate for studies on quantum confinement-induced phenomena[25] (detailed in section 2.3).

The huge potential of InAs could be further enhanced by the incorporation of antimony (Sb) to form the ternary alloy $InAs_{1-x}Sb_x$. InAsSb is currently a subject of huge research interest for high-performance nanoscale electronic device applications with enormous promise for extending the wavelength limit of InAs detectors (1–3.8 μm) to the long-wavelength infrared (LWIR) (8–12 μm) [26, 27] range to enable infrared photo detection of highly important gases such as CH_4, CO, CO_2, O_3 and N_2O[28] as well as increased carrier lifetime [29] with respect to InAs and improved carrier mobility, useful for highly efficient field-effect transistors[30, 31]. $InAs_{1-x}Sb_x$ is particularly attractive because it has the narrowest band gap among all the III-V semiconductors (145 meV, x = 0.63 at 0K) with a band gap covering most of the mid-infrared spectrum (3-12m) [31, 32]. Figure 2.3 shows the plot[14] of band gap and relative band off-sets as a function of lattice parameter for InAsSb, which clearly reveals the ternary alloy's tuneable band gap which would enable band gap engineering for controlled NWs characteristics and device application. It also offers the opportunity to investigate important

material-related properties[31]. InAs$_{1-x}$Sb$_x$ is a highly promising alternative to current HgCdTe-based infrared LWIR detectors which is plagued by concerns related to toxicity [33], surface instability, high growth and processing cost as well as non-uniformity resulting from variations in electrical properties [34].
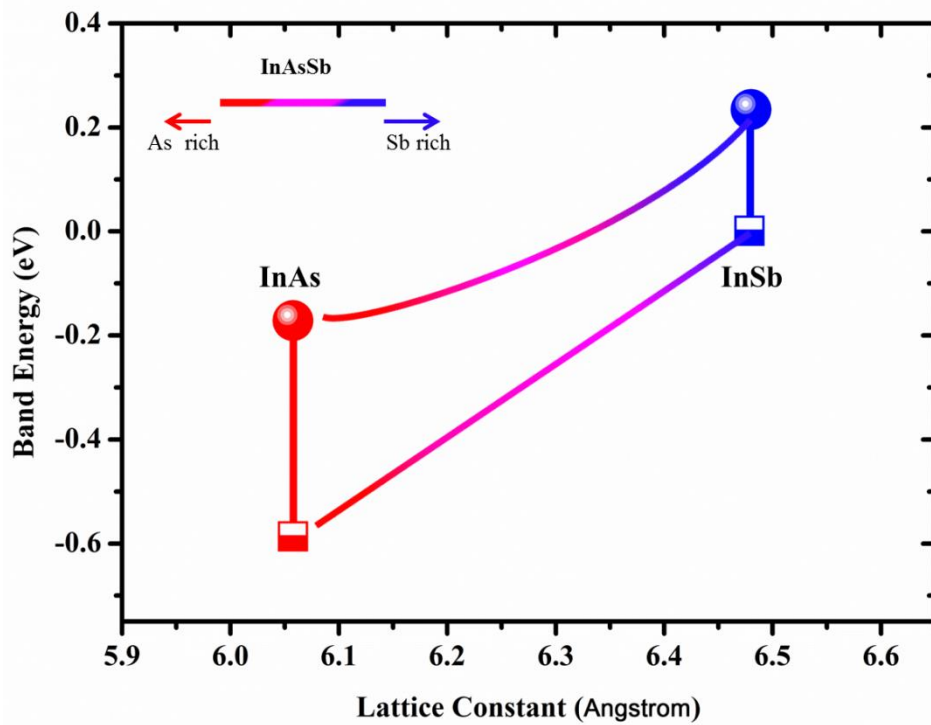
Figure 2.3 Plots of the band gap and relative band gap off-sets as a function of lattice constant for the InAsSb alloy. The length of the red and blue vertical lines connecting the rectangular (valence band off-set) and circular points (conduction band off-set) corresponds to the band gap of InAs and InSb respectively (Data adapted from Ref. 14)

2.2.2   Indium Nitride

InN materials have attracted considerable attention due to their excellent electronic and optoelectronic properties such as low effective mass, high carrier mobility, high saturation (drift) velocity and relatively high absorption coefficient[35]. Early studies of polycrystalline InN films grown by radio frequency (rf)-sputtering reported room temperature direct band gap

of 1.9eV[36], however due to improvements in epitaxial growth techniques high-quality single crystalline InN films with comparatively lower electron concentrations have been realized leading to a revision of the band gap to 0.7-0.9 eV[37, 38]. This downward band gap revision to the near-infrared spectral range has triggered enormous research interest due of its enhanced potential for applications in optoelectronic devices[39]. When alloyed with GaN to form $In_xGa_{1-x}N$, the ternary system spans from the near infrared region of InN to the ultraviolet of GaN (3.4eV) enabling the entire optical window to be encompassed by a single material[40, 41] rather than the system of several SC materials currently in use with huge implications for cost-effectiveness. Despite this huge potential, the growth of InN has been very challenging due to its low decomposition temperature, high equilibrium vapour pressure of nitrogen over indium and the lack of suitable lattice-matched substrates. The highly promising applications of InN in cost-effective and highly efficient nanolasers, LEDs and solar cells[42] has provided the motivation for its investigation in this work.

2.3 Semiconductor Nanowires

Nanostructures are defined as objects having at least one critical dimension in the nanometer (10^{-9}m) range. They are classified based on the number of nanoscale dimensionalities. Semiconductor nanowires (NWs) are wire-like structures with diameters constrained to tens of nanometers and lengths much longer, typically in the range of micrometres[5] (10^{-6} m). Specifically, they have two dimensions (diameters) confined to the nanometer scale while the third (length) is free. They are also referred to as one-dimensional (1D) nanostructures due to its single unconfined dimension. Conversely, nanostructures with three and one dimensional confinement along with 0 and 2 unconfined dimensions are described as quantum dots and quantum wells (2D) respectively. Usually in bulk materials, when two identical isolated atoms,

each with quantized energy levels are brought closer together due to a reduction in lattice constants, there is an overlap of the electron wave functions and the quantized energy levels hybridize and split into two different levels[43] consistent with the Pauli exclusion principle. More generally, when N atoms are moved closer, the energy levels split into closely spaced N levels resulting in the formation of two continuous bands known as the conduction and valence bands separated by a forbidden band. For instance, Figure 2.4 shows the formation of energy bands of electrons in a carbon crystal as a function of the inter-atomic distance "a". Isolated carbon atoms contain six electrons, which occupy the 1s, 2s and 2p orbital in pairs. An overlap of the 2s and 2p orbitals results in the emergence of two distinct energy levels, a lower valence band and an upper conduction band. The highest energy level of the valence band and the lowest energy level of the conduction band are denoted as E_v and E_c respectively[44]. The energy of an electron occupying the 1s orbital is not shown.
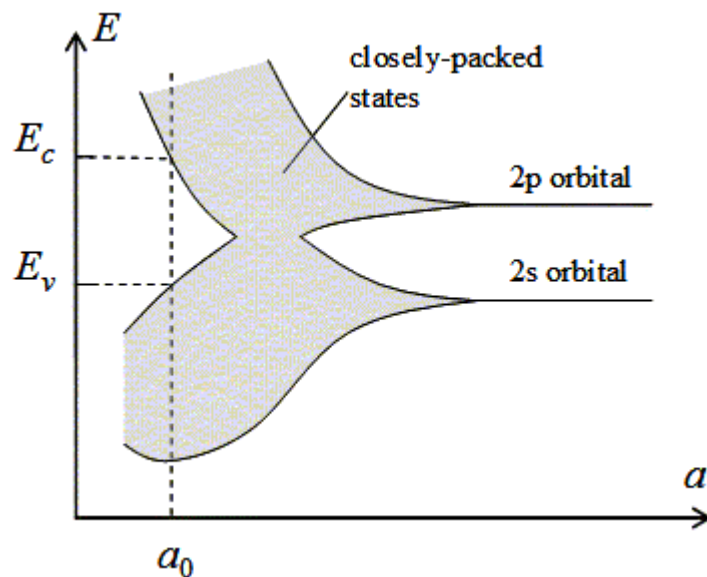
Figure 2.4 Energy bands for diamond versus lattice constant. (Adapted from Reference 44).

However, when the dimensions of bulk materials are scaled down to the nanometer range completely new and distinct electronic, optical and magnetic properties emerge due to quantum confinement effects. For an electron with an effective mass m*, the de Broglie's wavelength (λ_B) is as expressed in equation (2.1):

$$\lambda_B = \frac{h}{p} = \frac{h}{\sqrt{2m^*E}}$$

(2.1)

   where h is the Planck's constant and p is the electron momentum

When one or more dimension of a material is comparable to the wavelength of an electron, quantum size effect is introduced along such a dimension. Consequently, as the dimensions of nanostructures are confined to the nanometer (10^{-9} m) range, which is of the same order or less than the de Broglie wavelength of electrons (λ_B) quantum confinement is experienced, electron mobility is inhibited [5] and the energy-momentum relation modified. As a result, energy bands cease to be continuous or overlap and electrons populate discrete energy levels which is quite distinct from the energy bands found in conventional bulk materials[45, 46].

As schematically illustrated in Figure 2.5, electrons confinement radically transforms the density of states which is the number of available states per unit volume per unit energy in a crystal useful for estimating the occupancy of states and determination of optical properties of semiconductors including calculation of the optical transition probabilities and/or transition rates upon absorbing and emitting light[47]. In addition, NWs particlularly exhibit high aspect ratio and large surface-to-volume ratio compared to their bulk counterparts as shown in figure 2.6.

D (E)

Energy

D (E)

Energy

D (E)

Energy

D (E)

Energy

Bulk Semiconductor
3D

Quantum well
2D

Nanowire
1D

Quantum Dot
0D
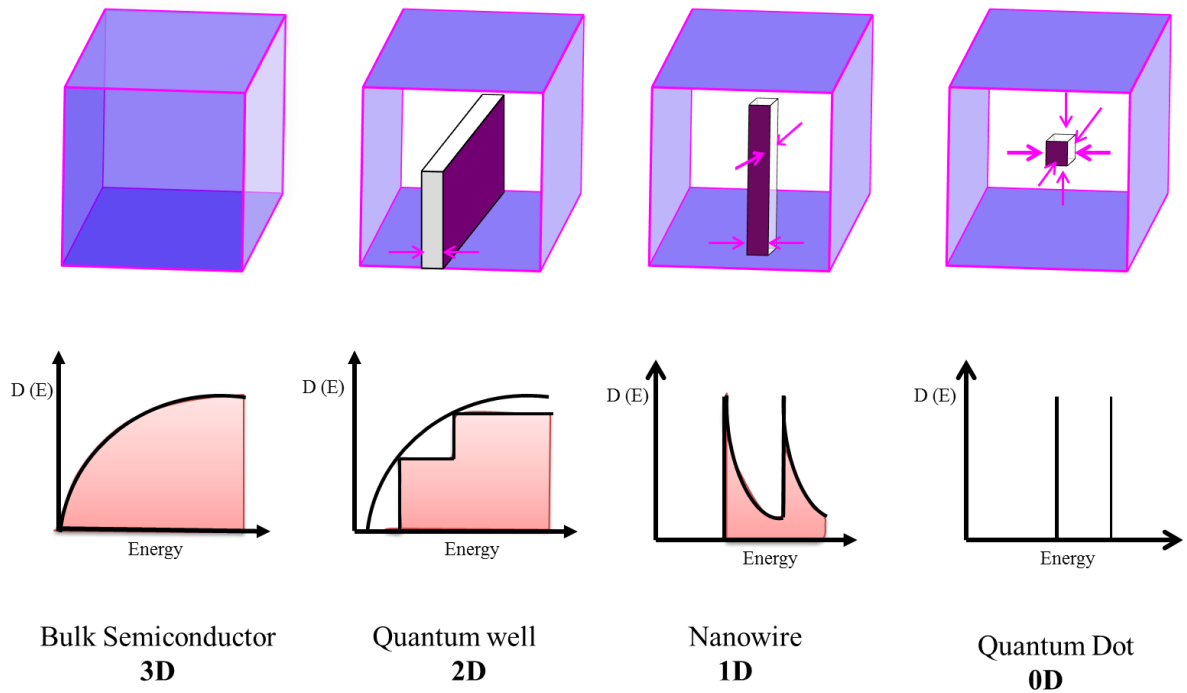
Figure 2.5 Schematic diagrams illustrating the electronic density of states for different dimensionalities of nanostructures

6cm

2cm   2cm   2cm

Volume = (6cm x 6cm x 6cm)   =   **216cm³**   Volume of each cube = (2cm x 2cm x 2cm)   =   8cm³
Total Volume of all cubes = 8cm³ x 27 cubes =   **216cm³**

Surface area = (6cm x 6cm) x 6 faces = **216 cm²**   Surface area of each cube = (2cm x 2cm) x 6 faces = 24 cm²
Total surface area = 24cm² x 27 small cubes = **648 cm²**

Volume of Big cube   =   **Total Volume of all small cubes**
Surface area of Big cube   <   **Total surface area of all small cubes**

Figure 2.6 Schematic illustration of the large surface to volume ratio of nanowires compared to their bulk counterparts

12

2.3.1 Why Nanowires

Semiconducting NWs have being touted as promising building blocks for a wide range of applications such as photonics and electronics [48-52]. They have garnered enormous research interest due to their novel electronic, optical and magnetic properties resulting from the two dimensional quantum confinements of carriers, large aspect ratio and large surface to volume ratio. Vertically-aligned NWs are particularly interesting for optoelectronic device applications such as solar cells and infrared photo detectors. This is because they have the potential to significantly enhance the efficiency and sensitivity of optoelectronic devices[53] due to an enhancement in light absorption resulting from their ability to efficiently function as optical waveguides. In addition, their unique geometry enables a reduction in optical reflectance[54-57], longer diffusion length and lifetime of minority carriers[58] and improved carrier collection efficiency[59] relative to conventional planar bulk geometry. Furthermore, NWs could open up new functionalities to optoelectronic applications because they can be grown in various architectures such as axial/radial heterostructures [60, 61] and in tandem with other nanostructures including quantum dots[62] enabling the realisation of devices otherwise impossible. Additionally, owing to the increasing influence of quantum confinement effect with decreasing diameter, NWs exhibit diameter-dependent band gaps[63] which has enormous consequences for band gap modulation. Their small footprint can be exploited for epitaxial growth on highly lattice mismatched substrates [64, 65]. The dislocation-free growth of high quality III-V NWs on foreign substrates resulting from its efficient lateral strain relaxation could be leveraged for harnessing the fascinating properties of highly lattice mismatched substrates such as silicon and graphene for the fabrication of new and sophisticated devices such as flexible solar cells[66]. From an economic perspective, a significant reduction in the volume of active materials has the potential to dramatically lower the manufacturing cost of NWs based devices translating to improved cost-effectiveness[66]. The realization of a new

generation of high-performance NWs based devices including solar cells [67-69], light emitting diodes [70, 71], transistors[48-50], lasers [51, 52], detectors [72, 73] and emerging new capabilities and applications[74] has further motivated more intensive research effort particularly on the growth of high quality NWs; although, not without challenges such as the large differences in lattice parameters and thermal expansion coefficients which has impeded the progress towards NWs based devices.

2.3.2   Nanowire Growth Mechanisms

Several strategies have been developed for the fabrication of 1D NWs including:

(I)   Metal catalyzed nanowire growth

(II)   Oxide assisted nanowire growth

(III)   SiO$_2$ mask assisted nanowire growth

(IV)   Self catalyzed nanowire growth

The following section details some of the key distinctive of each of the outlined growth mechanisms.

(I)   Metal catalyzed growth (MCG)

This is the dominant technique for the fabrication of semiconductor NWs, it employs foreign metallic catalyst for promoting NWs growth via the so-called vapour liquid solid (VLS) growth mechanism. It was first introduced in 1964 by Wagna and Ellis[75] for the growth of Au-assisted silicon whiskers with micrometer scale diameters using H$_2$ for the reduction of the SiCl$_4$ precursor. The formation of a eutectic Au-Si (catalyst-substrate) liquid alloy and diffusion of a continuous stream of Si vapour into the droplet alloy leads to supersaturation and precipitation at the liquid-solid interface and subsequent growth of Si whiskers. Some of their findings include: (i) Au catalyst is necessary for facilitating whisker growth (ii) The Au droplet is noticeably found on the whisker tip at growth

14

termination (iii) silicon whiskers growth was not promoted by screw dislocation. This technique further described by Givargizov[76] for Si whiskers deposited by chemical vapour deposition (CVD) is currently being employed for the fabrication of III–V semiconductor NWs but with diameters reduced typically to 10–100 nm[77]. In this mechanism, the catalyst serves as a collector and reservoir[78] of growth species which are introduced in their vapour phase and incorporated unto the catalyst via three possible routes[79] ; direct impingement on the catalyst, impingement on the substrate and subsequent diffusion towards the catalyst and finally adsorption on the NWs sidewall and eventual diffusion to the catalyst. The growth species first dissolves in the liquid droplet from the gas phase, then crystallizes at the liquid (catalyst droplet) – solid interface after supersaturation (i.e. contains excess of the growth species in the droplet), leading to the nucleation and epitaxial growth of NWs material under the liquid droplet [78]. Hence, the droplet remains in the liquid phase throughout the growth process and is visibly present on the NWs tip at the end of the VLS growth. However, concerns about the incompatibility of Au with the dominant and well-established silicon technology has adversely mitigated its potential for use in the monolithic integration of semiconductor NWs with silicon since it results in unintentional incorporation of Au impurities[80] which degrade the properties of the resulting NWs. Several foreign metals are currently being explored as potential alternative catalyst to Au for use in nucleating III-V semiconductor NWs including nickel, palladium, platinum, manganese, copper, silver, bismuth and iron[81].

(II)   Oxide assisted growth (OAG)

The OAG approach of NWs growth was proposed by Lee's group[82] after being successfully deployed for the fabrication of Si NWs[83] and nanoribbons[84]. Oxides were reported to play a critical role by inducing the nucleation and growth of high-quality semiconductor NWs. The nucleation of Si nanoparticles is assumed to occur at the

substrate via the following decompositions of Si oxide (Si_mO, where m>1) generated by thermal evaporation or laser ablation.

$$Si_mO \rightarrow Si_{m-1} + SiO \quad (m > 1) \quad and \quad (2.2)$$

$$2SiO \rightarrow Si + SiO_2 \quad (2.3)$$
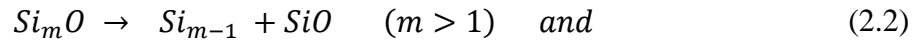
Enabled by the mobile oxide layer which surrounds its surface and passivates its side facets the Si nanoparticles functions as the nuclei for promoting the precipitation and growth of Si NWs[82]. In a similar vein, GaAs NWs have been obtained by oxide-assisted laser ablation of a mixture of GaAs and Ga_2O_3[85].

(III)   SiO$_2$ mask assisted growth (SMG)

This technique employs patterned holes in an oxide mask to facilitate the nucleation and growth of NWs which would imply the location of growth is dictated by the opening made prior to commencement of growth. The oxide layer plays a very crucial role for the growth of NWs. Openings in the SiO_2 mask which are either intentionally formed by lithographic etching or by interaction with group III adatoms results in the creation or expansion of previously existing nanocavities which functions as preferential nucleation sites for NWs growth while at the same time providing favourable conditions for droplet formation [86, 87]. In addition, the oxide sidewall serves as a scaffold for limiting adatom mobility to guide and establish 1D growth[88]. SiO_x islands are also believed to catalyze NWs growth especially in the absence of any catalyst[89]. SMG may be used in conjunction with other growth techniques such as MCG.

(IV)   Self catalyzed growth (SCG)

This growth technique otherwise called self-assisted growth involves the use of a low melting group III element, a constituent of the grown III-V NW material as catalyst for NWs growth initiation [81]. For instance, Ga could be furnished as a catalyst for the

growth of GaAs NWs. However, it should be noted that no SiO_2 template or foreign catalyst is required in SCG. This circumvents the problem of unwanted introduction of impurities usually associated with the use of foreign catalyst. Due to the fact that the catalyst is one of the constituent elements of the NWs, this technique could potentially provide extremely clean growth processes translating into high quality NWs structures. For instance, the Ga precursors supplied during the growth of the binaries compounds such as GaN, GaAs and GaSb could assist in the NWs deposition process as catalyst. SCG is often associated with the vapour solid (VS) growth mechanism, mostly evidenced by the absence of a catalyst on the NW tip at growth termination. Although, its disappearance could also be related to their consumption and crystallization during post-growth cooling[90].

2.4 Droplet Epitaxy Growth (DEG)

2.4.1   Growth of Nanostructures by Droplet Epitaxy

Droplet Epitaxy (DE), a new MBE growth method was first proposed by Koguch et al[91] in 1991 for InSb microcrystals growth on CdTe substrates. This method which was initially based on the formation of In droplets prior to growth initiation with the subsequent incorporation of Sb into the droplets to form InSb is thought to show great promise for the fabrication of quantum well boxes. DE has since being utilized for the 3D growth of GaAs epitaxial microcrystals on sulphur-terminated GaAs substrate[92]. The incorporation of As atoms into the pre-deposited Ga droplets from the vapour phase was found to promote the 3D growth of GaAs quantum dots (QDs). The nucleation of liquid Ga droplets and their crystallization into GaAs QD has being studied theoretically and experimentally[93]. It was found that all droplets transformed into crystalline QDs and the GaAs QD densities were well-defined by the Ga

17

droplet. In addition, it has been demonstrated that the nanostructure size and shape can be precisely controlled by the droplet size which itself is tuned by varying the As_4 flux and substrate temperature[94]. DE has the added advantage of dislocation-free coherent quantum structures due to the liquid nature of the droplet[95]. Strain-free $GaAs/Al_{0.33}Ga_{0.67}As$ quantum ring solar cells have been fabricated by DE[96]. As a result, this technique has been largely employed for the growth of strain-free, high-quality nanostructures including quantum dots[97, 98], single and double quantum rings[95], concentric multiple nanorings[99] and nanostructure complexes [94]. The highly flexible nature of DE technique compared with Stranski-Krastanov mode makes it more suitable for the fabrication of nanostructures on both lattice-mismatched and lattice-matched materials[100]. DE grown, strain-free GaAs QD Pairs infrared photodetectors have recently been demonstrated[100] indicating its enormous potential for optoelectronic devices application.

2.4.2   Growth of Nanowires by Droplet Epitaxy

Droplet Epitaxy (DE) growth potentially holds enormous promises for NWs growth owing to its well-established technique and successful deployment in the fabrication of high quality nanostructures. Due to the high surface tension exhibited by the group III elements such as Ga and In, they have a high tendency to aggregate on the substrate surface and function as reservoirs for facilitating the nucleation and growth of NWs. In the DE growth technique, NWs growth is preceded by the intentional activation of the substrate surface with a group III element to form liquid droplets which acts as preferential nucleation sites for the adsorption of incoming growth precursors when the shutters are opened for initiation of NWs growth. For clarity, DEG involves a deliberate introduction of a high concentration of group III element, whereas only a limited mole fraction of the group III element is spontaneously formed during the conventional SCG growth process.

18

This technique has been theoretically predicted[101] and experimentally verified[102] to exhibit unique features and advantages superior to other growth techniques for large-scale integration including better control of NWs dimensions, higher growth rate and lower growth temperature, higher stability and higher probability even for thinner structures. The exceptional properties of DEG including strain and dislocation free growth, precisely controlled size and shape of nanostructures and its flexibility could be exploited for the precise control of the size, position, diameter and distribution of high quality III-V semiconductor NWs.

2.5   Van Der Waals Epitaxy (VDWE) Growth

The epitaxial growth of III-V semiconductor materials on conventional substrates are promoted by the presence dangling bonds at the 3D/3D interface. In contrast, the nucleation and epitaxial growth of 3D materials onto 2D layers such as graphene/graphitic substrates devoid of unoccupied chemical bonds is driven by weak van der waals like interactions called quasi van der waals intermolecular forces. One of the key advantages of van der waals epitaxy (VDWE) is the absence of interfacial lattice mismatch induced strain and defects [103]. This is due to the fact that lattice matching requirements are unnecessary, given the distinct bonding mechanism in VDWE compared to conventional epitaxy with strong chemical bonding[104]. VDWE has been shown [103, 105, 106] to readily relieve interfacial strain promoting the formation of high-quality heterojunctions between highly mismatch materials. However, the lack of surface dangling bonds on graphene makes them chemically inert to foreign atoms, as a consequence the growth of 3D semiconductor NWs such as GaAs, InAs and InAsSb on muscovite mica, molybdenum disulphide (MoS_2) and graphitic substrates is very challenging[104]. Figure 2.7 schematically illustrate the difference between conventional epitaxy and VDWE growth.
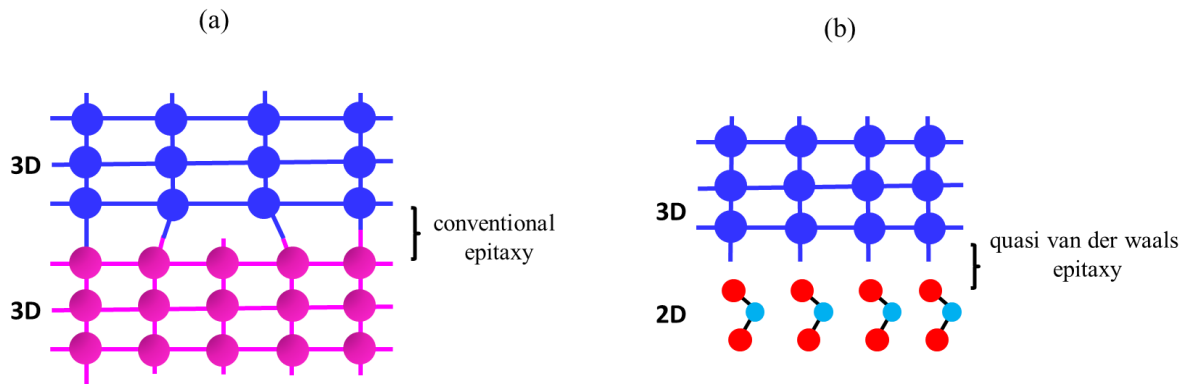
Figure 2.7 Schematic representations of conventional epitaxy (a) and quasi van der Waals epitaxy (b).

2.6 Nanowire Deposition Techniques

Several NWs growth techniques are currently being employed for the formation of semiconductor NWs but the most commonly used include the metal organic chemical vapour deposition and molecular beam epitaxy. Subsections 2.6.1 and 2.6.2 briefly describe these growth techniques.

2.6.1 Metal Organic Chemical Vapour Deposition (MOCVD)

Chemical Vapour deposition (CVD) is a broad family of processes whereby gaseous reactants are admitted into a reactor leading to the deposition of a solid material by a chemical reaction occurring on or within the vicinity of a heated substrate surface[107]. Metal organic chemical vapour deposition (MOCVD) otherwise called metal-organic vapor phase epitaxy (MOVPE) is a specific form of CVD involving chemical reactions between metal-organic (MO) precursors. It is generally defined as the growth of thin layers of compound semiconducting materials by the co-pyrolysis of various combinations of organometallic compounds and hydrides[108]. It employs a mixture of Group III metal-organic and Group V hydride

precursors in a carrier gas (H_2, N_2, or mixture of both) for the growth of III-V compound semiconductors. Although the process could be much more complex, ignoring intermediate steps and reactions the overall chemical reaction that occurs in a typical MOCVD sequence could be expressed in a simplified form[109] as:

$$R_3M\ (g)\ +\ EH_3\ (g) \rightarrow ME\ (s)\ +\ 3RH \uparrow\ (g) \qquad (2.4)$$
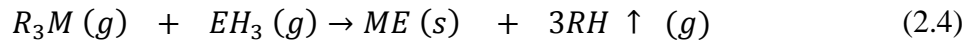
Where R = organic radical, typically a CH_3 (methyl) or C_2H_5 (ethyl), M = Group III metal atom, E = Group V atom; and H = atomic hydrogen.

The vapor phase reactants (R_3M and EH_3) are introduced into a reaction chamber at approximately room temperature and are thermally decomposed at elevated temperatures by a hot substrate and susceptor to form the nonvolatile product (ME) which is deposited on the substrate and the susceptor, while the volatile product (RH) is carried away by the flush gas (eg H_2) to the exhaust[108]. For instance, the chemical reaction between Ga $(CH_3)_3$ and AsH_3 results in the production of GaAs NWs and CH_4.

2.6.2   Molecular Beam Epitaxy (MBE)

Molecular beam epitaxy (MBE) is an advanced ultra-high vacuum epitaxial technique employed for the growth of compound semiconductor materials by the reaction of one or more thermal molecular or atomic beams of the constituent elements with a heated crystalline surface[110]. Derived from the Greek word "epi" meaning on, and "taxis" meaning arrangement, "Epitaxy" refers to a crystal growth technique in which thin layers of semiconductor materials are arranged layer by layer on the surface of a crystal (substrate). If the lattice structure of the layer and the substrate are identical it is termed "Homoepitaxy" if otherwise it is "Heteroepitaxy"[111]. As the name connotes, the MBE growth process involves the evaporation or sublimation, condensation and impingement of localized molecules or atomic beams in an ultra-high vacuum (UHV) environment (~10^{-11} Torr) from ultrapure

elements such as In, Ga and Al contained in crucibles confined in effusion or knudson cells on structurally suitable substrates heated to the required growth temperature. The substrate temperatuire provides sufficient thermal energy to the arriving atoms for them to migrate over the surface to lattice sites and eventually incorporate into the growing film [112, 113] as shown[114] in figure 2.8. The question that comes to mind is: Why the need for an UHV environment? Semiconductor NWs are very sensitive to the surface states or impurities induced by the fabrication processes hence the need for employing high purity growth technique for NWs growth [46]. In addition, the UHV environment minimizes contamination of the growing surface leading to the growth of high purity semiconductors.
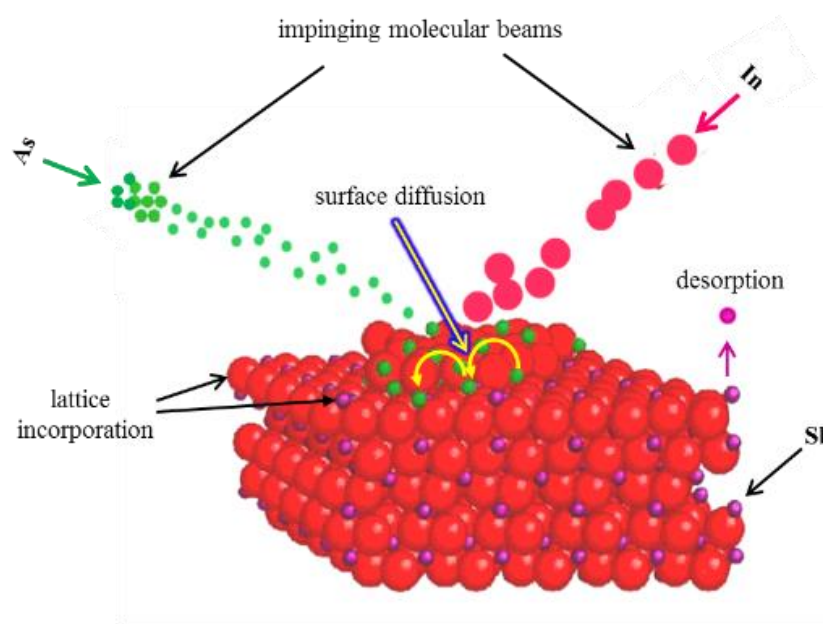
Figure 2.8 Illustration of typical processes occurring on a growing surface during MBE growth. It shows atoms impinging and migrating on the surface to lattice sites and eventually incorporating into the growing film (adapted from ref. 114)

It also creates the needed ambience for the atomic and molecular beam to travel in nearly collision-free paths until arriving either at the substrate or else at chilled walls of the chamber where they condense and are thus effectively removed from the system[112]. Due to the long

mean free path between collisions of atoms and molecules in a vacuum (10^{-11} Torr), the effect of scattering processes is minimal resulting in minimal degradation of injected beam which in turn leads to epitaxial growth of highly uniform films with controlled composition and atomic layer precision. Thanks to the UHV in the growth chamber, mechanical shutters are utilized for efficient and timely growth initiation, interruption and termination. The ability to easily and swiftly interrupt growth for composition modulation, along with the absence of boundary layers, both of which are critical requirements for the growth of abrupt interfaces on the atomic scale has huge implications for fundamental studies such as quantum confinement in NWs structures[115]. The non-equilibrium growth condition has given MBE additional advantages including low growth temperature[112], ability to produce multi-layered structures with extremely fine dimensional control and explication of new device phenomena. Furthermore, the UHV is advantageous for permitting in situ growth monitoring by sophisticated diagnostic methods including Auger Electron Spectroscopy (AEG) for examining the surface chemical composition of the substrate or growing epilayer [112, 116] and Reflection High-energy Electron Diffraction (RHEED) which enables direct measurements of the surface structure of the growing layer. The schematic diagram depicting the formation of a RHEED pattern during MBE growth is shown[117] in Figure 2.9.
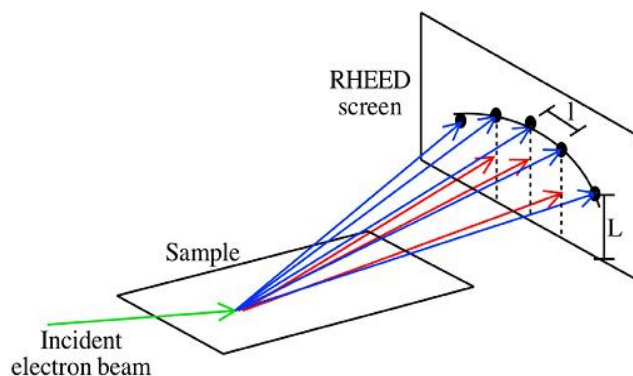
Figure 2.9 Diagram depicting the formation of a RHEED pattern during MBE growth
(Extracted from Ref. 117)

23

A high energy beam of electrons in the range of 5- 40 keV is directed at the sample surface at a low glancing angle and the RHEED diffraction pattern generated is displayed on a phosphor screen suitably located in the growth chamber[116]. The periodicity of the growing crystal is reflected in the diffracted orders produced which are used in determining the structure of the layer. Figure 2.10 shows[118] a real space representation of the formation of a complete monolayer of GaAs (001). Atoms arriving on the smooth substrate surface [monolayer thickness (θ) = 0] first nucleate in 2-D islands thereafter, arriving atoms migrate to the existing step edges resulting in an increase in monolayer thickness ($\theta > 0$), with an eventual transition back to a smooth surface corresponding to a complete monolayer ($\theta = 1$). Thus, the surface cycles between smooth and atomically rough, with a period corresponding to the time to complete a monolayer of growth. Owing to the fact that the rougher surface causes more diffuse scattering of the RHEED beam, the intensity of the diffracted beam is significantly low in comparison to that of a smooth surface. Consequently, the intensity of the diffraction beam provides useful information about the roughness of the growing sample. In addition, since the RHEED oscillation period corresponds to the monolayer growth rate, the RHEED oscillations also provides a precise method of measuring growth rates in real time[112]. These powerful facilities enable real time control and analysis during growth which could be exploited for the growth of sophisticated device structures thereby eliminating undue dependence on guess work. In comparison to MOCVD, MBE exhibit a number of advances such as low growth rate of typically 1 μmhr^{-1} (1 monolayer s^{-1}) which combined with the UHV permit precise real time composition and monolayer thickness control resulting in growth of high quality crystals with smooth surfaces[116]. Finally, no decomposition process is required in MBE compared to MOCVD which enables independent control of growth and precursor temperatures.

2D-Island Growth　　Surface scattering Centres　　Rheed Intensity
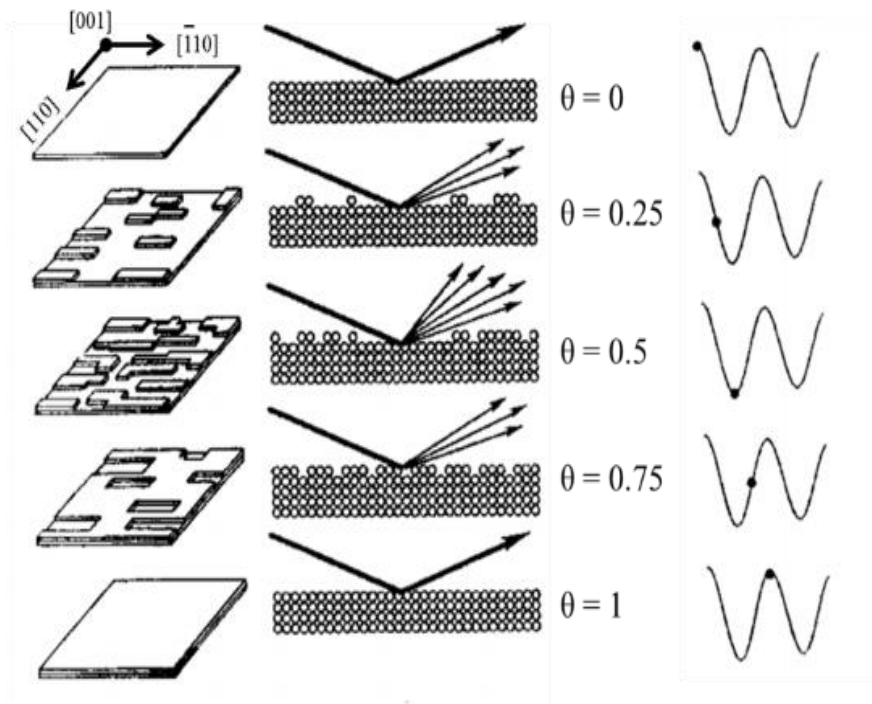
Figure 2.10 Real space representation of the formation of a complete monolayer of GaAs (001), θ = fractional layer coverage (Courtesy of Ref. 118)

2.6.3   Comparison between MBE and MOCVD

A comparison between MBE and MOCVD growth is summarised in tabulated 2.2.

Table 2.2 Comparison between Molecular Beam Epitaxy (MBE) and Metal organic Chemical vapour deposition (MOCVD)

MBE	MOCVD
1. Ultra-high vacuum environment ($\sim 10^{-11}$ Torr)	High vacuum environment
2. Precise and real time control of composition and monolayer thickness using in situ diagnostic tools eg RHEED	No precise and real time control of composition and monolayer thickness due to absence of in situ diagnostic tools
3. Beam produces very abrupt heterointerfaces and ultrathin layers	Absence of abrupt heterointerfaces and ultrathin layers
4. Large mean free path between collisions ($\sim 5 - 0.05$m)	Small mean free path between Collisions (~ 50 µm)
5. Low growth rate (1 µmhr^{-1})	High growth rate
6. Low growth Temperature	High growth Temperature
7. Independent control of precursor & growth Temperature due to absence of decomposition	No Independent control of precursor & growth Temperature due to the need for decomposition

Chapter 3

Literature Review

A review of relevant literature to semiconductor NW growth and fundamental concepts is presented in this chapter. The first part reviews the progress made with respect to NW growth over the past two decades while the second and third sections highlight recent development in NWs growth on III-V and Silicon substrates respectively. The final section provides an insight into recent advances in the growth of NWs on graphitic substrates via van der Waals epitaxy (VDWE).

3.1 Two decades of Nanowire Growth

Studies of semiconducting NWs date back to 1964 when for the first time R. S. Wagner and W. Ellis[75] fabricated silicon NWs via the VLS technique. It was however not until the early 1990s that renewed and pioneering research effort led to the demonstration of InAs [119, 120] and GaAs[121, 122] NWs following the earlier developed VLS mechanism. In the late 1990s, Liber's group at Harvard University, USA, made significant contributions [123, 124] to NWs research. However, the last decade has witnessed an explosion in NWs-based research as depicted in figure 3.1 with a record of over 20,000 NWs related publications within the last three years due to their highly promising potential applications. Significant progress has been made by several groups, including but not limited to the groups of Z.L. Wang (Georgia Tech) [125, 126], S.T. Lee (Soochow University, China) [127], CM lieber (Harvard University)[52] and L. Samuelson (Lund University, Sweden) [128]. NWs based research has matured over the last few years with several advances made on different fronts to develop new fundamental science as well as potential applications[129]. They have emerged as promising candidates for novel electronic and optoelectronic devices such as lasers, LEDs, photodiodes and solar cells. Significant progress has been made in the development of a new generation of high-

performance NWs based devices including transistor[48-50], solar cells [67, 68], light emitting diodes[70, 71], lasers[51, 52], detectors[72, 73] and other sophisticated applications[74].
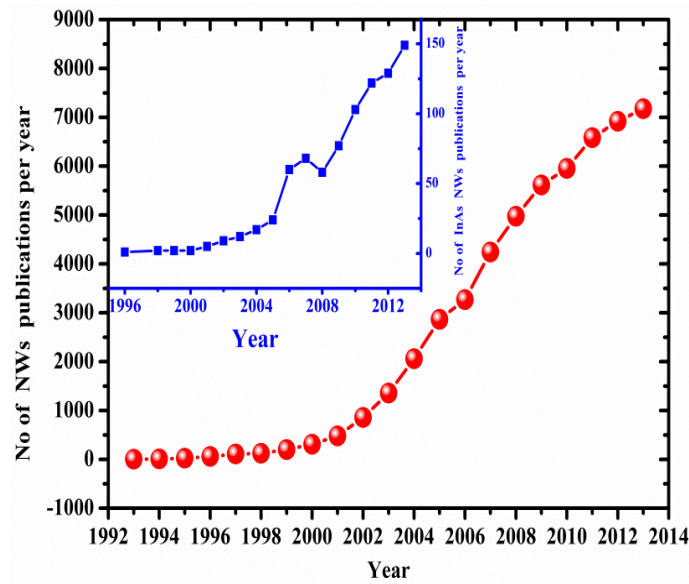
Figure 3.1 The rise in the number of research papers published per year on nanowire related topics. The inset shows the number of InAs nanowires papers published. (Source, ISI; keywords: nanowires and InAs nanowires).

Among the several materials been studied, InAs has been of great interest because of its small band gap and key role in infrared detectors. As shown in the inset of Figure 3.1, there has been an upward surge in InAs NWs related research particularly at the turn of the 21st century. However, shortly after concerns were raised by Allen et al[80] in a paper published in 2008 regarding Au contamination in Si NWs, there has been a significant increase in the number of papers devoted to NWs realized via the self-catalyzed technique. This is reflected in Figure 3.2 which shows the number of papers published per year on self catalyzed NWs and specifically InAs NWs (inset of Figure 3.2). Thus SCG is still in its formative stage and requires enormous research activity in order to fully exploit its inherent advantages.
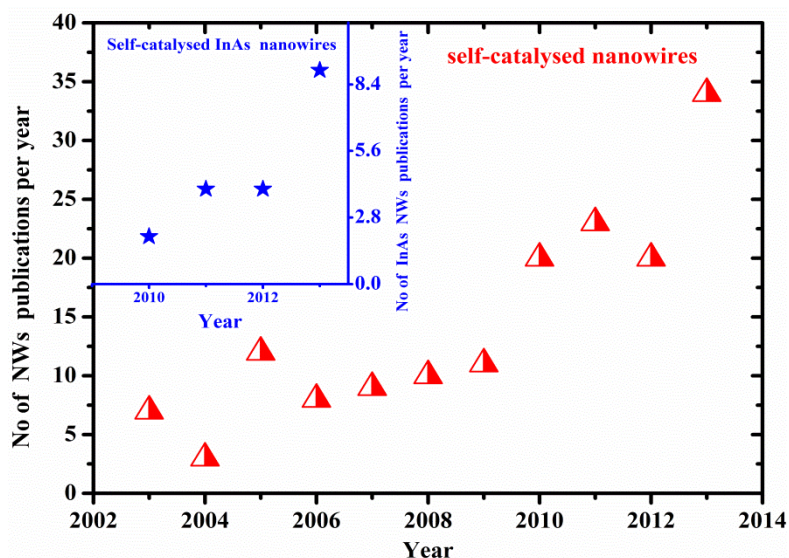
Figure 3.2 The rise in the number of publications per year on self– catalysed nanowire related topics. The inset shows a similar number of papers for InAs nanowires (Source, ISI; keywords: Self-catalysed nanowires and Self-catalysed InAs nanowires).

3.2   Nanowire Growth on III-V substrates

3.2.1   InAs Nanowires Growth

Au has undoubtedly been the most widely used catalyst for InAs NWs growth. Several reports of Au-catalyzed InAs NWs growth on III-V substrates are documented in literature. Here, an attempt is made to highlight some of the key findings.

In 2004, Jensen et al[130] investigated the growth of InAs NWs from lithographically positioned Au seeds on InAs (111)B substrates by chemical beam epitaxy (CBE). The influence of the NWs growth rate as a function of diameter was studied. Analysis of the NWs revealed 80% of the growth resulted from diffusion of In species from the (111) B substrate surface. In addition, it was established that the diffusion length on the {110} NWs side facet exceeded 10µm while the NWs axial growth rate was found to decrease with increasing NWs diameter.

Dick et al[131] grew InAs NWs by MOVPE on InAs (111)B substrates using Au aerosol seed particles. The variation of growth rate and morphology as a function of substrate type were investigated. NWs growth rate was found to decrease with increasing diameter due to the increase in collection area relative to particle volume for small particles. In addition, it was shown that the availability of In and NWs growth rate is highly dependent on the nature of substrates used.

Tchernycheva et al[132] reported the Au-assisted MBE growth of InAs NWs on InAs (111)B substrates. They investigated the variation of NWs growth rate with temperature and observed NWs can be produced only in a relatively narrow temperature window of 380 – 430 °C. No growth was observed at a lower temperature of 360°C or higher temperature of 440°C. At a relatively low temperature of 390 °C, the NWs developed a pencil-like shape and the NW top tapered in addition to the observation of side wall nucleation (Figure 3.3a).
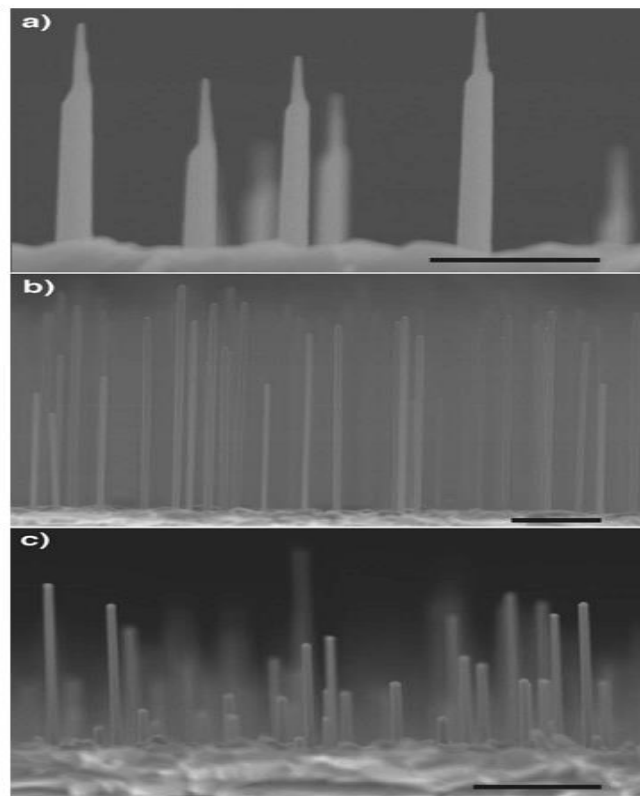
Figure 3.3 InAs NWs grown at (a) 390ºC; (b) 410 ºC ; and (c) 430 ºC for 20 min. scale bars correspond to 0.5µm. (Adapted from Ref. 132).

The mixed axial/lateral growth at low temperature was believed to occur when the mean diffusion length (λ_{diff}) of species on the NW facets becomes smaller than the NW height, in which case, the In adatoms cannot reach the catalyst to participate in axial growth. The temperature had to be raised to increase the adatom diffusion length and permit uniaxial NWs growth as revealed in figure 3.3b. However, at a slightly higher temperature of 430°C the average growth rate was reduced possibly due to increased desorption of growth precursors (Figure3.3c).

In 2011, Borg et al[28] demonstrated the MOCVD growth of axial InAs/InAsSb NWs heterostructures. It was shown that the InAsSb segment on top of the InAs segment had a larger diameter than that of the InAs stem. The incorporation of Sb in the NWs was significantly higher than that for the planar epitaxy under the same conditions; this was associated with the dramatically decreased effective V/III ratio at the growth front. Similarly, Ercolani et al[60] reported the CBE growth of InAs/InAs$_{1-x}$Sb$_x$ single and double heterostructured NWs by Au-assisted CBE. Significant lateral overgrowth in the InAs$_{1-x}$Sb$_x$ segments was observed at intermediate Sb compositions, this was linked to the nucleation and step-flow on the lateral {110} facets. Pea et al[33] reported a suppression of the lateral growth by increasing the growth temperature of the InAsSb segment and reducing the InAs stem length. This suppression was explained by the increased re-evaporation of material from the InAsSb sidewalls and the increase in diffusion length with increasing growth temperature. In addition, decreasing the InAs stem length was accompanied by a decline in lateral growth, probably because less material arrived at the InAs/InAsSb interface from the InAs stem.

More recently, the catalyst-free, MBE growth of InAsSb NWs ($0 \leq x \leq 0.15$) via short (150−200 nm) InAs nucleation NWs was demonstrated on silicon (111) substrates by Sourribes et al[30]. The influence of antimony incorporation on the defect density was also investigated. A sharp decrease in stacking fault density in the InAs$_{1-x}$Sb$_x$ NWs crystal structure with increasing

antimony content was observed. This decreased defect density led to a significant increase in the room temperature field-effect mobility by more than three times greater for the $InAs_{0.85}Sb_{0.15}$ NWs than for the InAs NWs. The suitability of InAsSb NWs for infrared photodetectors has also been demonstrated[72] using vertical arrays of $InAs/InAs_{1-x}Sb_x$ NWs. The spectrally resolved photocurrents are strongly diameter dependent, particularly for NWs with large diameters in the range of 269 to 661 nm (identical composition of 0.27%) which implies there is minimal surface leakage. As the diameter was increased, a clear peak in the response appears that is shifted toward longer wavelengths. In contrast, the photo response of smaller NWs strongly dependent on the composition of Sb. Consequently, the diameter and composition of the NWs can be adjusted to obtain peak photoresponse.

3.2.2   InN Nanowires Growth

A large direct band gap of 1.9eV was initially suggested for InN [133] in 1972 but this was later attributed to the poor crystal qualities of the polycrystalline films. Remarkable developments in epitaxial growth techniques led to a significant improvement in material quality which made it possible to obtain single-crystalline InN layers. In 2002, Davydov et al[37, 38] provided experimental evidence for a narrow fundamental band gap in the range 0.7 - 0.9 eV, much smaller than the previously reported value of 1.9eV resulting in a revision of the fundamental band gap of InN to the infrared (IR) region.

Hsiao et al[134] investigated the growth of various InN structures on AlN buffered Si(111) substrates by MBE. The structural evolution of InN from microsized grains to NWs and to 2D epifilm grown was reported by controlling the growth parameters including beam equivalent pressure (BEP) of N/In, substrate and buffer layer temperatures. Whereas polycrystalline InN grains were obtained at a higher substrate temperature, higher N/In BEP ratio and low-

temperature buffer layer by decreasing only the growth temperature while keeping all other variables fixed, columnar InN structures were formed. A high-quality InN epifilm was grown at a lower substrate temperature, lower N/In BEP ratio and a high-temperature grown AlN buffer layer. Similarly, Calleja et al[135] studied the growth condition to achieve group-III-nitride NWs by MBE from compact layers on AlN buffered-Si (111) layers. It was found that nitrogen rich condition favours the formation of NWs whereas stoichiometric conditions led to the coalescence of InN layers.

3.3   Nanowire Growth on Silicon Substrates

During the last few years, there has been renewed interest in the monolithic integration of III-V semiconductors on silicon in order to exploit the fascinating electronic and optoelectronic properties of NWs as well as the scalability, availability and high quality of silicon to enable cost-effective devices, new applications and integrated circuits based on well-established technology. Moreover, the heteroepitaxial growth of high quality III-V nanowires on Si substrates would undoubtedly open the flood gates for the experimental study of the band structure, carrier transport and other important fundamental properties of III-V NWs/Si heterojunctions which are not readily available in conventional thin film structures[53]. However, the epitaxial growth of III-V semiconductors on Si is challenging owing to large differences in lattice mismatch, thermal expansion coefficient and differences in crystal structure (III-Vs have a zinc blende or wurtzite structure whereas Si has a covalent diamond structure)[136]. Numerous growth techniques are currently being investigated for the growth of InAs NWs on Si including metal catalyzed growth (MCG), SiO_2 mask assisted growth (SMG) and self-catalyzed growth (SCG).

3.3.1   InAs Nanowire grown on SiO$_2$ Patterned Template

Recently, there has been an increasing research activity in Au free growth of NWs. InAs has enormous potential to be used in combination with Si for applications in high-speed electronics however, Au-assisted NWs growth impose severe restrictions because of the introduction of deep-level defects into Si[89]. For this purpose, several techniques are being explored to avert Au contamination, among these SiO$_2$ patterned template has been the predominant technique extensively utilized for the growth of InAs NWs.

A method for growing InAs NWs in MOVPE via SiO$_2$ patterned template without using Au or other metal as "catalyst" was first revealed by Mandl et al[89] in 2006. It was shown that InAs NWs can be epitaxially grown on various substrates including silicon without any metal catalyst by covering the substrates with a thin layer of SiOx (x$\approx$1) prior to the NWs growth. The thin film of SiO$_x$, evaporated onto the substrate surface functions as the "catalyst". The NWs were observed to grow randomly or epitaxially oriented on the substrate surface.

In 2008, Tomioka et al[7] demonstrated the position-controlled SMG-grown InAs NW arrays by MOVPE with much improved vertical directionality via control of the initial growth stages. The NWs were formed within pre-patterned regions (each 50$\times$50μm^2) fabricated by using electron-beam lithography and wet chemical etching. 60 nm sized openings with pitch in the range of 400 to 800 nm were used. The InAs NWs which were only realized in the opened circles were oriented perpendicular to the surface, ~ 60 nm in diameter and ~3μm in height.

Mandl et al[137] studied the nucleation and growth of InAs NWs on patterned SiO$_2$/Si(111) substrates. Several growth runs were performed with and without intentional In pre-deposition in order to investigate the influence of the In particle. It was found that In particles are required for the nucleation of NWs and there is an optimum In particle size range for NWs nucleation; The In particles outside of this range do not lead to NWs growth. It was shown that NWs only

nucleate if In droplets are smaller than 250 nm. In addition, the SiO_2 layer was found to be critically important for the suppression of In adatom mobility by limiting its migration within the oxide openings for the creation of required sized droplets necessary for nucleating the NWs. A series of equal patterns with different opening dimensions were created on single samples. A total of 12 different opening sizes in this range of 85 nm to 220 nm were arranged in regular triangles with a 800 nm pitch. It was discovered that the NWs yield was strongly dependent on the size of the etched holes in the SiO_2, where openings smaller than 180 nm led to a substantial decrease in nucleation yield, while openings larger than ≈500 nm promoted nucleation of crystallites rather than NWs. This observations strongly indicate that the optimum size of opening that facilitate NWs nucleation using liquid indium particle lies in the range of about 180-500nm.

Hertenberger et al[138] investigated the catalyst free SMG of InAs NWs by MBE for the first time. They addressed the crucial interplay between NW position (i.e., interwire distance), growth kinetics, and related size effects in III-As-based NWs on Si during noncatalytic growth processes leading to the growth of vertically oriented InAs NWs. Significant size variation in the NWs was found depending critically on the interwire distance and growth time. Two growth regimes were identified (i) a competitive growth regime with shorter and thinner NWs for narrow interwire distances and (ii) a diffusion-limited growth regime for wider distances where growth is limited by the surface diffusion length of In adatoms on the SiO_2 surface, providing good estimates for the surface diffusion lengths.

3.3.2   InAs Nanowire grown directly on bare Si (111)

It is well established that SMG offers the advantages of good control of NWs position, directionality and size. However, it relies heavily on electron beam lithography for patterning the SiO_2 template which is a slow, expensive and scarcely scalable[138, 139] process and

requires a considerable investment of material resources and technical expertise resulting in significantly increased cost and huge investment of valuable time. The growth of InAs NWs on bare (oxide-free) silicon substrates would be cost effective, fast and favourable for the monolithic integration of the NWs to current CMOS technology.

Significant revelations by Ihn and song[140] demonstrated the feasibility of NWs growth on bare Si substrate. They successfully grew InAs NWs on Si substrates by MBE with the assistance of Au catalyst. Epitaxial growth of InAs NWs was found to be very sensitive to the surface condition of the Si substrates. InAs NWs having a <111> growth direction were realized by a high-temperature pre-annealing process in the MBE growth chamber to remove residual oxides from the surface of the Si substrates as opposed to the randomly oriented NWs obtained without the pre-annealing sequence.

There are very limited reports of self catalyzed InAs NWs on bare Si substrates. Jing et al[139] studied the catalyst-free MOCVD growth of InAs NWs on Si substrates with various growth parameters and surface treatments. They suggested the complete removal of native oxide is critical to achieve InAs NW growth. In addition, it was shown that longer deposition time resulted in longer NWs with a larger length variation and higher density, which suggests nucleation of new NWs occurred during the growth process, leading to larger variation of the NW length and diameter and much longer NWs.

A significant contribution to SCG of InAs NWs was made by Dimakis et al[141] in 2011. They investigated the nucleation and growth of InAs nanowires on bare Si (111) by MBE without the use of catalyst particles. The study concluded InAs nucleation takes place in In-rich areas spontaneously formed on the substrate. A transition to As-rich conditions was observed and correlated with the subsequent NW formation and growth under As-rich conditions. The diameter, the number density, and the axial growth rate of the NWs were found to depend

exclusively on the surface diffusivity of In adatoms on the substrate, as a result, the surface diffusivity of In adatoms on Si is of major importance. However, the growth resulted in low dense, thick and less controllable NWs which require further investigation for improved NWs geometry and density to enable optimal device application.

Wei et al[53] accomplished the catalyst-free, direct heteroepitaxial growth of vertical InAs NWs on Si(111) substrates by MOCVD. Heterojunction photodiode devices based on heteroepitaxial n-type InAs NWs on p-type Si substrate (conduction band offset of InAs NWs/Si heterojunction ~0.10-0.15 eV) were demonstrated. Figure 3.4 shows the band alignment of n-InAs nanowire/p-Si heterojunction.
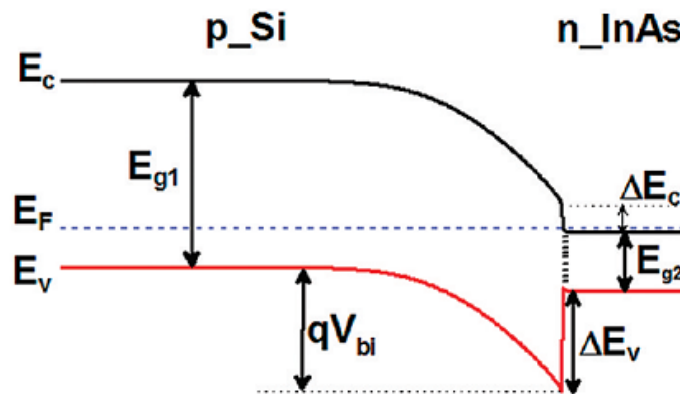
Figure 3.4 Band alignment of n-InAs nanowire/p-Si heterojunction. Adapted from Ref.53.

To understand the nucleation mechanism, growth was conducted on Si substrates with reoxidation, i.e. after etching, the native oxide was allowed to regrow by exposure to humid air (~85% relative humidity at room temperature) for various durations. Upon surface reoxidation, thin oxide (SiO_x) islands provided competing nucleation sites and reactant sinks which assisted in increasing the growth of nonvertical NWs. The nonvertical NW growth increased with reoxidation time of the substrates, becoming obvious and dominating after 130 h (Figure 3.5).

It was revealed that no NW growth was realized for unetched (with native oxide) or completely reoxidized Si substrates since the Si surface was unexposed.
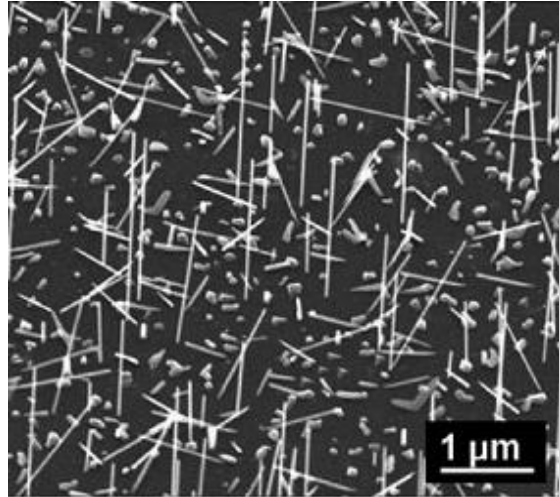
Figure 3.5 45° tilted FE-SEM image of InAs nanowires grown for 5 min on Si (111) substrate reoxidized for 130 h and grown at 535 °C (Adapted from Ref. 53).

It can therefore be concluded that SMG require a careful selection of critical experimental conditions resulting in the formation of randomly oriented InAs NWs if such conditions are not strictly satisfied[53, 140] as even a very thin layer of native oxide may sometimes be detrimental to epitaxial growth[136].

3.3.3 InAsSb Nanowire grown directly on Si (111)

The optimal exploitation of the enormous potential of InAsSb materials has been thwarted by the large differences in thermal expansion coefficients and lattice parameters between the ternary alloy and most conventional planar substrates leading to strain-induced defects and degradation of material quality[28, 60]. This has resulted in the quest for new techniques for circumventing this challenge among which the use of NWs stems such as InAs and InP[31] has

become a preferred alternative. This is due to its ability for lateral strain relaxation and dislocation-free growth on highly lattice mismatch substrates. In addition, the nucleation of polar (such as In or As-terminated) InAsSb NWs directly on nonpolar (neutral) Si substrates is hampered by the polar/nonpolar nature[7] of the InAsSb/Si system and the strong surfactant effect of Sb[142].

The growth of InAsSb NWs directly on Si substrates is scarce owing to the above outlined challenges. It was not until 2014 that Du et al[143] realized for the first time the growth of InAsSb NWs/Si via the self-seeded mechanism by MOVPE. Short (≤0.3μm) NWs were obtained for the limited growth duration of 2 minutes. The Sb content was found to have a significant effect on the morphology and crystal quality of the NWs. However, since the growth was realized after only 5 min annealing at 635°C, it is highly likely that a thin native oxide layer is still present.

To the best of my knowledge, there has been no report of InAsSb NWs growth directly on bare Si(111) substrates hence, the need for increased research activity in this direction.

3.3.4 InN Nanowire Growth

Various substrates are being explored for the growth of InN. However Si is the most suitable[144] one among the common substrates owing to the lowest thermal and lattice mismatch of 8% (compared to 25% for InN/Al$_2$O$_3$ and ~12% – 13% for InN/AlN[145]). In addition, it is competitively advantageous due to its relatively low cost, availability of large sized wafers and good thermal conductivity (3 times larger than sapphire) [64, 144, 146]. However, the formation of an amorphous SiN$_x$ layer at the growth interface during growth prevents the realization of vertically aligned NWs thus limiting its development.

Recently, Chang et al[146] performed a detailed investigation of the MBE growth and characterization of InN NWs spontaneously formed on Si(111) substrates under nitrogen rich conditions. By employing an in-situ deposited thin (∼0.5 nm) In seeding layer prior to growth initiation, single crystalline, non-tapered, epitaxial InN NWs, relatively free of dislocations and stacking faults were obtained. They achieved for the first time on Si the growth of NWs exhibiting record narrow spectral line widths of 14 and 40 meV at 5 K and 300 K respectively despite the presence of a relatively thick (>4–5 nm) SiN_x layer. The achievement of non-tapered, nearly homogeneous InN NWs also enabled the derivation of the band gap of InN directly from PL spectroscopy in the temperature range of 5–300 K.

Stoica et al[147] realized the growth of uniform InN NWs exhibiting high crystal quality using plasma-assisted MBE. They identified the optimal growth conditions including growth temperature (440-525℃) and its influence on InN NWs morphology. The NW structure was found to strongly depend on the growth temperature. A relatively high density of NWs with no visible tapering was obtained at a low growth temperature of 440^OC but the NWs displayed a tendency to coalesce into a compact layer. In comparison, the NWs deposited at a higher temperature of 475 ^{O}C were longer and more separated from each other. However, a further rise in growth temperature to 525^OC resulted in a low density of NWs which were highly non-uniform in height and shape as shown in Figure 3.6. Photoluminescence (PL) peak energy in the range of 0.76–0.82 eV was demonstrated, while the PL intensity increased with NWs length and growth temperature which suggests higher crystalline quality and less intrinsic doping at higher growth temperature.
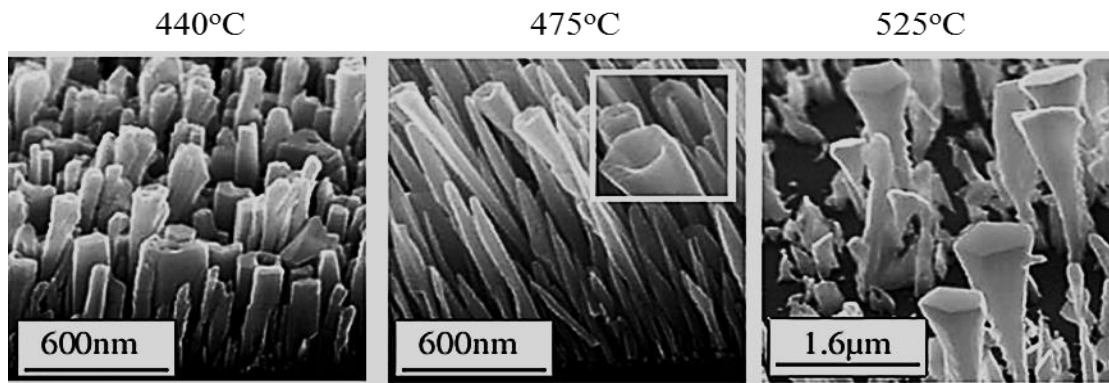
Figure 3.6 Influence of growth temperature on InN NWs morphology. The deposition was performed with In- BEP of 3.9 x 10⁻⁸, for 4 h. (Extracted from ref. 147).

3.4 Recent advances in Semiconductor Nanowire Growth on Graphite

The recent preparation and characterization of graphene by Geim and Novoselov[148, 149] in 2004 has triggered a new wave of optoelectronic revolution. This is due to its exceptional electronic and optical properties including extraordinary electrical and thermal conductivity, high optical transparency and flexibility [150, 151], which offers huge potential for the development of flexible devices. The monolithic integration of semiconductor NWs on graphene/graphitic substrates has stimulated huge research interest as it would enable the exploitation of the exceptional properties of both materials and provide a unique platform for the development of novel, sophisticated, high performance, transparent, foldable and flexible optoelectronic nanodevices including flexible displays, printable electronics and sensors with improved stability and relatively cheap cost[152, 153]. In addition, the scalability[154, 155] and relative abundance of graphene further provides greater opportunities for large scale fabrication and integration of photovoltaic technologies with non-conventional surfaces otherwise not possible[156]. Over the last few years, several graphene-based devices have been demonstrated including light emitting diodes[157], transistors[148], solar cells[66, 158], supercapacitors[159], transparent conductors[160], photodetectors[161, 162] and gas

detectors[163]. Recent advances in the growth of semiconductor NWs on graphene/graphitic substrates are reviewed in the following section.

Munshi et al[164] showed that the epitaxial growth of semiconductor NWs can be achieved on graphene. A generic atomic model by which semiconductor NWs materials can be epitaxially grown on graphene and other graphitic substrates was presented. The possible semiconductor adsorption sites on top of graphene includes (1) above the centre of the hexagonal carbon rings (H-site) of graphene (Figure 3.7 a, b, and d) and (2) above the bridge
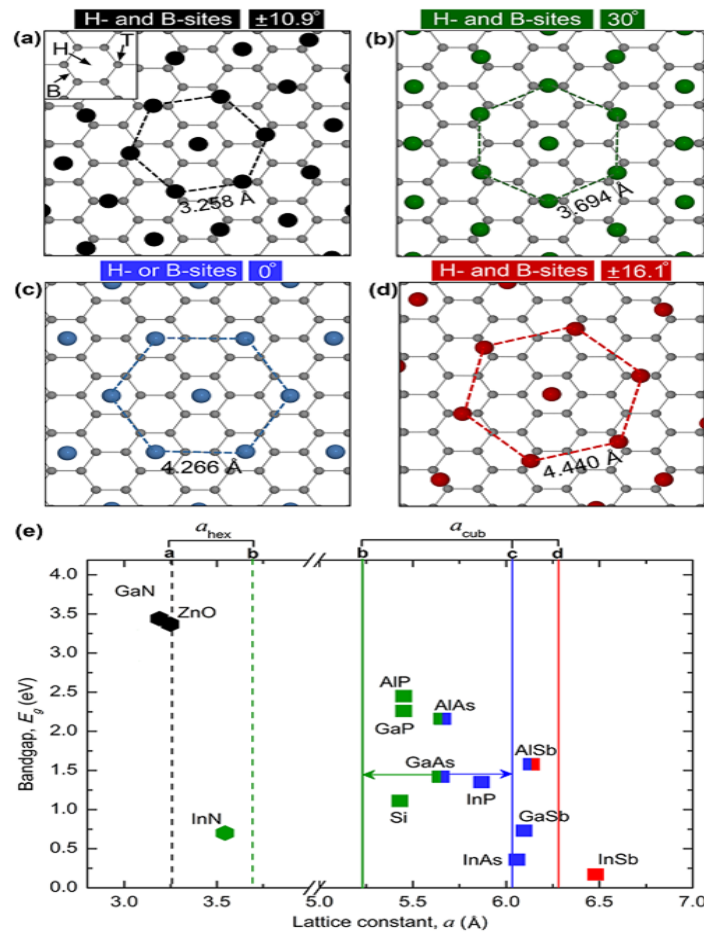
Figure 3.7 Possible adsorption sites for semiconductor atoms on H- and B-sites (a, b, d) and H- or B-sites (c). The bandgap energies of the III−V semiconductors (along with that of Si and ZnO) plotted as a function of their respective lattice constants (e). The lattice constants for lattice-matched atomic arrangements of atoms adsorbed on graphene as illustrated in figures (a) (black vertical line), (b) (green vertical lines), (c) (blue vertical line), and (d) (red vertical line) are also shown. Dashed and solid lines indicates the hexagonal (a_{hex}) and cubic ($a_{cub} = a_{hex} \times \sqrt{2}$) crystal phases of these lattices, respectively. The square (■) and the hexagon (⬢) represent the cubic and hexagonal phases, respectively, for Si, ZnO, and III−V semiconductors. (Extracted from Ref. 164).

between carbon atoms (B-site) as shown in Figure 3.7 c. Various degrees of strain is introduced at the NW/graphene interface depending on the sites taken up by the semiconductor atoms on top of graphene which in turn depends on the nature of semiconductor material and the symmetry of a cubic semiconductor in the (111) plane or hexagonal material on the (0001) plane. The band gap energies of the III−V semiconductors along with that of Si and ZnO are plotted as a function of their respective lattice constants in Figure 3.7e. As shown, ZnO and InAs materials are likely to exhibit heteroepitaxy (vertical directionality) with graphene owing to the near coherent lattice matching. The model was experimentally verified by the growth of vertically aligned GaAs NWs on graphite and few-layer graphene via the self-catalyzed VLS technique using MBE.

Recently, Hong et al[165] proposed a new mechanism of van der Waals epitaxy (VDWE) of InAs NWs growth on graphitic substrates. The graphitic substrates were processed by oxygen reactive ion etching (O_2 RIE) to artificially form monomolecular layer ledges or kinks on the graphitic surface to trap adatoms and facilitate NWs growth. Vertically oriented NWs were then realized by catalyst-free MOCVD growth. Cross-sectional transmission electron microscopy analysis revealed the 1-2 monomolecular layer ledges or kinks facilitated the heterogeneous nucleation of InAs on nonwetting graphitic surfaces, consequently forming the nuclei and promoting the subsequent NWs growth with strong VDW interactions at the heterojunction. In addition, the unconventional, noncovalent heteroepitaxial relationship between the InAs NWs and the graphitic surface was largely attributed to the nearly coherent in-plane lattice matching (misfit of 0.49%) between them. Otherwise, islands morphologies were observed for GaAs due to the high mismatch of 6.22% at the GaAs/graphite heterojunction. Furthermore, the NWs and island densities were investigated as a function of O_2 plasma treatment times for the graphite. A higher density of NWs with lower density of

islands were obtained at optimized O_2 plasma treatment times while longer O_2 plasma treatment times produced less dense NW arrays and higher island density.

In 2012, Hong et al[166] reported the VDWE growth of InAs NWs vertically aligned on large-area single-layer graphene films by MOCVD. The strong correlation between the growth direction of the InAs NWs and surface roughness of graphene substrates was investigated using various graphene films with different numbers of stacked layers. Whereas the single-layer graphene films yielded vertically well-aligned InAs NW arrays with a number density of about $(1.6\pm0.7)\times10^8$ cm^{-2}, the same growth conditions resulted in vertically less-aligned NWs on multilayer graphene films with an increased number density of $(6.9 \pm1.1) \times10^8$ cm^{-2}. The vertical alignment of the NW arrays depended strongly on the number of stacked layers in the graphene films with the thicker graphene films exhibiting higher surface roughness with many graphene ledges or kinks. Although the extremely flat graphene surfaces yielded vertically well-aligned NW arrays, the vertical directionality depreciated with increased root mean square roughness of the graphene substrates due to weakly bound VDW heterojunctions between InAs and graphene. It was shown that the NWs density increased as a function of graphene roughness due to the presence of ledges which facilitated the heterogeneous nucleation and growth of the NWs on the graphene surfaces.

The Au-seeded MOCVD growth of four common III−V materials (InAs, InP, GaP, and GaAs) on graphite was investigated by Wallentin et al[167]. The highest yield of undoped vertical NWs was obtained for InAs in comparison to the other materials. The challenges of growing III−V NWs by VLS on graphite or graphene in general were discussed using classical nucleation model based on the interfacial energies of the VLS system.

Finally, Mohseni et al[168] realized the MOCVD growth of InAs and InGaAs NWs on graphene. Spontaneous phase separation was observed in the InGaAs NWs starting from the

beginning of growth, yielding a well-defined InAs$-$In$_x$Ga$_{1-x}$As (0.2 < x < 1) core$-$shell structure. After attaining a height of ~2μm the core$-$shell structure was abruptly terminated leading to the axial growth of uniform composition In$_x$Ga$_{1-x}$As with constant diameter. An indium flow dependent In$_x$Ga$_{1-x}$As shell composition was observed however, the core and shell thicknesses and the onset of non-segregated In$_x$Ga$_{1-x}$As axial segments were reported to be independent of the indium composition. The phenomenon of phase segregation was elucidated as a special case of VDWE on 2D sheets. Given the near coherent lattice matching between the InAs and graphene, the InGaAs NW was forced to segregate into InAs core and InGaAs shell segments due to the lack of dangling bonds on the graphene layers and the absence of elastic deformation between the InGaAs NWs and the graphene film. In contrast, no phase segregation was observed in the InGaAs NWs when grown on Molybdenum disulphide (MoS$_2$).

Chapter 4

Experimental Techniques

This chapter provides a brief description of the MBE growth apparatus and the characterisation techniques employed for the investigation of morphological, structural and optical properties of as-grown nanostructures.

4.1 Substrate Preparation

In this study, all the NWs were grown on commercially available single-side polished Si (111) substrates and graphite thin film. The Silicon wafers were first soaked in acetone for a maximum of ~ 5 minutes, then rinsed in methanol and Isopropyl alcohol (IPA) to remove organic contaminants and subsequently cleaned in hydrofluoric (HF) acid via a two-step procedure. Firstly, the wafers were dipped in 12% HF solution for ~3 min to remove the native oxide then mounted on sample holders and cleaned with HF solution for ~ 2 min to get rid of any likely reoxidized layer and immediately loaded into the MBE system to avoid re-oxidation. The Si substrates were then thermally outgassed in an UHV environment at a temperature of $550 - 700^0C$ for at least one hour prior to growth initiation to possibly eliminate adsorbed gaseous contaminants. The graphite films used for the NWs growths were mechanically exfoliated from highly oriented pyrolytic graphite (HOPG) and transferred onto Si (111) substrates, then loaded into the MBE system and thermally outgassed as described above for the Si substrates.

4.2 MBE Apparatus

A Veeco (VG-V80H MBE) solid source MBE system equipped with Al, Ga and In effusion cells with crackers for As and Sb was used for the InAs(Sb) NWs growths. For the InN growth,

an Oxford Applied Research HD25 radio-frequency nitrogen plasma source was employed. Figure 4.1 shows the key components of the solid source MBE facility used for the growths including the load lock entry for loading and unloading wafers; the outgas unit for thermally desorbing gases out of the substrates; the preparation chamber which serves as a channel to transfer wafers/samples between the entry lock and the growth chamber where the actual layer by layer deposition of semiconductor materials takes place. In addition, the Reflection high-energy electron diffraction (RHEED) set-up allows for in-situ analysis of the surface structure of the growing layer while the view window enable the internal monitoring and control of the various growth stages. A schematic representation of an MBE growth chamber (Figure 4.2)[117] provides detailed insight of the essential components.
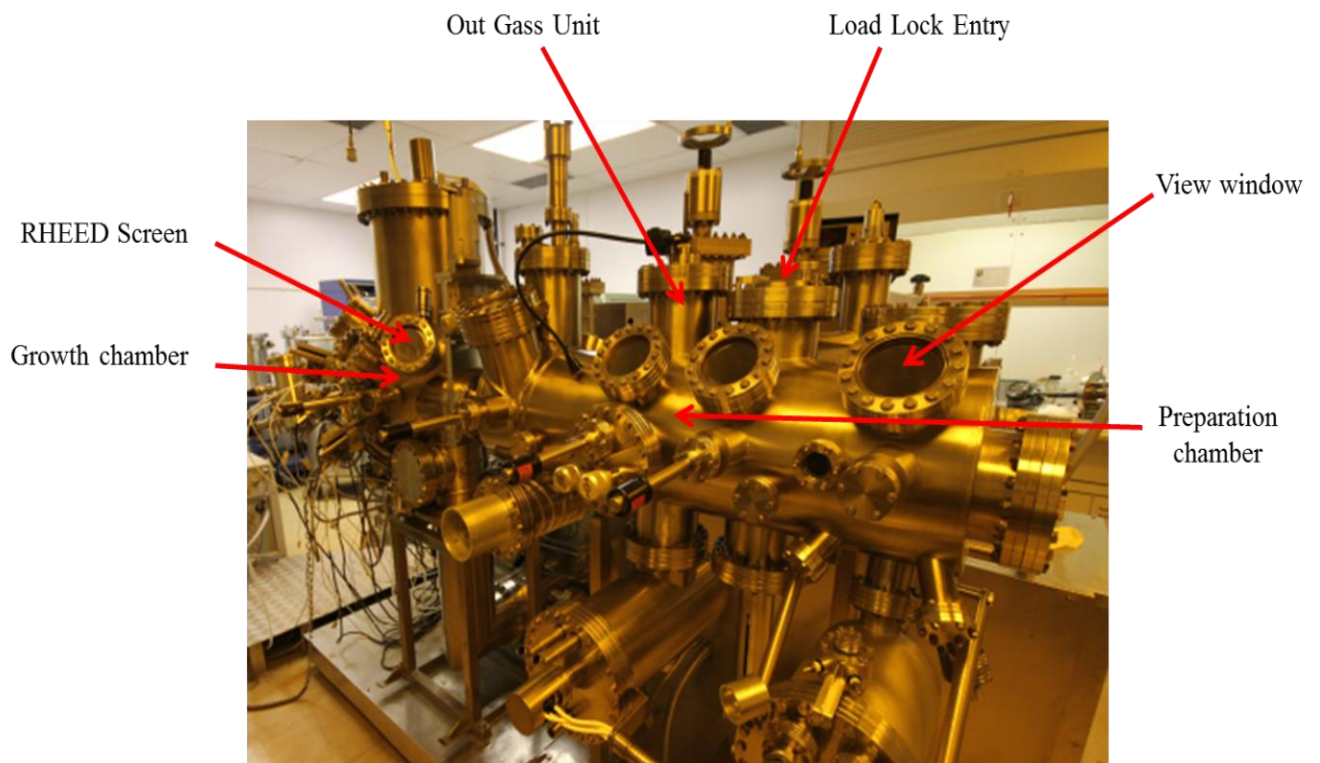
Figure 4.1 III-V solid source MBE system. The basic components are labelled.
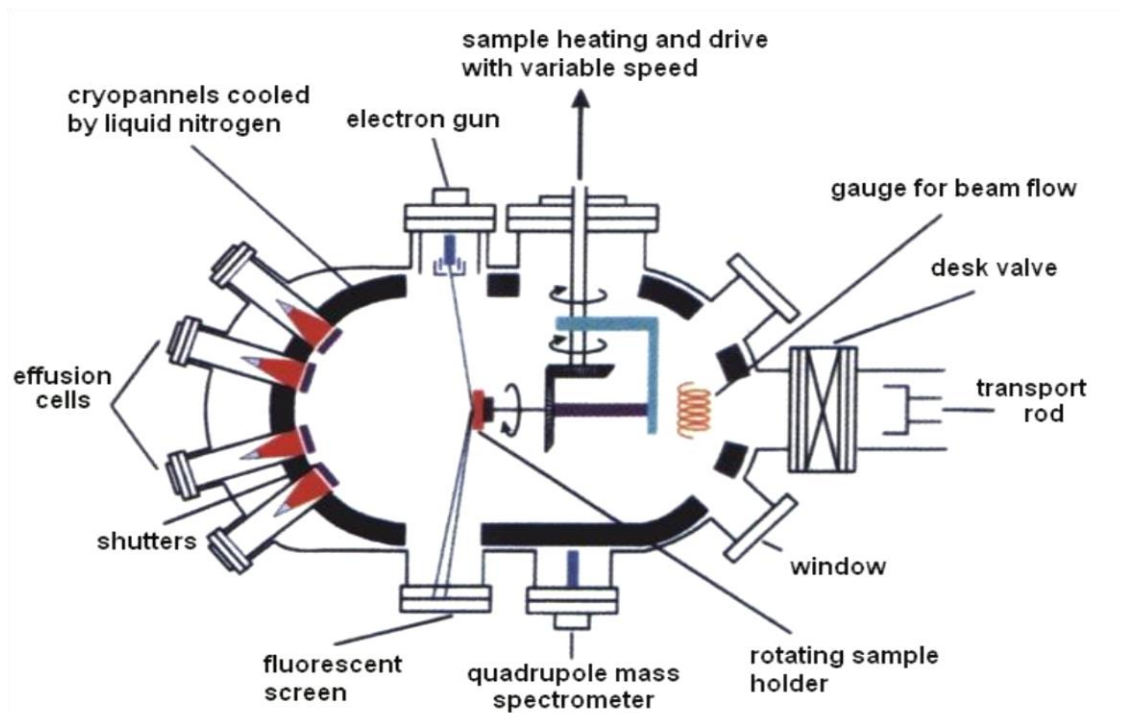
Figure 4.2 Schematic of the essential components of an MBE growth chamber showing the essential components including the effusion cells, shutters, and the RHEED system (Extracted from Ref 117).

Molecular beams are generated by thermal evaporation or sublimation of elemental sources (such as In, Ga, As) which are contained in high purity crucibles made of pyrolytic boron nitride or graphite which are in turn housed in effusion cells. The source temperature (and in effect the beam flux) is controlled by heating the crucibles with high performance proportional-integral-derivative (PID) feedback algorithms using a refractory metal wire wound noninductively either spirally around the crucible or from end to end and supported on insulators or inside insulating tubing. A flux stability of better than $\pm 1\%$ is obtained. Tantalum (Ta) heater elements and radiative shields are considered one of the best refractory metal because they are not fragile after heat cycling, have a high resistivity and are relatively easy to thoroughly outgas. Because of the strong dependence of the beam flux on temperature, the

homogeneity of the cells temperature is very crucial. Tungsten-Rhenium (W-Re) thermocouples in contact with cell bottom or sidewall are used for the chemical stability at high temperatures and for measuring the temperature of the crucibles. By choosing an appropriate cell and substrate temperature, epitaxial films of the desired chemical composition can be obtained[116]. The shutters usually made of Ta or Molybdenum (Mo) placed in front of the cell allows for switching of the beams on and off during growth initiation and interruption. To ensure uniformity in film thickness, the Ta or Mo substrate (with the sample) holder is rotated with the aid of a substrate manipulator which is capable of continuous azimuthal rotation around its axis. A heater placed behind the sample is designed to maximize temperature uniformity and minimize power consumption and impurity outgassing. Positioned directly opposite the substrate holder is an ionisation gauge (ion gauge) which monitors the beam flux[113]. The cryopanel which internally surround the main chamber wall is cooled by liquid nitrogen enable the extraction of condensable contaminants such as H_2O and CO_2 for an ultra-high vacuum environment and provide thermal insulation among the closely positioned cells permitting the independent control of beam fluxes[115].

4.3   Characterization Techniques

4.3.1   Scanning Electron Microscopy

The scanning electron microscope (SEM) is one of the most versatile instruments used for the examination and analysis of the morphology of nanostructures[169]. Invented in 1931 to circumvent the limitations imposed by the wavelength (410-660 nm) of photons (light rays), SEM uses electrons rather than visible light and have a greater depth of field compared to light microscopes. They are capable of higher resolution and magnification which allow for the visualization of structures on a nm to µm scale that would normally be invisible by optical

microscopy. The bombardment of an incident electron beam on the specimen material being investigated results in the production of different kinds of signals including secondary electrons, backscattered electrons, Auger electrons and X-rays. SEM investigation utilizes the secondary and backscattered electrons which are the imaging signals of greatest interest for SEM analysis due to their dependence on differences in surface topography while characteristic x-rays provide obtain compositional information[169, 170].

Secondary Electrons: Secondary electrons are loosely bound outer shell-electrons inelastically generated during the ionization of specimen atoms when excited by incident primary electron beams. Conventionally, they possess energies of less than 50 eV and can be used to image or analyse samples and capable of providing high resolution topographic information owing to their low energy (~3–5 eV) permitting their exit very close (a few nm) to the specimen surface.

Backscattered Electrons: Backscattered electrons are defined as one which has undergone a single or multiple scattering events which escapes from the surface with an energy greater than 50 eV. They are scattered backward or bounced out of specimens' atomic nucleus with wide-angle directional change after elastic collision with an electron. The back scattered signal is highly dependent on the specimens atomic number since atoms with higher atomic numbers possess more positive charges on the nucleus.

Characteristic X-Ray: A vacancy is created in the inner shell of a specimens' atom due to the generation of a secondary electron. As a result, an electron from the outer shell falls into the inner shell to fill this vacancy in order to compensate for the charge imbalance accompanied

by the emission of a characteristic x-ray unique to the specimen atom. This enables the determination of the distinct chemical composition of specimens, allowing for the identification of atoms.

Auger Electrons: Similar to characteristic x-rays, auger electrons are generated as a result of a vacant inner shell however, the surplus energy is transferred to a second (Auger) electron rather than being emitted in form of x-ray radiation. This leaves the atom doubly ionized. Auger electrons can also provide vital chemical information because of their unique and characteristic energy. They are mostly used in surface analysis due to their low energies and low depths (only a few nm).

The Schematic diagram[171] of a typical SEM is shown in Figure 4.3. The electron gun provides a steady stream of electrons of adjustable energy. Emitted electrons in the gun are accelerated from the high negative potential of the filament to the ground potential at the anode[170]. A hole in the anode allows for the transmission of the electrons towards the lenses. The Condenser and objective lenses are used for the demagnification of the spot size of the electron beam in addition to the use of the objective lens control to focus the beam on the specimen surface.

The FEI XL30 SFEG SEM at the University of Liverpool (Figure 4.4) was mostly utilized for the investigation of the morphology of as-grown NWs in addition to the Sirion field emission scanning electron microscope (FESEM) at Lancaster University.
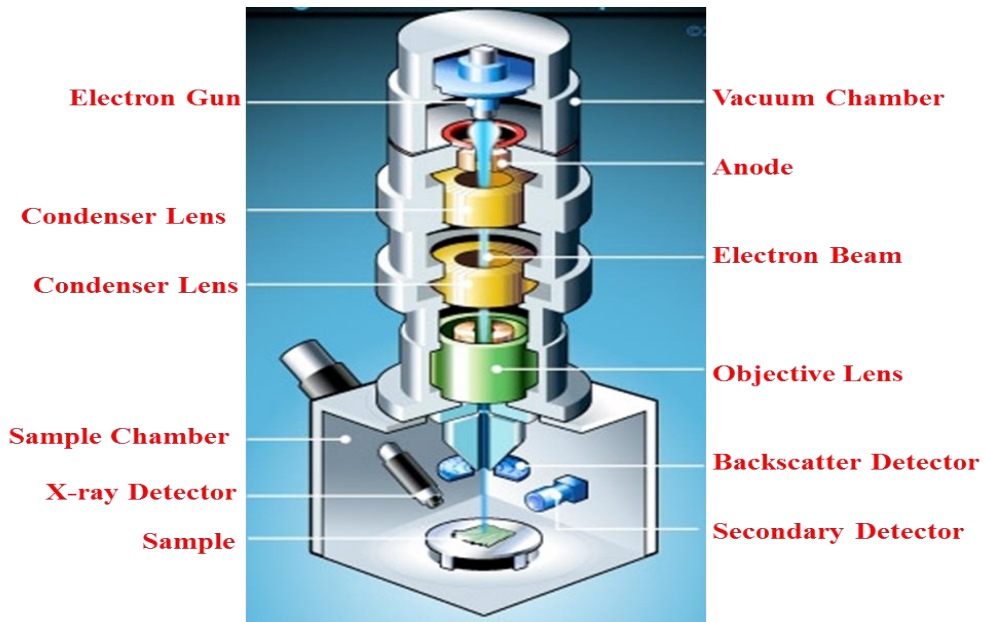
Figure 4.3 Diagram of a scanning electron microscope (Adapted from Ref. 171).

Figure 4.4 FEI XL30 SFEG Scanning Electron Microscope

4.3.2   Transmission Electron Microscopy

The Transmission Electron Microscope (TEM) is an indispensable, highly sophisticated instrument with unparalleled ability to provide detailed atomic scale structural information of nanomaterials with widespread application across different scientific disciplines[172]. It was developed by Ernst Ruska and Max Knolls in 1931[173]. The TEM consists of three essential components[174] (Figure 4.5): (1) An electron gun for producing the electron beam, and the condenser system, which focuses the beam onto the specimen; (2) The image-producing system, consisting of the objective, intermediate and projector lenses, for focusing the electrons passing through the specimen in order to form a highly magnified image and (3) The image-recording system, which converts the electron image into some forms perceptible to the human eye. The image-recording system is made up of a fluorescent screen for viewing the image as well as a digital camera for recording the image.
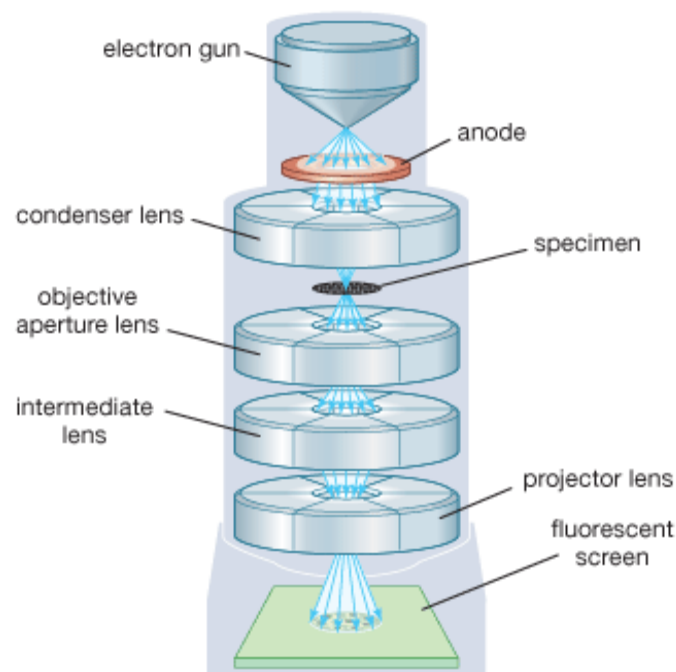
Figure 4.5 Schematic of a transmission electron microscope (Extracted from Ref.174).

Figure 4.6 Picture of JEOL 2100 LaB Transmission Electron Microscopy
(Extracted from Ref.175).

For this study, TEM analysis was performed with a JEOL 2100 LaB_6 working at 200kV and

housed at the university of Warwick (Figure 4.6)[175]. The specimens were prepared using

conventional method and transferred onto a TEM holey carbon grid. The analysis was carried

out with the electron beam perpendicular to the growth direction.

4.3.3 X-Ray Diffraction

X-rays were discovered in 1895 by the German physicist Wilhelm Roentgen for which he

earned the Nobel Prize for physics in 1901. They are electromagnetic waves similar to visible

light but of very much shorter wavelength, having wavelengths lying approximately[176] in

the range of 0.5-2.5Å (for x-rays used in diffraction), whereas the wavelength of visible light is of the order of 6000Å. X-ray diffraction (XRD) is a non-destructive and very sensitive technique for the determination of the structure of crystalline solids. Generally, diffraction occurs only when the wavelength of the wave motion is of the same order of magnitude as the repeat distance between scattering centers[176]. Since X-rays are primarily generated from inner atom core transitions, the photon wavelengths are in the region of 0.1nm (1Å), which is of the order of the interatomic spacing in materials[177], as a consequence, x-rays are generally utilized for the creation of diffraction patterns and analysis of crystal structures. According to Bragg's law, the interaction of an x-ray beam with the parallel planes of a crystal results in constructive interference if the difference in path length between the rays is an integral multiple of wavelength of the incident ray as illustrated[178] in Figure 4.7.
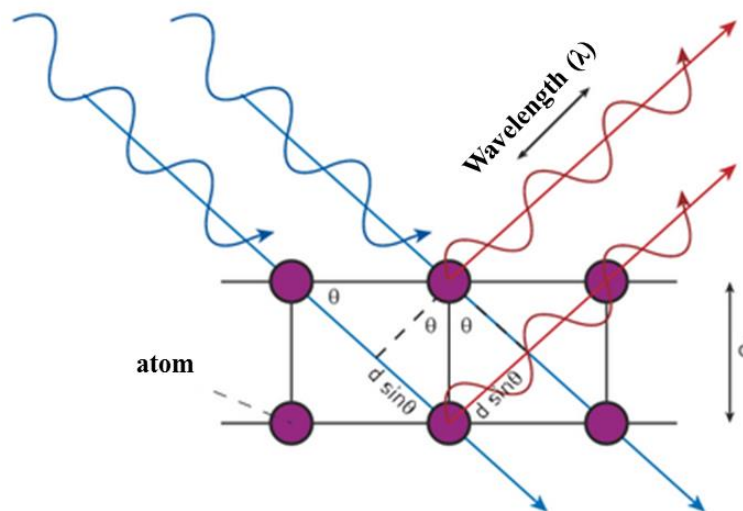
Figure 4.7 Illustration of Bragg law (Courtesy of Ref. 178).

This is mathematically represented as:

$$2d\sin\theta = n\lambda \qquad\qquad (4.1)$$

Where:

d is the distance between atomic layers in a crystal

θ is the incident angle

λ is the wavelength of the incident beam and

n is a positive integer

For this study, the Philips PW 1720 X-ray diffractometer (Figure 4.8) was employed using the Cu Kα₁ radiation line (1.54056Å). XRD measurements were firstly calibrated by the diffraction from Si (111) substrate.

Figure 4.8 Philips PW 1720 X-ray diffractometer used for this study

4.3.4. Atomic Force Microscopy

Scanning probe microscopy (SPM) is a technique used to image and measure the geometrical properties of materials by scanning across the surface with a sharp probe that monitors and assembles the tip–sample interactions. There are two forms of SPM: Scanning tunnelling microscope (STM) and atomic force microscope (AFM). Invented by Gerd Binnig and Heinrich Rohrer in the early eighties STM was limited by the fact that it could only analyse materials that conduct tunnelling current. AFM was then invented by Binnig and Quate in 1986 to overcome this limitation[179]. An AFM is a mechanical imaging instrument that measures the three dimensional topography as well as physical properties of a surface with a sharpened probe[180]. Extremely high-resolution (on the order of fractions of a nm) images are created in AFM by quantifying the forces between an ultra-small probe tip at the end of a cantilever and the sample surface[179].

There are 3 primary imaging modes in AFM: contact, tapping and non-contact modes with probe-surface separations of < 0.5nm, 0.5-2nm and 0.1-10nm respectively. In contact mode, the tip which softly makes contact with the specimen scans in a sideways direction across the surface of the sample while the contours of the surface are measured. On the other hand, in the tapping mode the cantilever is made to oscillate up and down at near its resonance frequency in order to measure the force between the cantilever probe and the specimen. In ambient conditions most samples develop a liquid meniscus layer; hence by keeping the probe tip close enough to the sample surface short-range forces become detectable. Finally, in order to measure long-range forces such as VDW force which are strongest from 1 nm to 10 nm above the surface, the non-contact mode is employed during which the tip of the cantilever makes no direct contact with the sample surface as the cantilever oscillates above the surface with small amplitude at a frequency larger than its resonance frequency[179, 181]. Figure 4.9

illustrates[182] the force sensor in an AFM constructed from a light lever. In the light lever, laser beams are focused on the backside of a cantilever and the reflection fed into a photodetector with two sections. The output of each of the photo-detector sections is compared in a differential amplifier. The interaction of a cantilever probe with the surface of a specimen results in the bending of a cantilever which in turn leads to changes in the light path causing the amount of light in the two photo-detector sections to change. Thus, the force between the probe and sample is proportional to the electronic output of the light lever force sensor. The resulting image provides an excellent view on the sample's topography at an extremely high level of resolution. The resulting image provides an excellent view on the sample's topography at an extremely high level of resolution. The resulting image provides an excellent view on the sample's topography at an extremely high level of resolution. [183].
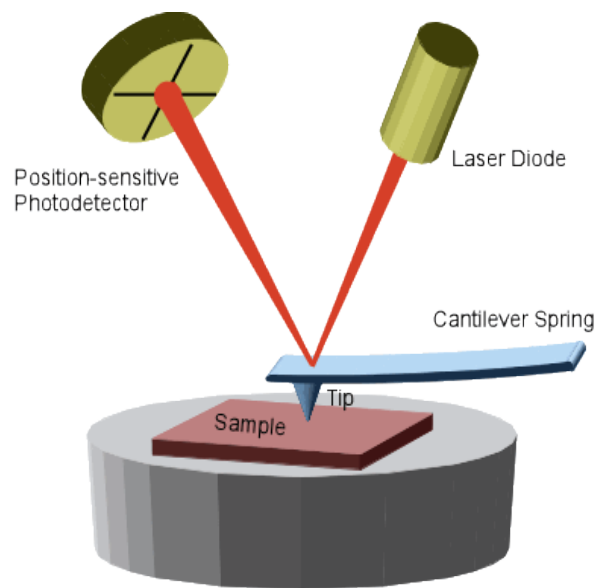
Figure 4.9 Illustration of the light force sensor of an atomic force microscope
(Image extracted from Ref. 182).

.

The morphology of the indium droplets in this work was investigated by AFM using Digital Instruments multimode scanning probe microscope (MM-SPM) fitted to a nanoscope IIIa controller unit (Figure 4.10) in the tapping mode.

58
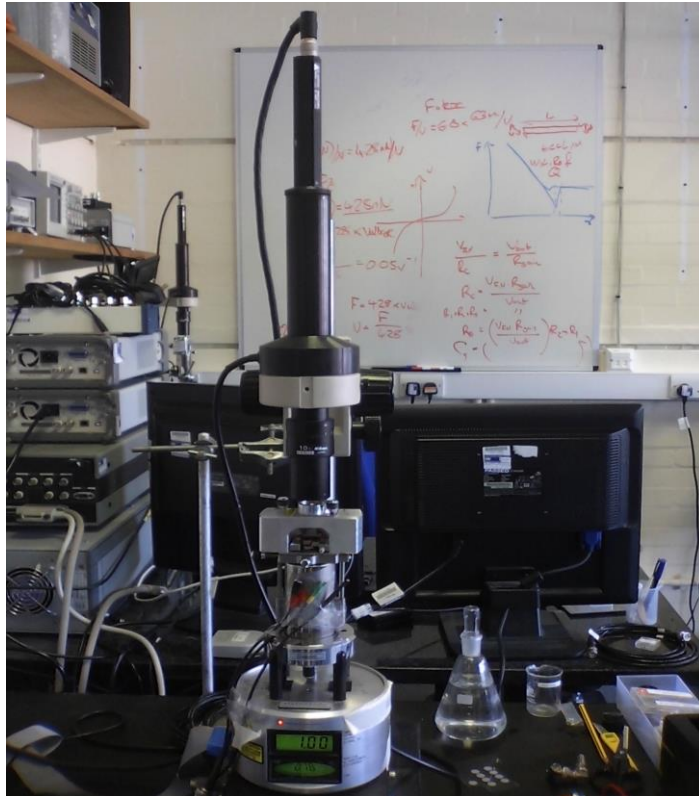
Figure 4.10 Digital Instruments multimode scanning probe microscope
(MM-SPM)

4.3.5   Photoluminescence Spectroscopy

Photoluminescence spectroscopy is a non-destructive and contactless technique used for the
optical characterization of semiconductors. When light of sufficient energy is incident on a
material, photons are absorbed and electronic excitations created. If radiative relaxation occurs,
the electrons return to the ground state with the spontaneous emission of light in a process
termed photoluminescence (PL). Analysis of the optical emission provides important
information including the electronic bands or states, impurity and defect levels. The radiative
recombination of electron (e) hole (h) pairs localized in different energy states results in distinct
optical emission typical of the respective transitions in the semiconductor. Figure 4.11 depicts
the possible radiative transitions during photoluminescence in semiconductor materials
including:
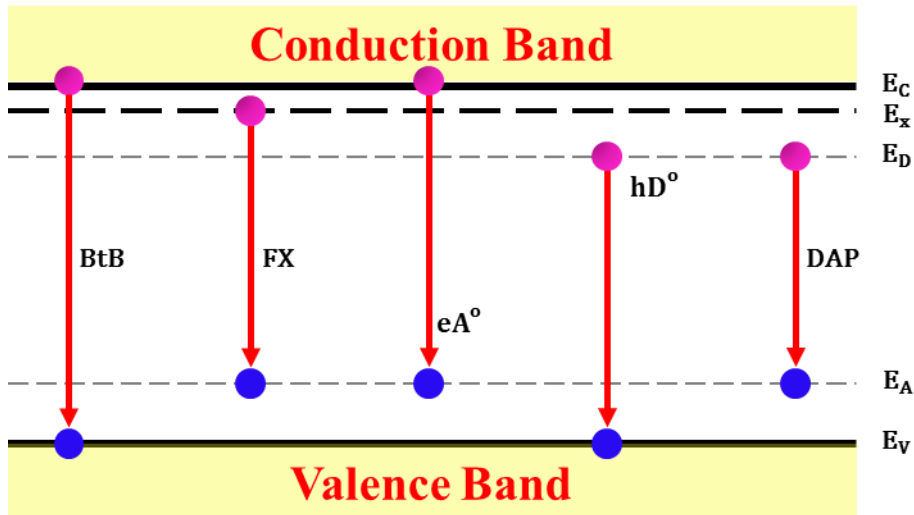
Figure 4.11 schematic illustrations of possible radiative transitions during photoluminescence in semiconductor materials. E_C, E_X, E_D, E_A and E_V denote the conduction band edge, free-exciton state, donor and acceptor levels & valence band edge respectively.

Band to Band transition: The radiative recombination of conduction band electrons and valence band holes leading to the emission of excess energy in the form of photons (light) is referred to as band to band (BtB) transition with energy similar to the semiconductor direct band gap (E_g) and equal to the difference between the lowest point of the conduction band (E_C) and the highest point of the valence band (E_V). This is the dominant transition in direct band gap semiconductors.

Excitonic Transitions: Excited electron and holes could be attracted to one another by Coulomb interactions leading to the formation of hydrogenic-like excitons which could participate in radiative transitions either as free excitons or bound excitons depending on the level of purity of the semiconductor. Owing to the absence of defects or impurities in quasi pure semiconductors, free electrons and free holes recombine to form free excitons (FX) emitting a narrow spectral line of photons with energy (E_{FX}) equal to the energy difference between E_g and the exciton binding energy (E_X). Conversely, in the presence of low concentrations of donors or acceptors (defects) localized in donor (E_D) and acceptor (E_A) levels

60

respectively, excitons could be trapped by the defects to form bound excitons. At low temperatures, donors bound excitons (D_0, X) and acceptors bound excitons (A_0, X) are created by the VDW attraction of excitons to neutral donors and acceptors respectively.

Free-to-bound Transitions: At low temperatures, photoexcited free electrons and holes could be trapped by carriers which are frozen (bound) at acceptors and donors sites accompanied by radiative emission. The radiative recombination of a free conduction band electron with a hole bound to an acceptor results in an eA^0 transition while a free hole recombination with a donor bound electron leads to a hD^0 transition (Figure 4.11). Hence the name "free to bound transition" denotes a transition which involves the recombination of a free carrier with an impurity bound carrier. However, at significantly high temperatures, the frozen carriers are unbound and excited to the conduction or valence band favouring BtB emissions while annihilating free to bound transitions.

Donor-acceptor pair Transition: Donors and Acceptors exist concurrently in some doped semiconductor materials. The donor-acceptor pair (DAP) transition is associated with the radiative recombination of neutral electrons from the donor level with holes on the acceptor levels. This could potentially result from an overlap between the electron and hole orbits if positioned sufficiently close to each other.

In practice, defect related emissions are distinguished from BtB PL spectrum using temperature dependent PL measurement due to their temperature sensitivity. At low temperatures, carriers can be trapped at defect sites however, as the temperature is raised, the carriers are unbound and excited to the conduction or valence band favouring BtB emissions. Consequently, defect related emissions are mostly absent at significantly high temperatures leaving the BtB emissions as the dominant emissions.

For this study, the PL setup at Lancaster University and Nanyang Technological University, Singapore was utilized. Figure 4.12 shows the diagram of a typical experimental set up used for PL investigation at Lancaster University. To perform PL measurements, the samples are first mounted on a copper cold finger which are then inserted in an oxford instruments continuous flow helium cryostat filled with helium gas to allow for thermal contact. Liquid helium was used for cooling down the sample from 300K to liquid helium temperature (4K) using a Bentham temperature controller. A spectra-physics model 2011 Ar+ ion laser was used as the excitation source. The beam was then pulsed using a Bentham 218 mechanical chopper and passed through a series of filters to cut off unwanted signals while exclusively allowing the 514 nm line. The sample loaded in the cryostat is sandwitched in between two lenses for collimating the light unto the sample and into the monochromator slit. The monochromator
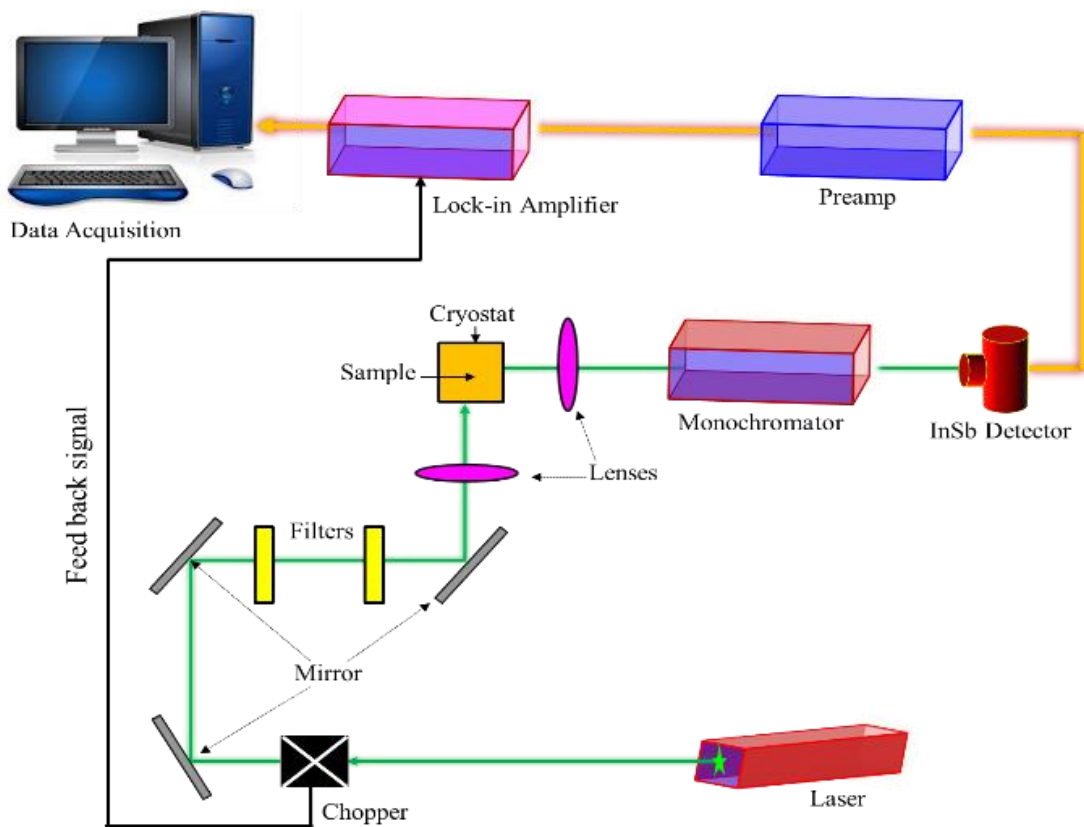
Figure 4.12 Schematic diagram of the experimental set-up for photoluminescence measurement

filters out stronger laser emissions not originating from the sample. The sample signal detected by liquid nitrogen cooled InSb photodiode detector was then fed into a lock-in-amplifier after amplification by a preamp. Using the reference chopper frequency the lock-in-amplifier isolated the sample signal which was then inputted into a computer for data collection.

Chapter 5

InAs Nanowires Growth on Bare Si (111) Substrates

In this chapter the optimal growth conditions for indium droplets suitable for nucleation and growth of NWs is first presented. Then, the In-assisted droplet epitaxy growth of InAs NWs on silicon substrates by MBE is detailed. Here, optimized indium droplets are employed for the preferential nucleation of the NWs without using any foreign catalyst or SiO_x mask. The morphology and structure of as-grown NWs were investigated using scanning electron microscopy, X-ray diffraction and transmission electron microscopy. In order to establish optimum growth conditions for In-assisted droplet epitaxy growth of InAs nanowires, an investigation of the influence of basic growth parameters such as growth duration, growth temperature, In/As flux ratio and the growth rate on the NWs morphology is elucidated.

5.1 Optimization of In Droplets for Nanowire Nucleation and Growth

In order to establish optimal growth conditions for indium droplets (In_{drop}) suitable for the preferential nucleation and growth of NWs, a series of four (A, B, C and D) In_{drop} samples were grown on bare Si substrates at various temperatures of 145–310 °C using In flux in the range of $2.2 - 6.0 \times 10^{-7}$ mbar for a nominal thickness of 3 ML. Prior to the deposition, the Si substrates were mostly cleaned in hydrofluoric acid solution as previously described in section 4.1 and immediately loaded into the MBE system to avoid re-oxidation and thermally outgassed. The morphology of the In_{drop} was then investigated by AFM using digital Instruments multimode scanning probe microscope (MM-SPM) fitted to a nanoscope IIIa controller unit in the AFM mode. Figure 5.1 shows the top-view (top panel) and 3D (bottom panel) AFM images of the droplets deposited at various growth conditions. The diameter,

height and number density of the droplets were deduced from AFM images and presented with the corresponding growth conditions in Table 5.1. It was found that the geometry of the droplets is sensitive to both growth temperature and In deposition rate. Low deposition temperature (145 °C) led to small and highly dense droplets with diameter, height and number density of about 10.73 ± 11.82 nm, 3.87 ± 4.72 nm and 7.78×10^{10} cm^{-2} respectively.
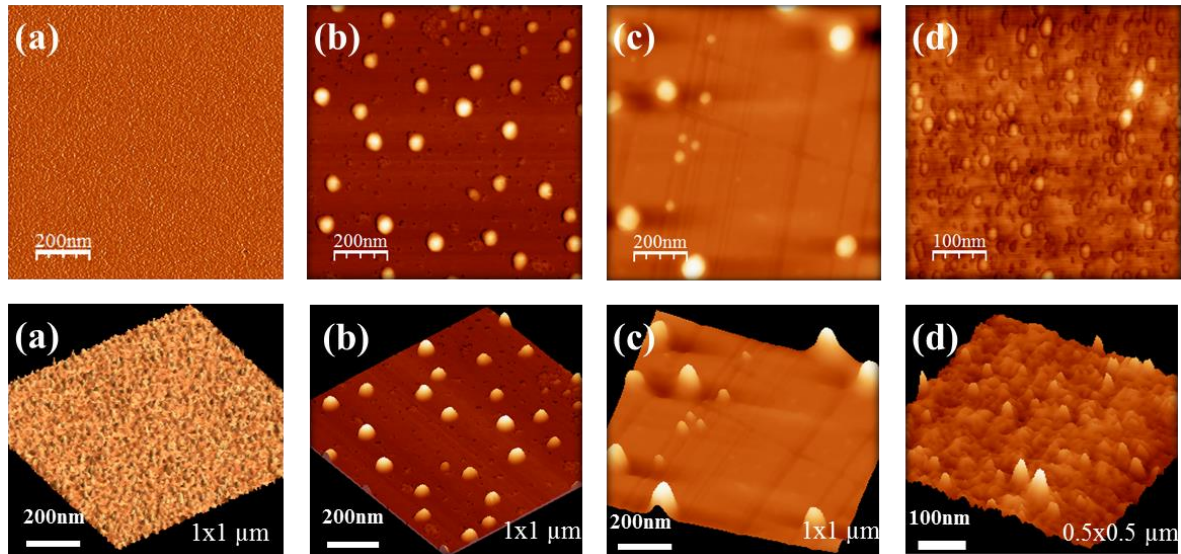
Figure 5.1 AFM images showing the top-view (top panel) and 3D view (bottom panel) of indium droplets deposited on Si (111) at various temperatures and Influxes: (a) 145 °C, 2.2×10^{-7} mbar; (b) 220 °C, 2.2×10^{-7} mbar; (c) 310 °C, 2.2×10^{-7} mbar and (d) 220 °C, 6.0×10^{-7} mbar

Table 5.1 Growth conditions and geometrical parameters of indium droplets grown on bare Si substrates

Sample	Deposition Temperature (^{0}C)	In-Flux (mbar) ($\times 10^{-7}$)	Group	Average Diameter (nm)	Average Height (nm)	Number Density (cm^{-2})
A	145	2.2	-	10.73 ± 11.82	3.87 ± 4.72	7.78×10^{10}
B	220	2.2	B$_S$	55.05 ± 0.65	19.66 ± 3.88	2.03×10^{9}
	220	2.2	B$_L$	70.36 ± 2.50	20.62 ± 1.21	6.33×10^{8}
C	310	2.2	C$_S$	111.53 ± 28.95	30.77 ± 4.99	6.15×10^{7}
	310	2.2	C$_L$	202.28 ± 8.48	82.71 ± 10.14	5.76×10^{7}
D	220	6.0	-	13.44 ± 7.55	01.85 ± 0.37	6.42×10^{10}

Higher deposition temperatures led to a bimodal size distribution of small (S) and large (L) droplets, hereafter referred to as B_S and B_L for sample B, C_S and C_L for sample C, respectively. Conditions for sample B led to uniform droplets with an average diameter, height and density of about 55.05 ± 0.65 nm, 19.66 ± 3.88 nm and 2.03×10^9 cm^{-2} for B_S, 70.36 ± 2.50 nm, 20.62 ± 1.21 nm and 6.33×10^8 cm^{-2} for B_L, respectively. A further rise in growth temperature resulted in droplets with increased diameter, height and reduced density (111.53 ± 28.95 nm, 30.77 ± 4.99 nm and 6.15×10^7 cm^{-2} for C_S, 202.28 ± 8.48 nm, 82.71 ± 10.14 nm and 5.76×10^7 cm^{-2} for C_L). The histograms in Figure 5.2 depict the diameter and height distribution of the indium droplets samples. It is believed that this behaviour is connected to the increased diffusion length of In adatoms which results in larger and less dense droplets [98]. An increase in In-flux led to the formation of nearly coalescent droplets with an average diameter, height and density of 13.44 ± 7.55 nm, 1.85 ± 0.37 nm and 6.42×10^{10} cm^{-2}, respectively. This observation is attributed to the reduced adatom diffusion time which leads to dense and small droplets.

There is a certain critical diameter for NWs growths below that value no growth is possible. This is due to the limitation posed by the Gibbs–Thomson effect[76, 184] which defines the thermodynamic dependence of the chemical potential and NWs growth rate on its curvature and hence droplet diameter. By implication, extremely small droplets do not favour NWs growth however, the diameter of NWs can still be controllably manipulated for larger droplet diameters. It can be inferred that sample B is the optimal droplets for NWs growth owing to its unique geometry and areal density. As a result, all InA(Sb) NWs samples reported in this work employed In droplets with identical conditions to sample B for facilitating NWs nucleation.
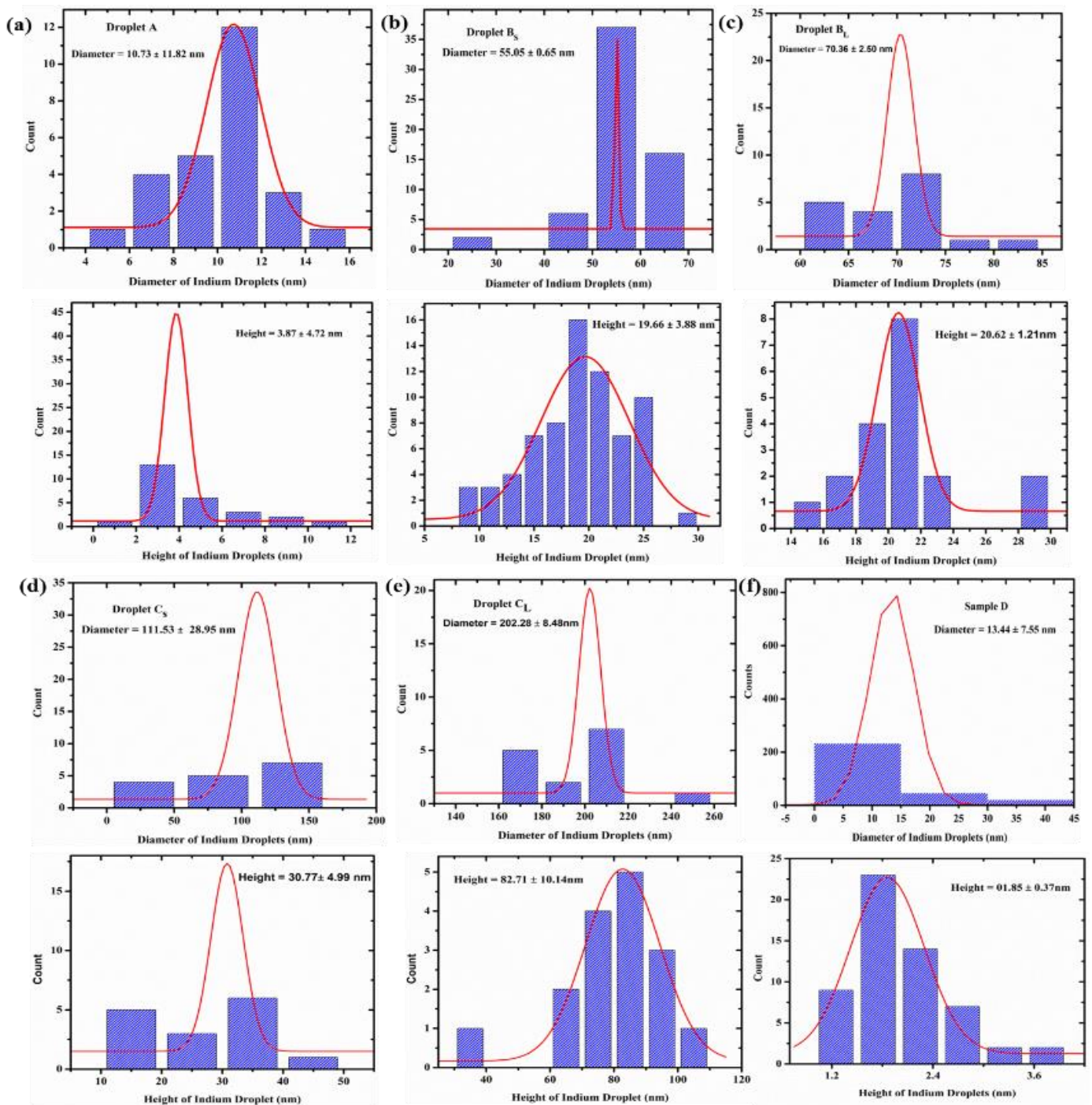
Figure 5.2 Histograms of the diameter (top) and height (bottom) size distributions of Indium droplets samples A (a); small B [B$_s$] (b); large B [B$_L$] (c); small C [C$_s$] (d) ; large C [C$_L$] (e) and D (f).

5.2 Growth Procedure of InAs Nanowires by In-assisted Droplet Epitaxy

A series of InAs NWs samples (t_{25}- t_{144}) were grown on bare Si substrates by In-assisted droplet epitaxy (DE) growth technique. In-droplets were pre-deposited on the Si substrates to act as preferential nucleation sites at pre-optimised growth conditions using a temperature of 220°C with an indium beam equivalent pressure (BEP) of 2.2×10^{-7} mbar for a nominal thickness of 3 ML. The substrate temperature was then ramped up to 440 - 500 °C followed by the simultaneous opening of the In and As shutters (As/In flux ratio > 45) for NWs growth. The growth was terminated by closing both shutters simultaneously. Except where otherwise mentioned, all the InAs NWs were fabricated under similar conditions with growth time of 25-144 min. The surface morphology of as-grown NWs (Figure 5.3 (a)–(d)) was investigated using a LEO 1530 Gemini FEG SEM working at 15 kV.
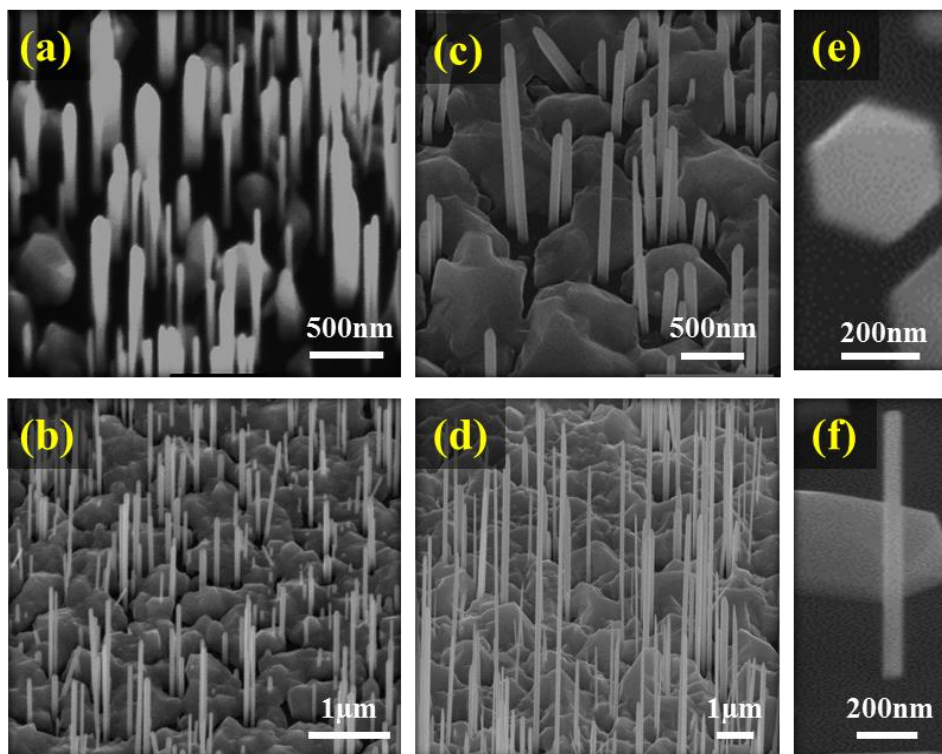
Figure 5.3 Tilted SEM images of vertically-aligned InAs NWs grown for (a) 25 min, (b) 40 min, (c) 60 min, and (d) 144 min. (e) and (f) are the cross-sectional and high-magnification images of NWs grown for 40 min. Tilt angles for (a) and (b) are 30°, while for (c) and (d) they are 40° and 60°, respectively.

As can be seen, the NWs are vertically-aligned and non-tapered, without kinking along the entire wire length with well-facetted hexagonal cross-sections (Figure 5.3(e)). The uniform diameter across the NWs length can also be observed in Figure 5.3(f). A plot of the NWs diameter (D_{NW}) and density (ND_{NW}) as a function of growth time (t_{gr}) is shown in Figure 5.4. The diameters and densities of the small (B_S) and large (B_L) optimal In_{drop} are also shown for comparison. It is clear that the NWs diameters are comparable to the diameter (70.36 ± 2.50 nm) of the large In droplets (B_L). This indicates that the lateral size of the NWs is likely determined by the diameter of the catalyst droplets as reported previously[184]. Furthermore, the NWs densities of $6.25 \times 10^8 cm^{-2}$ (25 min), $4.54 \times 10^8 cm^{-2}$ (40 min), $4.78 \times 10^8 cm^{-2}$ (60 min) and $1.58 \times 10^8 cm^{-2}$ (144 min) correlate to the density of the large (B_L) droplets ($6.33 \times 10^8 cm^{-2}$), but are much lower than that of the small (B_S) droplets ($2.03 \times 10^9 cm^{-2}$). These suggest only the droplets with diameter ≥ 70 nm contribute to the nucleation of the NWs suggestive of a size dependent nucleation associated with the Gibbs-Thomson effect which shows the diameter
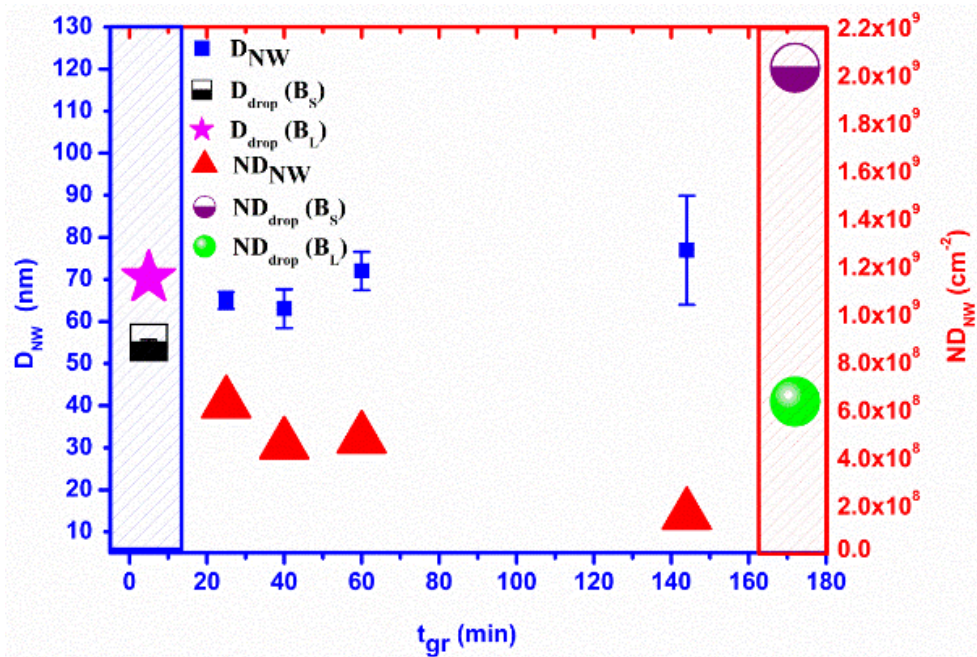
Figure 5.4 Plot of nanowire diameter (D_{NW}) and number density (ND_{NW}) as a function of growth time (t_{gr}). The diameters (D_{drop}) and densities (ND_{drop}) of small (B_S) and large (B_L) optimal indium droplets (In_{drop}) are also shown for comparison.

dependence of NWs growth rate. Specifically, it demonstrates that the growth rate of NWs scales inversely with the droplet diameter and curvature due to changes to the chemical potentials difference. This is particularly relevant at low supersaturation [185, 186] and in turn high In concentration. This demonstrates that the diameter and density of NWs are defined by the geometry and spatial distribution of pre-deposited droplets [187]. Worthy of note is the insignificant increase in D_{NW} (~ 10nm) for about 120 min of growth which sharply contrast the commonly observed diameter expansion as a function of growth time (more details in subsection 5.4.1). However, the slight decline in NW density particularly for $t_{gr} = 144$ min is attributed to its suppression with increased growth of large Islands.

5.3 Structural Characterization of Droplet Epitaxy Grown InAs Nanowires

The crystal quality of the NWs was investigated by XRD (Philips PW 1720). Figure 5.5 shows a typical XRD pattern (t_{144}) of as-grown InAs NWs. The visible peak at 2θ values of 25.4° and 52.2° are assigned to the (111) and (222) diffractions corresponding to zinc-blende (ZB) InAs which agree well with that of bulk ZB InAs[185] and ZB NWs structures[140]. The peak at 28.4° is associated with the diffraction from Si (111). The typical 2θ diffraction angles from wurtzite (WZ) InAs at 25.3° (002) and 27.2° (101) [90] are not visible in the XRD scan, this suggests a dominant ZB crystal in the NWs.

High-resolution TEM investigation was performed on a JEOL-JEM 2100 microscope working at 200kV to gain further insight into the structural property of the NWs. A representative HRTEM image (t_{60}) depicted in Figure 5.6a reveals that the NWs present a ZB structure with a high density of stacking faults (SFs) and twin boundaries. Typically, III−V semiconductor NWs crystallize either in the pure ZB phase, pure WZ phase or a combination of both ZB and WZ (ZB/WZ mixtures).
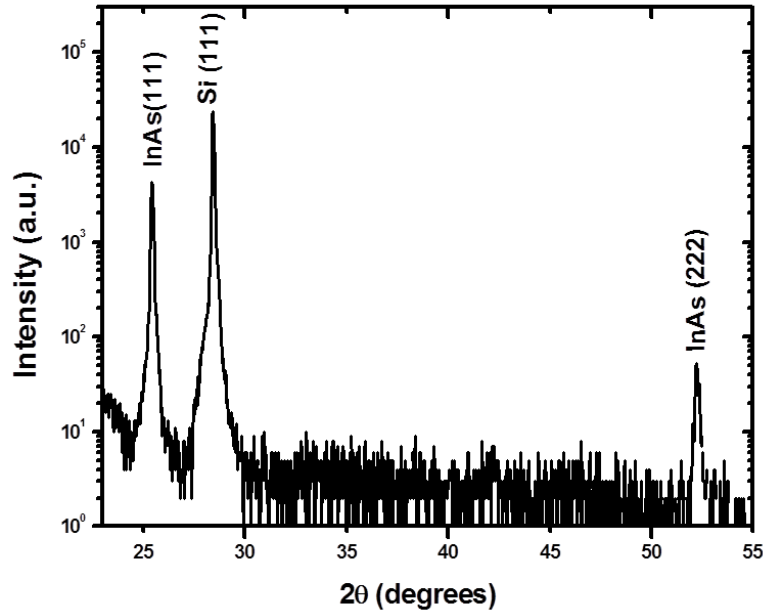
Figure 5.5 X-ray diffraction (XRD) patterns of InAs nanowires on Si (111)

A III-V semiconductor crystal bilayer (BL) is composed of a pair of a single group III and group V atom. The crystal structure of a NW is dictated by the sequential arrangement of the BL. A typical ZB sequence is …ABCABC… while a WZ sequence is …ABABAB… where each letter represents a bilayer. A SF results from a partial distortion of the vertical stacking sequence either by the absence of a segment in the normal sequence or the inclusion of a single segment of the other crystal structure. In the ZB phase, a sequence of ABC<u>AB</u>ABC indicates a SF with the fault line between C and A leading to the inclusion of a WZ unit (<u>AB</u>) between the ZB segments. Similarly, for a WZ phase a SF exists in a stacking sequence of the form ABA<u>C</u>BAB due to the inclusion of <u>C</u> which alters the regular WZ sequence. Closely related to SFs are rotational twins (RTs) which are created when a segment of a crystal is rotated by 60° around the growth axis (<111>) such that it is translated to a mirror image of the regular segment. The interface between the regular and mirror segments is referred to as the twin boundary. A stacking sequence of ABAB C BABA for WZ phase and ABC A CBA for the ZB phase illustrates the presence of RTs. The observed continuous streaks running parallel to ⟨111⟩

71

direction in the selected area electron diffraction (SAED) pattern (see inset in Figure 5.6(a)) further confirms the presence of microtwins and SFs in the NWs. This could be associated with the relatively high stability of the hexagonal phase of thin NWs owing to its lower surface energy in comparison to the corresponding ZB crystal orientation[186]. This phenomenon is consistent with previous reports of self-assisted InAs NWs growths [53, 139, 141]. The TEM image of a NW (Figure 5.6(b)) shows the uniform diameter along the entire NW length. A ~1– 2 nm thick amorphous layer surrounding the InAs NWs is also visible which could be linked to native indium oxidation upon exposure to ambient air[187].
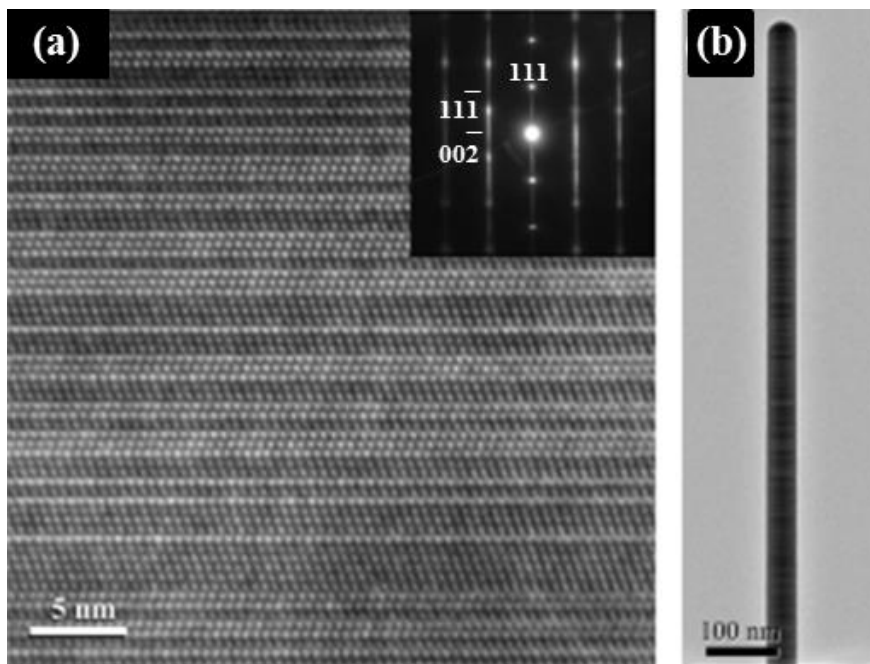
Figure 5.6 (a) Typical HRTEM image of NWs showing zinc-blende structure containing high density of stacking faults and twin boundaries (inset corresponds to an electron diffraction pattern recorded in areas containing InAs NWs); (b) Bright-field TEM image showing the uniform diameter along the NW length.

5.4 Effect of Growth Parameters on InAs Nanowires Growth on Silicon

5.4.1 Time Evolution of Nanowire Growth

The time dependent studies of NW morphology provides valuable insight into the nucleation and growth of these structures. In order to investigate the evolution of InAs NWs morphology as a function of growth time with a view to better understand the mechanism of NWs growth on Si as well as determine the required growth duration for realizing long NWs (with high aspect ratio), the effect of growth duration on InAs NWs growth was studied by examining the morphology of samples t_{25}- t_{144} (Figure 5.3) grown for 25, 40, 60 and 144 min respectively (details of growth methods can be found in subsection 5.2). In Figure 5.7, the evolution of average L_{NW} and D_{NW} as a function of growth time (t_{gr}) is depicted. A linear increase of L_{NW} with t_{gr} can be observed suggestive of a constant growth rate. It is generally accepted [132, 188] that NW lateral growth is activated when L_{NW} exceeds the adatom diffusion length (λ_L) along the sidewall which was not observed in the NWs evidenced by the almost constant NWs diameter along the entire length for all growth durations (L_{NW} = 3.82μm for t_{144}). It is well established that metal assisted NWs growth is comprised of two distinct regimes: at the initial stage, the NWs grow purely along the axial direction until they reach a certain critical length, where $L_{NW} > \lambda_L$. At this point, sidewall nucleation is triggered leading to diameter expansion[188]. The monotonic increase in L_{NW} (Figure 5.7) and the absence of any significant lateral broadening (only ~11nm increase in D_{NW} for t_{gr} increase from 25 to 144min) suggest a purely uniaxial growth regime ($\lambda_L \geq 3.82$μm). The axial growth of such thin NWs (D_{NW} <100 nm) is mainly dictated by adatom diffusion and not so strongly by the adsorption on the drop surface[189]. In addition, the axial growth rate of the InAs NWs is 15-20 times of the nominal deposition rate of 0.1μm/hr, a signature of diffusion induced (DI) InAs NWs growth typical of the MBE growth technique[190]. As a result, the observed high axial growth rate is attributed

73
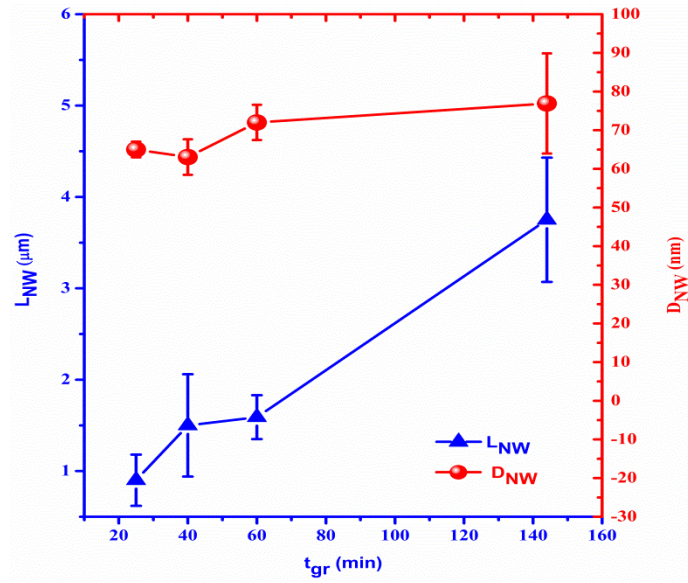
Figure 5.7 Evolution of the nanowire length (L_{NW}) and diameter (D_{NW}) as a function of growth time (t_{gr})
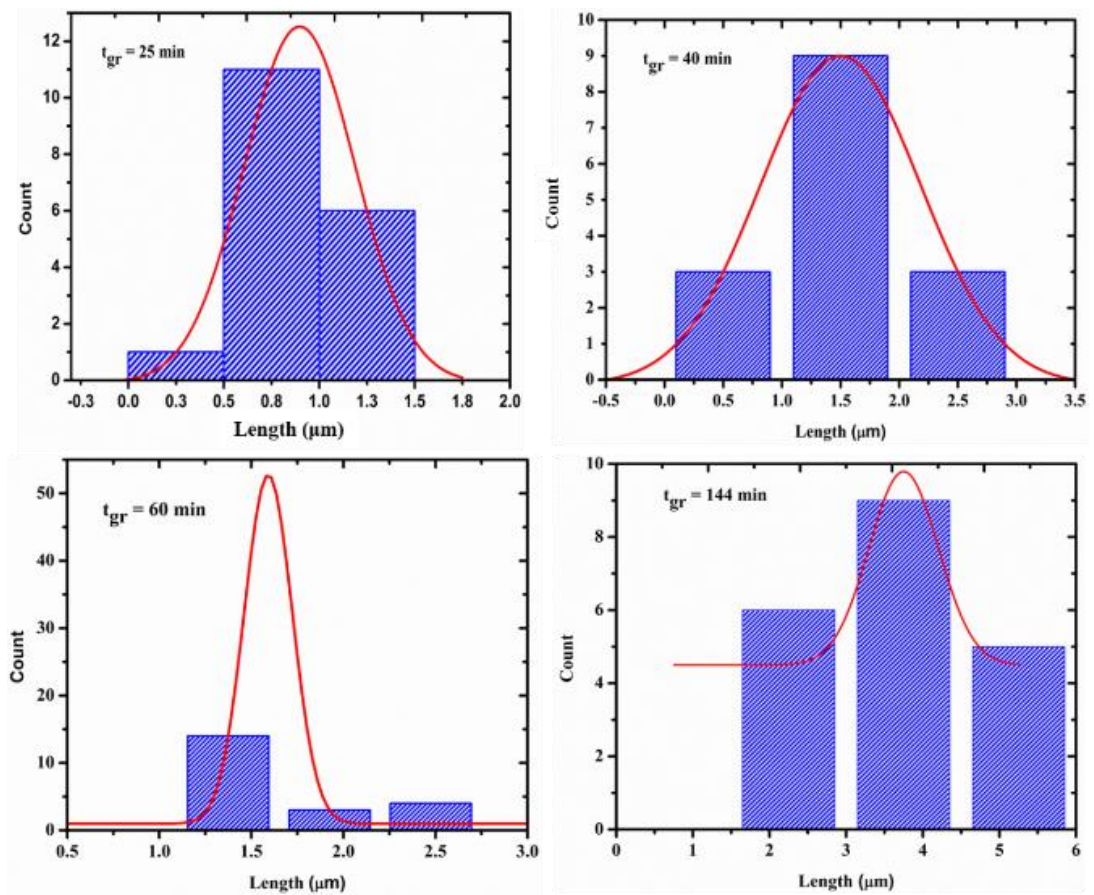
Figure 5.8 Histogram of InAs nanowires length as a function of growth time (t_{gr}).

to the large diffusivity of In adatoms along sidewall facets[141]. The observed large error bar for t_{144} possibly suggests a prolonged nucleation of NWs with time leading to large variations in L_{NW}. Figure 5.8 shows the statistical distribution of the lengths of as-grown NWs as a function of t_{gr}. This study demonstrates that InAs NWs growth on Si follows a diffusion induced growth technique characterized by high uniaxial growth rate resulting from large diffusivity of In adatoms along the NWs sidewall. In addition, long (~ 4µm) and high aspect ratio NWs suitable for high performance optoelectronic devices such as ballistic transistors operating in the quantum capacitance limit (QCL) were realized for a long growth duration (> 120 min).

5.4.2   Effect of Temperature on Nanowire Growth

Growth temperature is an essential parameter for tuning the NWs morphology owing to its significant influence on NWs growth kinetics. In order to investigate the influence of growth temperature (G_T) on NWs morphology as well as determine the optimum conditions for achieving a high yield of InAs NWs, a series of InAs NWs samples were deposited on Si (111) substrates under As-rich condition (As/In flux ratio > 45) for the about 1 hour while the temperature was varied in the range of 400 - 475°C at a fixed In [(1.75 - 2.25) x 10^{-7} mbar] and As ($8.0 \times 10^{-6} - 2 \times 10^{-5}$ mbar) flux. Prior to growth initiation, the Si substrates were first dipped in 12% hydrofluoric acid solution for 3 min to remove the native oxide, then immediately loaded into the MBE system to avoid re-oxidation and thermally outgassed. In droplets were then deposited on the substrates at pre-optimized conditions as described previously. The NWs densities in this work were mostly estimated from an area of about 25-100 µm^2 of the samples. Figure 5.9 shows the SEM micrographs of InAs NWs grown at different temperatures while Figure 5.10 shows the dependence of nanowire areal density (ND_{NW}) on temperature. Notably, at 400°C the growth was dominated by InAs clusters which suggests a kinetically limited
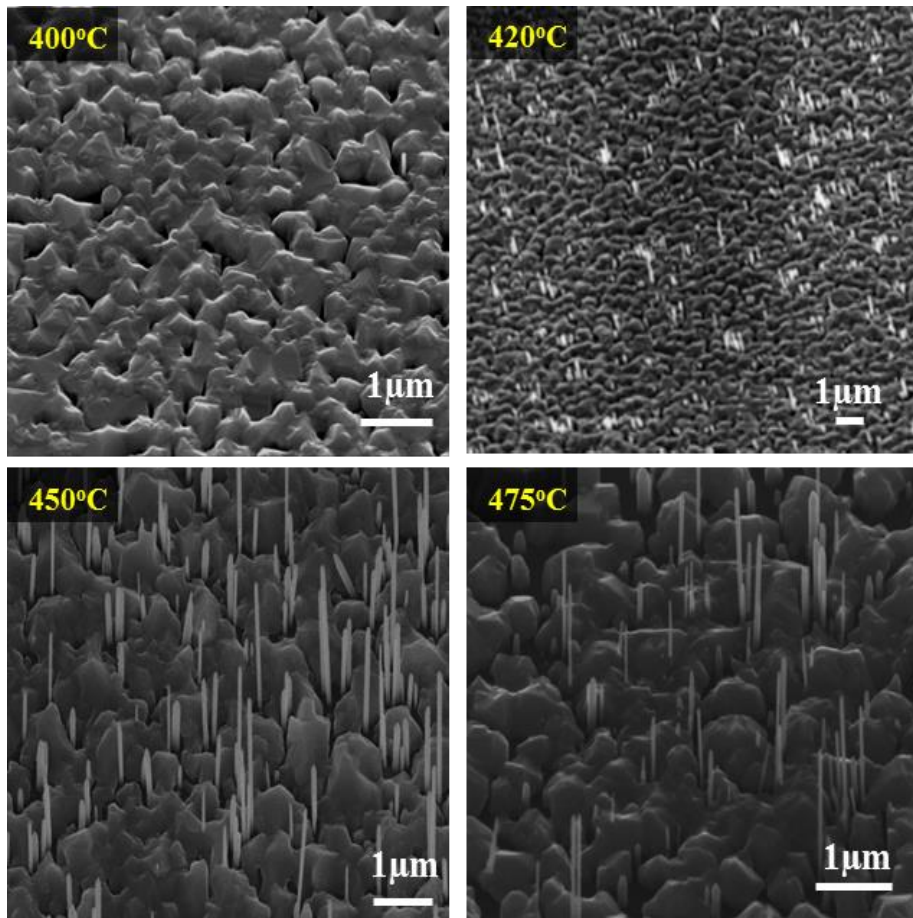
Figure 5.9 Tilted SEM images of InAs NWs grown on Silicon substrates with fixed In-flux of 1.75 x 10^{-7} mbar at various temperatures in the range of 400 - 475°C. Tilt angle for each figure is 45° except figure c which is 40°.
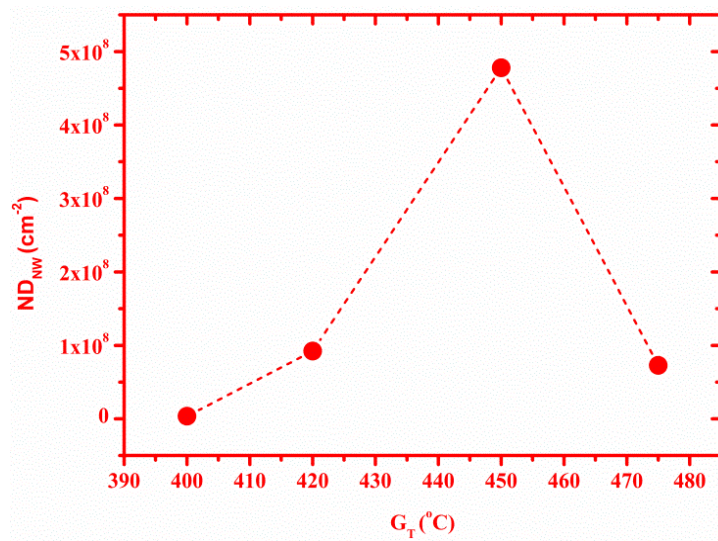
Figure 5.10 Plot of nanowire areal density (ND_{NW}) versus growth temperature (G_T).
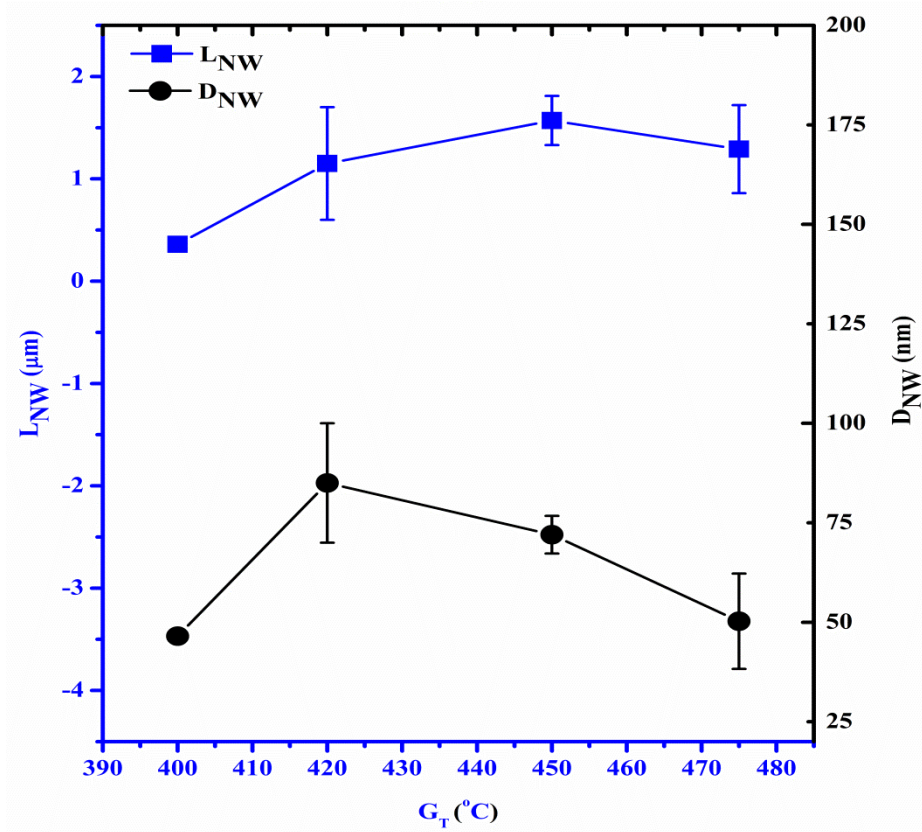
Figure 5.11 Plot of InAs nanowires length (L_{NW}) and diameter (D_{NW}) on silicon substrates as a function of growth temperature (G_T).

adatom diffusion owing to the significantly low temperature. In sharp contrast, NWs growth was realized within a narrow growth window of 420-475°C, with the highest yield of vertically-aligned NWs obtained at ~ 450°C while a low yield of NWs was obtained at 475°C resulting from a long adatom diffusion length. This indicates the strong influence of G_T on NWs growth kinetics. A plot of L_{NW} and D_{NW} as a function of G_T shown in Figure 5.11 reveals changes in the axial growth of the nanowires; initially L_{NW} slightly increases with temperature up to 450°C after which there was no significant change in L_{NW} resulting in the realization of maximum axial growth rate at 450°C. On the other hand, although thick NWs were realized at 420°C, the diameter of NWs decreased with increasing temperature in the range of 450°C to 475°C due to

the increased adatoms diffusion to the NWs tip in favour of axial growth. This observation suggests higher temperatures ($\geq 450^{\circ}$C) favour the growth of high aspect ratio NWs and can be interpreted in terms of the temperature dependent adatom diffusion flux from the substrate to the NWs tip [191, 192]. This study demonstrates that InAs NWs growth can be realized on bare Si by droplet epitaxy within a relatively narrow growth window of 420-475°C, with the highest yield of vertically-aligned NWs obtained at ~ 450°C.

5.4.3. Effect of V/III ratio on Nanowire growth

Aiming to elucidate the required V/III flux ratio suitable for realizing InAs NWs growth by droplet epitaxy on bare Si and the influence of the V/III flux ratio, three InAs NWs samples were grown on Si (111) substrates following established procedure at a constant temperature of 440 - 500 °C for growth duration of 20 minutes. The In –flux was fixed (~1.75 x 10^{-7} mbar) while the V/III flux ratio (As_{Fx}/In_{Fx}) was tuned from 27 to 55 by varying the As-flux from 4.8 - 9.6 x 10^{-6} mbar. Figure 5.12 demonstrates the variation of NWs morphology and density with As_{Fx}/In_{Fx} ratio. It is clear that NWs nucleation probability is strongly influenced by the As_{Fx}/In_{Fx} ratio. NWs growth was completely inhibited at relatively low As_{Fx}/In_{Fx} of ~27 evidenced by the growth of InAs clusters (islands). This is in good agreement with previous reports [193, 194] and can be understood given the fact that group V-rich conditions are required for the nucleation and growth of NWs[135] in contrast to excess In–rich conditions which prohibit NWs growth. It is well established that the axial growth of self- catalysed NWs is highly dependent on the group V flux [195, 196]. By slightly raising the As_{Fx}/In_{Fx} to ~ 51, a transition to the NWs morphology was induced with the realization of highly dense (ND_{NW}= 4.23 x 10^9) NW arrays. This demonstrates that As-rich conditions are required for the

78
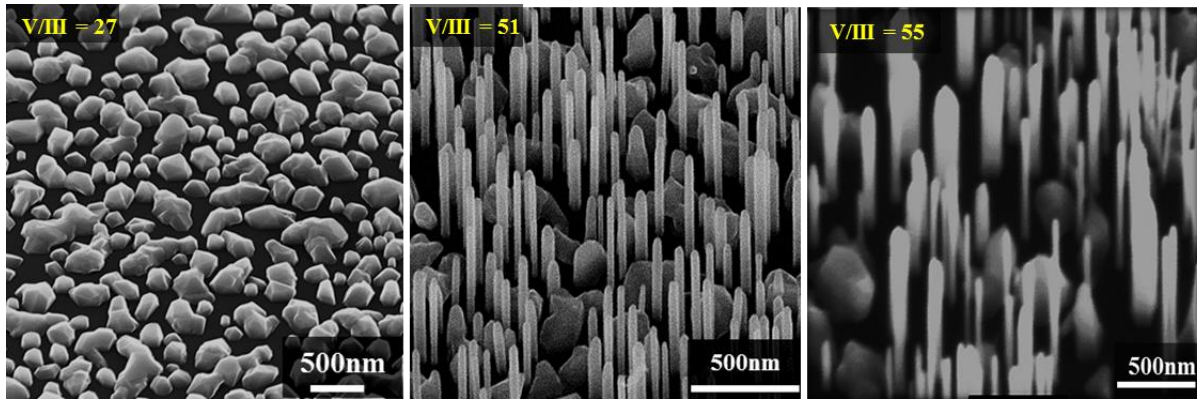
Figure 5.12 45º tilted SEM images of InAs nanowires on Si grown with a fixed growth temperature (G_T) of 450ºC and different V/III flux ratio (As_{Fx}/In_{Fx}) of 27 (a), 51(b) and 55(c).
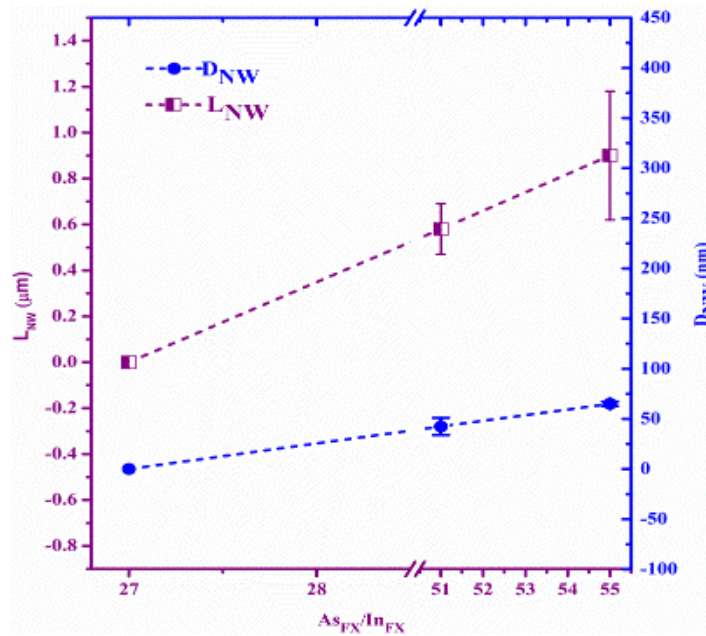
Figure 5.13 Plot of nanowire length (L_{NW}) and diameter (D_{NW}) as function of arsenic/indium flux ratio (As_{Fx}/In_{Fx}) at a constant temperature of 450ºC.

nucleation and growth of NWs via the droplet epitaxy technique similar to previous report[197]. A slight increase in As_{Fx}/In_{Fx} to 55 was accompanied by a slight decrease in the NWs number density due to the strong dependence of NWs nucleation on In-flux. This observation is consistent with previous studies by Dayeh et al[198]. It was shown that the NW nucleation rate drops as the effective V/III ratio is increased due to the depletion of In from the NW growth sites. Detailed analysis of the SEM images revealed a strong dependence of axial

NWs growth on the As_{Fx}/In_{Fx} (Figure 5.13). L_{NW} (and in effect axial growth) increases monotonically with increasing As-flux (high As_{Fx}/In_{Fx}) in good agreement with previous studies[197]. It has been demonstrated that self-catalyzed NWs elongation rate is controlled by the group V flux [195, 196]. On the other hand there was no significant change in D_{NW}. This demonstrates that As-rich conditions (As/In > 50) are required for the nucleation and growth of InAs NWs on bare Si via the droplet epitaxy technique and the axial growth of InAs NWs is limited by As-flux.

5.4.4   Effect of Growth Rate on Nanowire Growth

To investigate the dependence of NWs morphology on the growth rate, a series of experiments were performed at 440 - 500 °C and fixed As-flux ($8.0 \times 10^{-6} - 2 \times 10^{-5}$ mbar) while the 2D equivalent growth rate was tuned from 0.1 to 0.3μm/hr by varying the In-flux for the I hour growth duration. Figure 5.14 shows the SEM images of InAs NWs grown on Si as a function of growth rate. As can be seen, NWs nucleation decreases by an order of magnitude with increasing growth rate from 0.1 to 0.2 μm/hr at a constant G_T (Figure 5.15). Almost no NWs growth was observed at a growth rate of 0.3 μm/hr suggesting NWs growth is promoted by low growth rates. This could likely be associated with the availability of excess In adatoms possibly
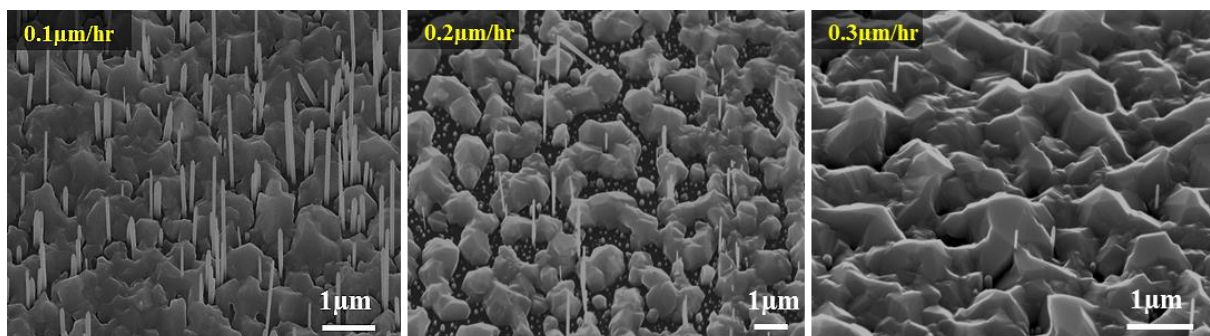
Figure 5.14 InAs nanowires growth on Si (111) at a constant temperature and different growth rates
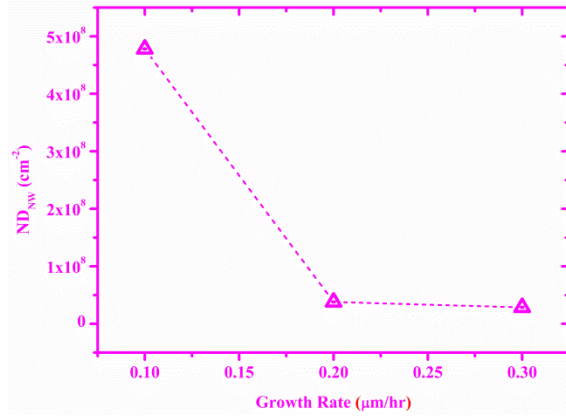
Figure 5.15 Variation of nanowire density (ND_{NW}) as a function of growth rate.
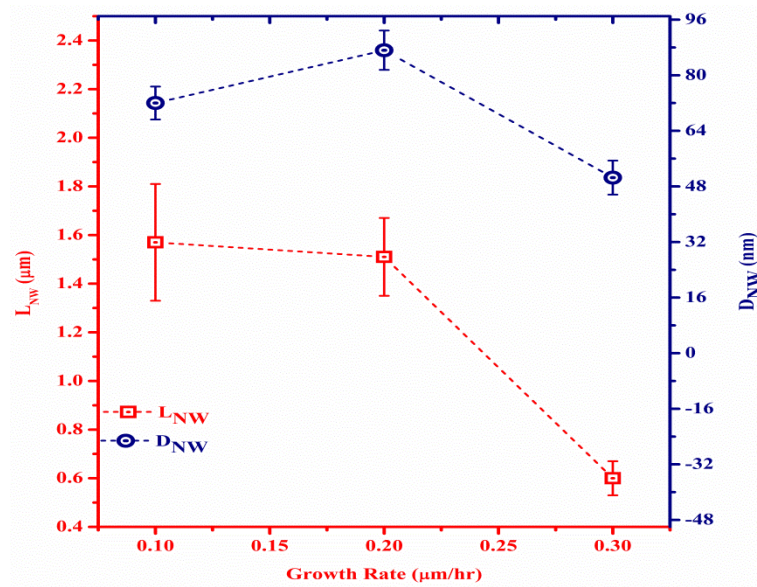
Figure 5.16 Dependence of InAs nanowire length (L_{NW}) and diameter (D_{NW}) on growth rate at a constant temperature.

as a direct consequence of contributions from the pre-deposited In drop. Excess accumulation of Indium and surface growths imposes certain restrictions in the collection area thereby inhibiting adatom mobility resulting in a suppression of NWs nucleation probability with reduced ND_{NW}. The high volume of InAs clusters (islands) shown in Figure 5.14 (0.3µm/hr) provides clear evidence of the presence of excess surface growth on the substrate[199]. Figure 5.16 shows the variation of L_{NW} and D_{NW} as a function of growth rate. There was almost no

significant change to L_{NW} and D_{NW} with increasing growth rate from 0.1µm/hr to 0.2µm/hr. However, when a growth rate of 0.3µm/hr was utilized, L_{NW} decreased by over two orders of magnitude while D_{NW} reduced by ~2x. The observed trend can be explained by the significant decrease in the available adatom at the growth front due to the suppressed adatom diffusion length with increased cluster growth as described earlier. This shows that a high yield of droplet epitaxy grown, vertically-aligned InAs NWs on bare Si is promoted by a low growth rate (~0.1µm/hr). These studies demonstrate that the size and density of NWs can be independently controlled by tuning any of the basic growth parameters such as growth duration, growth temperature, growth rate and V/III flux ratio while keeping the others fixed.

5.5 Photoluminescence Properties of Droplet Epitaxy grown InAs Nanowires on Bare Si

An understanding of the optical properties and the mechanisms of carrier recombinations in droplet epitaxy grown NWs is crucial for application in functional optoelectronic devices. The optical properties of as-grown InAs NWs samples t_{25} and t_{144} deposited for 25 and 144 min respectively (details of growth methods are provided in subsection 5.2 along with SEM images depicted in Figure 5.3) were investigated. In order to perform the PL measurements, the InAs NWs samples were first mounted on a copper coldfinger and then inserted in an oxford instrument continuous flow cryostat filled with helium gas to allow for thermal contact. Liquid helium was used for cooling down the samples from 300 to 10K using a Bentham temperature controller. A spectra-physics model 2011 Ar+ ion laser (514 nm) was used as the excitation source while a liquid N_2 cooled InSb photodiode detector was used for the detection of PL signal from the samples. A lock-in amplifier and an optical chopper were used to suppress unwanted noise. Typical low temperature (10k) PL spectra of as-grown InAs NWs and a

reference bulk InAs is depicted in Figure 5.17. As can be seen, the InAs NWs exhibit a multipeak emission which can be resolved into a series of five emission peaks. The labelled peaks α_3 and α_4 are assigned to deep Impurity or defect related (IDR) [63, 200-202] and donor acceptor pair (DAP) [200, 203]·[204]·[205] emissions respectively while peak α_5 is ascribed to the band to band (BtB) [202],[63] emission in good agreement with previous reports; however, likely contributions from type II related emission cannot be completely ruled out due to the presence of ZB/WZ crystal phase mixtures. The origin of peak α_1 also observed by Sun et al
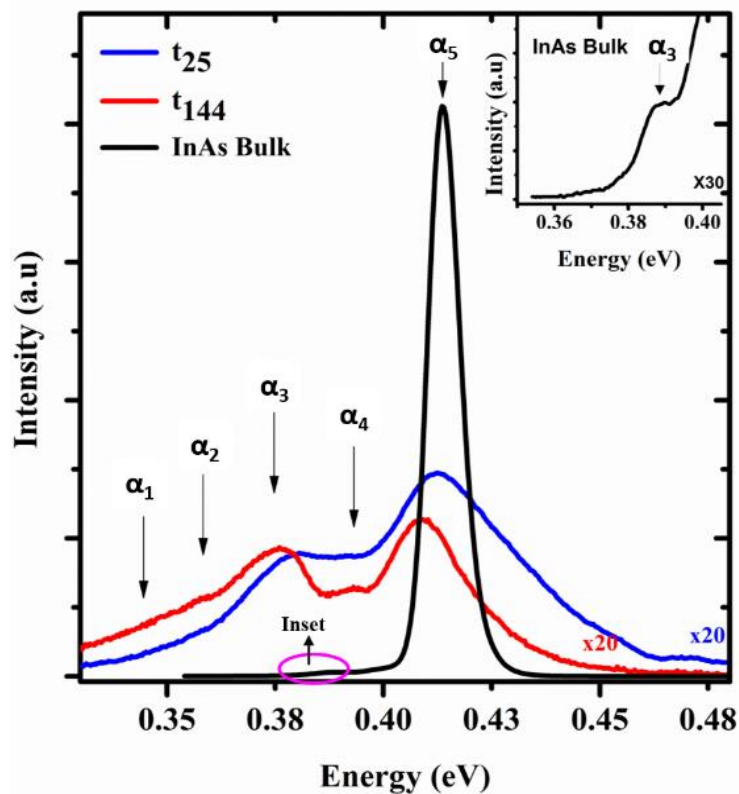
Figure 5.17 PL spectra of as-grown InAs NWs samples showing multipeak emissions at 10 K. The PL spectrum of InAs bulk is also shown for

[200] is yet unclear and requires further investigation while peak α_2 which has only been observed in InAs films corresponds to a phonon replica of IDR[202]. The InAs bulk shows a dominant peak α_5 and a low intensity peak α_3 (inset of Figure 5.17) while the PL spectra of

both samples show a strong and dominant peak emission (α_5) associated with the BtB recombination similar to the bulk InAs. Noticeable, there is no significant difference in the BtB PL peak position of as-grown InAs NWs samples with respect to the bulk sample which is a signature of optically superior NWs. No significant contribution from quantum confinement is anticipated due to the large diameters of the NWs (~65nm for t_{25}, ~77nm for t_{144}) relative to the InAs Bohr radius (~34 nm). However, the BtB peak position of sample t_{25} is slightly blue shifted by ~4meV with respect to that of t_{144}. This could be associated with the diameter-dependent blue-shift in PL peak energies[63] owing to the relatively small diameter of t_{25} compared to t_{144}. In order to gain further insight into the PL properties of as-grown NWs, the emission peaks were de-convoluted using Lorentzian approximations as shown in Figure 5.18 (a-c). The PL energies for the identified peaks are assigned to the various transitions in InAs NWs in comparison to that of bulk InAs as summarized in Table 5.2
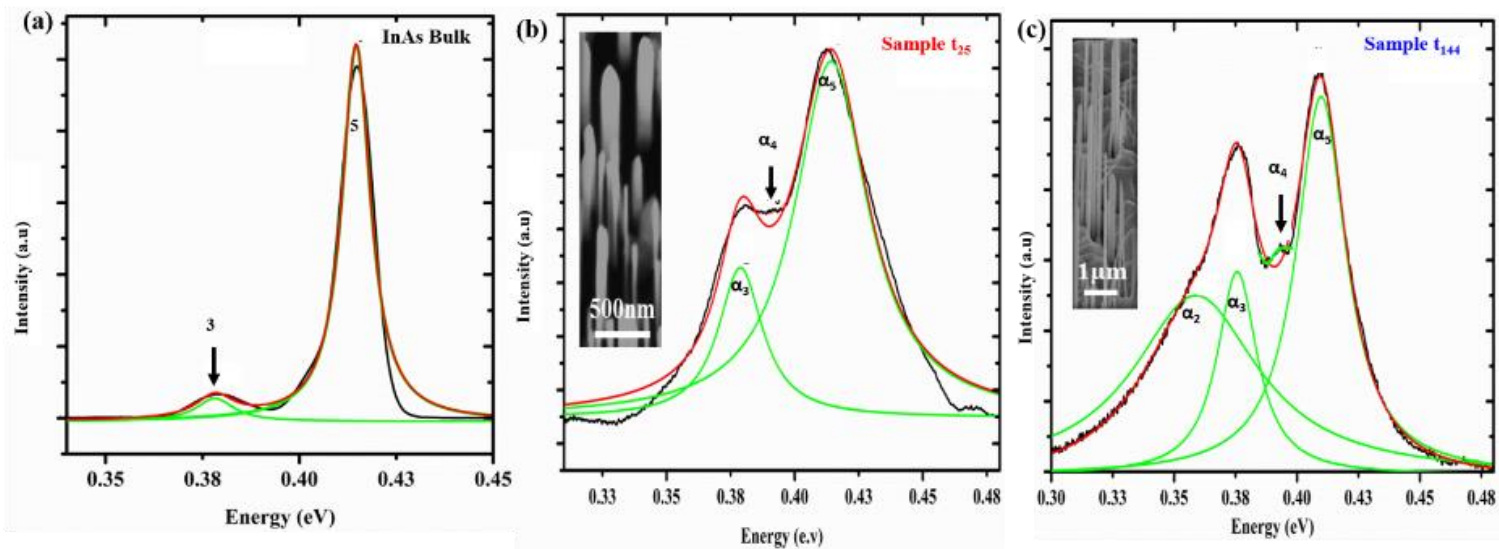
Figure 5.18 PL spectra of InAs bulk (a); InAs nanowires samples t_{25} (b) and t_{144} (c) deconvoluted into various Lorentz curves with peaks α_1 to α_5 (1-5 for bulk) corresponding to unknown peak, Phonon replica of deep impurity/defect related, deep impurity/defect related, donor-acceptor-pair and band-to-band emissions respectively.

Table 5.2 Assigned low Temperature (10k) PL emission energies of self-catalyzed InAs nanowires grown on Si compared to bulk InAs values with references (all energies are in eV).

Sample	(Peak α_1) Unknown	(Peak α_2) Phonon Replica of peak 3	(Peak α_3) Deep Impurity /Defect Related	(Peak α_4) Donor- Acceptor pair	(Peak α_5) Band-to-band
t_{25}	-	-	0.381	0.389	0.414
t_{144}	-	0.359	0.372	0.397	0.409
Film	-	-	0.388	-	0.414
Refs.	[200]	[202]	[63, 200-202]	[200, 203],[204],[205]	[202],[63]

Detailed analysis of peak α_5 of sample t_{25} revealed a spectral line width (full width at half maximum) of ~35meV which is ~5x that of the bulk InAs reference (~7meV). Intriguingly, peak α_5 of t_{144} exhibits a record narrow spectral linewidths of ~20 meV which is closer to the bulk value and relatively smaller than the commonly reported values (>29) meV[63, 200, 206].

In order to elucidate the origins of the various transitions in as-grown NWs, temperature and power-dependent PL measurements were performed at ~1W and 4K respectively. The temperature-dependent PL spectrum of bulk InAs depicted in Figure 5.19a shows a clear red-shift in peak α_5 PL energy. In sharp contrast, peak α_3 exhibits no significant shift in energy (insets) which provides further confirmation of its assignment to deep impurity or defect related emission. The temperature-dependent PL spectrum of sample t_{25} along with its corresponding Lorentz fits are shown in Figure 5.19(b-c) respectively. As can be seen, peaks α_3 and α_4 shows no obvious shift with increasing temperature which further confirms they are defect related. Conversely, peak α_5 shows an obvious red-shift of about 5meV with decreasing PL intensity for a rise in temperature from 10 to 160k while the FWHM increases from ~35 meV (10 K) to ~57 meV (120 K). Similarly for sample t_{144}, the peak intensity decreases with an increase in

temperature as expected. Peaks α₂ and α₄ (Figure 5.19(d-e)) exhibit a temperature independence over the investigated temperature range (10 – 250k) which is typical of defects or impurity related emissions[202]. However, peak α₃ slightly show an anomalous blue-shift with an increase in temperature from 80k to 250k, which sharply contrasts the usual band-gap shrinkage with increasing temperature. Owing to the large diameter of the NWs (77nm),
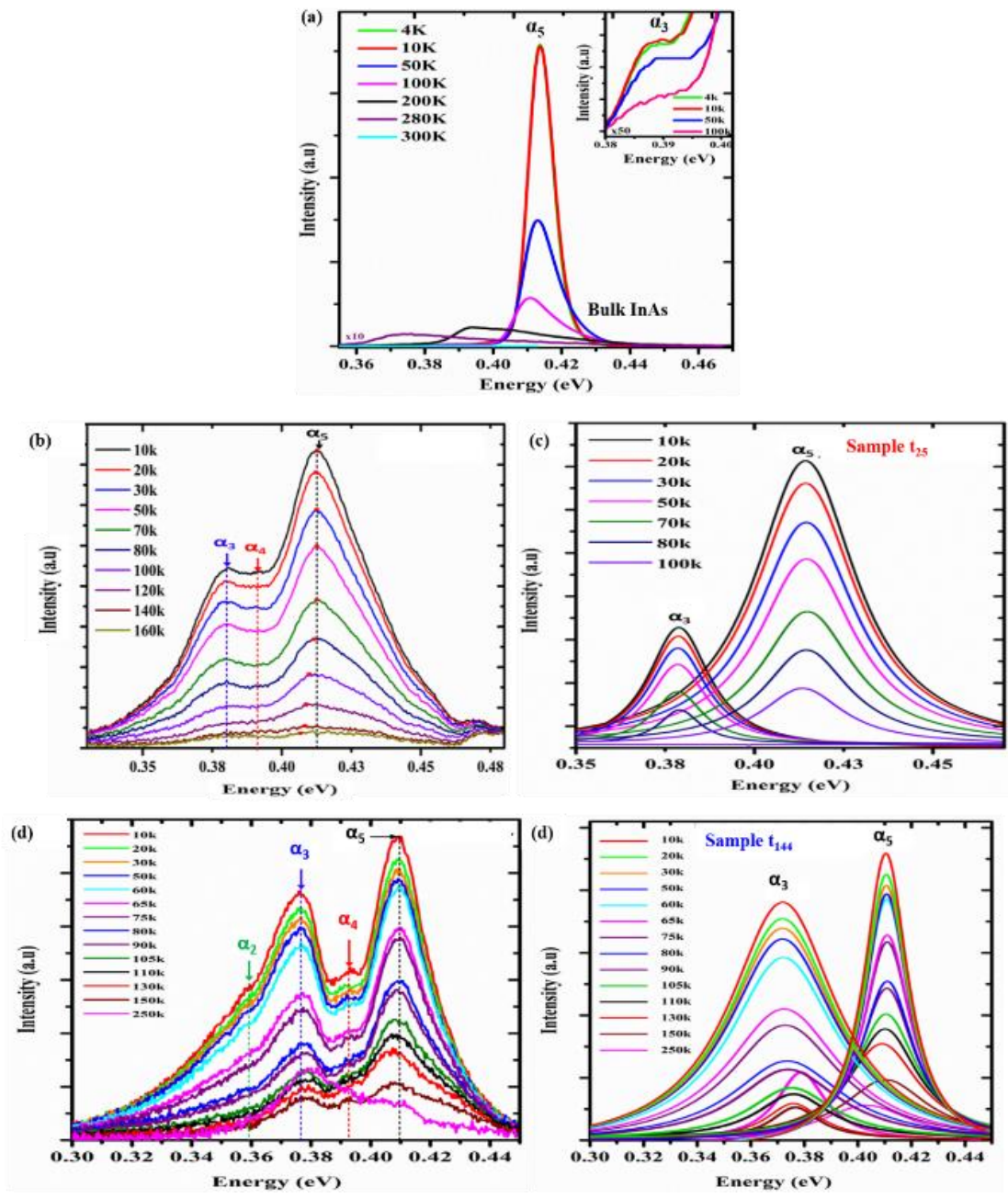
Figure 5.19 Temperature-dependent PL emission spectra of InAs bulk (a) and InAs nanowires samples t₂₅ (b) with its corresponding Lorentz curves for the dominant peaks [α₃ and α₅] (c) and sample t₁₄₄ (d) with its corresponding Lorentz curves for the dominant peaks [α₃ and α₅] (e).

quantum confinement effect is rule out and the behaviour is attributed to thermally-induced population of electrons localized at the defect state[207]. As shown in Figure 5.19 (e-f)), the PL peak α_5 shows an obvious red-shift with increasing temperature from a 0.409 to 0.403 eV with the PL FWHM increasing from ~20 to 42 meV for the investigated temperature range (10 K - 250 K) due to phonon scattering. The observed band gap shrinkage which is due to the temperature-induced lattice dilatation and electron-lattice interaction provides convincing evidence of a BtB emission of α_5. However, the slight temperature-induced shift exhibited by both NWs samples in comparison to bulk InAs[208] could be attributed to the influence of a native electron accumulation layer on the NWs surface resulting in the Fermi level (E_F) being pinned above the conduction band minimum[209-211]. In addition, the presence of WZ segments in the ZB dominant crystals could potentially modify the NWs energy gap due to its higher energy. It has been demonstrated [212-214] that the band gap of InAs NWs is crystal phase-dependent, with the WZ phase blue shifted by about 40–66 meV[212, 215, 216] in relation to their ZB counterpart. Interestingly, peak α_5 of sample t_{144} saturates at a significantly higher temperature (250k) than that of t_{25} (160k) as well as previously reported unpassivated (130-200k)[63, 200] and passivated (110k)[206] InAs NWs. This further confirms the presence of a relatively low density of defects in the NWs sample t_{144}. Figure 5.20a shows the variation of InAs NWs (samples t_{25} and t_{144}) PL peak energy as a function of temperature. It reveals the temperature dependence of the energy gap (E_g) of peaks α_5 agree reasonably well with the well-known Varshni empirical formula[217] [E_g (T) = E_0 - $AT^2/(B + T)$, where E_0 is the energy gap at 0K, T is the temperature, A and B are associated with the thermal expansion coefficient and the Debye temperature respectively] after the usual $k_BT/2$ correction which is generally applied to narrow-band gap semiconductors, where the dotted lines represents the Varshni fits. From the fitting, values of (1.98, 1.37 & 3.21) x 10^{-4} for "A" and 263, 218 & 267 for "B" were obtained corresponding to samples t_{25}, t_{144} and bulk InAs respectively.

In order to evaluate the temperature PL quenching process of sample t_{144}, the integrated PL intensities of peak α_5 was plotted as a function of 1/kT [Figures 5.20(b)] using Arrhenius equation which is expressed as I (T) = $(I(0))/[1 + Ae^{-\frac{E_a}{kT}} + Be^{-\frac{E_b}{kT}}]$, where I (0) is the spectral intensity at low temperatures, A and B measures the quenching mechanism, k_B is the Boltzmann constant and T the temperature while E_a and E_b denote the thermal activation energies at high and low temperatures respectively. Thermal activation energies of 24.87 meV and 9.59 meV for the bulk InAs and 24.28 meV and 24.29 meV for as-grown NWs sample t_{144} corresponding to electron-hole plasma emission[63] were extracted from the fitting within the regime of high and low temperatures respectively. This suggest similar quenching processes at both low and high temperatures in the droplet epitaxy grown InAs NWs. Illustrated in Figure 5.21 (a-b) are the PL spectra of InAs NWs samples t_{25} and t_{144} measured under various laser powers at ~4K compared to the InAs bulk. The α_5 peak position of t_{25} slightly blue- shifts by ~4meV due to band filling of photogenerated carriers while there was no significant shift
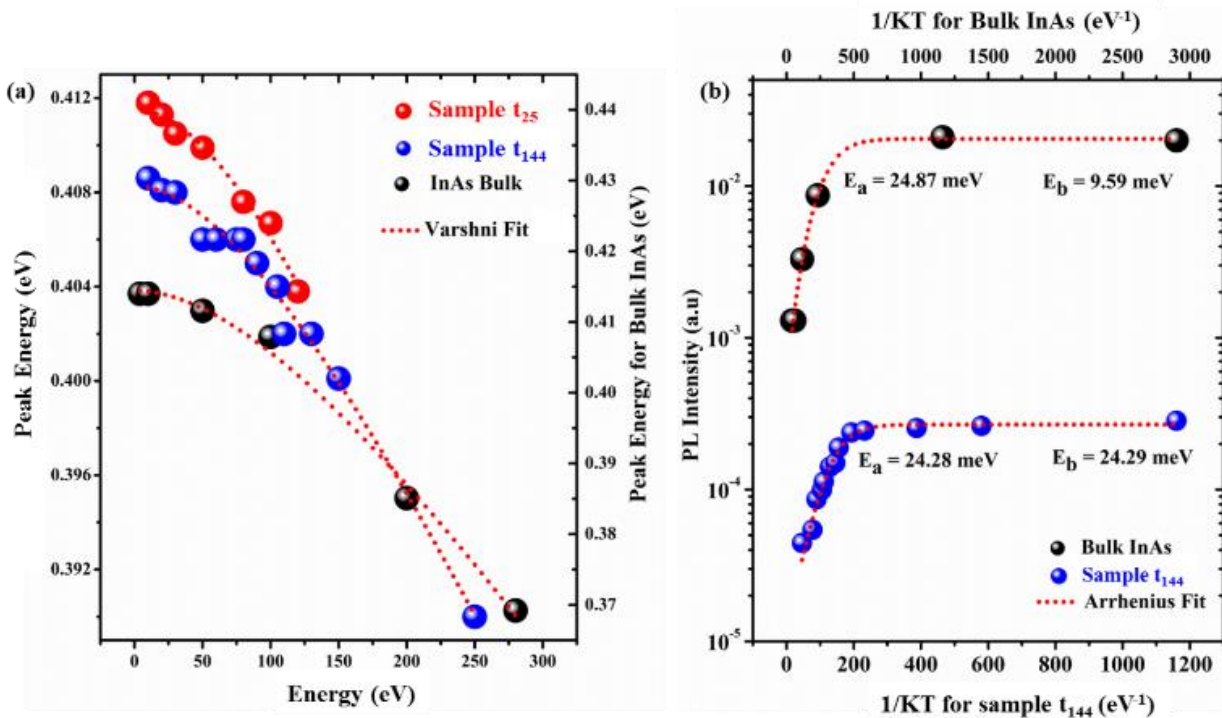
Figure 5.20 (a) Variation of PL peak energy of InAs nanowires (samples t_{25} and t_{144}) and InAs bulk as a function of temperature. The dotted curves represent the best varshni fits. (b) The Arrhenius plot of Integrated PL intensity versus 1/T for InAs bulk and sample t_{144}. The dotted curves represent the best arrhenius fit while E_a and E_b indicate the obtained activation energies at high and low temperatures.
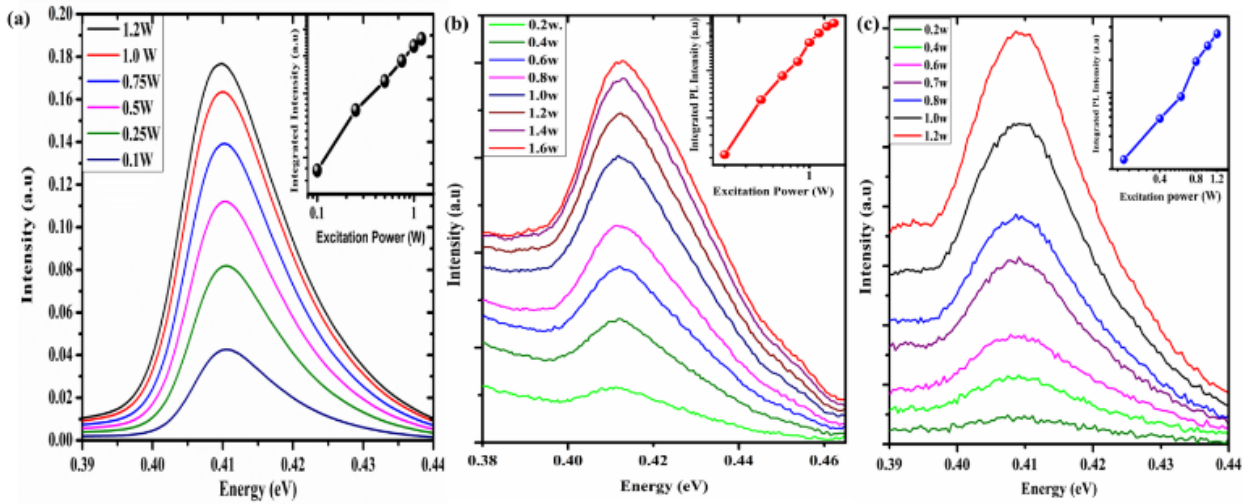
Figure 5.21 Power-dependent PL emission spectrum of InAs nanowires samples t_{25} (a) and t_{144} (b) measured at 4K compared to an InAs bulk (c). The inset shows the dependence of PL intensity on excitation power.

(0.19meV) in the t_{144} peak α_5 position as a function of varying excitation power which is consistent with previous report[200]. The near absence or weak excitation power dependence of the PL peak positions can be attributed to a slight broadening of the PL peak resulting in the local band filling effect being concealed[63, 218]. Such a near insensitive behaviour to variations in excitation power has being previously reported for high quality NWs [219] and was also observed in the InAs bulk sample (Figure 5.21c). It has been shown[214] that a quantum well related type-II band alignment between the WZ and ZB sections of polytypic crystals results in large blue-shift with significant broadening as a function of excitation power. A large blue shift of 15-30 meV with distinct peak broadening was observed for an increase in excitation power in the range of 0.01- 0.5w and was attributed to the band bending induced by the carrier accumulation at the interfaces and the band filling effect. However, the near insensitivity of the band energies to a large increase in excitation power (0.2 -1.6w) and the absence of a temperature dependent blue shift in as-grown NWs suggests any type II related emissions are possibly concealed by the dominant BtB peak. It is worthy to note however that the presence and intensity of the type II band alignment related emission in InAs NWs PL spectrum is highly dependent on the density of crystal phase mixtures and SFs which in turn

are significantly influenced by the growth conditions and NWs geometry. However, both samples exhibit higher PL efficiencies with increasing excitation power and the BtB emissions are linearly related to the excitation power (insets of Figure 5.21). This demonstrates the high optical properties of the droplet epitaxy grown InAs NWs.

Chapter 6

Growth and characterization of InAsSb Nanowires

The droplet epitaxy growth of InAsSb nanowires and the influence of Sb incorporation on the morphology and structural properties of InAsSb nanowires will be explicated in this chapter.

6.1   Growth Procedure for InAsSb Nanowires by Droplet Epitaxy

MBE growth of $InAs_{1-x}Sb_x$ NWs was performed under As-rich condition on bare Si (111) substrates initially cleaned following pre-established procedures (Section 4.1) and immediately loaded into the MBE system. In droplets were pre-deposited on the Si substrates as previously described (Section 5.1). The substrate temperature was then ramped up to 420-470°C for initiation of $InAs_{1-x}Sb_x$ NWs growth by the simultaneous introduction of all growth precursors. A time dependent series of two $InAs_{1-x}Sb_x$ NWs samples were grown with fixed In and As BEP (about 5.8 x10^{-6} mbar) for short growth (SG) time of 20 minutes and long growth (LG) time of 120 minutes, denoted as "SG" and "LG" respectively. Similar SG and LG Sb-free InAs NWs (previously discussed in sections 5.2 and 5.3) were used as reference. The Sb content in the NWs was controlled by tuning the Sb fractional flux (FF_{sb}) fed into the MBE chamber, where FF_{sb} is the ratio of Sb flux (ψ_{Sb}) to the combined group V (As + Sb) precursor fluxes (ψ_v) which is expressed as:

$$FF_{sb} = \frac{\psi_{sb}}{\psi_{As} + \psi_{sb}} \tag{6.1}$$

Here, ψ_{As} is the arsenic flux. Consequently, the Sb flux fluctuation in the range of 7.6x10^{-8} to 5x10^{-7} mbar led to a variation in FF_{Sb} of about 0.79%, 4.95%, 2.93% and 4.95% in samples

$S_{4.3}$, $S_{4.5}$, $L_{10.2}$ and $L_{14.5}$ respectively. The Sb content of the InAs$_{1-x}$Sb$_x$ NWs was determined by X-ray diffraction (XRD) performed on a Philips PW 1720 X-ray diffractometer with the Cu Kα1 radiation line (1.540Å) and further confirmed by Energy-dispersive X-ray spectroscopy (EDX) measurement using a FEI XL30 SFEG scanning electron microscope (SEM) at the University of Liverpool also utilized for investigation of the surface morphology of the as-grown NWs.

6.2   Sb Composition in InAsSb Nanowires

The percentage Sb mole fraction (x_m) in the NWs was evaluated by comparing the angular positions of the diffraction peaks from the (111) Zinc-blende (ZB) InAsSb (111) (Figure 6.1, FF$_{sb}$ = 0.79 - 4.68%) to that of the InAs NWs reference sample (Figure 6.1, FF$_{sb}$ = 0%). The peak at 28.4° is associated with the Si (111)[220] substrate while the diffractions at around 25° are assigned to the InAs$_{1-x}$Sb$_x$ NWs along the (111) direction. The interplanar spacing (d) between the (111) planes were extracted from the identified InAs$_{1-x}$Sb$_x$ (111) 2θ values using Bragg's law (equation 4.1) and the lattice parameters "a" deduced from the calculated lattice spacing. An increase in Sb incorporation was indicated by a shift in the (111) peak from 25.4° in the reference ZB InAs to lower angles with a corresponding increase in "a" values. The Sb content in the NWs was then deduced from the estimated lattice constants using the bulk[221] InSb (111) 2θ value (23.766[0]) according to Vegard's law [222].

$$x = \frac{a_{InAsSb} - a_{InAs}}{a_{InSb} - a_{InAs}} \qquad (6.2)$$

Where *a* is the lattice constant
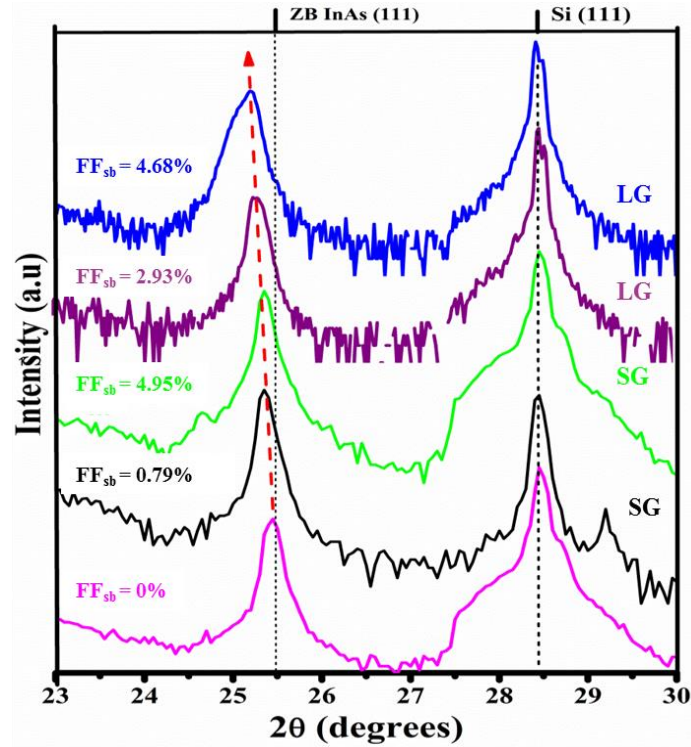
Figure 6.1 X-ray diffraction (XRD) patterns of InAs$_{1-x}$Sb$_x$ nanowires grown on Si. The Sb fractional flux ratio (FF$_{Sb}$) for the short growth (SG) and long growth (LG) samples are labelled with the associated spectrum.

The estimated Sb content in as-grown InAsSb NWs is detailed in Table 6.1. To further confirm successful Sb incorporation, sampled InAs$_{1-x}$Sb$_x$ films were analysed by energy dispersive x-ray (EDX) measurements. The obtained Sb content in most NWs closely correlates with the XRD values (XRD and EDX derived Sb content of 10.2% and 8.93% respectively were estimated for sample L$_{10.2}$). A typical EDX spectrum is depicted in Figure 6.2. Table 6.1 reveals a disproportionate dependence of Sb content on Sb flux particularly for the samples deposited for short growth duration. It is clear that the introduction of trace Sb flux (FF$_{Sb}$=0.79%) led to a significant incorporation of Sb (x_m = 4.3%) in contrast, a significant increase in FF$_{sb}$ (4.16%) resulted in only 0.2% rise in Sb incorporation[223]. A similar behaviour has been reported for self-catalyzed InAsSb NWs grown for 2 min[143]. Conversely, for the long growth time samples, a 1.75% rise in FF$_{sb}$ was accompanied by a significant (4.3%) increase in Sb mole

fraction. The following section explicates the surfactant effect of Sb on NWs morphology and adduces possible reasons for the observed trend.

Table 6.1 Growth parameters, "a" values and Sb content in $InAs_{1-x}Sb_x$ samples

Sample Name	Series	Growth duration (min)	FF_{sb} (%)	'a' (Å)	χ_m (%)
$S_{4.3}$	SG	20	0.79	6.076	4.3
$S_{4.5}$	SG	20	4.95	6.077	4.5
$L_{10.2}$	LG	120	2.93	6.101	10.2
$L_{14.5}$	LG	120	4.68	6.119	14.5
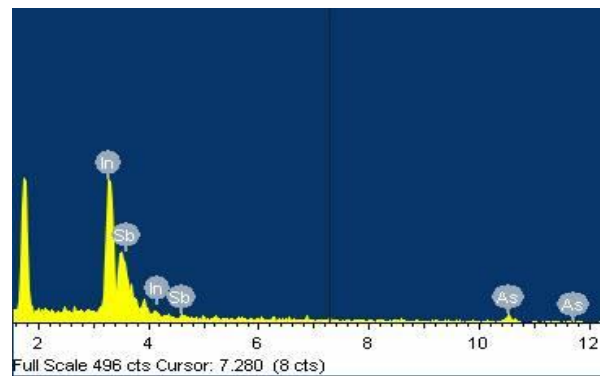
Figure 6.2 Typical EDX spectrum of as-grown $InAs_{1-x}Sb_x$ film confirming Sb incorporation with signals characteristic of As, In, and Sb.

6.3   Effect of Surfactant Sb on Nanowire Morphology

Figure 6.3 (a-d) shows the SEM images of SG (a) and LG (b-d) reference Sb-free InAs NWs with highly uniform diameter. Aiming to elucidate the effect of Sb incorporation on the morphology of the NWs, the detailed analysis of the geometry of Sb-free InAs NWs reference

samples was first undertaken. A plot of the NWs diameter (D_{NW}) and lateral growth rate (Lateral GR_{NW}) as a function of growth time (t_{gr}) are depicted in Figure 6.4. As can be
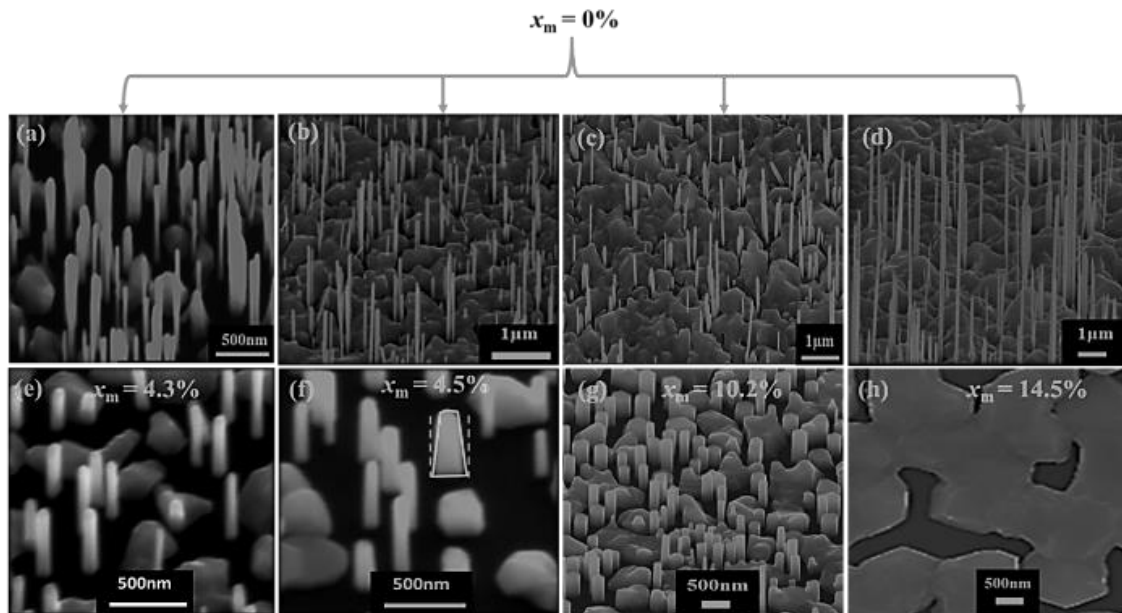
Figure 6.3 Tilted SEM images of short growth (a) and long growth reference InAs nanowires (NWs) grown for 40min (b) 60 min (c) and 144 min (d); Short growth (e-f) and long growth (g-h) InAs$_{1-x}$Sb$_x$ NWs with Sb incorporation (x_m) of 4.3% (e); 4.5 % (f); 10.2 % (g) and 14.5 % (h) respectively. A NW exhibiting a broad base is marked in f.
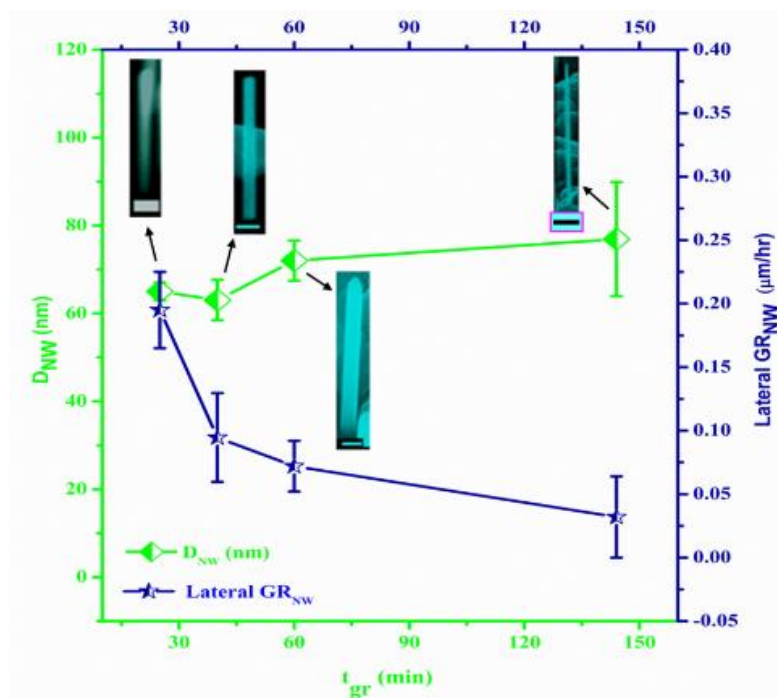
Figure 6.4 (a) Plot of nanowire diameter (D_{NW}) and lateral growth rate (Lateral Gr_{NW}) as a function of growth time (t_{gr}); the close-up SEM images for the various growth times are shown as insets. The scale bars correspond to 100 nm except t_{gr} = 144 which is 500nm.

seen, the lateral dimensions of the NWs vary in the range of ~65.00-76.57 nm. This indicates that there was no significant increase in the lateral dimensions of the NWs with increasing growth duration. The longest growth (144 minutes) led to NWs with diameter of ~76.57 nm, a slight increase of only 11.57nm in comparison with the shortest growth as shown in the insets (close-up SEM images of Figure 6.4). This observation indicates that there was no significant lateral growth (diameter expansion). Furthermore, detailed investigation of the evolution of NWs length (subsection 5.4.1) revealed a purely uniaxial growth of long NWs attributable to the large diffusivity of adatoms with a likely diffusion length $\geq 3.82 \mu m$. Typical SEM images of SG $InAs_{1-x}Sb_x$ (Figures 6.3 e-f) NWs reveal the addition of Sb led to the display of contrasting NWs geometries. Whereas the SG reference InAs NWs were ~65 nm in diameter and ~900 nm long, the introduction of Sb led to a clear increase in the lateral dimensions and a slight decrease in L_{NW}. The addition of trace Sb content (4.3%) in sample $S_{4.3}$ led to a significant increase (~ 68%) in D_{NW} and a slight drop (~3%) in L_{NW}. An increase in x_m to 4.5% (sample $S_{4.5}$) was accompanied by a disproportionate (~77%) expansion in D_{NW} and a corresponding shrinkage (~ 8%) in L_{NW} (Figure 6.5).
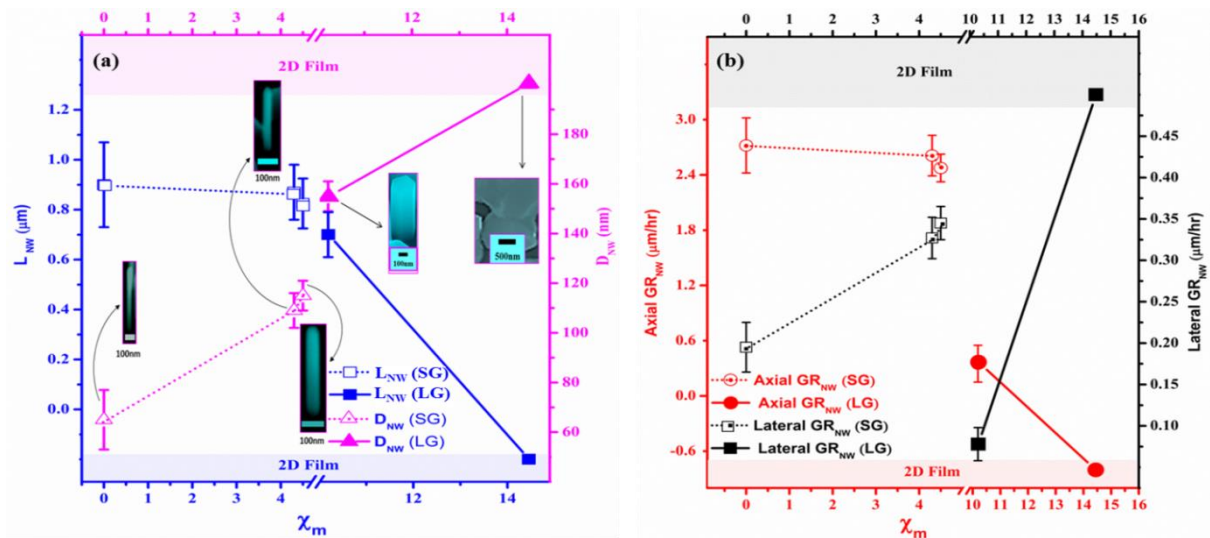
Figure 6.5 (a) The evolution of the nanowire length (L_{NW}) and diameter (D_{NW}) as a function of Sb mole fraction (x_m) for short growth (SG) and long growth (LG) durations. (b) Effect of Sb mole fraction (x_m) on nanowire lateral growth rate (Lateral GR_{NW}) and axial growth rate (Axial GR_{NW}) for both SG and LG grown samples.

Turning to the LG series (Figure 6.3 g-h), in comparison to the Sb-free InAs reference NWs deposited for long growth (LG) durations [60 min (D_{NW} = ~72nm, L_{NW} =1.57μm) and 144 min (D_{NW} = ~77nm, L_{NW} = 3.82 μm) shown in Figure 6.3c and d respectively], a dramatic modification to the geometry of the NWs was observed with Sb addition. Sample $L_{10.2}$ (x_m = 10.2%) exhibited a significantly large D_{NW} of ~155 nm with stunted L_{NW} of 0.7 μm (Figure 6.3g), and an increase in Sb content (x_m =14.5%) in sample $L_{14.5}$ favoured a further increase in lateral growth while significantly suppressing axial growth leading to the growth of 2D films (Figure 6.3h). Figure 6.5b shows the effect of x_m on the lateral GR_{NW} and axial growth rate (axial GR_{NW}) of $InAs_{1-x}Sb_x$ NWs. It is clear from the figure that the diameter expansion and axial growth shrinkage as a function of Sb content correlates with the growth rates. The observed geometrical modifications can therefore be attributed to the rapid rise in the lateral GR_{NW} with a corresponding contraction in axial GR_{NW}.

In order to fully understand the possible reasons for the observed changes in axial and lateral growth rate, an investigation of the thermodynamic mechanism that accounts for Sb segregation in InAsSb NWs was first carried out. The phenomenon of Sb segregation in InAs is linked to the bond energetics of the surfactant and the InAs binary alloy; the Sb-Sb bond is less tightly bound (30.2Kcal/mol)[224, 225] compared to the strong bonding of In-As (48.0Kcal/mol)[226, 227], hence there is a ready preference for the Sb atoms to be expelled and form a floating layer[228, 229]. This phenomenon is further promoted by the low volatility of the relatively heavy Sb atom (atomic number of 51) [230, 231]. Generally, Sb segregation is driven by three principal factors[232]:

(I)   The difference in surface energy between (Sb) and the solvent (InAs)

(II)   The difference in atomic size[233] and

(III)   The tendency towards phase separation.

Analysis of the ternary In-As-Sb system reveals: (I) Sb has a smaller surface energy $(0.38j/m^2)$[232] compared to Arsenic (As) [234], its addition will lead to a decrease in the surface energy of the binary alloy (InAs) which implies an increase in the Sb segregation enthalpy in favour of segregation; (II) Sb has a larger atomic size, its addition increases the alloy lattice parameter and thus decreases the steric effect, and (III) Sb/As is known to exhibit energy intermixing[235] and InAsSb has a strong tendency to phase separation[236] which further favours Sb segregation. This observation is consistent with previous studies[237, 238]. Owing to these reasons, Sb segregation is highly favourable and its inclusion mitigates the axial growth of InAsSb materials. Thus, a rise in Sb content with increasing flux results in heightened Sb segregation with increasing Sb coverage[239]. This explains the disproportionate 0.2% rise in Sb content in the SG samples corresponding to a significant FF_{sb} increase (4.16%) in sample $S_{4.5}$ when compared to $S_{4.3}$. In contrast, for the LG samples, a 1.75% rise in FF_{sb} was accompanied by a significant 4.3% increase in Sb mole fraction. This can be explained by the long Sb surface occupancy which enabled higher Sb incorporation probability for the long growth duration (120min) in comparison to the short duration (20min) employed for the SG samples.

The enhancement in lateral growth and suppression of axial growth is attributed to the surfactant effect of Sb with contributions from two distinct regimes. Regime I is concerned with the influence of Sb addition on the nucleation In droplet while regime II involves the Sb surfactant effect on the follow up NWs growth kinetics[240]. During the first regime, the introduction of trace amount of Sb species at growth initiation significantly modifies the geometry of pre-deposited In droplets by a combination of both thermodynamic and kinetic effects. From a thermodynamic perspective, the growth mode adopted by atoms of a crystallizing layer on a rigid dissimilar substrate is dictated by the balance of the equilibrium surface free energies[241]. The surface energies at the solid-vapour (Υ_{sv}), solid-droplet (Υ_{sd})

and droplet-vapour (Υ_{dv}) interfaces depicted in Figure 6.6 are combined in Young's equation[242]:

$$\gamma_{sv} = \gamma_{sd} + \gamma_{dv} \cos\beta \qquad (6.3)$$

Where β is the contact angle.

A slight modification of the surface energy on any of the interfaces would favour one of three possible growth modes: islanding (Volmer-Weber) [243] , layer-by-layer (Frank-Van der Merwe) [244], or layer-plus-island growth mode (Stranski-Krastanov) [242, 245]. The presence of the minutest concentration of Sb partially induces a decrease in surface energy at
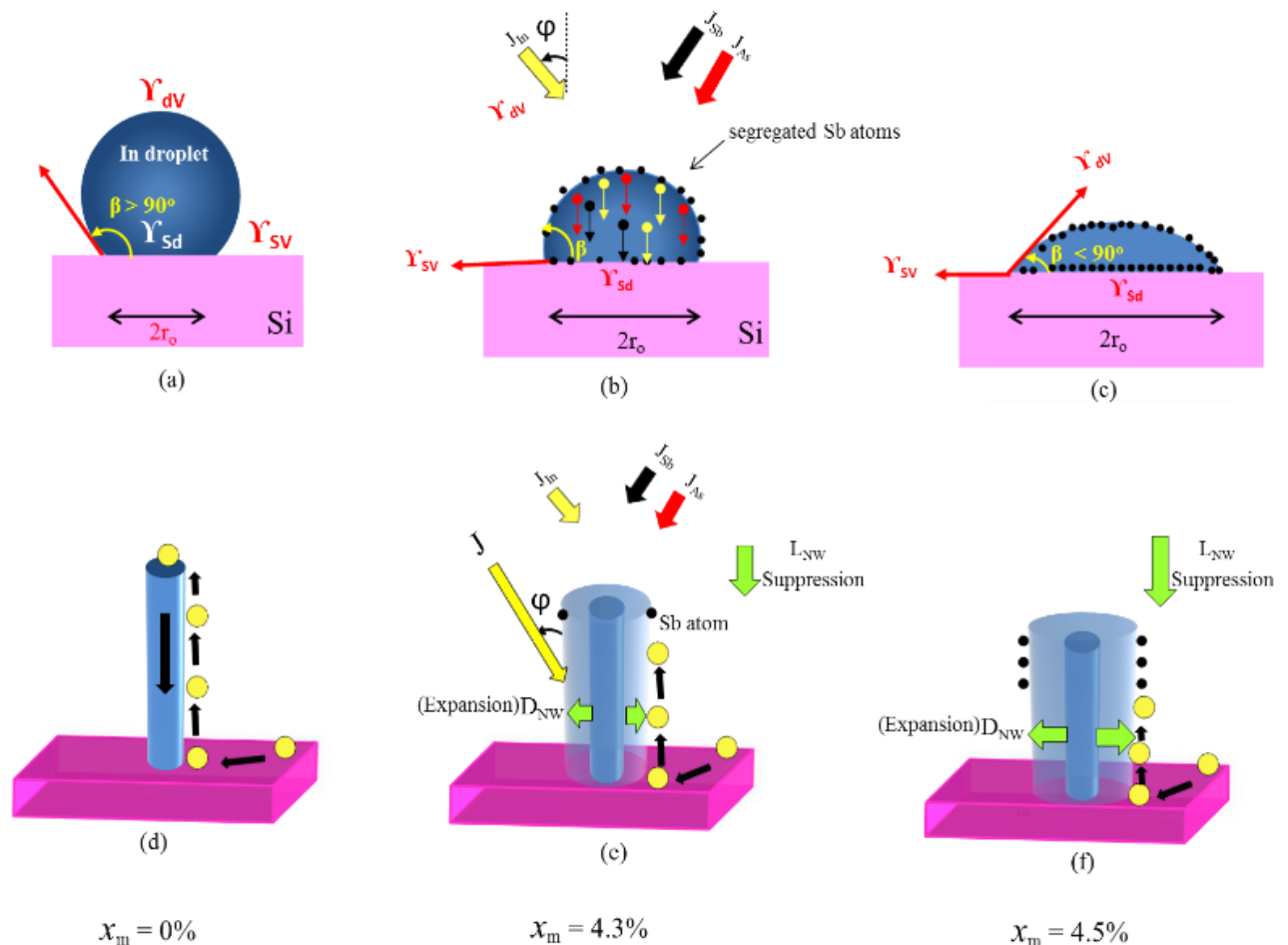
Figure 6.6 Schematic illustration of the effect of Sb surface segregation on the geometry of indium droplet (a-c) and suppression of InAs NWs axial growth (d-f). J_{In}, J_{Sb} and J_{As} denote the In, Sb and As flux respectively. The balance of forces acting on a droplet placed on a substrate are also shown with Υ_{dv}, Υ_{sd}, Υ_{sv} representing the surfaces energies at the droplet – vapour, solid-droplet and solid-vapour interface respectively, β is the contact angle between droplet and substrate. Note that the NWs dimensions are not drawn to scale and do not represent the extent of Sb-induced modification to NW geometry

the growth front and kinetically inhibits In adatom mobility[246]. The introduction and subsequent adsorption of Sb results in surface segregation which potentialcly lowers the surface free energy at the growth interface and Υ_{dv}[143] due to its small surface energy $(0.38j/m^2)$[232]. Such modifications in interfacial surface energy between the droplet and the substrate by the introduction of Sb flux (J_{Sb}) along with changes in composition[247] could lead to significant nucleus and contact angle changes[231] culminating in droplet expansion as depicted in Figure 6.6. It is well known that the shape of the catalyst droplet is determined by the concentration and type of material in the catalyst as well as a balance of the forces of free surface energy and interface forces at the triple phase line[248]. The dependence of the contact angle on the surface energy can be deduced by a rearrangement of equation 6.3 to obtain the classical Young's equation of the form:

$$\beta = cos^{-1} \frac{\gamma_{sv} - \gamma_{sd}}{\gamma_{dv}} \tag{6.4}$$

This implies Sb induced reduction in γ_{sd} and/or γ_{dv} would lead to a decrease in β.

On the other hand the reduced diffusion length of adatoms could be connected to the segregation of Sb at the growth interface which imposes an exchange reaction between adatoms and surfactant, resulting in subsurface incorporation and subsequent integration into the droplets thereby mitigating adatom mobility. In order to migrate, adatoms need to break out from its bonding with neighbouring atoms as well as with surfactant atoms which implies heightened energy barrier for hopping and eventual reduction of the adatom migration length[249, 250]. Hence, it is suggested that the introduction of minute concentration of Sb at NWs growth initiation results in a decrease in both surface energy and In adatom diffusion length [239, 246]. These are in addition to a reduction in contact angle which enables the enlargement of pre-deposited In droplets with a corresponding height reduction as illustrated in Figure 6.6. Using the reference InAs NWs diameter and length hereafter denoted as D_{REF}

and L_{REF} respectively as reference, the expansion in the lateral dimension (D_{EXP}) and corresponding reduction in length (L_{RED}) of the InAsSb NWs are expressed as $D_{EXP} = D_{NW} - D_{REF}$ and $L_{RED} = L_{NW} - L_{REF}$ respectively. The lateral size of NWs are defined by the diameter of pre-deposited In droplets[189] as a result the use of broader droplets translates to the nucleation of NWs exhibiting D_{EXP}. Similar results have been previously reported for InP/InSb heterostructures[247] and InAsSb NWs[143]. Modifications to In droplet geometry has profound effect on the NWs axial growth rate. Nebolsin[142] has shown that surfactant adsorption on the catalyst surface substantially impedes NWs growth.

The following section will be focused on the influence of Sb on InAsSb NWs growth in the second regime. Sb segregation modifies the InAs NWs growth mechanism leading to the observed D_{EXP}. Compared to the long length and growth time ($L_{NW} \leq 3.8\mu m$, $t_{gr} \leq 144$ min, $L_{NW} \leq \lambda_L$) of uniaxially grown Sb-free InAs NWs, the short L_{NW} (~700-870 nm) and limited growth duration ($t_{gr} = 20$ min and 120 min for SG and LG $InAs_{1-x}Sb_x$ NWs samples respectively) excludes the possibility of lateral base broadening for $L_{NW} > \lambda_L$. This suggests that the observed D_{EXP} in the $InAs_{1-x}Sb_x$ NWs is most possibly related to the presence of Sb. A number of factors related to Sb inclusion could be responsible for the observed trend. Firstly, Sb addition reduces the incorporation of growth species into the NWs as a result the axial growth rate is dramatically reduced as has been experimentally demonstrated[251]. Surfactants have been reported to induce a site blocking or "poisoning" effect on the incorporation of growth species [252, 253]. It is believed that Sb segregation at the In droplet surface (Υ_{dv}) blocks the incorporation of species (In and As) at the growth front (Figure 6.6 a-c) suppressing NWs growth which in turn results in a slight decrease in axial growth rate while favouring lateral GR_{NW}. This effect is schematically illustrated in Figure 6.6 (d-f) which is typically observed in the SG samples. However, worthy of note is the fact that whereas Sb inclusion significantly promotes lateral expansion, its influence on axial growth is relatively smaller for the SG

samples compared to that of LG samples, where axial NWs growth is completely suppressed due to high Sb incorporation leading to the growth of 2D film [Figures 6.3 (e-h) and 6.6].

Secondly, the diffusion induced (DI) growth exhibited by the reference samples would imply that the NWs growth proceeds via the diffusion of adatoms from the substrate along the side facets to the droplet. It has been theoretically and experimentally shown that the elongation of NWs during MBE growth is strongly dependent on adatom diffusion from the substrate to the droplet [189, 254]. The adsorption of Sb on the NWs side facets kinetically impose certain limitations on adatoms diffusion from the substrate and side walls towards the growth front, reducing the adatom diffusion flux to the NW top and mitigating axial growth. At higher Sb flux, the effective diffusion length is further suppressed by increased surface segregation due to high Sb coverage leading to more pronounced suppression of axial growth. The DI axial GR_{NW} as a function of its radius ($D_{NW}/2$) is given by[189]:

$$\text{Axial GR}_{NW} = V[\varepsilon - \gamma + \frac{R_c}{\frac{D_{NW}}{2}*\cosh(\lambda)}] \qquad (6.5)$$

where $\varepsilon \equiv (V-V_s)/V$ is the relative difference between the deposition rate V and surface growth rate V_s. R_c is the characteristic scale at which the DI effects become predominant, γ accounts for the desorption from the drop surface while $\lambda \equiv L_{NW}/L_f$ is the ratio of L_{NW} to the adatom diffusion length on the side surface (L_f). A careful inspection of equation 6.5 reveals the axial GR_{NW} scales inversely with $D_{NW}/2$ which is a key independent variable. Hence L_{NW} decreases with an increase in D_{NW}. Consequently a kinetically limited adatom diffusion and suppression of Axial GR_{NW} with L_{RED} would lead to increased lateral GR_{NW} with D_{EXP}. As depicted in Figure 6.6 (d) adatom migration is unhindered in the absence of Sb (InAs reference) whereas the presence of Sb (x_m = 4.3%) is accompanied with Sb segregation which inhibits adatom mobility and incorporation in the droplet leading to a suppression of axial growth along with

diameter expansion (Figure 6.6 e). However, increased Sb content in the range of 4.5-10.2 % is accompanied by heightened Sb accumulation and more pronounced axial growth suppression with lateral GR_{NW} leading to a monotonic L_{RED} and D_{EXP} with an eventual transition to 2D film.

Finally, NWs side wall nucleation could possibly contribute to modifications in NWs morphology. As can be seen in Figure 6.3f, there is slightly conical NW with a broad base which suggest a possible contribution of side wall nucleation to D_{EXP}. Cone shaped NWs with distinct lateral growth at low temperature have been experimentally observed[60, 255]. The observed morphology was attributed to nucleation on the side facets, followed by lateral growth and thickening of the NWs base. Hence, side wall nucleation may possibly play a role in the increase in lateral growth.

6.4   Effect of Sb Incorporation on the Structural Property of Nanowires

In order to investigate the influence of Sb incorporation on the structural property of NWs, the growth temperature was set in the range of 420 - 460°C with an As BEP of about 5.8 x10^{-6} mbar while the Sb BEP was varied in the range of 0.8 - 1.6 x10^{-7} mbar for total growth duration of 20-120 minutes. A reference InAs NWs sample was similarly grown with the Sb shutter closed. All investigated NWs were grown with the assistance of optimal In droplets (~70nm in size) on bare Si (111) substrate as previously described in section 5.1. The incorporated Sb content in the NWs was estimated using a combination of XRD and EDX measurements. FEI XL30 SFEG SEM at the University of Liverpool was utilized for the investigation of the surface morphology of the NWs. To gain insight on the NWs structure, transmission electron microscopy (TEM) analysis was carried out in JEOL 2100 LaB$_6$ and 2100F facilities at the University of Warwick working at 200kV. The specimens were prepared using conventional

method and transferred onto a TEM holey carbon grid. The analysis was carried out with the electron beam perpendicular to the growth direction and parallel to the $<110>_{ZB}/<11\text{-}20>_{WZ}$ direction. Low temperature (10 K) PL measurement was also performed at the Nanyang Technological University, Singapore to investigate the optical properties of the NWs. A diode laser (wavelength of 980 nm) was used for exciting the sample and the emission signal detected by liquid nitrogen cooled InSb photodiode detector with a standard digital lock-in amplifier. EDX estimated Sb content (x_m) of 2%, 4% and 10% was obtained for the InAs$_{1\text{-}x}$Sb$_x$ NWs exhibiting average diameters of about 61nm, 109nm and 155nm as revealed in Figures 6.7 (b-d) respectively.
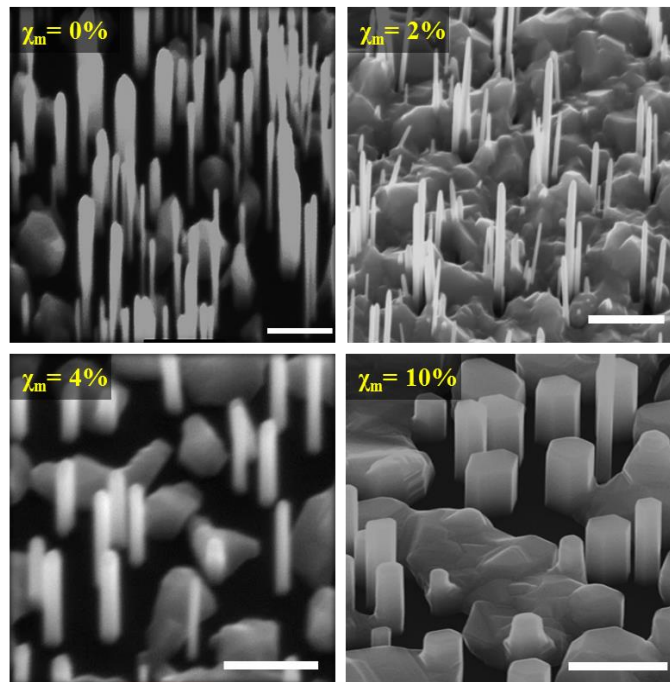
Figure 6.7 Tilted SEM images of vertically-aligned InAs$_{1\text{-}x}$Sb$_x$ NWs with varying Sb molar fraction (x_m) of 0% (a); 2% (b); 4% (c) and 10% (d). The scale bars correspond to 1μm.

High resolution TEM images in Figure 6.8 shows the evolution of NWs structure as a function of x_m from a zinc blende (ZB) dominant structure in the reference InAs NWs to a quasi-pure wurtzite (WZ) phase and then ZB dominant crystal phase with increasing x_m. Specifically, the InAs NWs (Figure 6.8a) show a polytypic ZB dominant (75%) crystal structure along with a

high density of defects (SFs and TPs) which are typical of self-catalyzed (SC) InAs NWs[53, 139, 141].

Bulk III-V materials with the highest ionicity such as the III-Nitrides often adopt the WZ phase whereas the ZB phase is favoured in other III–V materials. However, nearly all III–V NWs materials including InAs, InP, GaAs and GaP with moderate ionicity values generally have a strong tendency for the formation of stacking faults (SFs), twin planes (TPs), and polytypism which are independent of the growth synthesis methods[256, 257]. As a result, InAs NWs often display mixtures of ZB and WZ phases (polytypes) and is more pronounced in SC NWs with the ZB structure being the dominant phase[53, 139, 141]. This behaviour is often relevant to surface-to-volume ratio [186, 258].
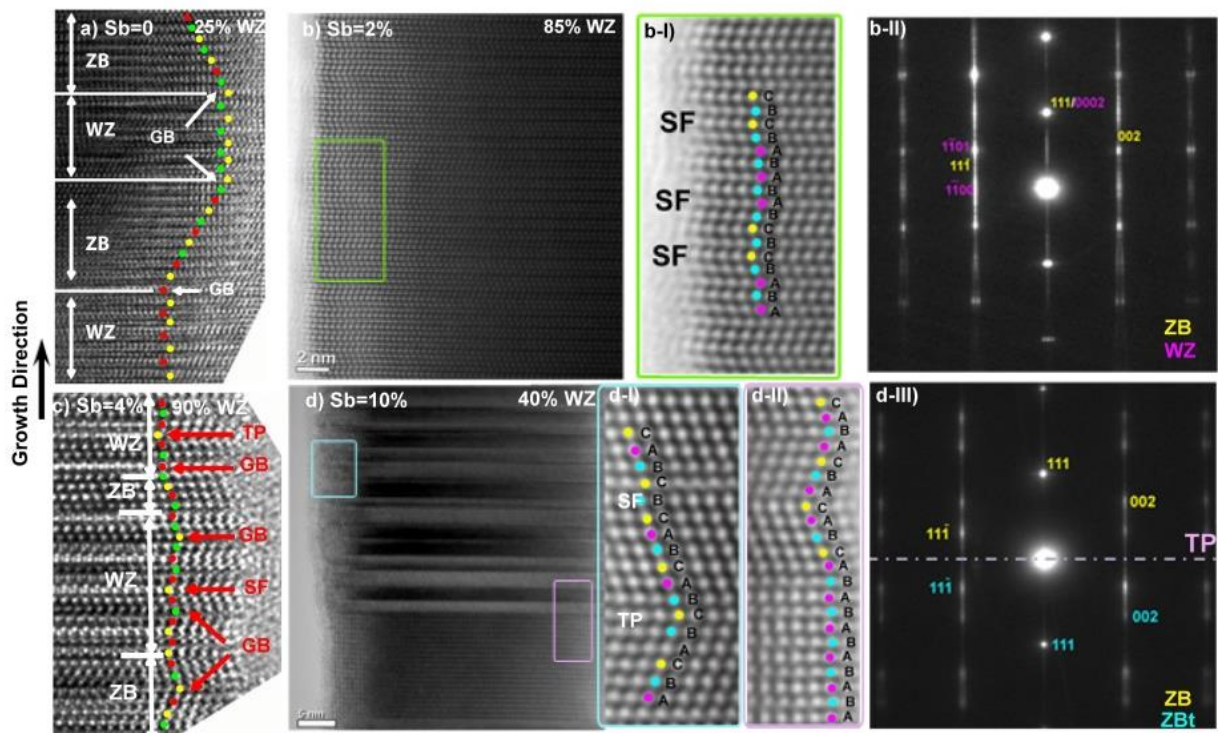
Figure 6.8 High-resolution TEM (HRTEM) images of InAs NWs (a) and $InAs_{1-x}Sb_xNWs$ with Sb content of 2% (b), 4% (c) and 10% (d). The pure InAs NWs have a ZB dominant structure with WZ fraction of 20%, while addition of 2-4% Sb resulted in a WZ dominant phase. A further rise in Sb content to 10% led to a ZB dominant structure. The magnified HRTEM image of the highlighted region is also shown (b-I) along with the selected area electron diffraction (SAED) pattern (b-II) of the $InAs_{0.98}Sb_{0.02}$ NWs. In addition, the magnified HRTEM images (d-I and d-II) of the highlighted region and the SAED pattern (d-III) of the $InAs_{0.90}Sb_{0.10}$NWs are shown. The magnified images show the ZB/WZ stacking in the structure with SF and TP present.

The WZ phase has a lower surface energy in comparison to the corresponding crystalline orientation of the same material in the ZB phase owing to its smaller third-nearest-neighbour atom spacing (resulting from its distinct stacking sequence); as a consequence, the WZ phase is more stable in NWs structures characterized by high surface-to-volume ratio. It has been shown[259] that the occurrence of polytypes (PTs) in ZB III-V NWs is correlated to the small radius of NWs, which generally results in a large relative contribution of lateral surfaces to the total free energy of fully formed NWs.

Turning to the InAsSb samples, the NWs with $x_m = \sim 2\%$ (Figure 6.8b) exhibit a WZ- dominant (87%) crystal structure which has not been previously reported. The magnified HRTEM image of a WZ phase section shown in Figure 6.8(b-I) reveals …ABAB… and ABAB CBCB stacking sequences corresponding to the WZ structure and SFs respectively. The quasi-pure WZ structure of the NWs is corroborated by the selected area electron diffraction (SAED) image depicted in Figure 6.8(b-II). The 111_{ZB} and/or 0002_{WZ} spot indicates the growth direction both in ZB and WZ phases. It is clear that the WZ reflections are more intense than the ZB ones confirming the dominant WZ structure. The streaks passing through the spots along the growth direction indicate the presence of stacking faults in the structure, lying on the $(111)_{ZB}/(0002)_{WZ}$ planes. For an increase in Sb content to 4% (Figure 6.8c) the WZ segments in the NWs increased to 90%. A further increase in x_m to 10% (Figure 6.8d) led to the observation of a ZB dominant structure with less WZ portion (40%) indicative of a WZ→ZB phase transition. Figure 6.8 (d-I) corresponds to a magnified image of the highlighted section of the HRTEM micrograph demonstrating the dominant ZB (….ABCABC….) stacking sequence with TPs (..CBA C ABC..) and SF (…ACBCBAC…).

106
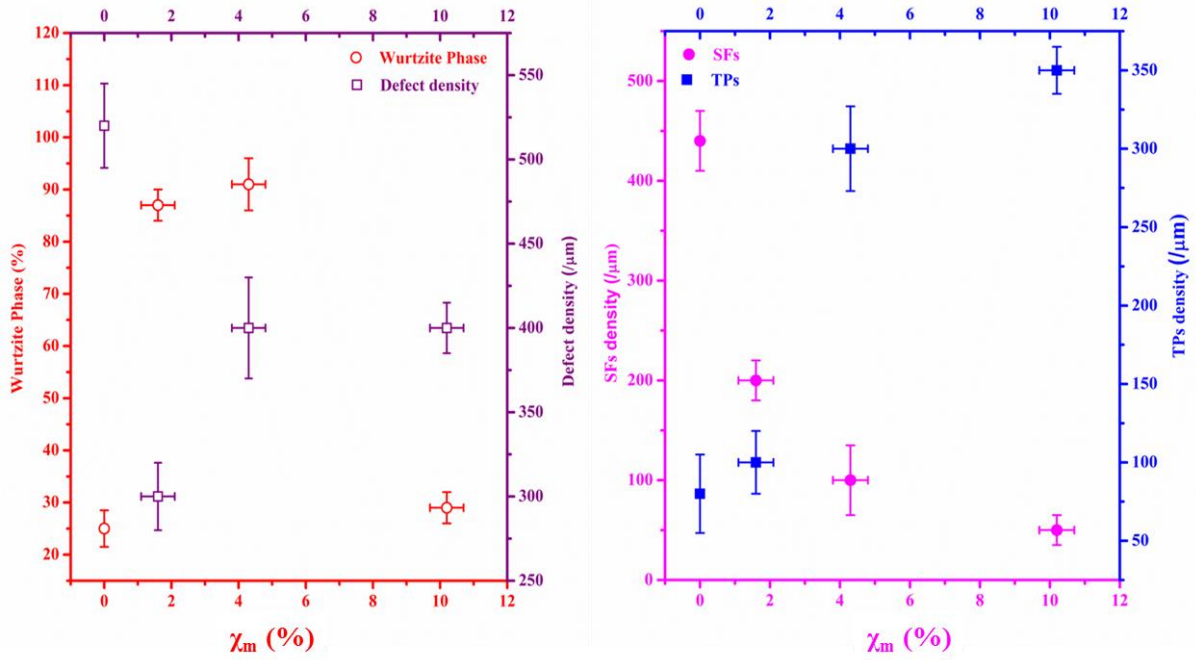
Figure 6.9 Plot of Wurtzite phase (in %) and total defect density (a), stacking faults (SFs) and twin plane (TPs) density in the $InAs_{1-x}Sb_x$ nanowires as a function of antimony composition.

Areas corresponding to the WZ structure were also observed in this sample (Figure 6.8 d-II). The observation of a ZB dominant structure was also corroborated by SAED (figure 6.8 d-III). The spots in the diffraction pattern indicate the ZB structure is predominant in addition to twinning. As before, the streaking indicates the presence of SFs however, it is less pronounced than the InAsSb NWs with 2% Sb [Figure 6.8 (b-II)] indicating a lower SFs density in this sample. To further clarify the effect of Sb incorporation on the crystal structure evolution, the dependence of the percentage WZ crystal inclusion is plotted as a function of χ_m (Figure 6.9a). It can be seen that the WZ sections increases with Sb content up to 4%, after which a further increase leads to a ZB phase dominant structure ($\chi_m = 10\%$) while the defect (combination of SFs and TPs) density is slightly reduced with Sb addition. Specifically, the SFs density monotonically decreases with increasing Sb content (Figure 6.9b) while at the same time the TPs density sharply increases. This demonstrates Sb potentially induces a ZB→WZ→ZB crystal phase transition in InAsSb NWs and significantly promotes a reduction in SFs density[260].

In section 6.3, the InAsSb NWs were shown to exhibit diameter expansion with Sb incorporation which is consistent with previous reports [60, 143]. Based on the Sb-induced morphological evolution, it is reasonable to conclude that the increase in NWs diameter with increased Sb content can be correlated to a decrease in contact angle[231, 240]. Therefore, the following section details the possible reasons for the observed increase in WZ phase in the NWs using the modified nucleation model proposed by Wallentin et al [261]. Considering the critical interfacial energies of γ_{dS} and γ_{dV} which determine the dominant crystal phase of NWs [262, 263] (excluding the phase independent γ_{SV}), one can conclude from equation 6.4 that cos $\beta \propto (-\gamma_{dS}/\gamma_{dV})$. This indicates an increase in NWs diameter with a corresponding decrease in contact angle would result in a decrease in the γ_{dS}/γ_{dV} ratio. The ratio (η) between the effective surface energies of the WZ (Γ^{WZ}) and ZB (Γ^{ZB}) phase is given by [254, 261]:

$$\eta = \frac{\Gamma^{WZ}}{\Gamma^{ZB}} = \frac{(1-x)\,\gamma_{dS}^1 - x\gamma_{dV}\,\sin\beta + \tau x\gamma_{wz}}{(1-x)\,\gamma_{dS}^1 - x\gamma_{dV}\,\sin\beta + x\gamma_{ZB}} \qquad (6.6)$$

Here, x is the fraction of the nucleus perimeter that is in contact with the vapour phase and $\tau = \gamma_{WZ}/\gamma_{ZB}$ is the ratio of the lateral solid-vapour surface energies of WZ and ZB NWs in contact with the vapour. The condition for the formation of NWs in the WZ phase is $\tau < 1$ due to the presence of less dangling bonds on the WZ surface [254, 261, 264]. The ratio (ξ) between the WZ (ΔG_{WZ}) and ZB (ΔG_{ZB}) nucleation barriers is expressed as [261, 263]:

$$\xi = \frac{\Delta G_{WZ}}{\Delta G_{ZB}} = \frac{\Delta\mu_{dS}\eta^2}{\Delta\mu_{dS} - \Psi_{WZ}} \qquad (6.7)$$

Where $\Delta\mu_{dS}$ is the supersaturation at the droplet-solid interface and Ψ_{WZ} is the additional cohesive energy required for the formation of a WZ layer at the triple phase line (TPL), representing the comparatively low cohesive energy of the ZB phase. As can be seen from equation 6.7, the deposited NWs would adopt the WZ structure when $\xi < 1$, which would imply $\eta \ll 1$. As a consequence, a significant lowering of γ_{dS} or an increase in γ_{dV} will promote a

decrease in both η and ξ, favouring the WZ phase nucleation probability. Thus, the WZ phase is preferentially formed at the TPL when its nucleation barrier is lower than that of its ZB counterpart although the latter is more stable in bulk form[190, 264]. This implies that an increased Sb incorporation in the NWs could possibly result in modifications to the surface energetics at the γ_{dS} and/or γ_{dv} interface leading to a ZB→WZ phase transition as observed in previous reports [265, 266]. Surfactants have been recognized as crucial elements for engineering NWs crystal and defect structure[262]. However, the decline in the WZ fractions at high Sb content (x_{sb} = 10%) is likely associated with modifications in the balance of forces and/or changes to the V/III flux ratio with increased Sb segregation and surfactant effect [143, 267]. This suggests that the Sb-induced tuning of crystal phase is composition dependent. Since the required condition for WZ phase formation involves altering the balance of surface energies, an appropriate choice and composition of surfactants would enable the control of the preferred crystal phases in NWs.

To further verify the observed structural evolution of InAsSb NWs as a function of Sb content, the optical properties of the InAsSb NW ensembles were investigated by low temperature (10 K) photoluminescence (PL) measurements. Typical PL spectrum of the reference InAs NWs and the $InAs_{0.957}Sb_{0.043}$ NWs are depicted in Figures 6.10a and 6.10b respectively. It shows that the InAs NWs displays peak emissions at ~0.389 and 0.415 eV. The lowest emission is attributed to the impurity or defect-related transition[63, 200-202] while the dominant emission centred at 0.415 eV is associated with the presence of the WZ/ZB mixture[214]. The WZ/ZB mixture of InAs crystals forms a type II related quantum wells (QW), where electrons are confined in the QWs of the ZB segments and holes localized in the WZ regions[215, 268] as schematically illustrated in Figure 6.11.
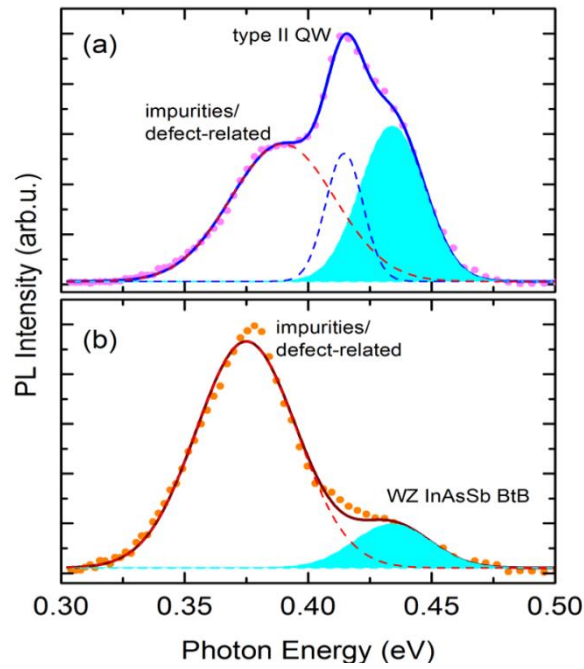
Figure 6.10 PL spectra of (a) InAs and (b) InAs$_{0.96}$Sb$_{0.04}$ NWs at 10 K.
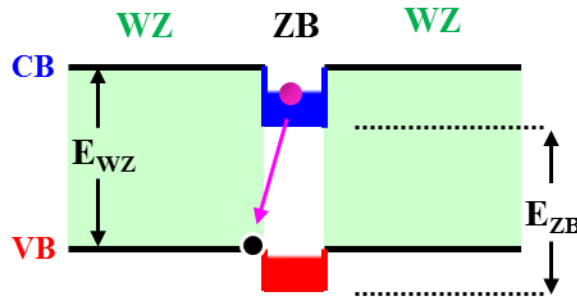
Figure 6.11 Schematic diagram of band alignment and recombination processes for carriers transiting between conduction band (CB) and valence band (VB) in InAs NW containing ZB and WZ phase mixtures.

Optically excited electrons undergo a transition from the ground state ZB conduction band to the top of the WZ valence band followed by radiative recombination[214] in the so-called "type II QW related emission". Similarly, for the InAs$_{0.96}$Sb$_{0.04}$ NWs sample, the PL spectrum shows two emission peaks, the first is positioned at 0.375 eV and the other at 0.437 eV, which are attributed to impurity or defects-related transition and BtB transition in WZ InAsSb respectively. Worthy of note is the conspicuous absence of the type II related QW emission

indicating the absence of crystal phase mixtures (quasi-pure WZ structure) in the NWs. This is consistent with the HRTEM studies. This provides further evidence of the phase transition from the highly polytypic ZB dominant InAs crystal to a quasi-pure WZ phase in the $InAs_{0.96}Sb_{0.04}$ NWs. The observation of the BtB emission from the WZ $InAs_{0.96}Sb_{0.04}$ NWs at a slightly higher energy (~0.437 eV) than the ZB InAs NWs BtB emission (0.415 eV) [208] is contradictory to the predicted lower bandgap energy resulting from Sb incorporation. This can be explained by the difference in bandgap energy between the WZ and ZB phases. Previous reports indicates that the WZ phase InAs NWs has a larger bandgap energy in comparison to that of ZB InAs[212-214] by a predicted value of 40–66 meV[212, 215, 216]. This has been experimentally verified (~ 0.46 eV)[214]. Assuming the bandgap energy difference between the WZ and ZB phases is same for InAsSb alloys at low Sb composition, the bandgap energy of WZ InAsSb NWs can be estimated from that of ZB InAsSb. At ~4% Sb content, the ZB InAsSb alloy gives a bandgap energy of 0.375 eV if a bowing effect of 0.67 eV is taken (shrinkage of 0.035 eV)[64]. This gives an estimated bandgap of WZ $InAs_{0.957}Sb_{0.043}$ NWs of around 0.415-0.441 eV, which is in good agreement with the obtained value. It is obvious that the impurities and defects related emission is quite strong in both samples. This could be associated with the presence of high density of crystal twinning defects which corroborates the earlier HRTEM and SEAD results.

Chapter 7

InAs(Sb) Nanowires Growth on Graphitic Substrates

This chapter will provide insight into the van der Waals epitaxy growth of InAsSb nanowire (NWs) alloys on highly oriented Pyrolytic graphite (HOPG) via the In droplet-assisted growth technique. The chapter starts with the growth of InAs NWs including the effect of growth parameters on NWs growth, followed by the growth of InAsSb NWs. Finally, a comparison between the droplet epitaxy growth of InAs NWs on Si (111) and graphitic thin films will be elucidated.

7.1 Growth of InAs Nanowires on Graphite

7.1.1 Growth and Characterization of InAs Nanowires on Graphite

InAs NWs were grown on graphite using In droplet (as described in section 5.1) for preferential NWs nucleation. The graphitic films were mechanically exfoliated from HOPG, transferred onto Silicon substrates then loaded into the MBE system and thermally outgassed at a temperature of $550 – 700^0$C for at least one hour prior to growth initiation. The substrate temperature was then ramped down to 440-500ºC for NWs growth followed by the spontaneous opening of In and As shutters for NWs growth initiation. A series of samples were then grown using As-rich conditions (As/In flux ratio > 45) for total growth duration of 10-144 min. The morphology of the resulting NWs was examined by SEM while XRD and HRTEM investigations were performed to investigate the crystalline quality of the NWs.

Figure 7.1 shows the 45º tilted SEM images of InAs NWs on graphite. All the NWs are vertically-aligned without tapering. It can be seen from the SEM images that the NWs exhibit

a homogeneous diameter distribution with a hexagonal cross-section and no metal droplets present at the wire top. A typical XRD pattern of InAs nanowires deposited on graphitic thin films is depicted in Figure 7.2. The identified 2θ diffraction angle of 25.45° is indexed to ZB InAs (111). This coincides with that of bulk ZB InAs which suggests a ZB dominant crystal structure in the NWs with no remaining strain. The peaks at 26.5° and 54.6° correspond to the graphite (002) and (004) diffractions respectively. The WZ InAs (111) peak usually observed at 2θ values of 25.3° could not be resolved in the scan. The InAs (111) peaks exhibit a narrow full width at half maximum (FWHM) of ~0.14° indicating the low-crystal tilt, superior
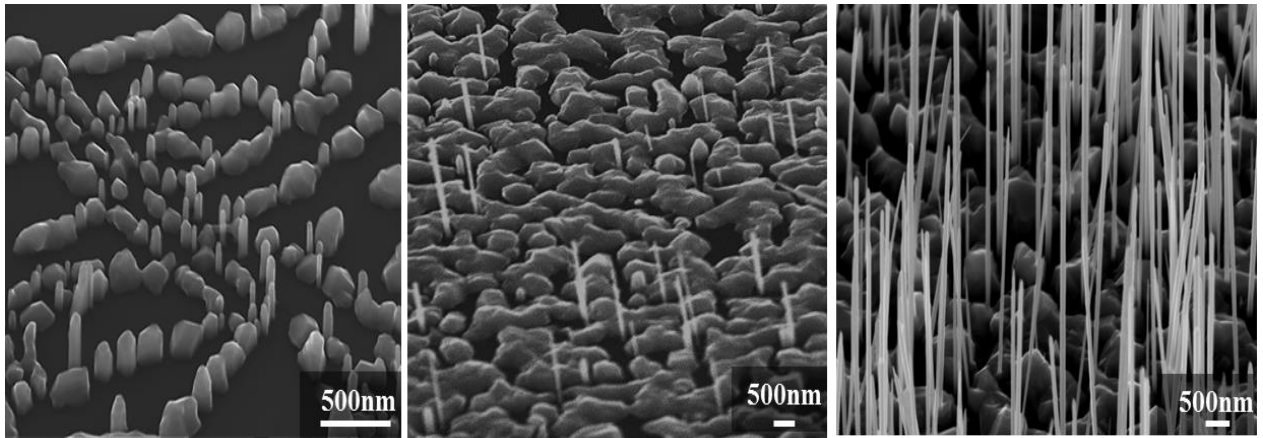
Figure 7.1 45° tilted SEM images of InAs nanowires grown on graphite for (a) 10, (b) 60 and(c) 144 min.
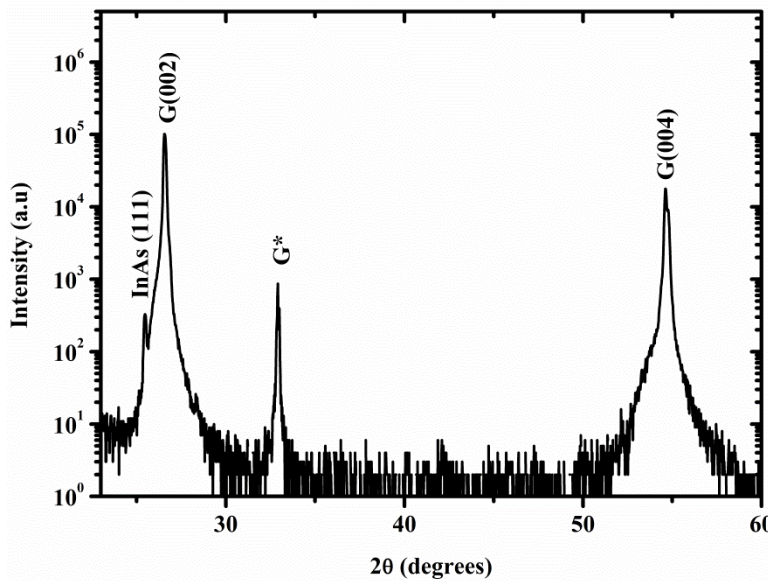
Figure 7.2 X-ray diffraction pattern of InAs nanowires deposited on graphitic thin films

crystalline quality and vertically-aligned directionality (InAs[111]‖Graphite[0001]) of the InAs NWs[138]. To gain further insight into the crystal structure of the InAs NWs, high resolution TEM experiments were performed. The typical TEM image shown in Figure 7.3a reveals the presence of SFs on the (111) plane. This was further confirmed by HRTEM (Figure 7.3b) which also suggests the NWs exhibits a mixture of ZB/WZ crystal phases. The polytypic structure of the NWs is corroborated by the selected area electron diffraction (SAED) image shown in Figure 7.3c evidenced by the presence of streaks passing through the spots along the growth direction.
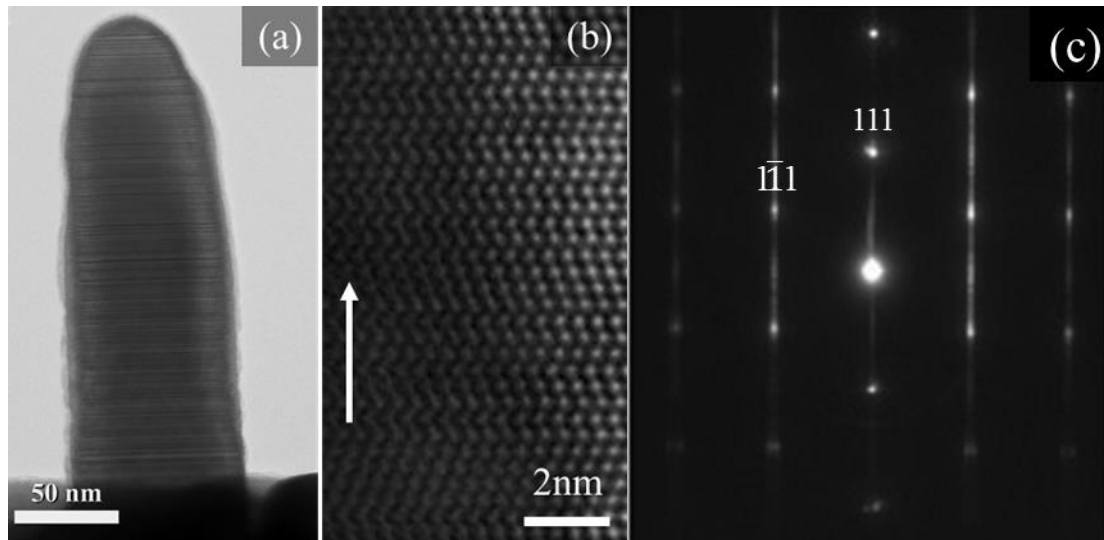
Figure 7.3 Typical TEM image (a); HR-TEM micrograph (b) and selective area electron diffraction pattern (c) of zinc-blende InAs nanowires grown on graphitic thin films.

7.2 Effect of Growth Parameters on InAs Nanowires Growth

7.2.1 Time Evolution of Nanowire Growth

To investigate the influence of growth duration on the morphological evolution of InAs NWs on graphite as well as determine the growth time necessary for realizing high aspect ratio NWs, the geometry of as-grown InAs NWs deposited for various growth durations (details of growth

conditions are described in subsection 7.1.1) were evaluated. The strong dependence of NWs morphology on growth duration is revealed by the changes to length and diameter with increasing growth time as shown in Figure 7.4. Axial growth rate shows two different dependences on growth time i.e. in the beginning it increases quickly but after 20 min, the rate of increase lessens[269]. NWs growth is enabled by the impingement and diffusion of adatoms from three possible pathways: direct impingement on the solid-droplet interface, adsorption on the NWs sidewalls and impingement on the substrate. Direct impingement on the growth interface contribute to axial NW growth whereas adatoms adsorbed on the NW sidewall can either contribute to axial growth, lateral growth or simply desorb. Finally, adatoms adsorbed on the substrate will either migrate toward the NWs and diffuse along the NW sidewalls to contribute to axial growth, contribute to 2D film growth or desorb[188]. However, owing to the diffusion-induced growth observed in the NWs, the diffusion of adatoms from the substrate to the wire top is the crucial determinant of axial NWs growth. Axial growth is promoted by the unperturbed migration of adatoms from the substrate surface to the wire top leading to the fast increasing growth rate observed in the beginning. Conversely, for the longer growth time, more and larger parasitic islands are deposited on the surface which reduces the collection area and results in a significant decline in the adatom contribution from the substrate surface. It has been demonstrated that InAs NWs growth on graphite which is strongly dependent on adatom diffusion exhibits two dependences as a function of growth time; the NWs initially grows rapidly in an axial direction within the first few minutes (20min) after which axial NWs growth slows down. Ultra-long (> 6µm) InAs NWs with enormous potential for applications in high performance transistors were realized for the longest growth time > 120 min).
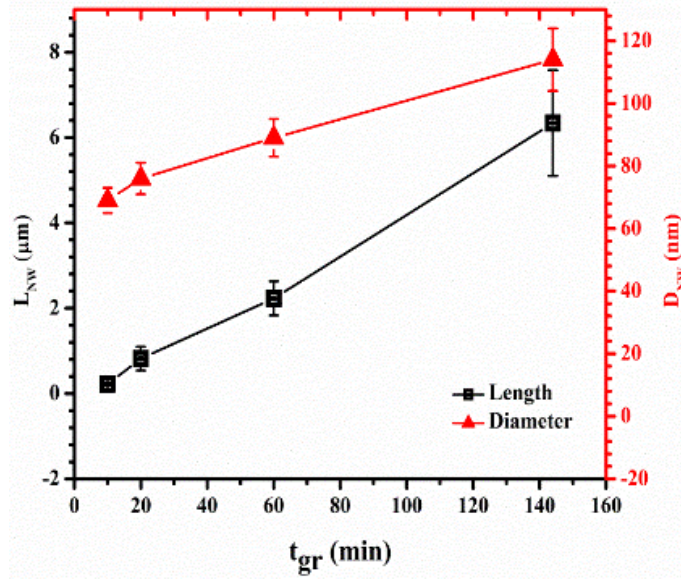
Figure 7.4 Dependence of nanowire length (L_{NW}) and diameter (D_{NW}) on growth time (t_{gr}).

7.2.2 Effect of Temperature on Nanowire Growth

To identify the optimal temperature for obtaining a high yield of InAs NWs on graphite, a series of InAs NWs samples were grown under As-rich conditions following previously established procedures (subsection 7.1.1) at various growth temperatures (400 - 475^{0}C) with fixed In [(1.75 - 2.25) x 10^{-7} mbar] and As (8.0x10^{-6} – 2x10^{-5} mbar) flux for about 1 hour. The SEM micrographs in Figure 7.5 show the distribution and morphology of the NWs as a function of growth temperatures (G_T). All the NWs exhibit homogenous diameter across the entire length without any measurable tapering. As can be seen in Figure 7.6, a dominant cluster (surface Islands) growth was observed at a lower temperature of 400°C. A slight increase in G_T to 420°C yielded a sparse NWs distribution ($\sim$5.28 $\times$10^8 cm^{-2}) while a further increase in temperature to 435°C led to a high density ($\sim$8.09 $\times$10^8 cm^{-2}) of NWs. Conversely, a further rise in G_T (450°C-475°C) led to a monotonic decrease in NWs density.
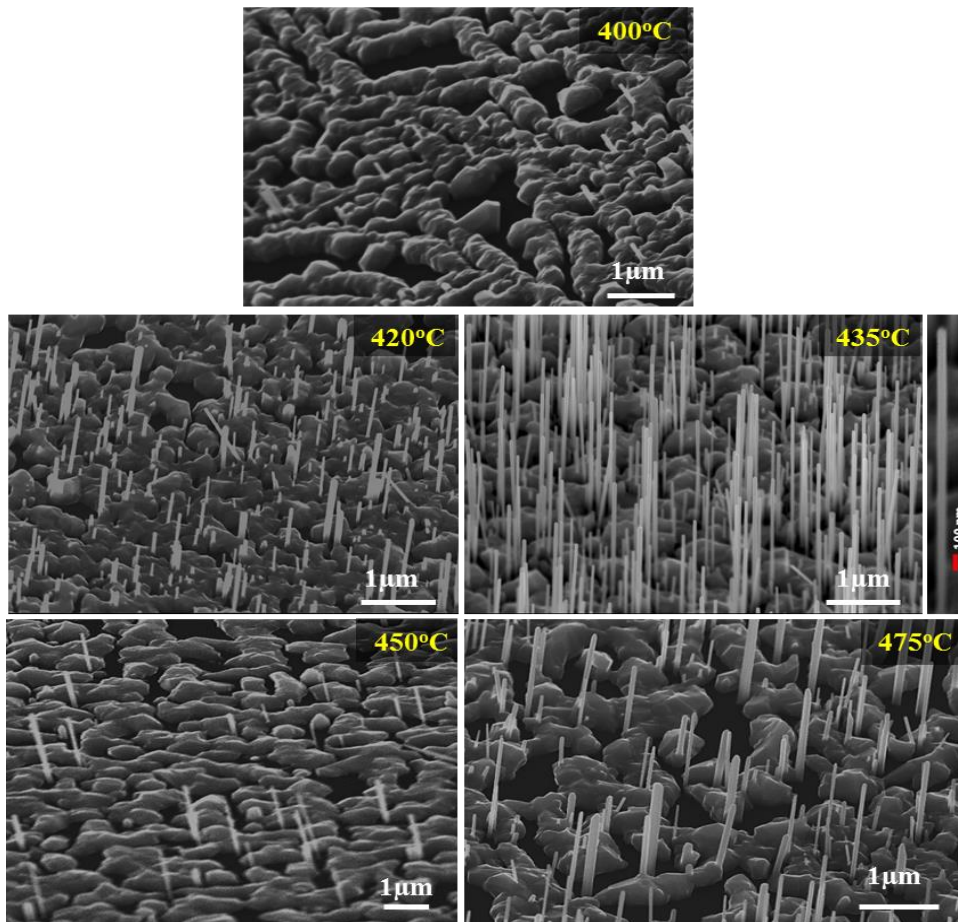
Figure 7.5 45° tilted SEM images of InAs NWs grown on graphitic substrates with a fixed In -flux of 1.75 x 10^{-7} mbar and different temperatures.
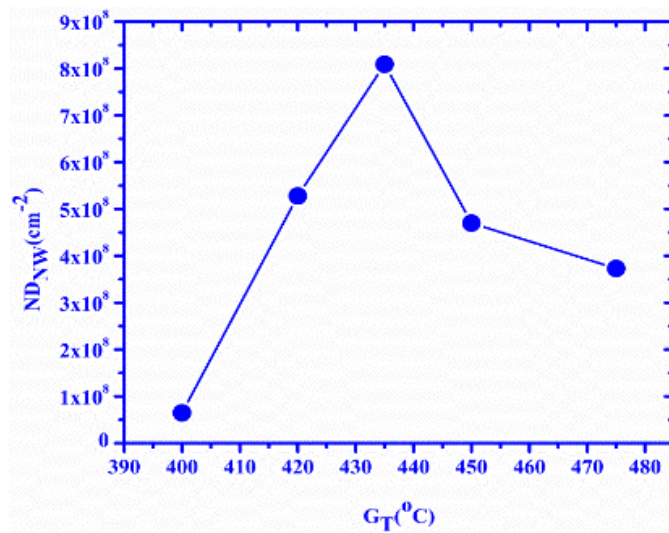
Figure 7.6 Plot of nanowire areal density (ND_{NW}) as a function of growth temperature (GT).

The dependence of NWs density on G_T can be explained by the kinetic modification to adatom mobility as a function of temperature. At a low growth temperature (400°C), the kinetically inhibited adatom mobility promotes the development of surface clusters at the expense of NWs. A rise in G_T increases the adatoms diffusion length leading to the realization of peak NWs density (8.09×10^8 cm^{-2}) at 435°C. However, for a further increase in temperature (435°C $\leq G_T$ ≤ 475°C) the adatom diffusion length is further increased and the surface coverage of adatoms longer but fewer resulting in the nucleation of less dense NWs[88]. Figure 7.7 shows a strong dependence of NWs length (L_{NW}) on G_T. as summarised in Table 7.1. It clearly indicates a temperature dependent increase in L_{NW} for G_T in the range of 400-435°C which is in contrast to the drop in L_{NW} at high temperatures (435°C $< G_T \leq 475$°C). Maximum L_{NW} was observed at a G_T of 435°C consistent with previous report[90]. Conversely, the rise in G_T to 435°C is accompanied by a decrease in NWs diameter (D_{NW}) with the reversed effect on D_{NW} for a further increase in G_T to 475 °C. At an optimal temperature of 435°C the longest (2.58$\pm$ 0.34μm) and narrowest (~31.21$\pm$ 6.59nm) NWs with high aspect ratio (>82) was realized.
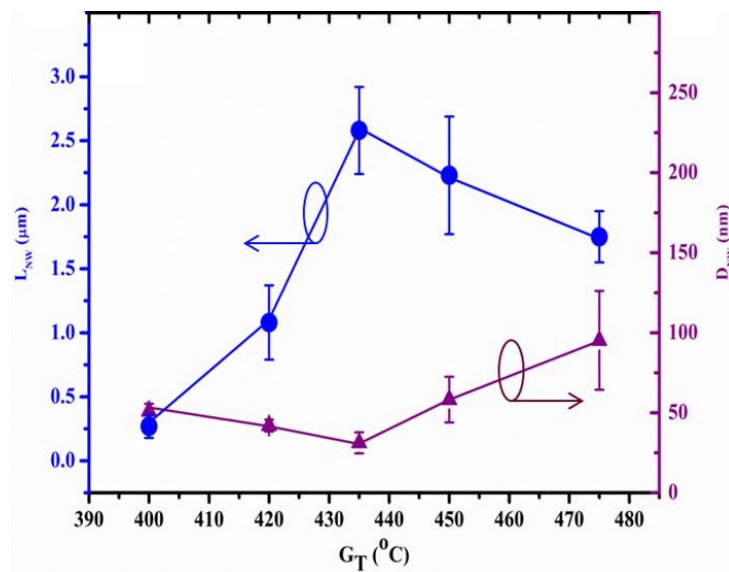
Figure 7.7 Plot of length (L_{NW}) and diameter (D_{NW}) of InAs nanowires on graphite as a function of growth temperature (G_T).

118

Table 7.1 Geometries of InAs Nanowires on Graphite as a function of growth temperature

Growth Temperature (^{0}C)	Average Length (µm)	Average Diameter (nm)	Number Density (cm^{-2})
400	0.27 ± 0.09	51.03 ± 4.65	6.47 ×10^7
420	1.08 ± 0.29	42.10 ± 3.73	5.28 ×10^8
435	2.58 ± 0.34	31.21 ± 6.59	8.09 ×10^8
450	2.23 ± 0.40	54.02 ± 21.36	4.70 ×10^8
475	1.75 ± 0.20	86.83 ± 30.50	3.73 ×10^8

This also corresponds to the temperature at which a dense array of NWs was formed. Notably, despite the high aspect ratio, the NWs are vertically-aligned with no randomly oriented NWs. This provides an insight into the optimal temperature for the fabrication of InAs/graphite NWs with geometries within the technologically important range for fundamental studies such as size-dependent quantum confinement effect. The observed phenomenon is understandable considering the diffusion-limited growth of NWs by MBE. It has been theoretically and experimentally shown that the elongation of NWs during MBE growth is strongly dependent on adatom diffusion from the substrate to the droplet [189, 254]. As a result, at low G_T (400°C) adatom diffusion is kinetically limited which impedes the diffusivity of adatoms and suppresses axial NWs growth while favouring cluster growth. A slight increase in G_T to 420°C increases the diffusion length of adatoms resulting in the initiation of NWs growth which explains the observed growth of short and thick NWs. A further rise in G_T to 430°C induces faster diffusion of adatoms which in turn leads to increased diffusion flux to the NW top at a low desorption rate from the sidewalls. This results in a surge in L_{NW} and a shrinkage in D_{NW} as reported previously [191, 192, 270]. However, for the upper temperature limit ($G_T > 435^o$C), the adatom incorporation probability and diffusion flux towards the growth front is significantly reduced. This is attributed to the increased adatom desorption from the NWs sidewalls[191] and the

unfavourable chemical potential gradient[132]. This study has demonstrated that the growth of InAs NWs on graphite via the droplet epitaxy technique is strongly dependent on growth temperature; a high yield of vertically-aligned NWs was realized within a narrow temperature regime of 420-475°C while long (> 2.5μm) and high aspect ratio NWs were obtained at temperatures of ~435°C.

7.2.3   Effect of III/V Ratio on Nanowire Growth

In order to investigate the dependence of InAs NWs growth on graphite a series of samples were deposited. The In-flux was fixed at ~1.75 x 10^{-7} mbar while the V/III flux ratio (As_{Fx}/In_{Fx}) was varied from 27 to 55 by changing the As-flux from 4.8 - 9.6 x 10^{-6} mbar at a constant temperature of 440 - 500 °C for a growth duration of 20 minutes. Figure 7.8 depicts the influence of V/III flux ratio on the growth of InAs NWs on graphite at a constant In-flux and temperature. It reveals a strong dependence of NWs nucleation on the As_{Fx}/In_{Fx} flux ratio. No NWs growth was realized at a relatively low As flux, an increase in the As_{Fx}/In_{Fx} flux ratio to 27 enabled the growth of NWs. The NWs nucleation probability was further enhanced by utilizing a significantly high As flux (As_{Fx}/In_{Fx} = 55). This demonstrates that high As flux is required for suppressing cluster growth for the realization of vertically-aligned NWs structures and for increasing the nucleation of InAs NWs. Worthy of mention is the presence of InAs Islands grown alongside the NWs in all the samples. An evaluation of the NWs geometry indicates axial NWs growth is favourable at high As_{Fx}/In_{Fx} ratio of 51 evidenced by the increase in L_{NW} with increasing As flux (Figure 7.9), although there was no significant change in L_{NW} for a further rise in As_{Fx}/In_{Fx} ratio to 55. Interestingly, As-rich conditions (As_{Fx}/In_{Fx} = 55) enhanced the growth of thin NWs. This shows that As-rich conditions (As/In > 50) are necessary for the suppression of Island growth in favour of InAs NWs nucleation and growth
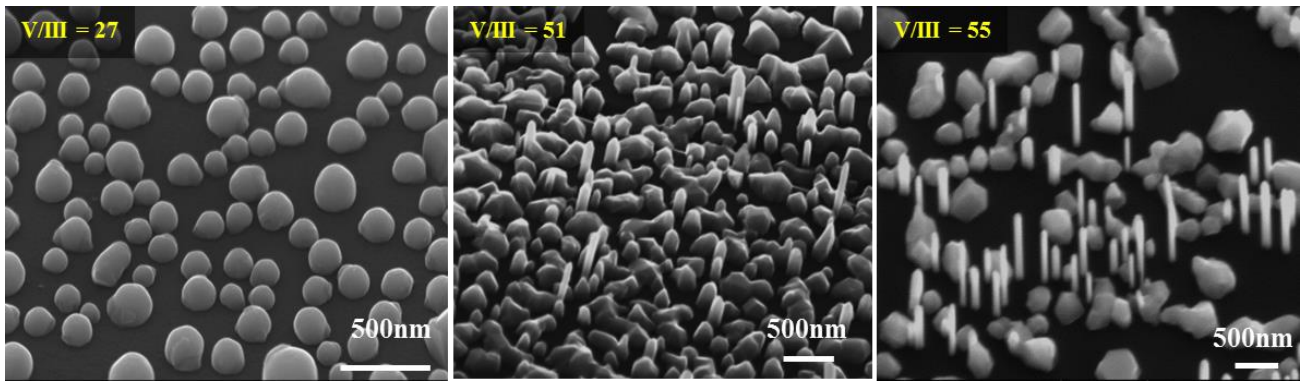
Figure 7.8 45° tilted SEM images of InAs nanowires deposited on graphite with a constant In-flux and varied As flux
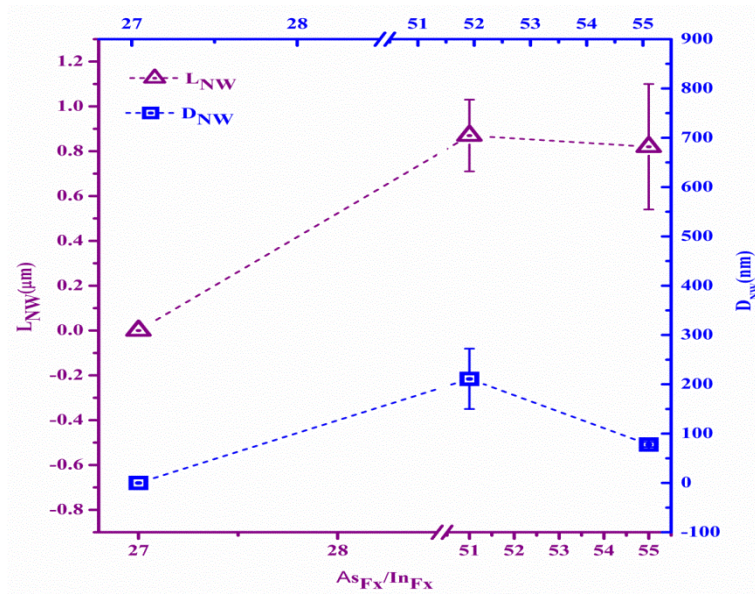
Figure 7.9 Plot of nanowire length (L_{NW}) and diameter (D_{NW}) as a function of As/In flux ratio (As_{FX}/In_{Fx})

on graphite via the droplet epitaxy technique in addition, axial NWs growth is highly dependent on As-flux.

7.2.4 Effect of Growth Rate on Nanowire Growth

To investigate the influence of growth rate on InAs NWs, a series of samples were deposited at a fixed As-flux (8.0×10^{-6} – 2×10^{-5} mbar) and constant growth temperature of 440 - 500 °C for the 60min growth duration, while the growth rate was adjusted between 0.1- 0.3μm/hr. The

SEM images and the plot of areal density as a function of growth rate are depicted in Figures 7.10 and 7.11 respectively. It reveals InAs NWs/graphite nucleation probability is strongly dependent on the growth rate. The use of high growth rate yielded a dense array of vertically-aligned NWs which implies the graphitic substrate enables growth at high growth rate which is favourable for the fabrication of cost-effective devices. The increase in NWs density with increasing growth rate is associated with the dependence of NWs nucleation on the effective In-flux. Intriguingly, the average L_{NW} slightly decreased with increasing growth rate while D_{NW} remained almost constant (Figure 7.12). The slight decline in axial growth rate (Figure 6.12) is understandable given the sharp rise in NWs density at constant supply of precursor flux. This implies a reduction in the available growth species due to the huge material consumption for
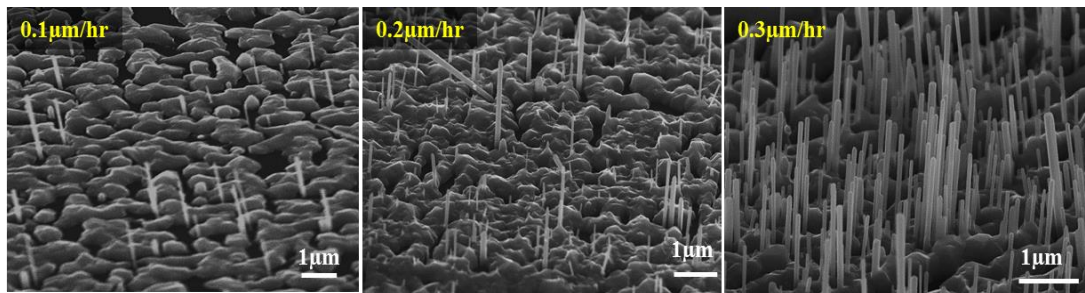
Figure 7.10 45° tilted SEM micrographs of InAs NWs/graphite grown with a constant growth temperature and In-flux but at
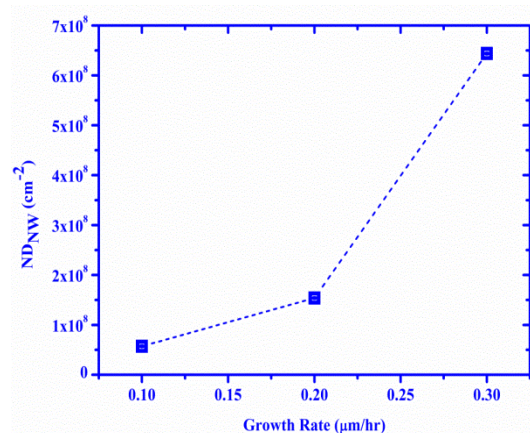
Figure 7.11 Plot of nanowire areal density (ND_{NW}) as a function of growth rate.

NWs nucleation. In addition, it can be seen that an increase in growth rate leads to increased surface coverage and heightened cluster (InAs islands) deposition. This in turn results in the suppression of adatom surface diffusion and reduced diffusion flux from the substrate towards the growth interface leading to a reduction in L_{NW}. This research has demonstrated that the droplet epitaxy growth of InAs NWs on graphite is strongly dependent on the growth rate. A high yield of NWs is promoted by a high growth rate of 0.3µm/hr.
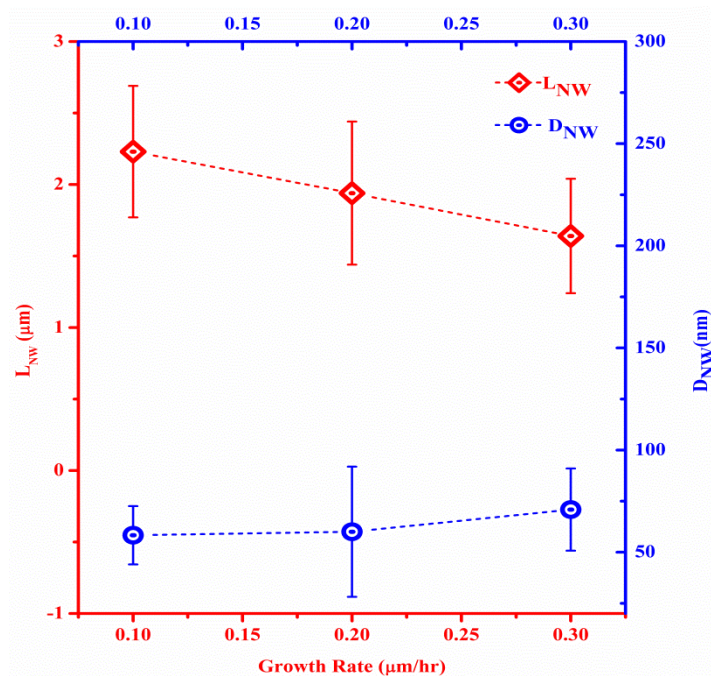
Figure 7.12 Dependence of the length (L_{NW}) and diameter (D_{NW}) of InAs nanowires deposited on graphite on growth rate.

7.2.5   Comparison between InAs Nanowires growth on Si (111) and Graphite

To elucidate the influence of the substrate on the droplet epitaxy growth of InAs NWs, the distribution and geometry of as-grown NWs deposited on Si (111) and graphitic thin film with similar growth conditions were compared as function of various growth parameters.

The Influence of various growth parameters on the lengths (L_{NW}) [top panel] and diameters (D_{NW}) [bottom panel] of InAs nanowires deposited on Silicon and graphitic substrates is depicted in Figure 7.13. It reveals the morphology of the InAs NWs reveal axial growth is more strongly influenced by increasing growth time for the NWs deposited on graphite in comparison to the NWs on Si (Figure 7.13a). NWs as long as ~ 6μm were realized on graphite whereas the InAs NWs/Si was only ~4μm long for the maximum growth duration (144 min). This suggests a longer adatom diffusion length (λ_{diff}) on graphite in comparison to Si. This behaviour has huge implication for the quick and time-saving growth of NWs on graphite with
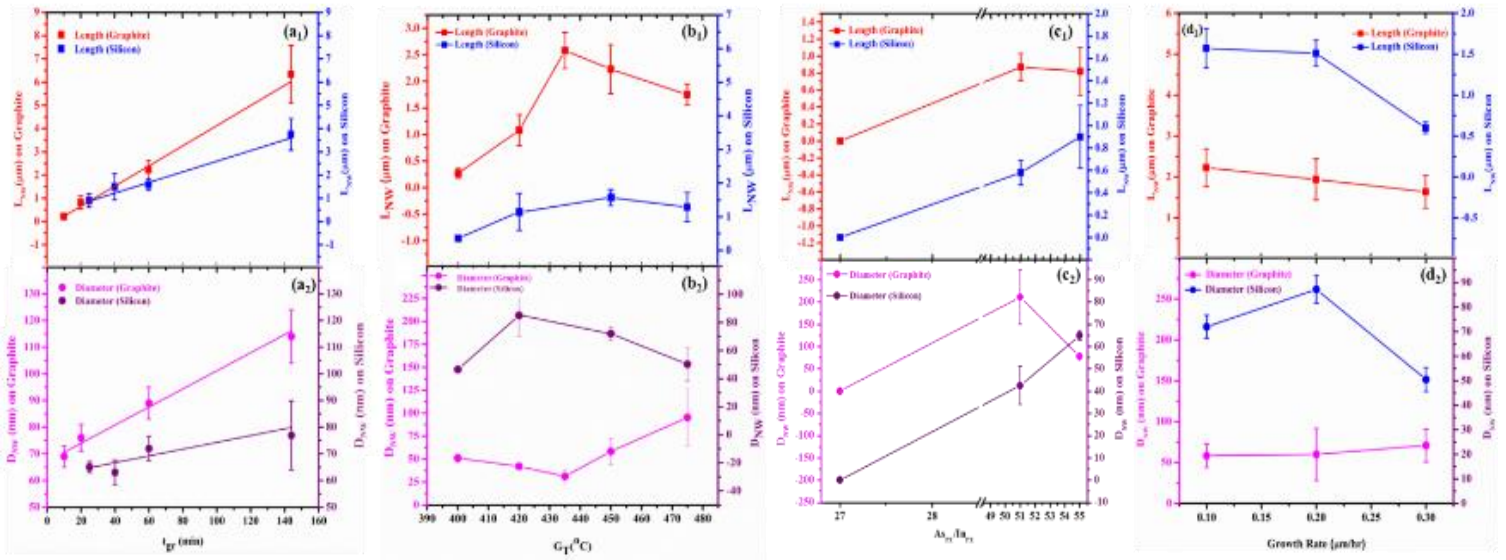
Figure 7.13 The influence of various growth parameters on the lengths (L_{NW}) [top panel] and diameters (D_{NW}) [bottom panel] of InAs nanowires deposited on Silicon and graphitic substrates.
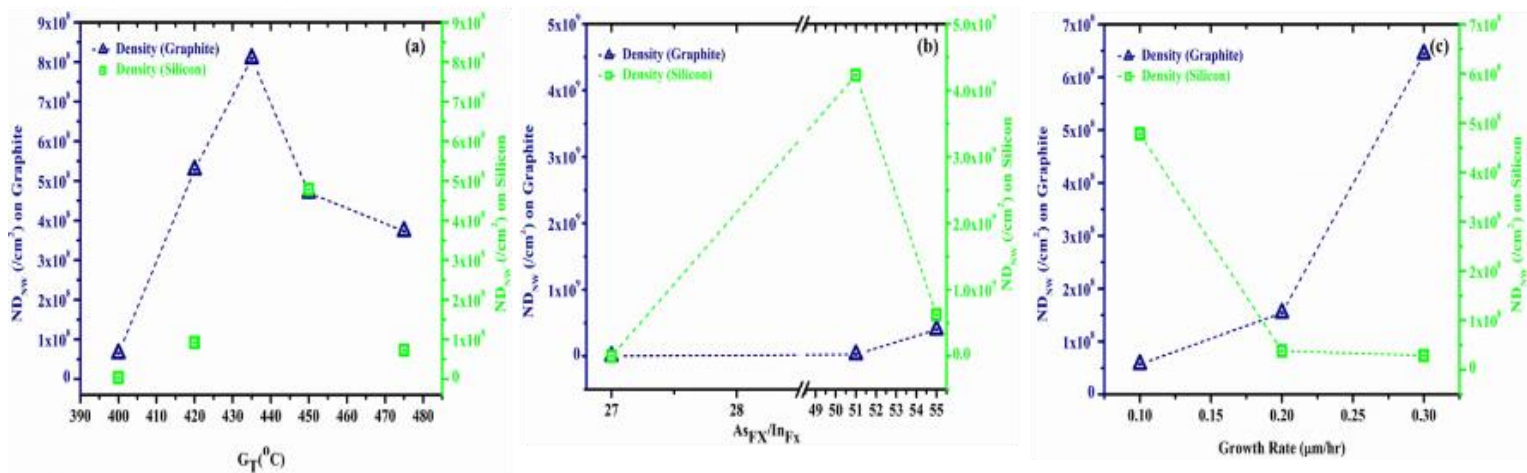
Figure 7.14 Effect of (a) growth temperature (G_T); (b) As/In flux ratio and (c) growth rate on the density of InAs nanowires deposited on graphite and Silicon.

enormous promise for the fabrication of cost-effective devices. The maximum diameter of the NWs on graphite is nearly double that of the corresponding NWs on Si (for t_{gr} = 144 min) which could be related to the differences in the growth mechanisms on both substrates. This observations suggests NWs growth is strongly dependent on the substrate. Furthermore, although the growth on both substrates displayed a high density of islands at a low temperature of 400°C, a relatively high yield of NWs (6.47 $\times 10^7$ cm^{-2}) was obtained on graphite in comparison to that on Si (3.66 $\times 10^7$ cm^{-2}). A similar pattern of NWs density was mostly observed for a further increase in growth temperature in the range of 420-475°C with the NWs on graphite displaying a higher yield of vertically-aligned NWs compared to that on Si (Figure 7.14a). The growth of InAs NWs on graphite is more strongly dependent on temperature than on Si (Figure 7.13b). This is evidenced by the significant enhancement in axial growth in response to a slight increase in growth temperature on graphite. A maximum L_{NW} of 2.58 μm was realized on graphite while only 1.57 μm long NWs were obtained on Si for the investigated temperature range. In addition, the behaviour of the NWs diameter on graphite is in complete contrast to that on Si due to the increase in axial growth in the temperature range of 400-435°C and its subsequent decline for G_T > 435°C. The strong temperature dependence of InAs NWs on graphite in comparison to Si could possibly be related to the high thermal conductivity of graphite (19.1 W/cm/K at 300 K)[271] which enhances adatom mobility. Turning to the influence of As_{Fx}/In_{Fx} flux ratio, although the evolution from the islands morphology to NWs structures was realized on both substrates at a relatively high As_{Fx}/In_{Fx} ratio (51), the nucleation of NWs on Si is more strongly influenced by the As_{Fx}/In_{Fx} ratio (Figure 7.14b). For instance, an As-rich condition (As_{Fx}/In_{Fx} ratio = 51) yielded a dense array (4.23 x 10^9 cm^{-2}) of NWs on Si, whereas a sparse distribution of NWs (2.55 x 10^7 cm^{-2}) was obtained on graphite. Similarly, a higher yield of NWs was obtained on Si when compared to the NWs on graphite for As_{Fx}/In_{Fx} ratio of 55. Although, axial NWs growth on both substrates is enhanced by As-rich condition

(Figure 7.13c), as expected there was a decrease in NWs diameter on graphite in favour of axial growth due to enhanced adatom mobility in excess As-flux (>50). Conversely, the insignificant increase in NWs diameter observed on Si is possibly due to insufficient As-flux which limits adatoms diffusion to the growth front. The opposite trend observed on both substrates (graphite and Si) reflects the differences in NWs sensitivity to changes in As/In flux ratio as a function of substrate type. Finally, it is clear from (Figure 7.14c), that NWs nucleation on Si is suppressed at relatively high growth rate, in sharp contrast, there was a monotonic increase in areal density of NWs on graphite leading to the realization of a high yield of vertically-aligned NWs at a growth rate of 0.3µm/hr which is possibly associated with the higher adatom mobility on graphite (Figure 7.13a) favouring an increase in NWs density. In addition, the large lattice mismatch between Si and InAs (>11%) promotes the growth of InAs Islands consequently, the use of higher growth rate favours an increase in Islands growth which mitigates adatom diffusion leading to a suppression of NWs density. Conversely, the absence of dangling bonds on the graphitic substrate minimizes the influence of strain and results in the growth of less dense and smaller InAs Islands which promotes a high yield of NWs. This indicates the graphitic thin films present enormous promise for the fabrication of cost-effective nanodevices because it enables NWs growth at high growth rate. In addition, the NWs deposited on graphite as a function of growth rate exhibited longer L_{NW} in comparison to the NWs/Si for all investigated samples. This further indicates that InAs NWs have longer diffusion length on graphite compared to Si.

7.2.6   Influence of the Graphitic Substrate on the Structural property of InAs Nanowires

In order to elucidate the influence of the graphitic substrate on the defect density, a structural analysis of the HRTEM image of as-grown InAs NWs on graphite was conducted in comparison to a reference InAs NWs grown on Si (111) under identical growth conditions [In flux - 1.75 x 10^{-7} mbar, As flux – (8.0×10^{-6} – 2×10^{-5}) mbar) and growth temperature in the range of 440 - 500 °C]. A representative HRTEM image of optimal InAs NWs/graphite depicted in Figure 7.15a shows the NWs exhibits a mixture of ZB/WZ crystal phases. An enlarged segment of the HRTEM image (Figure 7.15b) clearly demonstrates the transition between the ZB and WZ phases with SFs present. The typical HRTEM image of the InAs NWs/Si shown in Figure 7.16(a-b) indicates a very high density of SFs along with RTs. The HRTEM images of both NWs samples were then analysed for defects distribution, particularly SFs and RTs.
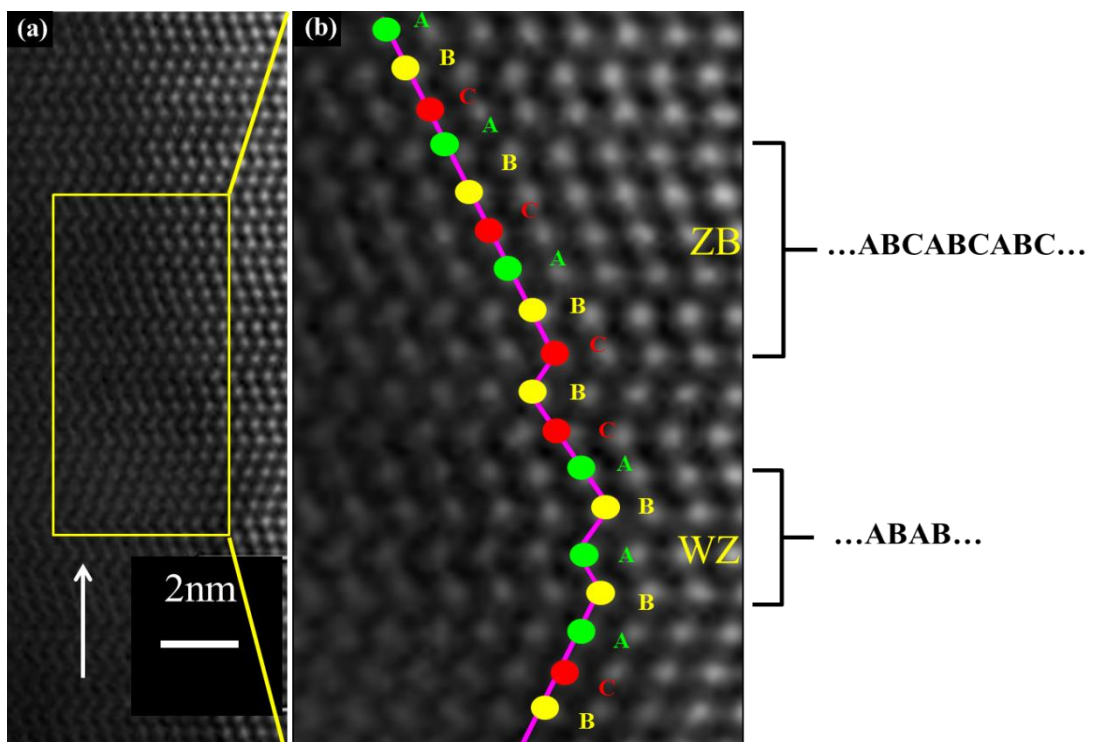
Figure 7.15 Typical HR-TEM image of InAs nanowires grown on graphite (a); an enlarged section of the HRTEM image highlighting the ZB/WZ mixture in the nanowires (b).

127
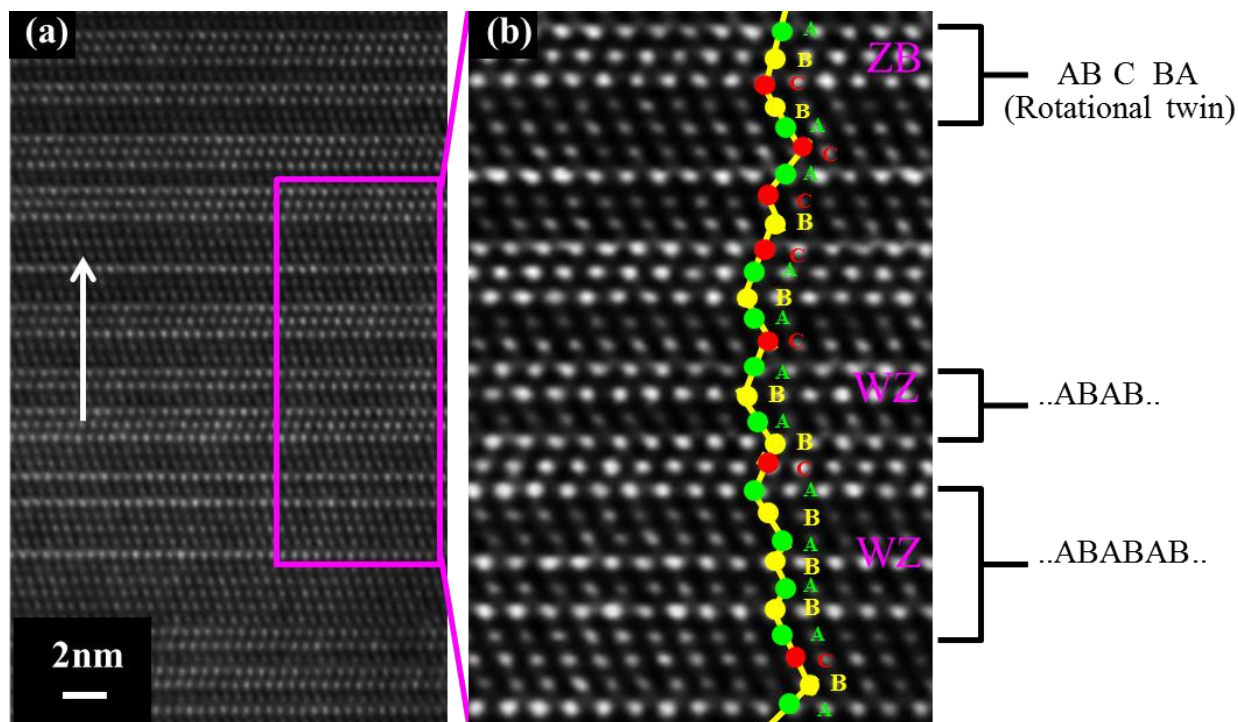
Figure 7.16 Typical HR-TEM image of InAs nanowires grown on Si (111) (a); an enlarged section of the HRTEM image highlighting the high density of SFs and the ZB/WZ mixture in the nanowires (b).
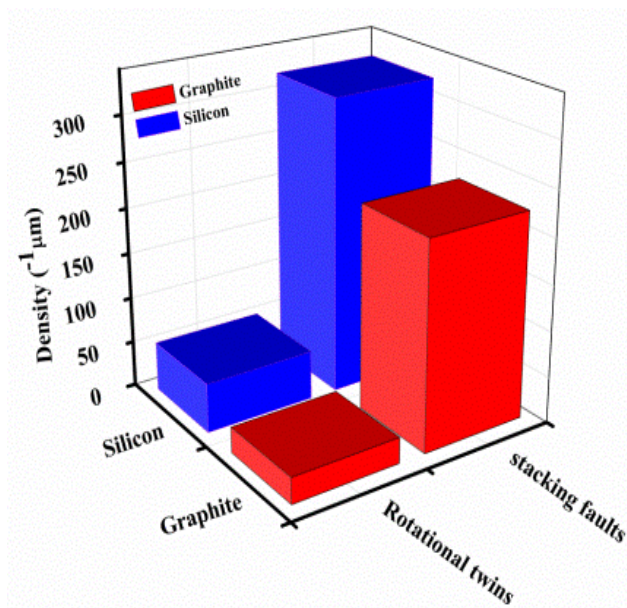
Figure 7.17 Comparison of the stacking faults and rotational twins' density in InAs nanowires deposited on silicon and graphitic substrates.

As illustrated in Figure 7.17, the InAs/graphite NWs exhibit a SF population of 225.35 ± 56.34 per µm which is significantly lower than the InAs/Si value (321.42±53.58 per µm) in addition

to the displayed low RTs distribution in comparison to that of NWs on Si. Although self-catalyzed NWs usually display a high defects density in addition to a high tendency to exhibit polytypism, this observation suggests the use of graphitic substrates could potentially improve the structural property of NWs. This exceptional crystal quality of the NWs/graphite is attributed to the non-covalent van der Waals epitaxy (VDWE) growth technique employed. The mechanism driving NWs growth on graphite is largely diverse from that of NWs deposited on conventional substrates such as Si owing to the absence of surface dangling bonds on graphitic substrates [164-166, 269]. One of the key advantages of VDWE is the absence of strain and defects [103, 272] owing to the fact that lattice matching requirements are unnecessary given its distinct bonding mechanism compared to conventional heteroepitaxy which is enabled by strong chemical bonding[104]. VDWE has shown the capacity to readily relieve interfacial strain [103, 105, 106] in addition to promoting the formation of high-quality heterojunctions between highly mismatch materials. Recently, Utama et al[273] demonstrated that VDWE enables a nearly complete lattice relaxation at the NWs-substrate heterointerface leading to the growth of defect-free NWs. The seedless and catalyst-free growth of nearly defect-free ZnO NWs on phlogopite mica has recently been reported[274]. This demonstrates that VDWE could be potentially exploited for the growth of structurally superior III-V semiconductor NWs while circumventing lattice matching restrictions between the NWs material and its substrate.

7.3 MBE Growth and Characterization of InAsSb Nanowires on Graphite

7.3.1 Growth of InAsSb on Graphite by Droplet Epitaxy

Aiming to elucidate the conditions for realizing high aspect ratio (AR) NWs, a series of InAsSb NWs samples ($M_{8.33G}$, $M_{1.26G}$, $M_{12.46G}$) and $H_{4.8G}$ were grown on graphite by MBE under moderately As-rich (MAR) condition [(7.5 ± 2.2) x 10^{-6} mbar] and highly As-rich (HAR) condition (~1.4 x 10^{-5} mbar) respectively. The graphitic films were mechanically exfoliated from HOPG and transferred unto Si (111) substrates and subsequently loaded into the system and thermally outgassed. As described before, the In droplet-assisted growth technique was employed for the preferential nucleation of NWs. The growth of $InAs_{1-x}Sb_x$ NWs was initiated
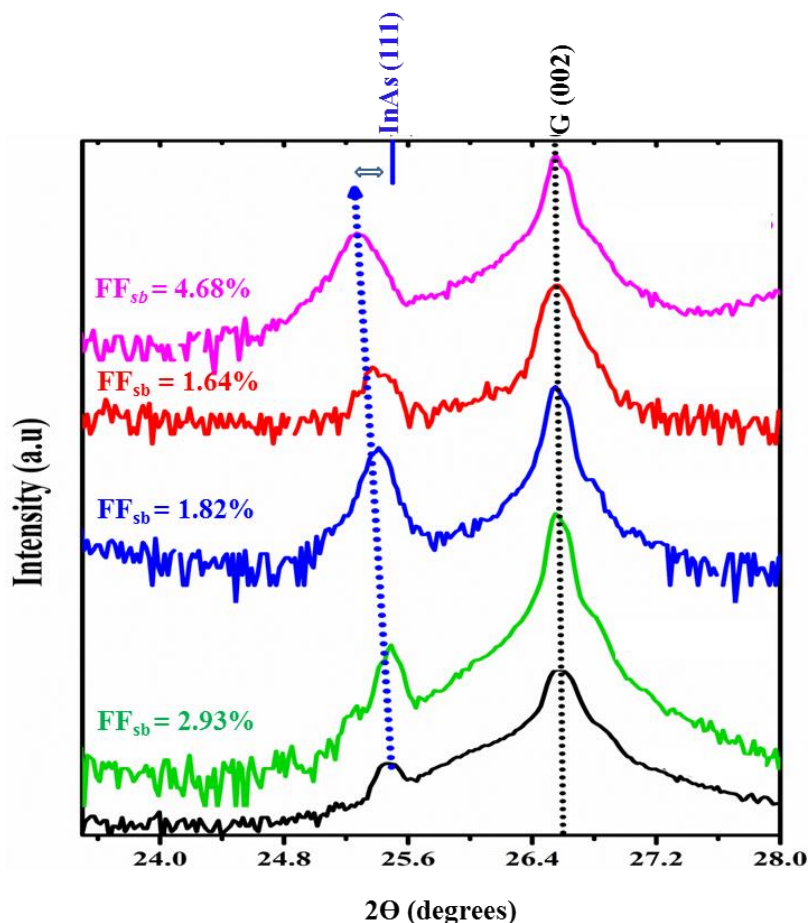
Figure 7.18 X-ray diffraction patterns of $InAs_{1-x}Sb_x$ nanowires grown on graphite at a constant growth temperature and varied Sb fractional flux (FF_{sb}).

by the simultaneous introduction of all growth precursors at a fixed In beam equivalent pressure (BEP) and growth temperature of 420-470°C for a total growth duration of ~2 hours. The Sb incorporation in the NWs was controlled by varying the Sb fractional flux (FF$_{sb}$) in the range of 1.64 – 4.68%. Where (FF$_{sb}$) is the Sb fractional flux representing the ratio of Sb flux (ψ_{Sb}) to the combined group V (As + Sb) precursor fluxes (ψ_v) as previously expressed in equation 5.1. The Sb composition (x_m) in as-grown NWs was estimated from XRD and SEM-EDX measurements and further confirmed by TEM-EDX. The morphology was investigated by SEM. Figure 7.18 is the XRD spectra of InAsSb NWs along with a reference InAs spectrum ($x_m = 0$). The (111) ZB InAs diffraction peak was used as reference for the determination of x_m. The two diffraction peaks present in all samples positioned at ~ 25° and 26.5° are indexed to the (111) ZB InAsSb and graphite (002) respectively. Compared to the InAs ZB (111) peak[185] at 25.4° from the reference InAs, the InAs$_{1-x}$Sb$_x$ NWs (111) peaks shifts to lower angles with increasing Sb content. The Sb incorporation in the NWs was deduced from the diffraction angles with an assumption of Vegard's law[222] and full relaxation (to be confirmed by EDX measurements). For the samples grown within the MAR regime, the EDX spectra (Figure 7.19) gave Sb composition of 8.33%, 1.26% and 12.46% corresponding to samples
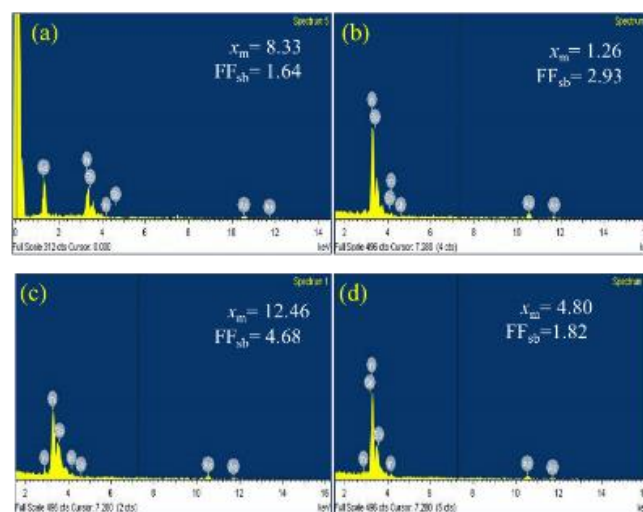
Figure 7.19 EDX spectrum of InAsSb nanowires grown on graphitic thin films with varying Sb fractional fluxes (FF$_{sb}$) at moderately As-rich (a-c) and highly As-rich (d) conditions respectively. Each sample display signals characteristic of As, In, and Sb.

$M_{8.33G}$, $M_{1.26G}$ and $M_{12.46SG}$ grown with FF_{sb} of 1.64, 2.93 and 4.68 respectively. 4.8% Sb was incorporated in sample $H_{4.8G}$. These x_m values which closely correlate with the results of XRD measurements indicate the NWs are fully relaxed without any strain. In order to further verify the presence of Sb as well as ensure consistency of Sb content along the length of individual NWs, TEM-EDX measurements were taken at different positions (ranging from the top, middle to bottom) on sampled NWs as shown in Figure 7.20. It shows the Sb composition is consistent at different positions of the NWs. The average Sb content in these NWs samples is comparable to the SEM-EDX derived values which demonstrates the reproducibility of Sb incorporation in

Spectrum	As(%)	Sb(%)
Spectrum 1	92	8
Spectrum 2	92	8
Spectrum 3	89	11
Spectrum 4	90	10
Spectrum 5	88	12
Spectrum 6	89	11
Spectrum 7	91	9

Spectrum	As(%)	Sb(%)
Spectrum 2	98	2
Spectrum 3	98	2
Spectrum 4	98	2
Spectrum 5	97	3
Spectrum 6	98	2
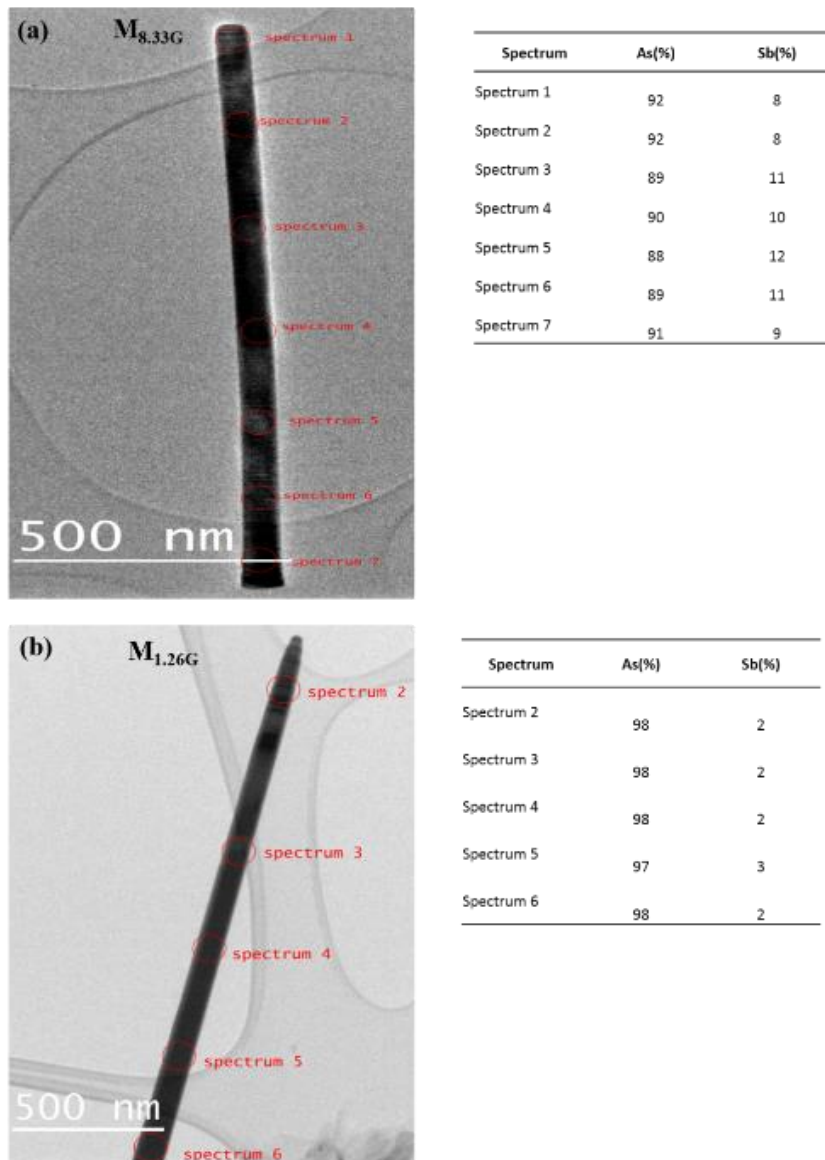
Figure 7.20 TEM-EDX measurements shows comparable Sb content along the length of individual nanowires.

the NWs. Representative low and high magnification SEM images of as-grown MAR $InAs_{1-x}Sb_x$ NWs are shown in Figure 7.21(a-c). The NWs exhibits a 6-fold symmetry (inset of Figures 7.21b and 7.21c) of the side facets characteristic of NWs growing along the ⟨111⟩B direction. Analysis of the SEM images revealed the NWs are ~71 - 356 nm in diameter and ~1.7-2.3 μm in length. No In droplet is present at the wire tip possibly due to their consumption under excess As flux. Aiming to investigate the influence of high (excess) As-flux on axial NWs growth and AR, sample $H_{4.8G}$ was grown within the HAR regime by slightly increasing the As-flux, with the In BEP fixed while utilizing similar FF_{sb} (1.82%) to that of sample $M_{8.33G}$. Figure 7.21d shows a high yield (1.46×10^8 cm^{-2}) of NWs arrays with a typical length of 4.70 ± 0.89 μm and diameter of 45.97 ± 6.94 nm were realized. Worthy of note is the high density of vertically well-aligned and non-tapered (highly uniform diameter along the entire length) NWs. The side-view
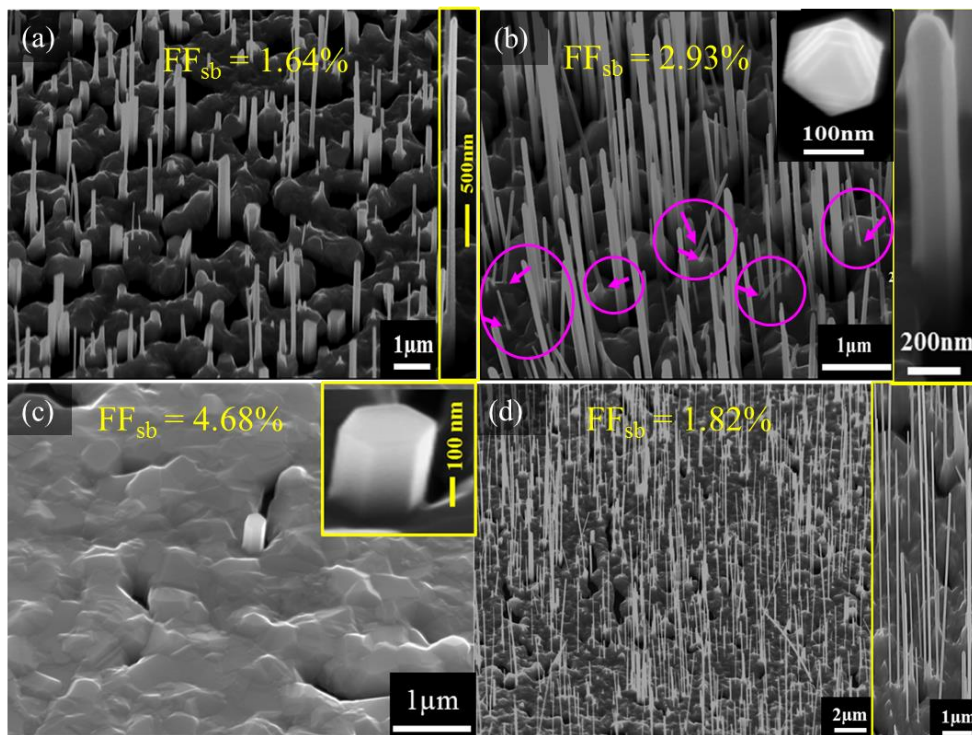
Figure 7.21 45° tilted low and high magnification SEM images of as-grown $InAs_{1-x}Sbx$ nanowires on graphite with Sb compositions of (a) 8.33% (b) 1.26% (c) 12.46% for the moderately As-rich samples and 4.80% for the highly As-rich sample (d).

close-up image of a typical NW (inset of Figure 7.21d) indicates there was no diameter broadening or wire bending along the entire length despite the high AR which are distinct signatures of morphologically superior NWs.

The plot of the NWs length (L_{NW}) and diameter (D_{NW}) as a function of x_m is depicted in Figure 7.22a. It reveals a strong dependence of NWs geometry on x_m for the samples grown under MAR conditions ($M_{8.33G}$, $M_{1.26G}$ and $M_{12.46G}$). The monotonic decrease in L_{NW} and expansion in D_{NW} with increasing Sb content clearly indicates a suppression of axial NWs growth with a corresponding enhancement in radial growth which is attributable to Sb surfactant effect [30, 143, 240]. In sharp contrast, axial NWs growth is promoted by the HAR condition evidenced by the large L_{NW} and small D_{NW} exhibited by sample $H_{4.8G}$. The observed trend is more evident in figure 7.22b which shows a strong dependence of NWs AR on x_m. As can be seen, the MAR samples show a monotonic decrease in AR (maximum AR of ~32) while the HAR sample ($H_{4.8G}$) exhibits an exceptionally high AR of ~102 (over 3x the maximum AR of the MAR samples). Specifically, increased Sb incorporation in the range of 8.33 - 12.46% resulted in a sharp fall in AR from ~16 (sample $M_{8.33G}$) to ~1 (sample $M_{12.46G}$) while sample $M_{1.26G}$ with only trace Sb content (1.26%) exhibited a small AR of ~32 (L_{NW} = 2.33±0.54 µm, D_{NW} =
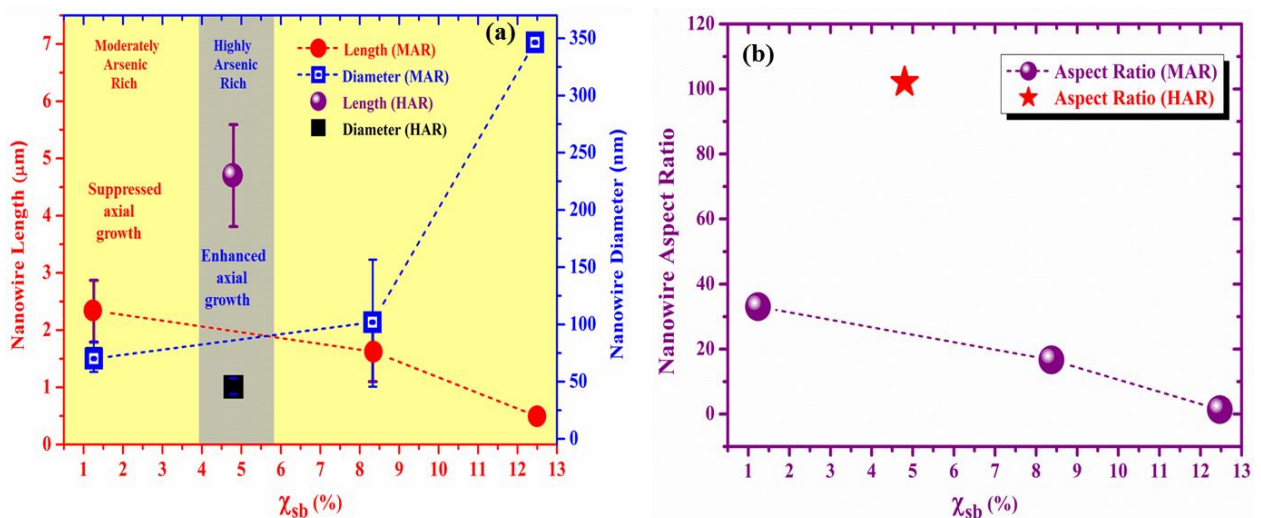
Figure 7.22 Measured InAs$_{1-x}$Sbx nanowire (a) length (L_{NW}) & diameter (D_{NW}) and (b) aspect ratio as a function of Sb content (x_m) for moderately As rich (MAR) and highly As rich (HAR) samples.

71.79±13.27 nm). Such behaviour is attributed to the Sb-induced modifications in thermodynamic and kinetic processes[240]. Intriguingly, despite the relatively high Sb content (4.80%) in sample $H_{4.8G}$, a marked surge in AR to a maximum of ~102 (L_{NW} = 4.70±0.89 μm, D_{NW} = 45.97±6.94 nm) was observed. Minute Sb concentrations has been previously reported to significantly induce an increase in lateral growth with a corresponding suppression in axial growth [143, 275] leading to the growth of short and thick NWs. As discussed earlier (subsection 6.3), the introduction of small (4.3%) amount of Sb induces a significant increase in lateral growth. Also, previous investigations (subsections 5.4.3. 7.2.3 and 7.2.5) revealed the axial growth of In-assisted NWs are strongly dependent on As-flux. Consequently, the exceptional morphology (high AR) observed in sample $H_{4.8G}$ is attributed to an enhancement in axial growth and a suppression of lateral growth owing to the significantly high As-rich conditions employed for the growth. This indicates that an As-rich condition is highly crucial for the suppression of the commonly observed Sb-induced lateral NWs expansion and axial growth shrinkage. At moderate As-flux, axial NWs growth is suppressed due to the Sb surfactant effect resulting in NWs diameter expansion with reduced AR however, at significantly high As-flux the Sb surfactant effect is inhibited leading to the suppression of lateral growth while at the same time favouring an increase in AR.

7.3.2   Comparison between InAsSb Nanowires Growth on Si (111) and Graphite

In order to investigate the influence of the graphitic substrate on NWs growth, a set of InAsSb NWs samples (hence forth referred to as $M_{1.63S}$, $M_{7.28S}$ and $H_{3.88S}$) were grown on Si (111) substrates at identical conditions to the InAsSb samples $M_{1.26G}$, $M_{12.46G}$ and $H_{4.8G}$ (grown with FF_{sb} of 2.93 4.68 and 1.82% respectively on graphite). Prior to commencement of growth, the
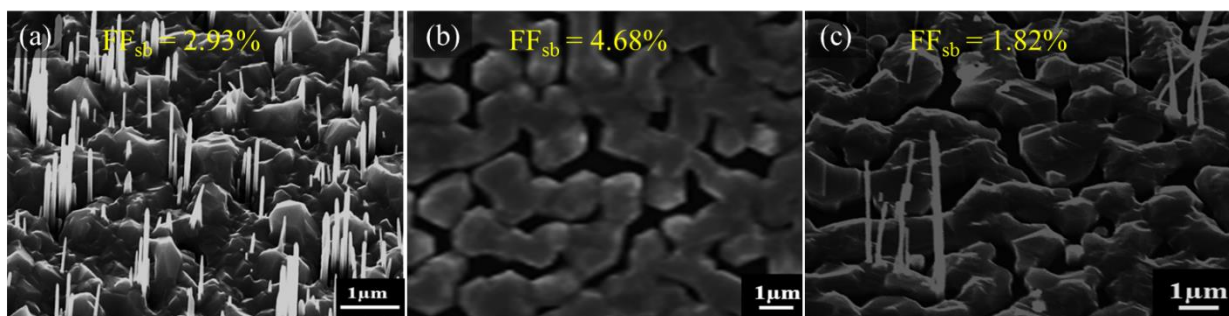
Figure 7.23 45° tilted low and high magnification SEM images of as-grown InAs$_{1-x}$Sbx nanowires on Si (111) as a function of Sb fractional fluxes (FF$_{sb}$).

Si substrates were cleaned as described previously. Figure 7.23(a-c) depicts the SEM images of as-grown InAsSb NWs samples M$_{1.63S}$, M$_{7.28S}$ and H$_{3.88S}$ on Si. Table 7.2 shows the growth parameters and Sb content of the InAsSb NWs grown on graphite and Si with identical conditions. EDX analysis (Figure 7.24) revealed Sb incorporation of 1.63%, 7.28% and 3.88%, for samples M$_{1.63S}$, M$_{7.28S}$ and H$_{3.88S}$ respectively. Intriguingly, the Sb incorporation in the InAsSb/GS samples M$_{12.46G}$ and H$_{4.8G}$ are higher than the corresponding InAsSb/Si samples M$_{7.28S}$, and H$_{3.88S}$ respectively, while samples M$_{1.26G}$ and M$_{1.63S}$ have comparable Sb content.

Table 7.2 Growth Parameters and Sb content of InAs$_{1-x}$Sb$_x$ Nanowires grown on Graphite and Silicon

Substrate	Sample	Growth time (min)	Sb fractional flux (FF$_{sb}$)	Sb content [χ_m](%)
Graphite	M$_{8.33G}$	120	1.64	8.33
Graphite	M$_{1.26G}$	120	2.93	1.26
Graphite	M$_{12.46G}$	120	4.68	12.46
Graphite	H$_{4.8G}$	120	1.82	4.80
Silicon	M$_{1.63S}$	120	2.93	1.63
Silicon	M$_{7.28S}$	120	4.68	7.28
Silicon	H$_{3.88S}$	120	1.82	3.88
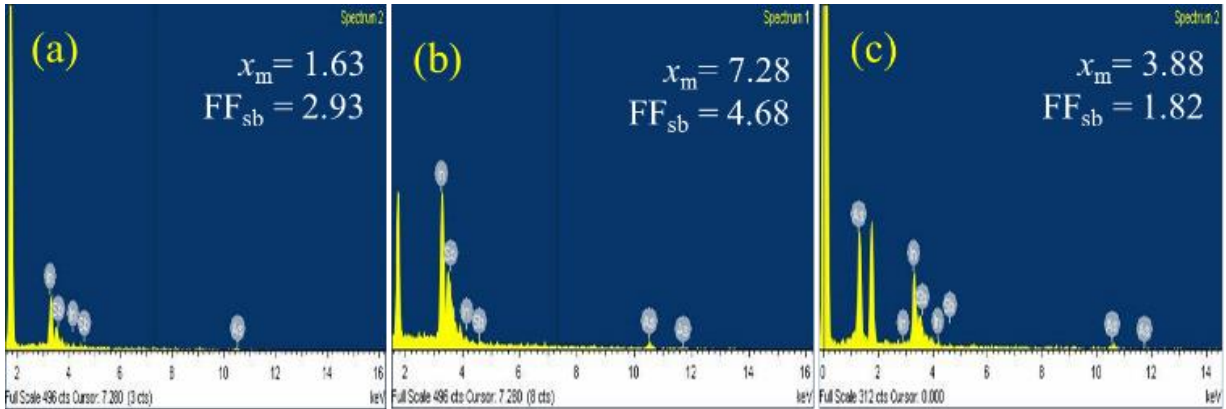
Figure 7.24 EDX spectra of InAsSb nanowires grown on Si (111) with varying Sb fractional fluxes (FF_{sb}) and moderately As-rich (a-b) and highly As-rich (c) conditions respectively . Each sample display signals characteristic of As, In, and Sb.

This suggests the graphitic substrates promote Sb incorporation in InAsSb NWs possibly due to differences in adatom migration length and the absence of surface dangling bonds. However, it can be observed in Figure 7.25a that x_m scales inversely with FF_{sb} (for $FF_{sb} \leq 2.93$). Incidentally, this corresponds to the region within which dominant NWs growth was realized and can be associated with the increased segregation and surfactant effect of Sb[240] which is more pronounced in the NWs structures owing to their high surface to volume ratio.
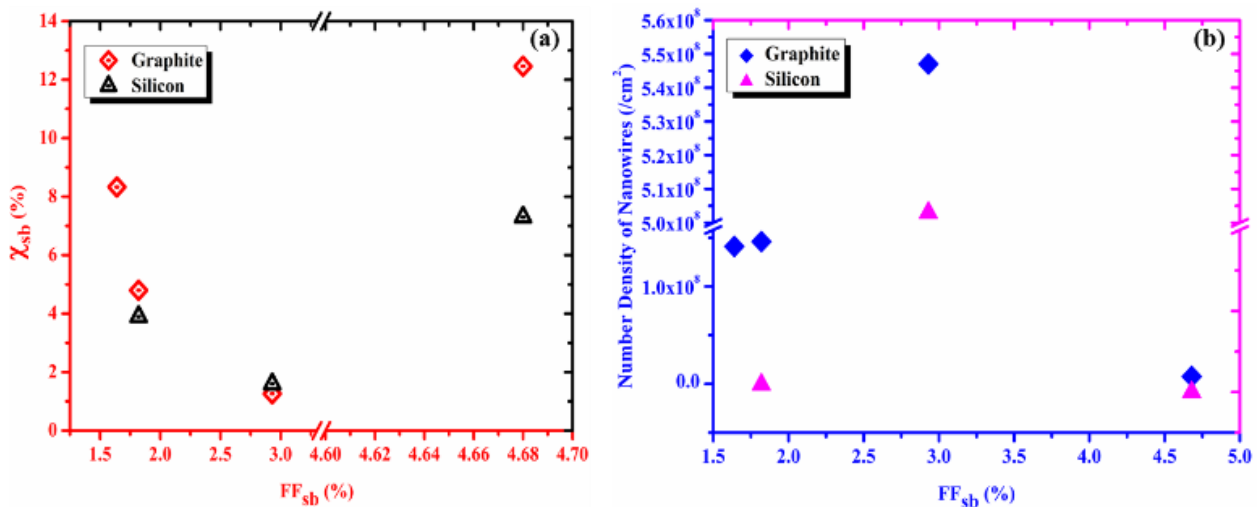
Figure 7.25 Plot of Sb fractional flux (FF_{sb}) as a function of Sb content (a) and number density (b) of InAsSb nanowires grown on graphite and Si (111).

137

A disproportionate Sb incorporation has previously been demonstrated[223] in InAsSb NWs. Conversely, for higher FF_{sb} the samples on both substrates show maximum Sb incorporation accompanied by a morphological evolution from the NWs morphology to a dominant 2 dimensional (2D) films growth. This can be explained by the Sb induced kinetically inhibited In adatom mobility[240]. Surfactant Sb is known to delay 2D→3D growth mode transition while promoting layer by layer growth[246]. A plot of FF_{sb} as a function of the number density of InAsSb NWs grown on graphite and Si (111) is depicted in Figure 7.25b. It indicates the density of NWs increases with FFsb (for $FF_{sb} \leq 2.93\%$) which is understandable given the decline in Sb incorporation with FF_{sb} in NWs grown within this regime. Increased Sb content has been shown to quench the yield of vertically-aligned NWs in favour of cluster growth[143]. More interestingly, Figure 7.25b shows a relatively high yield of NWs on graphite compared to the NWs grown on Si. Sample $H_{4.8G}$ on graphite yielded a high NWs density of 1.46 x 10^8 cm^{-2}, while only a sparse distribution of NWs (9.36 x 10^6 cm^{-2}) was obtained on Si (sample $H_{3.88S}$) despite being grown with identical conditions (FF_{sb} = 1.82). In addition, NWs growth was completely suppressed in sample $M_{7.28S}$ deposited on Si while sample $M_{12.46G}$ yielded a sparse NWs distribution (7.67 x 10^6 cm^{-2}) on graphite. Due to the relatively high Sb content in most InAsSb NWs/graphite, a low yield of NWs was anticipated[143] in comparison to the corresponding NWs on Si (Table 7.2). However, the NWs density on graphite was higher than that on Si despite the relatively high Sb content. This suggests the graphitic thin films are more favourable for InAsSb NWs growth which is highly promising for Sb-based flexible optoelectronic device applications. This could be associated with differences in the interfacial surface energy between the droplet and the substrates which in turn results in variations in the extent of Sb-induced suppression of NWs nucleation[240].

Finally, the high magnification SEM images (Figure 7.21b) reveals sample $M_{1.26G}$ yielded a relatively high percentage of vertically less-aligned NWs in comparison to the other $InAs_{1-x}Sb_x$

NWs/graphite samples. In order to clarify the effect of the graphitic substrate on the vertical directionality of the NWs, the morphology of sample M grown on Si (111) with identical growth condition was further analysed. The SEM image (Figure 7.23a) revealed the NWs show a high yield (~95%) of vertically well-aligned NWs arrays which suggests the observed high density of randomly aligned NWs in $M_{1.26G}$ could be attributed to the influence of the graphitic substrate. A close evaluation of the SEM image of the sample indicates the unaligned NWs grew on the Islands (clusters) which were grown alongside the NWs as signified by arrows (Figure 7.21b). A similar behaviour was reported by Mohseni et al[168] . The growth of non-vertical NWs on islands which themselves preferentially grew along graphene line defects was observed. It is likely that the rough sections of the graphite promotes the formation of large and dense InAs island which in turn mitigates the epitaxial growth of NWs in agreement with previous report[165].

Chapter 8

Growth of InN Nanostructures on Bare Si (111)

This chapter explicates the droplet epitaxy growth procedure for InN nanostructures and growth temperature effects on the morphology of the nanostructures.

8.1 Growth procedure of InN Nanostructures by Droplet Epitaxy

InN samples were grown on Si (111) substrates by plasma-assisted molecular beam epitaxy (VG-V80H MBE) equipped with an Oxford Applied Research HD25 radio-frequency nitrogen plasma source. The substrates were cleaned chemically using 10% hydrofluoric acid solution to remove the surface native oxide then quickly loaded into the MBE system to avoid re-oxidation. The substrates were then out-gassed at temperature of $550 - 700^0C$ for at least one hour prior to growth initiation. The nitrogen plasma power, Nitrogen (N) and In BEP were set at 270W, 7.0×10^{-5} and 2.3×10^{-7} mbar respectively. The substrates were first activated by In droplets followed by the growth of InN films by simultaneously opening the shutters for In and nitrogen plasma. All the InN samples were grown with similar N/In BEP ratio (≈ 300) but at different growth time and substrate temperatures (G_T). The surface morphology of the resulting samples was determined by a Sirion field emission scanning electron microscope (FESEM). X-ray diffraction (XRD) was employed to investigate the crystalline quality. Photoluminescence (PL) measurements were used to investigate the optical properties of the InN nanocolumns in comparison to a 2D InN thin film reference sample using an Ar+ ion laser (514 nm) with a cooled InSb detector.

8.2　Effect of Temperature on InN nanostructure growth on Silicon

The surface morphologies of as-grown nanostructures along with growth parameters are summarised in Table 8.1. The morphological evolution of the 3D InN films grown with G_T ranging from 490 to 630^0C is depicted in Figures 8.1(a-e). The morphology of InN films exhibits 3D features varying from nanometre to micron size structures of various shapes ranging from columnar, lightly faceted to deeply faceted microislands, indented hemispheres and smooth hemispherical microislands. Figure 8.1(a) shows the FESEM image of InN thin film grown at 490^0C which has protruding 3-dimensional (3D) nano column (NC) structure. Some of the NCs are c-axis oriented and non-tapered while others are tilted with respect to the substrate normal. The inset of Figure 8.1(a) highlights the NCs which are oriented normal to the substrate, non-tapered (NT) and aligned along the [0001] direction. Detailed examination of the NCs ($G_T = 490^0C$) reveal the initial stages of longer InN NCs reported in literature[276]. As highlighted in Figure 8.2, the tilted NCs have different angles of inclination (denoted as Θ_1 and Θ_2 in the inset) with respect to the Si (111) substrate. Thus on the basis of inclination they are categorized as left-tapered (LT), right-tapered (RT), fully-tapered (FT) and pyramidal (PM). The identified crystal planes of the NCs side facets correspond to hexagonal InN as summarized in Table 8.2.

Table 8.1 Growth parameters and morphologies of the investigated samples

Sample	Growth Temp (°C)	Growth Time (hrs)	Morphology	Distinctive features
A	490	3.18	NanoColumns	Untapered, Tapered and Pyramidal
B	520	0.87	Microislands	Lightly faceted (LF)
C	540	2.48	Microislands	Deeply faceted (DF)
D	560	3.02	Microislands	Indented hemispheres (IH)
E	630	4.23	Microislands	Smooth hemispheres (SH)
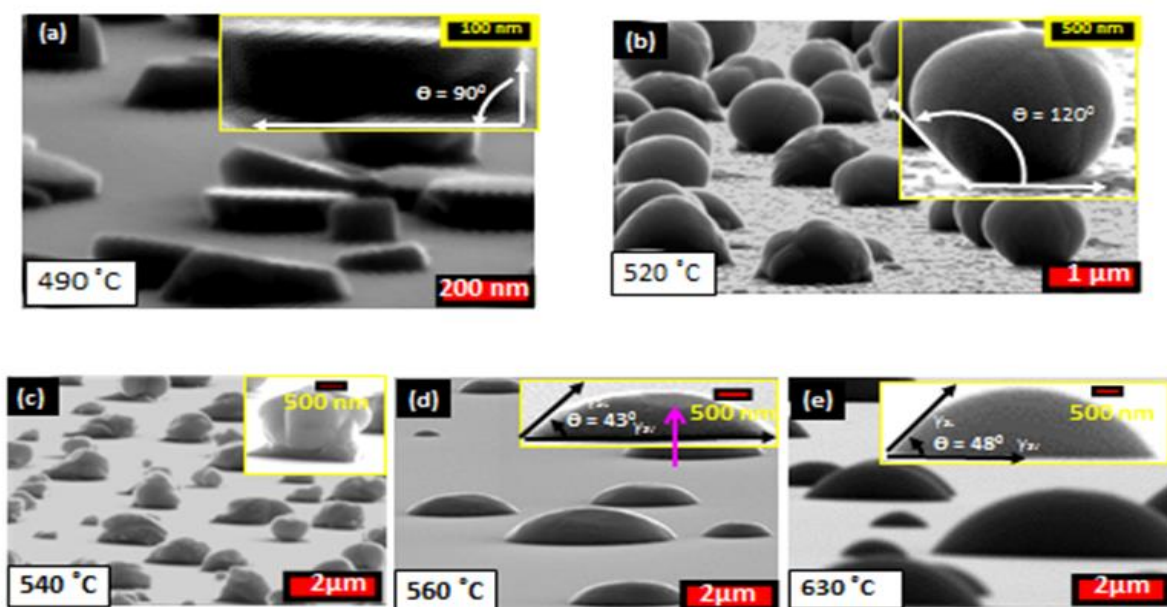
Figure 8.1 Typical FESEM images of InN NCs deposited at a temperature of 490°C (a); and microislands grown at (b) 520°C, (c) 540°C , (d) 560°C and (e) 630°C. The insets show the high magnification images of the representative features
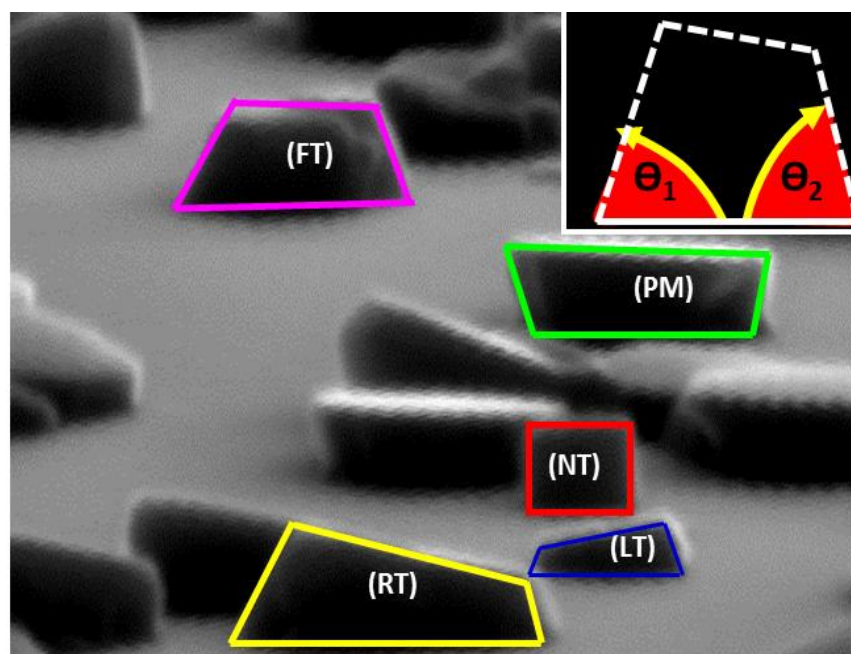
Figure 8.2 SEM micrograph showing the NCs structures with different orientations to the Si (111) substrate

Table 8.2 Morphologies and crystal planes of InN Nanocolumns grown at 490^{0}C

Typical NC	Morphology of NCs	Angle of inclination to Si (111) substrate (θ_1)(degrees)	Crystal plane	Angle of inclination to Si (111) substrate (θ_2)(degrees)	Crystal Plane
A	Non-tapered	90	(10-10)	90	(10-10)
B	Left-tapered	58	(30-34)	75	(20-21)
C	Right-tapered	58	(30-34)	75	(20-21)
D	Fully-tapered	61	(10-11)	61	(10-11)
E	Pyramidal	79	(30-31)	72	(50-53)

The observed NCs morphologies could be associated with kinetic processes governing the initial InN NWs growth phase of tapered and non-tapered structures. In adatom diffusion from the substrate to the NCs sidewall and from the sidewall to the tip is crucially important for the growth of non-tapered NCs, as a result, the tapering and random alignment of the NCs relative to the substrate could be associated with the non-uniform availability of In adatoms at the NCs base, sidewalls and tip during nucleation and the early stage of NCs growth. 3D InN microislands grown at temperatures above 490°C exhibits various morphologies. The inset of Figure 8.1(b) shows the high magnification image of emerging lightly faceted (LF) microislands observed in the InN film grown at 520^{0}C. It appears to be the commencement of faceted islands growth with less conspicuous cusp. These islands evolve into deeply faceted (DF) 3D island with more pronounced, distinct and outwardly bulging cusps with an increase in G$_T$ to 540°C (higher magnification image shown in the inset of Figure 7.1 (c)). The evolution of these DF films can be explained using the wulff construction[277] which is illustrated in Figure 8.3. It has been demonstrated that wurtzite InN microstructures grow along the [0001] direction under high N/III flux while low N/III flux leads to growth along <10-10> directions[278]. Although a high N/III flux ratio was initially supplied during growth, the high growth temperature increases N desorption leading to an indium rich condition, which results in a preferential adsorption of In atoms. Consequently, the <10-10> direction possesses the
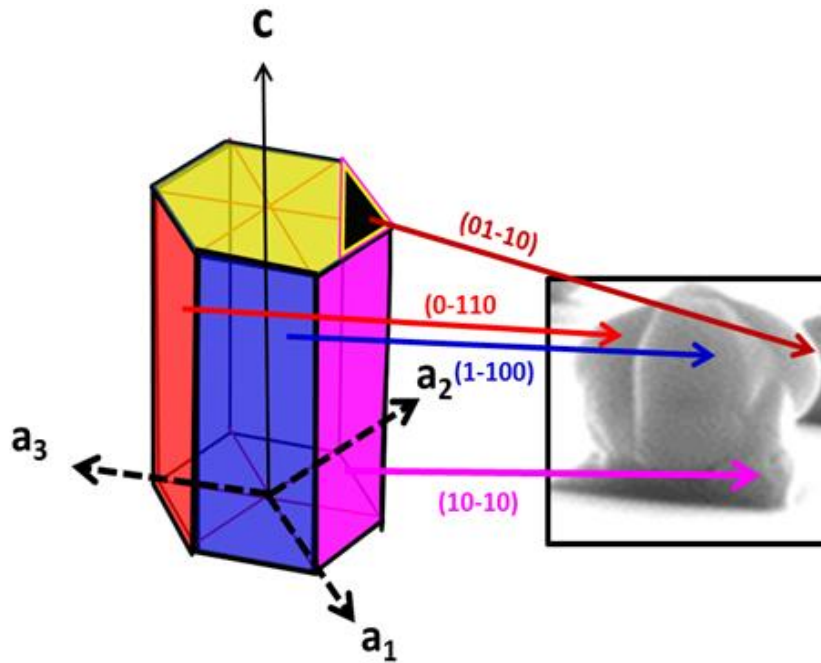
Figure 8.3 Schematic of hexagonal lattice showing c-plane and m-plane InN surfaces

lower surface energy in comparison to the [0001]. The slower growth rate along the m-direction <1-100> leads to concave facets and relative faster growth along "a" direction <11-20> thereby tending toward convex facets. This imbalance in growth rate along m and a direction creates six cusps along the closed curve, which can be observed if the cross-section of these microstructures can be seen. These exterior facets are distinctive of the early stage of island development. With an increase in G_T to 560 ℃, the microislands morphology transforms to indented hemispherical (IH) structures (shown in the inset of Figure 8.1d) with a typical contact angle of 43^0 and shallow pits (as denoted by the pink arrow) which eventually disappeared as G_T was further increased to 630 ℃. Extremely high growth temperature led to the formation of spherical hemispherical (SH) islands with a contact angle of 48^0. These SH were very smooth with hemispherical shape (Figure 8.1e). Both IH and SH microislands are morphologically different to the LF and DF samples with no observable facets.

The unique features of the InN microislands prompted further investigations by XRD and optical microscopy in order to better understand the formation of the films. Figure 8.4 shows the XRD pattern of InN NCs at 490 °C and microislands (520 – 630 °C). The relative intensities of the diffraction peaks are plotted against the growth temperature (Figure 7.5) to identify the dominant diffraction peak and crystal orientations of the grown samples. Depicted in the inset of Figure 8.5 is the schematic of (0002) and (10-11) InN crystal planes for the observed reflections from the samples. Analysis of the XRD result suggests that the InN NCs formed at 490°C have single crystalline wurtzite structure, aligned along the [0001] direction. The presence of the reflection from (10-11) s-plane is due to the preferential growth of some nanocrystals along the s-direction [10-11].
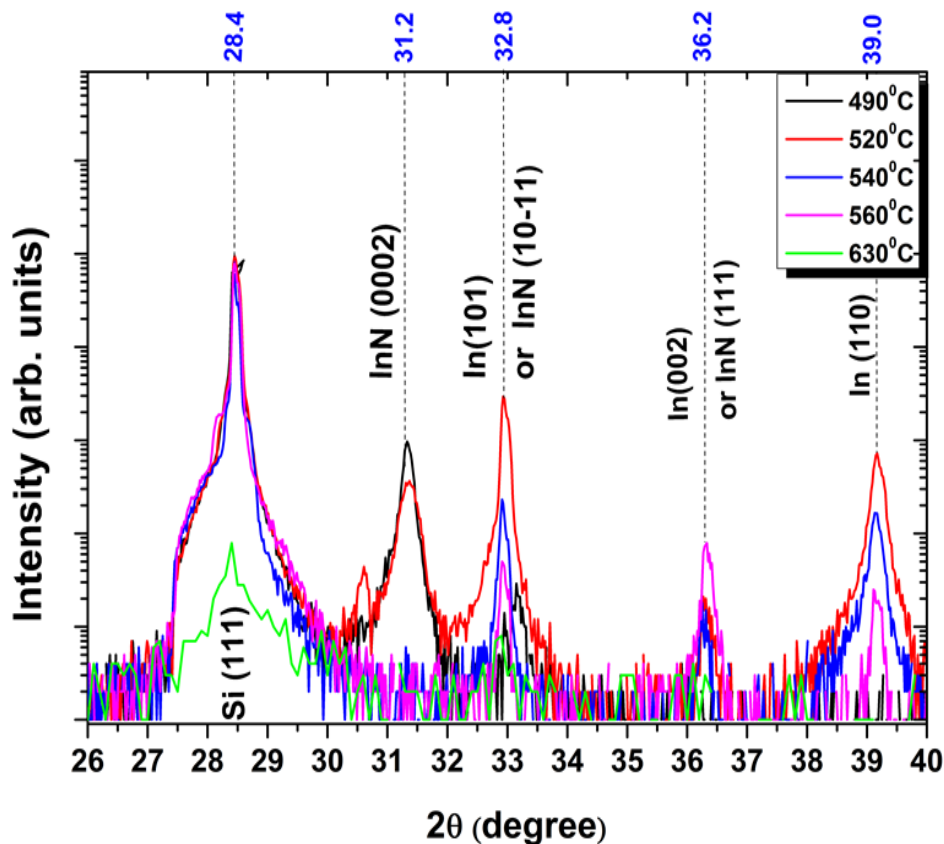
Figure 8.4 X-ray diffraction patterns of InN nanocolumns and microislands grown at 490°C and (520°C- 630°C) respectively

145
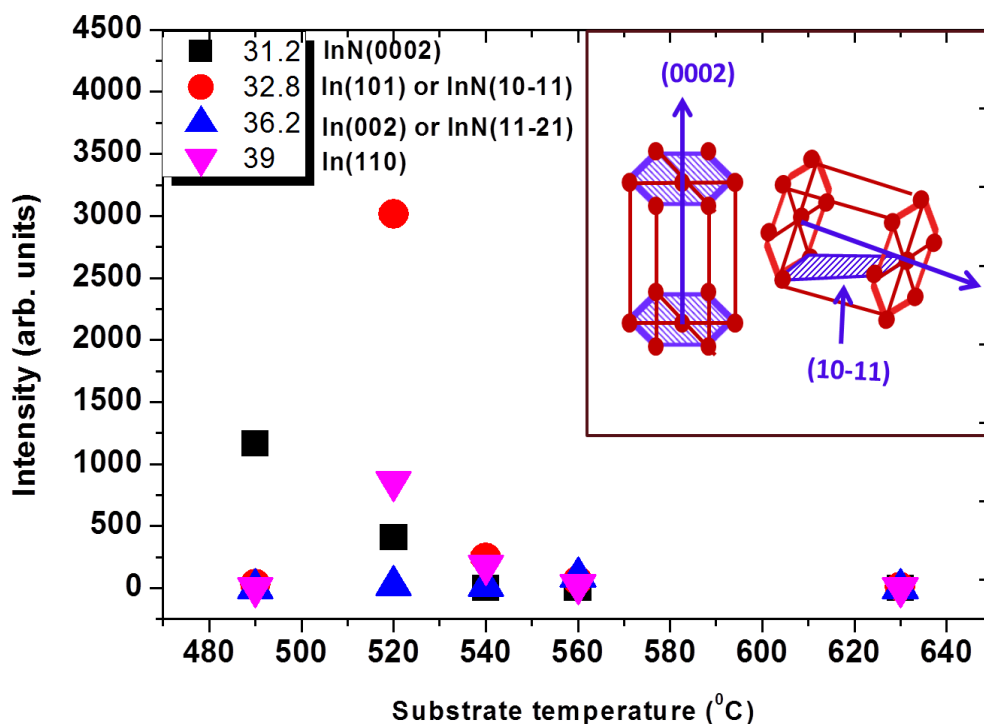
Figure 8.5 Plot of X-ray diffraction peak intensities of InN nanostructures as a function of growth temperature. The inset is the schematic of the (0002) and (10-11) InN crystal planes

The InN microislands grown at 520^0C exhibit similar preferences, moreover, the presence of other reflections suggests the formations of In adlayer on the surface between the microislands. Although the InN microislands deposited at 540 ^{0}C are single crystalline and wurtzite, the presence of strong (10-11) reflection suggests the microislands grew with (10-11) s-plane parallel to the substrate or the single crystalline In adlayer grew alongside. The XRD patterns of films grown at 560 ℃ and 630 ^{0}C clearly show that none of the reflections matches that of wurtzite InN. This indicates there was no formation of wurtzite InN, instead In adlayer was deposited. Under optical microscope the sample grown at 490 ^{0}C has a dark surface. Whereas the samples grown at 520 ^{0}C and 540 ^{0}C are grey in appearance, the samples grown at 560 ℃ and 630 ℃ are shiny. Based on these investigations, it can be concluded that no In adlayer is present on the surface of the single crystalline InN NCs sample grown at 490℃. Although the InN micrograins samples grown at 520 ^{0}C and 540 ^{0}C are both single crystalline aligned along the [0001] and [10-11] directions respectively, both had the presence of In adlayer on the

146

sample surface grown alongside the InN. The appearance of films grown at 560-630 ^{0}C suggests the possibility of amorphous InN or In film [279].

8.3   Optical characterization of InN Nano Columns

Low temperature PL investigation was performed on the InN NCs. The 4K PL spectrum compared to that of a 2D thin film is depicted in Figure 8.6. The bright emissions at ~ 0.75 eV is attributed to the band to band InN NCs emission consistent with previous report[280].
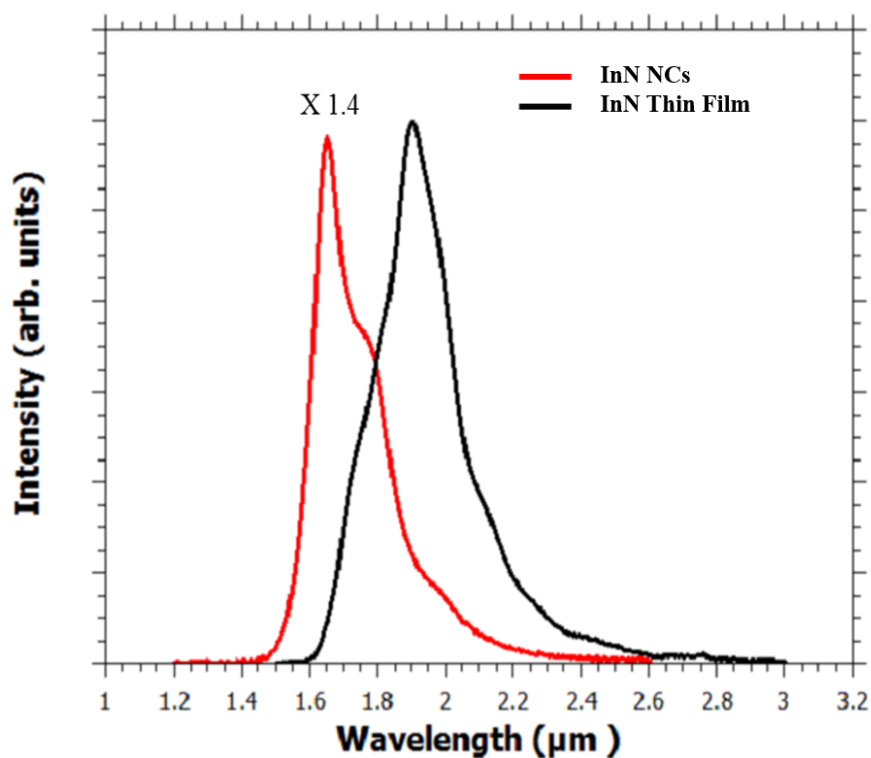
Figure 8.6 4K Photoluminescence spectra of InN nanocolumns compared with InN
         Thin film

The slight blue shift with respect to the InN thin film emission is associated with the Burstein-Moss[281] shift resulting from the pinning of the fermi level in the conduction band due to the presence of excess electrons in degenerate InN. This effect is particularly pronounced in the

147

NWs structures characterized by very large surface to volume ratio. The low energy shoulder is attributed to the Urbach tail populated by the transition of degenerate electrons to the shallow acceptor states[282, 283]. Finally, the NCs exhibit a narrower full width at half maximum (FWHM) of 50meV which is much narrower than that of the thin film (105meV) indicating its considerably high optical property.

Chapter 9

Conclusion

9.1 Conclusion

Semiconducting nanowire (NWs) are potential building blocks for novel, high performance optoelectronic devices. In particular, narrow band gap semiconductors NWs have attracted enormous research interest due to their unique band gap and exceptional properties. In this thesis, fundamental studies on the droplet epitaxy growth of InAs(Sb) alloys and InN NWs have been performed on Si and graphite substrates.

Although the Ga-assisted growth of GaAs NWs has been well-established, the In- assisted growth of NWs remains underexplored, particularly InAs NWs on Si. In this study the optimal growth conditions for In droplets suitable for the preferential nucleation and growth of NWs has been identified. Optimal In droplets were utilized for the nucleation and growth of all NWs without the use of foreign catalysts such as Au to avoid unwanted introduction of impurities. Vertically-aligned and non-tapered InAs NWs were then realized on bare Si (111). High-resolution TEM reveals the NWs present the zinc-blende structure with a high density of stacking faults and twin boundaries. The NWs exhibit a dominant PL peak associated with the band to band (BtB) emission in addition to a distinct BtB temperature dependent red-shift, strong emission efficiency (up to 250^0C) and record narrow spectral linewidth of ~20 meV (at 10K) which is relatively smaller than the commonly reported values. This demonstrates the high optical properties of the droplet epitaxy grown InAs NWs.

InAsSb NWs are highly challenging to nucleate directly on planar substrates (as all Sb-based NWs) as a result they are mostly grown on NWs stems to facilitate nucleation and growth. The

growth of vertically-aligned and non-tapered $InAs_{1-x}Sb_x$ NWs is demonstrated directly on bare Si without the commonly used NWs stems. The effect of Sb addition on the morphology of self-catalyzed InAsSb NWs was systematically investigated. It is shown that InAs NWs morphology can be manipulated with the addition of surfactant Sb. The injection of Sb even at very low concentrations produces a significant increase in the lateral growth rate with a suppression of axial growth rate. This is attributed to the surfactant effect of Sb which results in modifications to the kinetic and thermodynamic processes. By tuning the composition of antimony, the complete control of the crystal structure of $InAs_{1-x}Sb_x$ NWs grown directly on Si substrates is elucidated for the first time. This is substantiated by high-resolution transmission electron microscopy (HRTEM) combined with selected area electron diffraction (SAED) and photoluminescence spectroscopy investigations. Generally, pure InAs NWs show a mixture of Wurtzite (WZ) and Zinc-Blende (ZB) phases, however InAs crystal structure evolved to a quasi-pure WZ phase with the addition of ~2 to 4% Sb. A further increase (~10%) in Sb content resulted in a quasi-pure ZB InAsSb NWs. This is evidenced by photoluminescence (PL) measurements, where a dominant emission related to the WZ/ZB phase mixtures was observed in the pure InAs reference NWs but absent in the $InAs_{0.96}Sb_{0.04}$ NWs which instead show the band-to-band emission. It is also revealed that Sb addition significantly reduced the stacking fault density in the NWs.

This study also provides new insights on the optimized growth conditions for the growth of InAs NWs on graphite. By tuning basic growth parameters the optimal growth conditions for realizing morphologically and structurally superior InAs NWs on graphitic substrates has been established. Vertically well-aligned and thin InAs NWs were obtained in a narrow growth window of 420-450°C along with the realization of a high yield of NWs within a restricted domain of growth rate and V/III flux ratio. In addition, the dependence of NWs morphology on growth parameters was investigated on Si and Graphite. It is shown that axial InAs NWs

growth is more strongly influenced by growth duration for the NWs/graphite compared to the NWs/Si. The NWs on graphite exhibits a longer adatom diffusion length than that on Si. This has huge benefits for time-saving NWs synthesis and fabrication of cost-effective devices. Furthermore, the InAs NWs/graphite exhibit stronger temperature dependence in comparision to the InAs NWs/Si. This is evidenced by the significant enhancement in axial growth with a slight increase in growth temperature. A relatively high yield of NWs was obtained on graphite in comparison to Si for the investigated temperature range of 400 - 475°C. Although axial NWs growth on both substrates is favourable at As-rich conditions, NWs nucleation on Si shows a stronger dependence on the V/III flux ratio. In addition, NWs nucleation on Si is suppressed at relatively high growth rate while the graphitic substrates favour NWs growth at high growth rate. This indicates the graphitic thin films are highly promising for the fabrication of cost-effective nanodevices since it enables growth at high growth rate.

The monolithic integration of semiconductor NWs such as $InAs_{1-x}Sb_x$ on graphitic substrates holds enormous promise for high-performance, cost-effective and flexible optoelectronic devices and high-speed electronics. High aspect ratio nanowires are essential for functional device applications however, the growth of thin $InAs_{1-x}Sb_x$ NWs is extremely challenging owing to Sb-induced radial growth. For the first time, the self-catalyzed growth of vertically well-aligned, non-tapered and ultra-high aspect ratio (>100:1) $InAs_{1-x}Sb_x$ nanowires ($0 \leq x \leq 0.12$) is demonstrated on graphitic substrates at highly As-rich conditions by molecular beam epitaxy. This opens up a promising route towards the fabrication of $InAs_{1-x}Sb_x$ NWs/graphite hybrid structures for ultra-sensitive, eco-friendly and wearable gas sensing technology as well as flexible and cost-effective thermo photovoltaics. Compared to Si substrates, the graphitic thin films promote Sb incorporation and are more favourable for InAsSb NWs growth which is highly promising for Sb-based flexible optoelectronic device applications.

Finally, the In-assisted growth of InN NCs and microislands on bare Si (111) is explicated. A morphological evolution from NCs to three dimensional (3D) islands was observed with increasing growth temperature which is attributable to lowered surface free energy of the growing crystals with disproportionate growth velocities along different growth fronts. A strong correlation between the morphological and structural properties of the 3D films is established. XRD studies reveal that the NCs and the faceted microislands are single crystalline whereas the hemispherical microislands grown at extremely high growth temperature contain In adlayers. Finally, photoluminescent emissions were observed at ~ 0.75 eV from the InN NCs.

9.2   Outlook and future directions

Although significant contributions have been made to understand the droplet epitaxy growth of InAs NWs on Si, the NWs show a high density of stacking faults and twin boundaries consistent with previous reports of self-catalyzed growth, further research effort is needed to fully understand this phenomenon and improve the crystal structure without the addition of foreign elements such as Sb. In order to allow for the modulation of electrical properties as well as investigate the influence of dopants on the optical and electronic properties of InAs NWs, it will be interesting to fabricate doped InAs NWs; although it is especially challenging to make p-type InAs NWs because of Fermi level pinning around 0.1 eV above the conduction band. InAs Islands were observed to grow alongside the NWs; further research strategies are needed to provide new insights on strategies for the suppression of such clusters.

The growth of InAsSb NWs directly on Si and graphite has been demonstrated, however, further investigations such as tuning the growth parameters are required to further increase the Sb content beyond 10% to extend the band gap to the lower energies to enable applications

beyond the mid infrared range. More studies focused on the TEM and PL investigation of InAsSb NWs is crucial for device applications. Furthermore, the fabrication of InAsSb NWs based optoelectronic devices including infra-red detectors will be highly interesting.

Finally, the growth of InN NCs has been highly challenging. After an enormous amount of time (about two years) and research effort aimed at obtaining InN NWCs only the growth of large InN NCs and Islands were realized. It was observed that InN NCs growth is highly sensitive to surface treatments.

References

[1]   I. Ferain, C. A. Colinge, and J. P. Colinge, Nature **479**, 310 (2011).
[2]   J. A. D. Alamo, Nature **479**, 317 (2011).
[3]   G. E. Moore, Proceedings of IEEE **86**, 82 (1998).
[4]   http://www.deepspar.com/wp-data-loss.html.
[5]   K. A. Dick, Prog. Cryst. Growth Charact. Mater. **54**, 138 (2008).
[6]   A. Fasoli and W. I. Milne, Mater. Sci. Semicond. Process. **15**, 601 (2012).
[7]   K. Tomioka, J. Motohisa, S. Hara, and T. Fukui., . Nano. Lett. **8**, 3475 (2008).
[8]   Y. C. Chou, K. Hillerich, J. Tersoff, M. C. Reuter, K. A. Dick, and F. M. Ross, Science **343**, 281 (2014).
[9]   L. Y. Cao, J. S. White, J. S. Park, J. A. Schuller, B. M. Clemens, and M. L. Brongersma, Nat. Mater. **8**, 643 (2009).
[10]   A. I. Hochbaum, R. Fan, R. R. He, and P. D. Yang, Nano Lett. **5**, 457 (2005).
[11]   S. A. Fortuna and X. L. Li, Semicond. Sci. Technol. **25**, 024005 (2010).
[12]   W. Lu and C. M. Lieber, Nature Materials **6**, 841 (2007).
[13]   C. Kittel, Introduction to solid state physics (Hoboken, N.J. : Wiley, Hoboken, N.J., 2005).
[14]   I. Vurgaftman, J. R. Meyer, and L. R. Ram-Mohan, J. Appl. Phys. **89**, 5815 (2001).
[15]   T. C. McGill and D. A. Collins, Semicond. Sci. Technol. **8**, S1 (1993).
[16]   K. A. Dick, C. Thelander, L. Samuelson, and P. Caroff, Nano Lett. **10**, 3494 (2010).
[17]   I. Vurgaftman and J. R. Meyer, J. Appl. Phys.**94**, 3675 (2003).
[18]   R. Erdélyi, M. Hannibal Madsen, G. Sáfrán, Z. Hajnal, I. Endre Lukács, G. Fülöp, S. Csonka, J. Nygård, and J. Volk, Solid State Commun. **152**, 1829 (2012).
[19]   X. Wallart, J. Lastennet, D. Vignaud, and F. Mollot, Appl. Phys. Lett. **87**, 043504 (2005).
[20]   A. L. Eros and M. Rosen, Annu. Rev. Mater. Sci. **30**, 475 (2000).
[21]   A. C. Bleszynski, F. A. Zwanenburg, R. M. Westervelt, A. L. Roest, E. P. A. M. Bakkers, and L. P. Kouwenhoven, arXiv:cond-mat/0610514 [cond-mat.mes-hall] (2006).
[22]   M. J. Zheng, X. Y. Zhang, L. Yang, C. H. Liang, and L. D. Zhang, Semicond. Sci. Technol. **16**, 507 (2001).
[23]   E. Lioudakis, A. Othonos, G. C. Hadjisavvas, P. C. Kelires, and A. G. Nassiopoulou, Physica E **38**, 128 (2007).
[24]   J. Derr, K. Dunn, D. Riabinina, F. Martin, M. Chaker, and F. Rosei, Physica E **41**, 668 (2009).
[25]   Z. Zanolli, M. E. Pistol, L. E. Froberg, and L. Samuelson, J. Phys.: Condens. Matter **19,** 295219 (2007).
[26]   M. Z.Tidrow, Mater. Sci. Eng. B **74**, 45 (2000).
[27]   A. Rogalski, Infrared Phys. Technol. **43**, 187 (2002).
[28]   B. M. Borg, K.A. Dick, J. Eymery and L. E. Wernersson, Appl. Phys. Lett. **98**, 113104 (2011).
[29]   B. V. Olson, E. A. Shaner, J. K. Kim, J. F. Klem, S. D. Hawkins, L. M. Murray, J. P. Prineas, M. E. Flatté, and T. F. Boggess, Appl. Phys. Lett. **101**, 092109 (2012).
[30]   M. J. L. Sourribes, I. Isakov, M. Panfilova, H. Liu, and P. A. Warburton., Nano. Lett. **14**, 1643 (2014).
[31]   C. Thelander, P. Caroff, S. Plissard, K. A. Dick, Appl. Phys. Lett. **100**, 232105 (2012).
[32]   M. Y. Yen, R. People, K. W. Wecht, A. Y. Cho, Appl. Phys. Lett. **52**, 489 (1988).
[33]   M. Pea, D. Ercolani, A. Li, M. Gemmi, F. Rossi, F. Beltram, and L. Sorba, J.Cryst. Growth **366**, 8 (2013).
[34]   A. Rogalski, Progress in Quantum Electronics **27**, 59 (2003).
[35]   J. Q. Wu, J. Appl. Phys. **106**, 011101 (2009).
[36]   T. L. Tansley and C. P. Foley, J. Appl. Phys.**59**, 3241 (1986).
[37]   V. Y. Davydov, A. A. Klochikhin, V. V. Emtsev, S. V. Ivanov, V. V. Vekshin, F. Bechstedt, J. Furthmuller, H. Harima, A. V. Mudryi, A. Hashimoto, A. Yamamoto, J. Aderhold, J. Graul, E. E. Haller, Phys. Status Solidi B **230**, R4 (2002).

[38] V. Y. Davydov, A. A. Klochikhin, R. P. Seisyan, V. V. Emtsev, S. V. Ivanov, F. Bechstedt, J. Furthmuller, H. Harima, A. V. Mudryi, J. Aderhold, O. Semchinova, J. Graul, Phys. Status Solidi B **229**, R1 (2002).

[39] J. Chen, G. Cheng, E. Stern, M. A. Reed, and P. Avouris, Nano Lett. **7**, 2276 (2007).

[40] I. Mahboob, T. D. Veal, C. F. McConville, H. Lu and W. J. Schaff, Phys. Rev. Lett. **92**, 036804 (2004).

[41] J. Wu, W. Walukiewicz, K. M. Yu, J. W. Ager, E. E. Haller, H. Lu and W. J. Schaff, Appl. Phys. Lett. **80**, 4741 (2002).

[42] Y. J. Dong, B. Z. Tian, T. J. Kempa, and C. M. Lieber, Nano Lett. **9**, 2183 (2009).

[43] http://www.optiqueingenieur.org/en/courses/OPI_ang_M05_C02/co/Grain_OPI_ang_M05_C02.html

[44] http://ecee.colorado.edu/~bart/book/

[45] S. V.N. T. Kuchibhatla and A. S. Karakoti, D. Bera, S. Seal, Prog. Mater Sci. **52**, 699 (2007).

[46] N. Wang, Y.Cai, and R. Q. Zhang., Mater. Sci. Eng. R **60**, 1 (2008).

[47] M. Kuno, *Introductory Nanoscience: Physical and Chemical Concepts*. (Garland Science:Taylor and Francis group, Connecticut, United States of America, 2011).

[48] J. P. Colinge, C.-W. Lee, A. Afzalian, N. D. Akhavan, R. Yan, I. Ferain, P. Razavi, B. O'Neill, A. Blake, M. White, A. M. Kelleher, B. McCarthy and R. Murphy, Nat. Nanotechnol. **5**, 225 (2010).

[49] Y. Tian, R. Huang, Y. Wang, J. Zhuge, R. Wang, J. Liu, X. Zhang, and Y. Wang, IEEE IEDM Tech. Dig. 895 (2007).

[50] K. Tomioka, M. Yoshimura, and T. Fukui, Nature **488**, 189 (2012).

[51] X. Wang, J. Tong, X. Chen, B. Zhao, Z. Ren, D. Li, X. Zhuo, J. Zhang, H. Yi, C. Liu, F. Fang and S. Li, Chem. Commun. **50**, 682 (2014).

[52] X. Duan, Y. Huang, R. Agarwal, and C. M. Lieber, Nature **421**, 241 (2003).

[53] W.Wei, X.-Y. Bao, C. Soci, Y. Ding, Z.-L. Wang, and D. Wang, . Nano. Lett. **9**, 2926 (2009).

[54] M. D. Kelzenberg, S. W. Boettcher, J. A. Petykiewicz, D. B. Turner-Evans, M. C. Putnam, ,E. L. Warren, J. M. Spurgeon, R. M. Briggs, N. S. Lewis, H. A. Atwater, Nature Materials **9**, 239 (2010).

[55] J. Zhu, Z. Yu, G. F. Burkhard, C.-M. Hsu, S. T. Connor, Y. Xu, Q. Wang, M. McGehee, S. Fan and Y. Cui, . Nano. Lett. **9**, 279 (2009).

[56] C. Lin and M. L. Povinelli, Opt. Express **17**, 19371 (2009).

[57] L. Hu and G. Chen, Nano Lett. **7**, 3249 (2007).

[58] G. K. Mor, K. Shankar, M. Paulose, O. K. Varghese and C. A. Grimes, . Nano. Lett. **6**, 215 (2005).

[59] C. Y. Jiang, X. W. Sun, G. Q. Lo, D. L. Kwong, and J. X. Wang., Appl. Phys. Lett. **90**, 263501 (2007).

[60] D. Ercolani, M. Gemmi, L. Nasi, F. Rossi, M. Pea, A. Li, G. Salviati, F. Beltram, and L. Sorba, Nanotechnology **23**, 115606 (2012).

[61] T. Rieger, T. Schapers, D. Grützmacher, and M. I. Lepsa., Cryst. Growth Des. **14**, 1167.

[62] K. Weis, S. Wirths, A. Winden, K. Sladek, H. Hardtdegen, H. Lüth, and D. Gruetzmacher, T. Schäpers, Nanotechnology **25**, 135203 (2014).

[63] G. Koblmuller, K. Vizbaras, S. Hertenberger, S. Bolte, D. Rudolph, J. Becker, M. Doblinger, M. C. Amann, J. J. Finley and G. Abstreiter, Appl. Phys. Lett. **101**, 053103 (2012).

[64] J. Grandal, M. A. Sánchez-García, E. Calleja, E. Luna, and A. Trampert., Appl. Phys. Lett. **91**, 021902 (2007).

[65] L. C. Chuang, M. Moewe, C. Chase, N. P. Kobayashi, C. Chang-Hasnain, and S. Crankshaw, Appl. Phys. Lett. **90**, 043115, 043115 (2007).

[66] P. K. Mohseni, A. Behnam, J. D. Wood, X. Zhao, K. J. Yu, N. C. Wang, A. Rockett, J. A. Rogers, J. W. Lyding, E. Pop and X. Li., Adv. Mater. **26**, 3755 (2014).

[67] P. Krogstrup, H. I. Jorgensen, M. Heiss, O. Demichel, J. V. Holm, M. Aagesen, J. Nygard, and A. F. I. Morral, Nature Photonics **7**, 306 (2013).

[68] B. Tian, X. Zheng, T. J. Kempa, Y. Fang, N. Yu, G. Yu, J. Huang, and C. M. Lieber., Nature **449**, 885 (2007).

[69] E. C. Garnett and P. Yang, J. Am. Chem. Soc. **130**, 9224 (2008).

[70] F. Qian, S. Gradecak, Y. Li, C.-Y. Wen, and C. M. Lieber, Nano Lett. **5**, 2287 (2005).

[71] H. P. T. Nguyen, S. Zhang, K. Cui, X. Han, S. Fathololoumi, M. Couillard, G. A. Botton, and Z. Mi, Nano Lett. **11**, 1919 (2011).

[72] J. Svensson, N. Anttu, N. Vainorius, B. M. Borg, and L. E. Wernersson, Nano Lett. **13**, 1380 (2013).

[73] M. S. Vitiello, D. Coquillat, L. Viti, D. Ercolani, F. Teppe, A. Pitanti, F. Beltram, L. Sorba, W. Knap and A. Tredicucci, Nano Lett. **12**, 96 (2012).

[74] V. Mourik, K. Zuo, S. M. Frolov, S. R. Plissard, E. P. A. M. Bakkers, and L. P. Kouwenhoven., Science. **336**, 1003 (2012).

[75] R.S.Wagner and W. C. Ellis, Appl.Phys.Lett. **4**, 89 (1964).

[76] E. I. Givargizov, J.Cryst. Growth **31**, 20 (1975).

[77] V. G. Dubrovskii, N. V. Sibirev, R. A. Suris, G. E. Cirlin, J. C. Harmand, and V. M. Ustinov, Surf. Sci. **601**, 4395 (2007).

[78] R. R. LaPierre, A. C. E. Chia, S. J. Gibson, C. M. Haapamaki, J. Boulanger, R. Yee, P. Kuyanov, J. Zhang, N. Tajik, N. Jewell and K. M. A. Rahman, Phys. Status Solidi (RRL) **7**, 815 (2013).

[79] J. Johansson, C. P. T. Svensson, T. Mårtensson, L. Samuelson, and W. Seifert, J. Phys. Chem. B **109**, 13567 (2005).

[80] J. E. Allen, E. R. Hemesath, D. E. Perea, J. L. Lensch-Falk, Z. Y. Li, F. Yin, M. H. Gass, P. Wang, A. L. Bleloch, R. E. Palmer and L. J. Lauhon, Nature nanotechnology **3**, 168 (2008).

[81] K. A. Dick and P. Caroff, Nanoscale **6**, 3006 (2014).

[82] W. S. Shi, Y. F. Zheng, N. Wang, C.-S. Lee, and S.-T. Lee, Adv. Mater. **13**, 591 (2001).

[83] S. T. Lee, Y. F. Zhang, N. Wang, Y. H. Tang, I. Bello, C. S. Lee, and Y. W. Chung, J. Mater. Res. **14**, 4503 (1999).

[84] W. S. Shi, H. Y. Peng, N. Wang, C. P. Li, L. Xu, C. S. Lee, R. Kalish, and S. T. Lee, JACS **123**, 11095 (2001).

[85] W. S. Shi, Y. F. Zheng, N. Wang, C. S. Lee, and S. T. Lee, Appl. Phys. Lett. **78**, 3304 (2001).

[86] A. F. I. Morral, C. Colombo, G. Abstreiter, J. Arbiol, and J. R. Morante, Appl. Phys. Lett. **92**, 063112, 063112 (2008).

[87] C. Colombo, D. Spirkoska, M. Frimmer, G. Abstreiter, and A. F. I. Morral, Phys. Rev. B: Condens. Matter **77**, 155326 (2008).

[88] B. Mandl, J. Stangl, E. Hilner, A. A. Zakharov, K. Hillerich, A. W. Dey, L. Samuelson, G. Bauer, K. Deppert and A. Mikkelsen, Nano Lett. **10**, 4443 (2010).

[89] B. Mandl, J.Stangl, T. Mårtensson, A. Mikkelsen, J. Eriksson, L. S. Karlsson, G. Bauer, L. Samuelson, and W. Seifert., Nano. Lett. **6**, 1817 (2006).

[90] G. Koblmüller, S. Hertenberger, K. Vizbaras, M. Bichler, F. Bao, J.-P. Zhang, and G. Abstreiter, Nanotechnology **21**, 365602 (2010).

[91] N. Koguchi, S. Takahashi, and T. Chikyow., Journal of crystal growth **111**, 688 (1991).

[92] N. Koguchi and K. Ishige, Jpn. J. Appl. Phys. **32**, 2052 (1993).

[93] C. Heyn, A. Stemmann, A. Schramm, H. Welsch, W. Hansen, and A. Nemcsics, Phys. Rev. B: Condens. Matter **76**, 075317, 075317 (2007).

[94] J. H. Lee, Z. M. M. Wang, Z. Y. AbuWaar, and G. J. Salamo, Cryst. Growth Des. **9**, 715 (2009).

[95] H. Shesong, N. Zhichuan, F. Zhidan, N. Haiqiao, G. Zheng, and X. Jianbai, Appl. Phys. Lett. **89**, 031921 (2006).

[96] J. Wu, Z. M. M. Wang, V. G. Dorogan, S. B. Li, Z. H. Zhou, H. D. Li, J. Lee, E. S. Kim, Y. I. Mazur and G. J. Salamo, Appl. Phys. Lett. **101**, 043904 (2012).

[97] D. P. Kumah, S. Shusterman, Y. Paltiel, Y. Yacoby, and R. Clarke, Nature Nanotechnology **4**, 835 (2009).

[98] J. S. Kim and N. Koguchi, Appl. Phys. Lett. **85**, 5893 (2004).

[99] C. Somaschini, S. Bietti, N. Koguchi, and S. Sanguinetti, . Nano. Lett. **9**, 3419 (2009).

[100] J. Wu, D. L. Shao, V. G. Dorogan, A. Z. Li, S. B. Li, E. A. DeCuir, M. O. Manasreh, Z. M. Wang, Y. I. Mazur and G. J. Salamo, . Nano. Lett. **10**, 1512 (2010).
[101] S. N. Mohammad, Jpn. J. Appl. Phys. **110**, 084310 (2011).
[102] C. Cheze, L. Geelhaar, O. Brandt, W. M. Weber, H. Riechert, S. Munch, R. Rothemund, S. Reitzenstein, A. Forchel, T. Kehagias, P. Komninou, G. P. Dimitrakopulos and T. Karakostas, Nano Research **3**, 528 (2010).
[103] W. Jaegermann, R. Rudolph, A. Klein, and C. Pettenkofer., Thin solid Films **380**, 276 (2000).
[104] A. M. Munshi and H. Weman, Phys. Status Solidi (RRL) **7**, 713 (2013).
[105] A. Koma, J.Cryst. Growth **201**, 236 (1999).
[106] A. Koma, Thin Solid Films **216**, 72 (1992).
[107] J.-O. Carlsson and P. M. Martin, in Handbook of Deposition Technologies for Films and Coatings, edited by P. M. Martin (Elsevier Inc., Oxford, UK, 2010).
[108] J. L. Zilko, in Handbook of Thin Film Deposition Processes and Techniques: Principles, Methods, Equipment and Applications, edited by K. Seshan (Noyes Publications, New York, U.S.A., 2002).
[109] J.-H. Ryou, R. Kanjolia, and R. D. Dupuis., in Chemical vapour deposition [electronic resource] : precursors, processes and applications, edited by A. C. Jones, and M. L. Hitchman (Cambridge : Royal Society of Chemistry, Cambridge, 2009).
[110] A. Y. Cho and J. R. Arthur, in progress in Solid State Chemistry (Pergamon, New York, 1975).
[111] S. M. Sze, Semiconductor devices, physics and technology (Hoboken, N.J. : Wiley, Hoboken, N.J., 2002).
[112] J. R. Arthur, Surf. Sci. **500**, 189 (2002).
[113] G. Biasiol and L. Sorba, in Crystal growth of materials for energy production and energy-saving applications, edited by L. S. R. Fornari (Edizioni ETS, Pisa, Italy, 2001).
[114] http://iramis.cea.fr/en/Phocea/Vie_des_labos/Ast/ast_sstechnique.php?id_ast=494.
[115] S. Franchi, in Molecular beam epitaxy : from research to mass production, edited by M. Henini (Elsevier Inc, Oxford, 2013).
[116] M. A. Herman and H. Sitter, Molecular beam epitaxy : fundamentals and current status (Springer, Berlin, 1996).
[117] A. R. Barron, (Rice University course CHEM-496: Chemistry of Electronic Materials, 2009).
[118] B. A. Joyce, P. J. Dobson, J. H. Neave, K. Woodbridge, J. Zhang, and P. K. Larsen, B. Bolger, Surf. Sci. **168**, 423 (1986).
[119] M. Yazawa, M. Koguchi, and K. Hirutna., Appl. Phys. Lett. **58**, 1080 (1991).
[120] M. Yazawa, M. Koguchi, A. Muto, M. Ozawa, and K. Hiruma., Appl. Phys. Lett. **61**, 2051 (1992).
[121] J. A. Lebens, C. S. Tsai, J. Vahala, and T. F. Kuechi, Appl. Phys. Lett. **56**, 2642 (1990).
[122] E. Colas, S.Simhony, E. Kapoon, R. Bhat, D.M.Hwang, and P. S. D. Lin., Appl. Phys. Lett. **57**, 914 (1990).
[123] H.Dai, E. W. Wong, Y. Z. Lu, S. Fan, and C. M. Lieber, Nature **375**, 769 (1995).
[124] P. Yang and C. M. Lieber, Science **273**, 1836 (1996).
[125] T. C. Hou, Y. Yang, Z. H. Lin, Y. Ding, C. Park, K. C. Pradel, L. J. Chen, and Z. L. Wang, Nano Energy **2**, 387 (2013).
[126] Y. F. Hu, B. D. B. Klein, Y. J. Su, S. M. Niu, Y. Liu, and Z. L. Wang, . Nano. Lett. **13**, 5026 (2013).
[127] K. Q. Peng, X. Wang, L. Li, Y. Hu, and S. T. Lee, Nano Today **8**, 75 (2013).
[128] J. Wallentin, N. Anttu, D. Asoli, M. Huffman, I. Aberg, M. H. Magnusson, G. Siefer, P. Fuss-Kailuweit, F. Dimroth, B. Witzigmann, H. Q. Xu, L. Samuelson, K. Deppert and M. T. Borgstrom, Science **339**, 1057 (2013).
[129] P. Yang, R. Yan, and M. Fardy., . Nano. Lett. **10**, 1529 (2010).
[130] L. E. Jensen, M. T. Björk, S. Jeppesen, A. I. Persson, B. J. Ohlsson, and L. Samuelson., Nanotechnology **4**, 1961 (2004).
[131] K. A. Dick, K. Deppert, L. Samuelson, and W. Seifert, J. Cryst. Growth **297**, 326 (2006).
[132] M. Tchernycheva, L. Travers, G. Patriarche, F. Glas, J.-C. Harmand, G. E. Cirlin, and V. G. Dubrovskii, J. Appl. Phys. **102**, 094313 (2007).

[133] K. Osamura, A. Ohtsuki, P. H. Shingu, Y. Murakami, and K. Nakajima, Solid State Commun. **11**, 617 (1972).

[134] C.-L. Hsiao, L.-W. Tu, M. Chen, Z.-W. Jiang, N.-W. Fan, Y.-J. Tu, and K.-R. Wang., Jpn. J. Appl. Phys. **44**, pp. L1076 (2005).

[135] E. Calleja, J. Ristic, S. Fernandez-Garrido, L. Cerutti, M. A. Sanchez-Garcia, J. Grandal, A. Trampert, U. Jahn, G. Sanchez, A. Griol and B. Sanchez, Phys. Status Solidi (RRL) **244**, 2816 (2007).

[136] T. Mårtensson, C. P. T. Svensson, B. A. Wacaser, M. W. Larsson, W. Seifert, K. Deppert, A. Gustafsson, L. R. Wallenberg, and L. Samuelson., . Nano. Lett. **4**, 1987 (2004).

[137] B. Mandl, A. W. Dey, J. Stangl, M. Cantoro, L. E. Wernersson, G. Bauer, L. Samuelson, K. Deppert, and C. Thelander, J. Cryst. Growth **334**, 51 (2011).

[138] S. Hertenberger, D. Rudolph, M. Bichler, J. J. Finley, G. Abstreiter, and G. Koblmüller., J. Appl. Phys. **108**, 114316 (2010).

[139] Y. Jing, X. Bao, W. Wei, C. Li, K. Sun, D. P. R. Aplin, Y. Ding, Z.-L. Wang, Y. Bando and D. Wang, J. Phys. Chem. C **118**, 1696 (2014).

[140] S.-G. Ihn and J.-I. Song., Nanotechnology **18**, 355603 (2007).

[141] E. Dimakis, J. Lähnemann, U. Jahn, S. Breuer, M. Hilse, L. Geelhaar, and H. Riechert., Cryst. Growth Des. **11**, 4001 (2011).

[142] V. A.Nebol'sin, and A. A. Shchetinin, Inorg. Mater. **39**, 899 (2003).

[143] W.-N. Du, X.-G. Yang, X.-Y. Wang, H.-Y. Pan, H.-M. Ji, S. Luo, T. Yang, and Z.-G. Wang., J.Cryst. Growth **396**, 33 (2014).

[144] S. Gwo, C. L. Wu, C. H. Shen, W. H. Chang, T. M. Hsu, J. S. Wang, and J. T. Hsu., Appl. Phys. Lett. **84**, 3765 (2004).

[145] D. C. Look, H. Lu, W. J. Schaff, J. Jasinski, and Z. Liliental-Weber., Appl. Phys. Lett. **80**, 258 (2002).

[146] Y.-L. Chang, F. Li, A. Fatehi, and Z. Mi, Nanotechnology **20**, 345203 (2009).

[147] T. Stoica, R. Meijers, R. Calarco, T. Richter, and H. Lüth, J.Cryst. Growth **290**, 241 (2006).

[148] K. S. Novoselov, A. K. Geim, S. V. Morozov, D. Jiang, Y. Zhang, S. V. Dubonos, I. V. Grigorieva, and A. A. Firsov., Science **306**, 666 (2004).

[149] K. S. Novoselov, D. Jiang, F. Schedin, T. J. Booth, V. V. Khotkevich, S. V. Morozov, and A. K. Geim, Proceedings of the National Academy of Sciences of the United States of America **102**, 10451 (2005).

[150] A. K. Geim and K. S. Novoselov, Nature materials **6**, 183 (2007).

[151] Z.-S. Wu, W. Ren, L. Gao, J. Zhao, Z. Chen, B. Liu, D. Tang, B. Yu, C. Jiang and H.-M. Cheng., ACS Nano **3**, 411 (2009).

[152] H. Park, S. Chang, J. Jean, J. J. Cheng, P. T. Araujo, M. Wang, M. G. Bawendi, M. S. Dresselhaus, V. Bulović, J. Kong and S. Gradečak., . Nano. Lett. **13**, 233 (2012).

[153] Y. J. Kim, J. H. Lee, and G. C. Yi, Appl. Phys. Lett. **95**, 213101 (2009).

[154] L. G. De-Arco, Y. Zhang, C. W. Schlenker, K. Ryu, M. E. Thompson, and C. Zhou., Nano. Lett. **4**, 2865 (2010).

[155] X. Li, W. Cai, J. An, S. Kim, J. Nah, D. Yang, R. Piner, A. Velamakanni, I. Jung, E. Tutuc, S. K. Banerjee, L. Colombo and R. S. Ruoff., Science **324**, 1312 (2009).

[156] J. P. Alper, A. Gutes, C. Carraro, and R. Maboudian, Nanoscale **5**, 4114 (2013).

[157] J. M. Lee, J. W. Choung, J. Yi, D. H. Lee, M. Samal, D. K. Yi, C.-H. Lee, G.-C. Yi, U. Paik, J. A. Rogers and W. I. Park, . Nano. Lett. **10**, 2783 (2010).

[158] X. C. Miao, S. Tongay, M. K. Petterson, K. Berke, A. G. Rinzler, B. R. Appleton, and A. F. Hebard, Nano Lett. **12**, 2745 (2012).

[159] J. J. Yoo, K. Balakrishnan, J. Huang, V. Meunier, B. G. Sumpter, A. Srivastava, M. Conway, A. L. M. Reddy, J. Yu, R. Vajtai and P. M. Ajayan., Nano. Lett. **11**, 1423 (2011).

[160] J. K. Wassei and R. B. Kaner Materials today **13**, 52 (2010).

[161] F. Xia, T. Mueller, Y.-m. Lin, A. Valdes-Garcia, and P. Avouris., Nature Nanotechnology **4**, 839 (2009).

[162] Z. Sun and H. Chang, ACS Nano. **8**, 4133 (2014).

[163] F. Schedin, A. K. Geim, S. V. Morozov, E. W. Hill, P. Blake, M. I. Katsnelson, and K. S. Novoselov, Nature Materials **6**, 652 (2007).

[164] A. M. Munshi, D. L. Dheeraj, V. T. Fauske, D. C. Kim, A. T. J. van Helvoort, B. O. Fimland, and H. Weman, Nano Lett. **12**, 4570 (2012).

[165] Y. J. Hong and T. Fukui., Nano Lett.**5**, 7576 (2011).

[166] Y. J. Hong, W. H. Lee, Y. Wu, R. S. Ruoff, and T. Fukui., . Nano. Lett. **12**, 1431 (2012).

[167] J. Wallentin, D. Kriegner, J. Stangl, and M. T. Borgström., Nano Lett.**14**, 1707 (2014).

[168] P. K. Mohseni, A. Behnam, J. D. Wood, C. D. English, J. W. Lyding, E. Pop, and X. L. Li, . Nano. Lett. **13**, 1153 (2013).

[169] W. Zhou, R. P. Apkarian, Z. L. Wang, and D. Joy., Scanning Microscopy for Nanotechnology:Techniques and Applications, edited by Z. L. W. W. Zhou (Springer, New York, 2007).

[170] J. Goldstein, D. E. Newbury, D. C. Joy, C. E. Lyman, P. Echlin, E. Lifshin, L. Sawyer, and J. R. Michael, Scanning electron microscopy and x-ray microanalysis (Springer, New York, 2003).

[171] http://science.howstuffworks.com/scanning-electron-microscope2.htm.

[172] D. J. Smith, in Nanocharacterisation, edited by A. I. Kirkland, and J. L. Hutchison. (Royal Society of Chemistry, Cambridge, 2007).

[173] E. Ruska, Bioscience Reports **7**, 607 (1987).

[174] http://www.britannica.com/EBchecked/topic/183561/electron-microscope.

[175] http://www2.warwick.ac.uk/fac/sci/physics/research/condensedmatt/microscopy /facilities/jeol2100/

[176] B. D. Cullity, Elements of X-ray diffraction (Reading, Mass., Addison-Wesley Pub. Co., Reading, Mass., 1956).

[177] P. F. Fewster, X-ray scattering from semiconductors (River Edge, NJ : Imperial College Press, River Edge, NJ, 2003), 2nd ed. edn.

[178] http://neel.cnrs.fr/spip.php?article1010&lang=fr

[179] S. Chatterjee, S. S. Gadad, and T. K. Kundu., Resonance **15**, 622 (2010).

[180] P. E. West, Introduction to Atomic Force Microscopy:Theory, Practice, Applications (Pacific Nanotechnology, Santa Clara, CA, 2007).

[181] http://en.wikipedia.org/wiki/Atomic_force_microscopy

[182] http://www3.physik.uni-greifswald.de/method/afm/eafm.htm

[183] http://www.herzan.com/applications/techniques/afmspm.html.

[184] V. G. Dubrovskii and N. V. Sibirev, Phys. Rev. E: Stat. Phys., Plasmas, Fluids, **70**, 031604 (2004).

[185] The International Centre for Diffraction Data (ICDD) Newtown Square, PA, Powder Diffraction File 65-6115, (1994)

[186] J. Johansson, K. A. Dick, P. Caroff, M. E. Messing, J. Bolinsson, K. Deppert, and L. Samuelson, J. Phys. Chem. C **114**, 3837 (2010)

[187] F. Werner, F. Limbach, M. Carsten, C. Denker, J. Malindretos, and A. Rizzi, Nano Lett. **9**, 1567 (2009)

[188] M. C. Plante and R. R. LaPierre, J. Appl. Phys. **105**, 114304 (2009).

[189] V. G. Dubrovskii, G. E. Cirlin, I. P. Soshnikov, A. A. Tonkikh, N. V. Sibirev, Y. B. Samsonenko, and V. M. Ustinov, Phys. Rev. B: Condens. Matter **71**, 205325 (2005).

[190] G. E. Cirlin, V. G. Dubrovskii, Y. B. Samsonenko, A. D. Bouravleuv, K. Durose, Y. Y. Proskuryakov, B. Mendes, L. Bowen, M. A. Kaliteevski, R. A. Abram and D. Zeze., Phys. Rev. B: Condens. Matter **82**, 035302 (2010).

[191] V. G. Dubrovskii, N. V. Sibirev, G. E. Cirlin, J. C. Harmand, and V. M. Ustinov, Phys. Rev. E: Stat. Phys., Plasmas, Fluids **73**, 021603 (**2006**).

[192] J. C. Harmand, M. Tchernycheva, G. Patriarche, L. Travers, F. Glas, and G. Cirlin, J.Cryst. Growth **301**, 853 (2007).

[193] S. A. Dayeh, E. T. Yu, and D. Wang, . Nano. Lett. **9**, 1967 (2009).

[194] P. Caroff, M. E. Messing, B. M. Borg, K. A. Dick, K. Deppert, and L.-E. Wernersson, Nanotechnology **20**, 495606, 495606 (2009).

[195] F. Glas, M. R. Ramdani, G. Patriarche, and J. C. Harmand, Phys. Rev. B: Condens. Matter **88**, 195304 (2013).

[196]   M. R. Ramdani, J. C. Harmand, F. Glas, G. Patriarche, and L. Travers, Cryst. Growth Des. **13**, 91 (2013).

[197]   J. B. Babu and K. Yoh, J.Cryst. Growth **323**, 301 (2011).

[198]   S. A. Dayeh, E. T. Yu, and D. Wang, Nano. Lett. **7**, 2486 (2007).

[199]   A. I. Persson, L. E. Froberg, S. Jeppesen, M. T. Bjork, and L. Samuelson, J. Appl. Phys. **101**, 034313 (2007).

[200]   M. H. Sun, E. S. P. Leong, A. H. Chin, C. Z. Ning, G. E. Cirlin, Y. B. Samsonenko, V. G. Dubrovskii, L. Chuang and C. Chang-Hasnain., Nanotechnology **21**, 335705 (2010).

[201]   P. Gladkov, D. Nohavica, Z. Sourek, A. P. Litvinchuk and M. N. Iliev, Semicond. Sci. Technol. **21**, 544 (2006).

[202]   R. D. Grober, H. D. Drew, J. I. Chyi, S. Kalem and H. Morkoc, J. Appl. Phys. **65**, 4079 (1989).

[203]   M. Fisher and A. Krier, Infrared Phys. Technol. **38**, 405 (1997).

[204]   M. I. Guseva, Zotova, N.V., Koval', A.V., Nasledov, D.N, Sov. Phys. Semicond. **9**, 591 (1975).

[205]   Y. Lacroix, C. A. Tran, S. P. Watkins and M. L. W. Thewalt, J. Appl. Phys. **80**, 6416 (1996).

[206]   M. H. Sun, H. J. Joyce, Q. Gao, H. H. Tan, C. Jagadish and C. Z. Ning, Nano Lett. **12**, 3378 (2012).

[207]   B. Cao, W. Cai and H. Zeng, Appl. Phys. Lett. **88**, 161101 (2006).

[208]. Z. M. Fang, K. Y. Ma, D. H. Jaw, R. M. Cohen and G. B. Stringfellow, J. Appl. Phys. **67**, 7034 (1990).

[209]   L. O. Olsson, C. B. M. Andersson, M. C. Hakansson, J. Kanski, L. Ilver and U. O. Karlsson, Phys. Rev. Lett. **76**, 3626 (1996).

[210]   J. Du, D. Liang, H. Tang and X. P. A. Gao, Nano. Lett. **9**, 4348 (2009).

[211]   Y. Chen, J. C. Hermanson and G. J. Lapeyre, Phys. Rev. B: Condens. Matter **39**, 12682 (1989).

[212]   Z. Zanolli, F. Fuchs, J. Furthmueller, U. von Barth and F. Bechstedt, Phys. Rev. B: Condens. Matter **75**, 245121 (2007).

[213]   J. Bao, D. C. Bell, F. Capasso, N. Erdman, D. Wei, L. Froberg, T. Martensson and L. Samuelson, Adv. Mater. **21**, 3654 (2009).

[214]   M. Moller, M. M. de Lima, Jr., A. Cantarero, T. Chiaramonte, M. A. Cotta and F. Iikawa, Nanotechnology **23**, 375704 (2012).

[215]   M. Murayama and T. Nakayama, Phys. Rev. B: Condens. Matter **49**, 4710 (1994).

[216]   A. De and C. E. Pryor, Phys. Rev. B: Condens. Matter **81**, 155210 (2011).

[217]   Y. P. Varshni., Physica **34**, 149 (1967).

[218]   T. Stoica, R. J. Meijers, R. Calarco, T. Richter, E. Sutter and H. Luth, Nano. Lett. **6**, 1541 (2006).

[219]   S. Zhao, S. Fathololoumi, K. H. Bevan, D. P. Liu, M. G. Kibria, Q. Li, G. T. Wang, H. Guo and Z. Mi, Nano. Lett. **12**, 2877 (2012).

[220]   P. Zaumseil and T. Schroeder, J. Appl. Phys. **104**, 023532 (2008).

[221]   The International Centre for Diffraction Data (ICDD) Newtown Square, PA, Powder Diffraction File 89-3667 (1994).

[222]   L. Z. Vegard, phys. **5**, 17 (1921).

[223]   E. A. Anyebe and Q. Zhuang, Mater. Res. Bull. **60**, 572 (2014).

[224]   E. A. El-wahabb, S. S. Fouad, and M. Fadel, J. Mater. Sci. - Mater. Electron. **38**, 527 (2003).

[225]   S. S. Fouad, A. H. Ammar, and M. Abo-Ghazala., Physica B. **229**, 249 (1997).

[226]   S. W. Kim, J. P. Zimmer, S. Ohnishi, J. B. Tracy, J. V. Frangioni, and M. G. Bawendi, J. Am. Chem. Soc. **127**, 10526 (2005).

[227]   Q. Gong, R. Nötzel, P. J. van Veldhoven, T. J. Eijkemans, and J. H. Wolter., Appl. Phys. Lett. **84**, 275 (2004).

[228]   J. Steinshnider, J. Harper, M. Weimer, C. H. Lin, S. S. Pei, and D. H. Chow, Phys. Rev. Lett. **85**, 4562 (2000).

[229]   D. P. Woodruff and J. Robinson, J. Phys.: Condens. Matter **12**, 7699 (2000).

[230]   F. Dimroth, C. Agert, and A. W. Bett, J. Cryst. Growth **248**, 265 (2003).

[231]   B. M. Borg and L.-E. Wernersson, Nanotechnology **24**, 202001, 202001 (2013).

[232] F. Aqra and A. Ayyad, Appl. Surf. Sci. **257**, 6372 (2011).
[233] G. Pindoria, R. A. A. Kubiak, S. M. Newstead, and D. P. Woodruff., Surf. Sci. **234**, 17 (1990).
[234] X. Yang, M. J. Jurkovic, J. B. Heroux, and W. I. Wang., Appl. Phys. Lett. **75**, 178 (1999).
[235] C. Jiang and H. Sakaki, Physica E **26**, 180 (2005).
[236] H. Miyoshi, R. Suzuki, H. Amano, and Y. Horikoshi, J.Cryst. Growth **237**, 1519 (2002).
[237] A. Portavoce, I. Berbezier, P. Gas, and A. Ronda, Phys. Rev. B: Condens. Matter **69,** 155414 (2004).
[238] G. Tréglia, B. Legrand, F. Ducastelle, A. Saúl, C. Gallis, I. Meunier, C. Mottet, and A. Senhaji, Comput. Mater. Sci. **15**, 196 (1999).
[239] Q. Zhuang, A. Godenir, A. Krier, G. Tsai, and H. H. Lin., Appl. Phys. Lett. **93**, 121903 (2008).
[240] E. A. Anyebe, M. K. Rajpalke, T. D. Veal, C. J. Jin, Z. M. Wang and Q. Zhuang., Nano Research (Just accepted) DOI 10.1007/s12274-014-0621-x
[241] K. A. Dick, S. Kodambaka, M. C. Reuter, K. Deppert, L. Samuelson, W. Seifert, L. R. Wallenberg, and F. M. Ross, Nano Lett. **7**, 1817 (2007).
[242] M. Copel, M. C. Reuter, E. Kaxiras, and R. M. Tromp., Phys. Rev. Lett. **63**, 632 (1989).
[243] M. Volmer and A. Z. Weber, Phys. Chem. **119**, 277 (1926).
[244] F. C. Frank and J. H. Van der Merwe, Proc. R. Soc. **A198**, 205 (1949).
[245] M. Zinke-Allmang, Thin Solid Films **346**, 1 (1999).
[246] A. Portavoce, I. Berbezier, and A. Ronda, Mater. Sci. Eng., B **101**, 181 (2003).
[247] M. Pozuelo, H. Zhou, S. Lin, S. A. Lipman, M. S. Goorsky, R. F. Hicks, and S. Kodambaka, J.Cryst. Growth **329**, 6 (2011).
[248] D. N. McIlroy, A. Alkhateeb, D. Zhang, D. E. Aston, A. C. Marcy, and M. G. Norton, J. Phys. Condes. Matter **16**, R415 (2004).
[249] J. Massies and N. Grandjean, Phys. Rev. B: Condens. Matter **48**, 8502 (1993).
[250] E. Tournié, N. Grandjean, A. Trampert, J. Massies, and K. H. Ploog, J. Cryst. Growth **150**, 460 (1995).
[251] P. Nimmatoori, Q. Zhang, E. C. Dickey, and J. M. Redwing, Nanotechnology **20**, 025607 (2009).
[252] B. A. Joyce, J. M. Fernández, M. H. Xie, A. Matsumura, J. Zhang, and A. G. Taylor., J.Cryst. Growth **164**, 214 (1996).
[253] M. H. Xie, J. Zhang, A. Lees, J. M. Fernandez, and B. A. Joyce, Surf. Sci. **367**, 231 (1996).
[254] V. G. Dubrovskii, N. V. Sibirev, J. C. Harmand, and F. Glas., Phys. Rev. B: Condens. Matter **78**, 235301 (2008).
[255] K. A. Dick, K. Deppert, T. Mårtensson, B. Mandl, L. Samuelson, and W. Seifert., Nano. Lett. **5**, 761 (2005).
[256] P. Caroff, J. Bolinsson, and J. Johansson, IEEE J. Sel. Top. Quantum Electron. **17**, 829 (2011).
[257] T. Akiyama, K. Sano, K. Nakamura, and T. Ito, Jpn. J. Appl. Phys., Part 2 **45**, L275 (2006).
[258] K. A. Dick, P. Caroff, J. Bolinsson, M. E. Messing, J. Johansson1, K. Deppert, L. R. Wallenberg, and L. Samuelson., Semicond. Sci. Technol. **25**, 024009 (2010).
[259] V. G. Dubrovskii and N. V. Sibirev, Phys. Rev. B: Condens. Matter **77**, 035414 (2008).
[260] Q. D. Zhuang, E. A. Anyebe, R. Chen, H. Liu, A. M. Sanchez, M. K. Rajpalke, T. D. Veal, Z. M. Wang, Y. Z. Huang and H. D. Sun., Nano. Lett. **15**, 1109 (2015).
[261] J. Wallentin, M. Ek, L. R. Wallenberg, L. Samuelson, K. Deppert, and M. T. Borgstrom, . Nano. Lett. **10**, 4807 (2010).
[262] R. E. Algra, M. A. Verheijen, L. F. Feiner, G. G. W. Immink, W. J. P. van Enckevort, E. Vlieg, and E. P. A. M. Bakkers, . Nano. Lett. **11**, 1259 (2011).
[263] S. Lehmann, J. Wallentin, D. Jacobsson, K. Deppert, and K. A. Dick, . Nano. Lett. **13**, 4099 (2013).
[264] F. Glas, J. C. Harmand, and G. Patriarche, Phys. Rev. Lett. **99**, 146101 (2007).
[265] B. Mandl, K. A. Dick, D. Kriegner, M. Keplinger, G. Bauer, J. Stangl, and K. Deppert, Nanotechnology **22**, 145603, 145603 (2011).

[266] J. Wallentin, K. Mergenthaler, M. Ek, L. R. Wallenberg, L. Samuelson, K. Deppert, M.-E. Pistol, and M. T. Borgstrom, . Nano. Lett. **11**, 2286 (2011).

[267] K. Kawaguchi, M. Ekawa, T. Akiyama, H. Kuwatsuka, and M. Sugawara, J.Cryst. Growth **291**, 154 (2006).

[268] M. H. Sun, E. S. P. Leong, A. H. Chin, C. Z. Ning, G. E. Cirlin, Y. B. Samsonenko, V. G. Dubrovskii, L. Chuang, and C. Chang-Hasnain., Nanotechnology **21**, 335705 (2010).

[269] Q. Zhuang, E. A. Anyebe, A. M. Sanchez, M. K. Rajpalke, T. D. Veal, A. Zhukov, B. J. Robinson, F. Anderson, O. Kolosov and V. Falko., Nanoscale Res. Lett. **9**, 321 (2014).

[270] S. N. Mohammad, J. Chem. Phys. **131**, 204703 (2009).

[271] P. G. Klemens and D. F. Pedraza., Carbon **32**, 735 (1994).

[272] M. I. B. Utama, Q. Zhang, J. Zhang, Y. Yuan, F. J. Belarre, J. Arbiol, and Q. H. Xiong, Nanoscale **5**, 3570 (2013).

[273] M. I. B. Utama, F. J. Belarre, C. Magen, B. Peng, J. Arbiol, and Q. Xiong, . Nano. Lett. **12**, 2146 (2012).

[274] Y. Zhu, Y. Zhou, M. I. B. Utama, M. de la Mata, Y. Y. Zhao, Q. Zhang, B. Peng, C. Magen, J. Arbiol and Q. H. Xiong, Nanoscale **5**, 7242 (2013).

[275] S. R. Plissard, D. R. Slapak, M. A.Verheijen, M. Hocevar, G. W. G. Immink, I. van Weperen, S. Nadj-Perge, S. M. Frolov, L. P. Kouwenhoven and E. P. A. M. Bakkers, . Nano. Lett. **12**, 1794 (2012).

[276] M. A. Sánchez-García, J. Grandal, E. Calleja, S. Lazic, J. M. Calleja, and A. Trampert., Phys. Status Solidi B **243**, 1490 (2006).

[277] B. Leung, Q. Sun, C. D. Yerino, J. Han, and M. E. Coltrin, Semicond. Sci. Technol. **27**, 024005 (2012).

[278] H. Liu, L. Shi, X. Geng, R. Su, G. Cheng, and S. Xie, Nanotechnology **21**, 245601 (2010).

[279] A.M.S. ElAhl, M. He, P. Zhou, G. L. Harris, L. Salamanca-Riba, F. Felt, H. C. Shaw, A. Sharma, M. Jah, D. Lakins, T. Steiner and S. N. Mohammad, J. Appl. Phys. **94**, 7749 (2003).

[280] M. Kumar, T. N. Bhat, M. K. Rajpalke, B. Roul, A. T. Kalghatgi, and S. B. Krupanidhi, Nanoscale Res. Lett. **6**, 609 (2011).

[281] J. Wu, W. Walukiewicz, S. X. Li, R. Armitage, J. C. Ho, E. R. Weber, E. E. Haller, H. Lu, W. J. Schaff, A. Barcz and R. Jakiela., Appl. Phys. Lett. **84**, 2805 (2004).

[282] A. Klochikhin, V. Davydov, V. Emtsev, A. Sakharov, V. Kapitonov, B. Andreev, H. Lu, and W. J. Schaff, Phys. Status Solidi A **203**, 50 (2006).

[283] A. A. Klochikhin, V. Y. Davydov, V. V. Emtsev, A. V. Sakharov, V. A. Kapitonov, B. A. Andreev, H. Lu, and W. J. Schaff., Phys. Rev. B: Condens. Matter **71**, 195207 (2005).